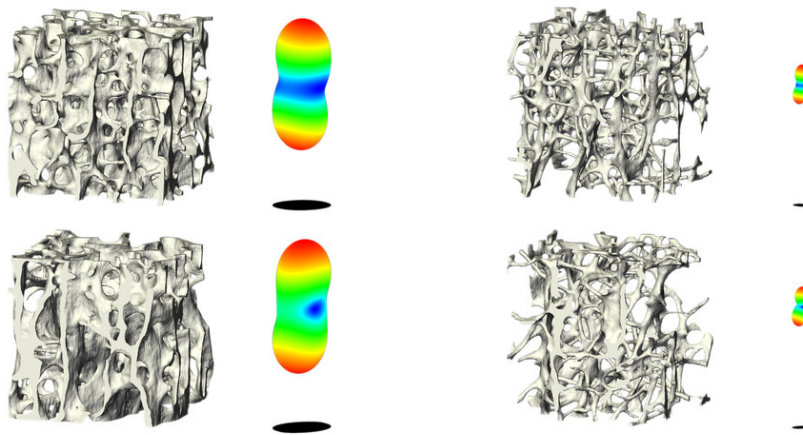


Composite Finite Elements for Trabecular Bone Microstructures



Dissertation

zur Erlangung des Doktorgrades (Dr. rer. nat.)
der Mathematisch–Naturwissenschaftlichen Fakultät
der Rheinischen Friedrich–Wilhelms–Universität Bonn

vorgelegt von Lars Ole Schwen
aus Düsseldorf

Bonn, Juli 2010

Angefertigt mit Genehmigung der Mathematisch–Naturwissenschaftlichen Fakultät
der Rheinischen Friedrich–Wilhelms–Universität Bonn
am Institut für Numerische Simulation

Diese Dissertation ist auf dem Hochschulschriftenserver der Universitäts- und Landesbibliothek Bonn http://hss.ulb.uni-bonn.de/diss_online elektronisch publiziert sowie als Buch mit der ISBN 978-3-938363-78-2 bei HARLAND media erschienen.

Erscheinungsjahr: 2010

1. Gutachter: Prof. Dr. Martin Rumpf
2. Gutachter: Prof. Dr. Alexey Chernov

Tag der Promotion: 07. Oktober 2010

To my aunt Helga (1947 – 2006)

This document was typeset using pdfL^AT_EX, the KOMA-Script scrbook document class, Palladio/Mathpazo and Classico fonts, and (among many others) the microtype package.

Cooperations and Previous Publications

This thesis was written as part of a joint research project with Prof. Dr. Hans-Joachim Wilke and Dipl.-Ing. Uwe Wolfram (Institute of Orthopaedic Research and Biomechanics, University of Ulm), Prof. Dr. Tobias Preusser (Fraunhofer MEVIS, Bremen), and Prof. Dr. Stefan Sauter (Institute of Mathematics, University of Zurich).

Parts of this thesis have been published or submitted for publication in the following journal and proceedings articles:

- Florian Liehr, Tobias Preusser, Martin Rumpf, Stefan Sauter, and Lars Ole Schwen, *Composite finite elements for 3D image based computing*, Computing and Visualization in Science **12** (2009), no. 4, pp. 171–188, reference [217]
- Tobias Preusser, Martin Rumpf, and Lars Ole Schwen, *Finite element simulation of bone microstructures*, Proceedings of the 14th Workshop on the Finite Element Method in Biomedical Engineering, Biomechanics and Related Fields, University of Ulm, July 2007, pp. 52–66, reference [282]
- Lars Ole Schwen, Uwe Wolfram, Hans-Joachim Wilke, and Martin Rumpf, *Determining effective elasticity parameters of microstructured materials*, Proceedings of the 15th Workshop on the Finite Element Method in Biomedical Engineering, Biomechanics and Related Fields, University of Ulm, July 2008, pp. 41–62, reference [311]
- Uwe Wolfram, Lars Ole Schwen, Ulrich Simon, Martin Rumpf, and Hans-Joachim Wilke, *Statistical osteoporosis models using composite finite elements: A parameter study*, Journal of Biomechanics **42** (2009), no. 13, pp. 2205–2209, reference [379]
- Lars Ole Schwen, Tobias Preusser, and Martin Rumpf, *Composite finite elements for 3D elasticity with discontinuous coefficients*, Proceedings of the 16th Workshop on the Finite Element Method in Biomedical Engineering, Biomechanics and Related Fields, University of Ulm, 2009, accepted, reference [310]
- Tobias Preusser, Martin Rumpf, Stefan Sauter, and Lars Ole Schwen, *3D composite finite elements for elliptic boundary value problems with discontinuous coefficients*, 2010, submitted to SIAM Journal on Scientific Computing, reference [281]
- Martin Rumpf, Lars Ole Schwen, Hans-Joachim Wilke, and Uwe Wolfram, *Numerical homogenization of trabecular bone specimens using composite finite elements*, 1st Conference on Multiphysics Simulation – Advanced Methods for Industrial Engineering, Fraunhofer, 2010, reference [296]

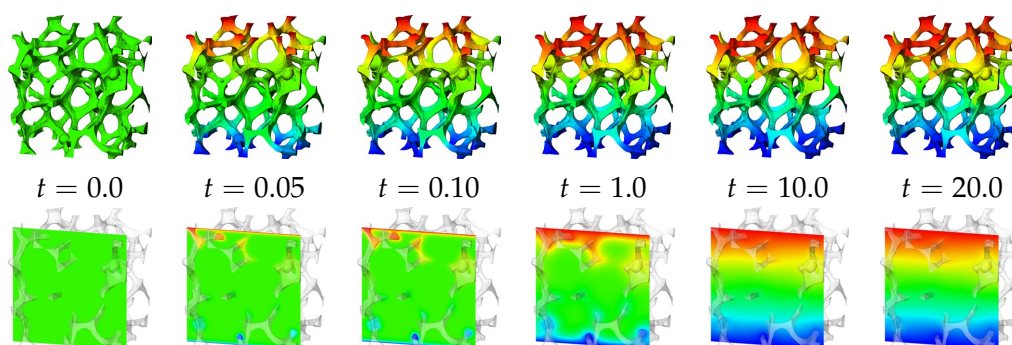
Most C++ code developed for this dissertation has been published as part of the QuocMesh software library by AG Rumpf, Institute for Numerical Simulation, University of Bonn.

AMS Subject Classifications (MSC2010)

65D05, 65M55, 65M60, 65N30, 65N55, 74B05, 74Q05, 74S05, 80M10, 80M40, 92C10

Summary

In many medical and technical applications, numerical simulations need to be performed for objects with interfaces of geometrically complex shape. We focus on the biomechanical problem of elasticity simulations for trabecular bone microstructures. The goal of this dissertation is to develop and implement an efficient simulation tool for finite element (FE) simulations on such structures, so-called composite FE. We will deal with both the case of material/void interfaces ('complicated domains') and the case of interfaces between different materials ('discontinuous coefficients').



For an aluminum foam embedded in polymethylmethacrylate subject to heating and cooling at the top and bottom, respectively, heat diffusion is simulated and the temperature is visualized.



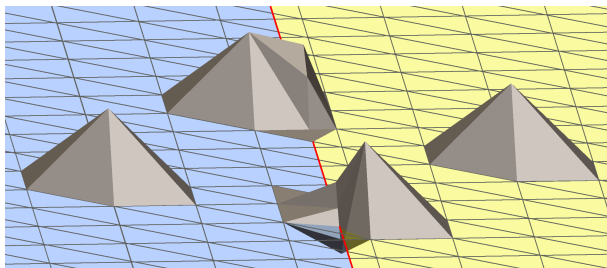
Shearing simulation for a cylindrical specimen of porcine trabecular bone. Zooms to one corner of the specimen are shown on the right. All deformations are scaled for better visualization.

Compression simulation for a cuboid specimen of porcine trabecular bone embedded in polymethylmethacrylate. Color in both cases encodes the von Mises stress at the interface.

Construction of Composite FE. In classical FE simulations, geometric complexity is encoded in tetrahedral and typically unstructured meshes. Composite FE, in contrast, encode geometric complexity in specialized basis functions on a uniform mesh of hexahedral structure. Other than alternative approaches (such as, e.g., fictitious domain methods, GFEM, immersed interface methods, partition of unity methods, unfitted meshes, and XFEM), the composite FE are tailored to geometry descriptions by 3D voxel image data and use the corresponding voxel grid as computational mesh, without introducing additional degrees of freedom, and thus making use of efficient data structures for uniformly structured meshes.

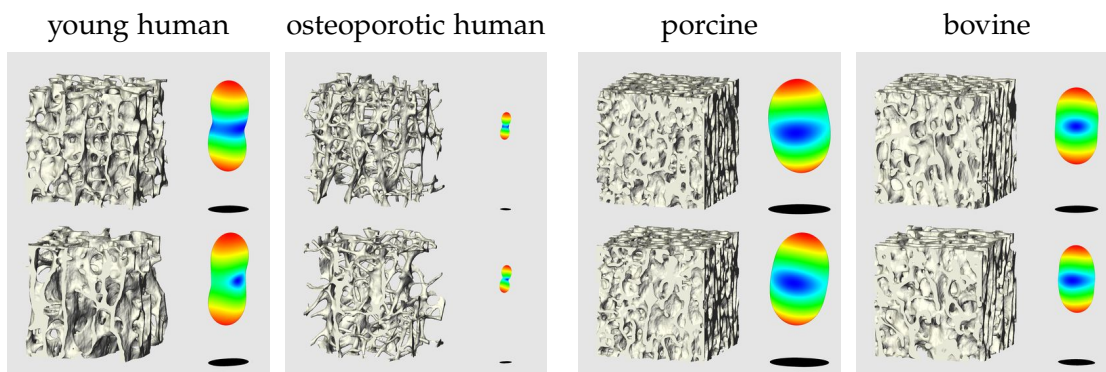
The composite FE method for complicated domains goes back to Hackbusch and Sauter [Numer. Math. **75** (1997), 447–472; Arch. Math. (Brno) **34** (1998), 105–117] and restricts standard affine FE basis functions on the uniformly structured tetrahedral grid (obtained by subdivision of each cube in six tetrahedra) to an approximation of

the interior. This can be implemented as a composition of standard FE basis functions on a local auxiliary and purely virtual grid by which we approximate the interface. In case of discontinuous coefficients, the same local auxiliary composition approach is used. Composition weights are obtained by solving local interpolation problems for which coupling conditions across the interface need to be determined. These depend both on the local interface geometry and on the (scalar or tensor-valued) material coefficients on both sides of the interface. We consider heat diffusion as a scalar model problem and linear elasticity as a vector-valued model problem to develop and implement the composite FE. Uniform cubic meshes contain a natural hierarchy of coarsened grids, which allows us to implement a multigrid solver for the case of complicated domains.



Near an interface (red line) which is not resolved by the regular computational grid, composite FE basis functions are constructed in such a way that they can approximate functions satisfying a coupling condition (depending on the coefficients) across the interface.

Homogenization. Besides simulations of single loading cases, we also apply the composite FE method to the problem of determining effective material properties, e.g., for multiscale simulations. For periodic microstructures, this is achieved by solving corrector problems on the fundamental cells using affine-periodic boundary conditions corresponding to uniaxial compression and shearing. For statistically periodic trabecular structures, representative fundamental cells can be identified but do not permit the periodic approach. Instead, macroscopic displacements are imposed using the same set as before of affine-periodic Dirichlet boundary conditions on all faces. The stress response of the material is subsequently computed only on an interior subdomain to prevent artificial stiffening near the boundary. We finally check for orthotropy of the macroscopic elasticity tensor and identify its axes.



For specimens of vertebral trabecular bone of bipeds and quadrupeds, effective elasticity tensors are visualized (where elongation indicates directional compressive stiffness). The human tensors are scaled by 4 relative to the animal tensors.

Notation

$\mathbb{1}$	constant-1 function $\mathbb{1}(x) = 1$
a	thermal diffusivity tensor (p. 13)
$\mathbb{A}(z)$	set of simplices adjacent to virtual node z (p. 34)
B	(local) matrices for construction of CFE weights (pp. 43 and 48)
c	mass-specific heat capacity (p. 13)
χ_M	characteristic function of a set M (p. 36)
C^k	space of real-valued, k times continuously differentiable functions
$(C^k)^3$	space of \mathbb{R}^3 -valued, k times continuously differentiable functions
C	elasticity tensor (p. 14)
d	space dimension, typically 2 or 3
$\mathbb{D}(r)$	set of virtual nodes constrained by a regular node r (p. 34)
$\mathbb{D}(f)$	'descendants' in multigrid coarsening (p. 90)
$\delta_{i,j}$	Kronecker symbol (p. 17)
e_i	i^{th} unit vector
E	Young's modulus (p. 16); FE elasticity block matrix (p. 60)
$\epsilon[u]$	strain (p. 14)
\mathcal{G}	grid/mesh: \mathcal{G}^\square regular cubic grid (p. 28), \mathcal{G}^\boxtimes regular tetrahedral mesh (p. 28), \mathcal{G}^Δ virtual (tetrahedral) mesh (p. 30)
γ	curved interface (p. 28)
Γ	(piecewise) planar interface (p. 29)
H_\pm	halfspaces (subdomains for a planar interface; p. 19)
$H^{m,p}$	Sobolev space (p. 14)
Id	identity function $\text{Id}(x) = x$ or identity matrix
\mathcal{I}	index set for a node set \mathcal{N} : \mathcal{I}^\square (p. 28), \mathcal{I}^Δ (p. 30); interpolation operators
j	global index (p. 28, 98)
K, L	(local) matrices arising in coupling conditions across an interface (p. 22, 23)
L	FE stiffness matrix (p. 58)
λ	first Lamé-Navier number (p. 16); thermal conductivity (p. 13)
Λ	generic domain for model problems (p. 13)
$\Lambda^\#$	computation domain for cell problems, $\Lambda^{\#\beta}$ evaluation domain (p. 64)
M	FE (block) mass matrix (p. 58)
μ	second Lamé-Navier number (p. 16)
n	normal direction (p. 19)
\mathcal{N}	node sets: $\mathcal{N}^\square = \mathcal{N}^\boxtimes$ (p. 28), \mathcal{N}^Δ , $\mathcal{N}^{\text{virt}}$ (p. 30), \mathcal{N}^{DOF} (p. 34)
ν	Poisson's ratio (p. 16)
Ω_\pm	subdomains (material/void or different coefficients; p. 28)
Ω_\pm^Δ	piecewise tetrahedral approximation of Ω_\pm (p. 29)
$\Omega^\#$	fundamental cell of exactly or statistically periodic microstructure (p. 64)
$\mathbb{P}(z)$	set of regular nodes constraining a virtual node z (p. 34)
$\mathbb{P}^\setminus(z), \mathbb{P}^\boxplus(z)$	constraint sets (p. 34)
$\mathbb{P}(c)$	'parents' in multigrid coarsening (p. 90)

\mathcal{P}	multigrid prolongation (p. 88)
$\mathcal{P}_{T,z,n}$	local interpolation (p. 41, 47)
φ	continuous level set function (p. 28)
Φ	piecewise affine approximation of φ (p. 29)
ψ	FE basis function: ψ_z^Δ virtual (p. 34), ψ_r^{CFE} CFE basis function (p. 34)
Ψ	CFE basis function for vector-valued problems $\Psi_{r;\alpha}^{\text{CFE}}$ (p. 35)
\mathcal{Q}	periodic restriction, \mathcal{Q}^{-1} periodic extension (p. 78)
q	heat flux (p. 14)
r, s	regular nodes in \mathcal{N}^\square (p. 28)
\mathcal{R}	multigrid restriction (p. 88)
ρ	density (p. 13)
$\varrho_{s,v}$	unreliability measure (p. 103)
s	tangential direction (p. 19)
$\mathcal{S}(n)$	'siblings' in MG context (p. 90)
\mathcal{S}	periodic collapsion (p. 78)
σ	stress (p. 14)
ζ	signature of a cube (element) (p. 29)
t	tangential direction (p. 19); time variable
T	simplex (triangle, tetrahedron)
u	continuous scalar or vector-valued function in the PDE (temperature, displacement, ...), $U(x)$ discretization of u , U value vector
$V_l(m, n)$	multigrid V cycles (p. 88)
$\mathcal{V}^{\text{local}}[T, z, n]$	space of locally admissible functions (p. 41)
$\mathfrak{w}_{z,r;T}$	simplex-wise CFE construction weight, scalar case (p. 42)
$\mathfrak{w}_{z,r}$	CFE construction weight from virtual node z to regular node r (p. 34, 43)
$\mathfrak{w}_{f,c}$	MG coarsening weight from fine node f to coarse node c (p. 90)
$\mathfrak{W}_{z,r;T}$	simplex-wise CFE construction weight, elasticity case (p. 47)
$\mathfrak{W}_{z,r}$	construction weight in the vector-valued case (p. 48)
x	space variable
z, y	virtual nodes $z = \hat{r}s$ on the edge between r and s (page 30, 34)
\overline{pq}	straight line through two points p and q
$[p, q]$	line segment between two points p and q , edge between two nodes
$[\bullet]$	SI unit of a physical quantity; tensors in Voigt's notation (p. 15)
$[g]_\gamma$	jump of a function g across an interface γ (p. 19)
\rightsquigarrow	'is discretized to'
$\dot{\cup}$	union of disjoint sets
$\#$	cardinality of a finite set
$\ A\ $	Frobenius norm (p. 15) of a matrix A
$a_i b_i$	Einstein summation convention: summation over indices appearing twice
$\langle a, b \rangle$	scalar product of two vectors $a, b \in \mathbb{R}^n$
$A : B = A_{ij} B_{ij}$	scalar product of two matrices $A, B \in \mathbb{R}^{m \times n}$
$[f = a]$	$\{x \mid f(x) = a\}$

Contents

Notation	vi
1 Introduction	1
1.1 Simulations with Geometrically Complicated Interfaces	1
1.2 Biomechanics of Bone Microstructures	2
1.3 Review of Related Simulation Methods	4
1.4 Composite Finite Elements	7
1.5 Image Data Acquisition and Domain Preprocessing	7
1.6 A Brief Review of Multilevel and Multigrid Methods	9
1.7 Homogenization	10
1.8 Outline	11
2 Model Problems and Interfacial Coupling Conditions	13
2.1 Heat Diffusion	13
2.2 Linear Elasticity	14
2.3 Coupling Conditions Across Interfaces	19
3 Construction of Composite Finite Elements	27
3.1 Hexahedral Voxel Grids and Local Auxiliary Meshes	28
3.2 CFE for Complicated Domains	36
3.3 CFE for Discontinuous Coefficients	40
3.4 Boundary Conditions	56
3.5 CFE Discretization and Matrices	57
4 Numerical Homogenization	63
4.1 Homogenization for Periodic Specimens	65
4.2 Homogenization for Statistically Periodic Specimens	73
4.3 Composite Finite Element Discretization	76
4.4 Solvers for the Constrained Systems	82
4.5 Orthotropy Directions	83
5 Multigrid Solvers for Composite Finite Elements	87
5.1 Geometric Coarsening	87
5.2 Multigrid Coarsening for Complicated Domains	90
5.3 Homogenization Multigrid Solvers (Complicated Domains)	94
5.4 Multigrid Coarsening for Discontinuous Coefficients	96

6	Algorithms and Implementation	97
6.1	Global Indexing	98
6.2	Virtual Meshes and CFE Basis Functions	98
6.3	Data Vectors and Composite Finite Element Matrices	105
6.4	Iterative and Multigrid Solvers	108
7	Numerical Results and Applications	109
7.1	Numerical Tests	109
7.2	Heat Diffusion Simulations	121
7.3	Linear Elasticity Simulations	127
7.4	Homogenization	136
8	Conclusions and Outlook	147
8.1	Summary and Open Problems	147
8.2	Ideas for Improved Coarsening for Complicated Domains	149
8.3	Ideas for a Discontinuous Coefficients Coarsening Procedure	151
	Bibliography	155
	Index	175

1 Introduction

BEGINNING WITH an overview of simulation applications in which one deals with geometrically complicated interfaces in Section 1.1, we motivate which tasks can benefit from efficient simulation tools. We are particularly interested in biomechanical applications involving osteoporosis and summarize this background in Section 1.2. Related numerical approaches are discussed in a literature review in Section 1.3, the background of Composite Finite Elements (CFE) can be found in Section 1.4. Section 1.5 deals with image acquisition and postprocessing techniques relevant for us. Multigrid solvers are briefly reviewed in Section 1.6. Finally, Section 1.7 gives an introduction to homogenization.

1.1 Simulations with Geometrically Complicated Interfaces

Numerical simulations of physical processes are performed in many fields and often require the numerical solution of partial differential equations (PDE). Often, simulation methods are validated experimentally in non-complex test scenarios, and they are subsequently used to gain deeper insight into physical or biological phenomena occurring in presence of more complicated geometric situations (such as microscales) that are difficult to observe experimentally *in vitro* or even *in vivo*. In particular for medical applications, *in vivo* experiments are not applicable but simulations provide surgeons and radiologists with therapy parameters for treatment planning. As computational power has significantly increased over the last decades, while costs have significantly decreased, such *in silico* experiments have become more and more popular.

In many applications, these simulations involve objects of geometrically complicated shape (object-void interfaces) or geometrically complicated interfaces between materials with different material parameters representing internal object structures. This translates to PDEs being solved on geometrically complicated domains or with discontinuous coefficients across geometrically complicated interfaces. Examples include (but are not limited to) medical and technical applications such as:

- heat conduction in chip design [129]
- heat conduction (and other physical effects) in cold chain management for transport of food [363, 353] or medicine [111]
- electric potentials in the chest or the brain [182, 391] as the forward [314, 145, 67] and inverse problems of electrocardiography [146, 224] involving a bioelectric source and surface potentials

- distribution of heat in radio frequency ablation techniques [200, 272] and the thermo-regulation by blood perfusion (capillary blood flow) [94] to determine therapy parameters in treatment planning and for optimization of the antennae in medical equipment design
- elastic behavior of composite materials, e.g., dental posts in endodontics [274]
- brain-shift [377] occurring in neurosurgery
- computation of elastic stresses in the femur [138] and trabecular bone microstructures [138] to estimates the risk of fractures
- effects of vertebroplasty on macroscopic elasticity properties of trabecular microstructures [198]

1.2 Biomechanics of Bone Microstructures

A particular focus in this thesis will be on trabecular microstructures found in vertebral bodies. We refer to [190] for an overview on the biomechanics of trabecular bone and to [134] for more general trabecular solids. Raising life expectancy and frequent occurrence of osteoporosis has caused this material to be of particular focus in biomechanics.

Osteoporosis [232, 255] is a widely spread disease [287] characterized by a loss of bone mass (which induces a loss of stiffness and structural integrity, see Figure 1.1) [189, 231] and the occurrence of non-traumatic fractures (fractures occurring from trauma less than or equal to a fall from standing height) [131]. For elderly Caucasian women, 90 % of all fractures can be attributed to osteoporosis [242]. Vertebral fractures in older women lead to an increased age-adjusted mortality rate [186]. [124] estimate the direct costs from about 3.79 million osteoporotic fractures in 2000 to 31.7 G€. These costs are estimated [187] to rise to 76.7 G€ in the year 2050. The total cost per fracture in Australia (in the early 1990s) is about 10 k\$A (including medical, diagnostic, hospital, drug, and community costs) [287].

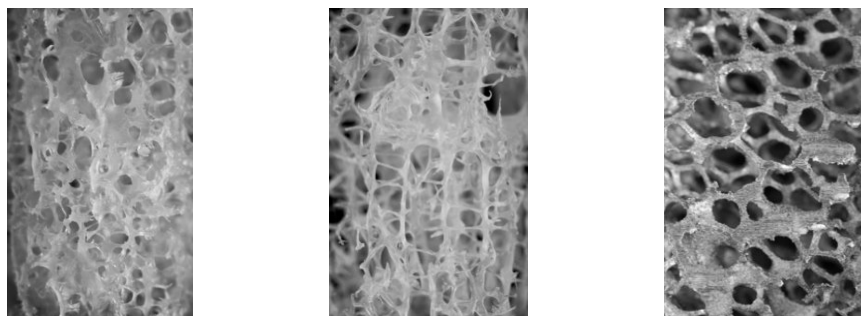


Figure 1.1. Photos of specimens of the spongy interior of human vertebral bodies (*left*: non-osteoporotic T11, *middle*: osteoporotic T10 vertebra) and a photo of an aluminum foam (*right*)

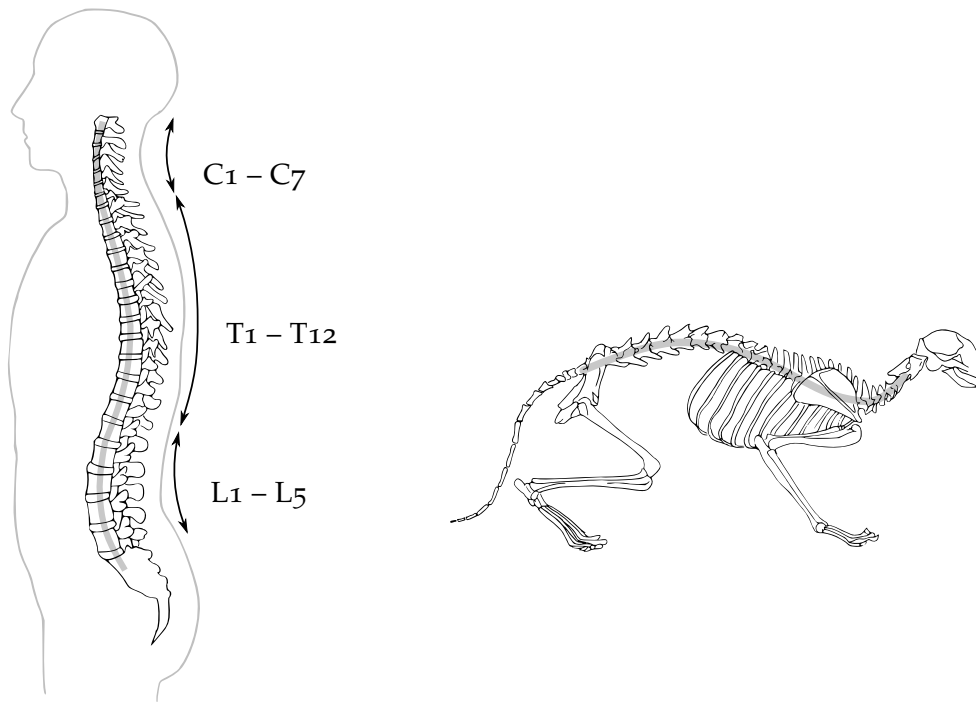


Figure 1.2. The *left* sketch shows a human spine consisting of 7 cervical (C1 – C7), 12 thoracic (T1 – T12) and 5 lumbar (L1 – L5) vertebrae (adapted from [308, p. 78/79]). For comparison, a sketch of a feline skeleton is shown (*right*, adapted from [308, p. 19], not the same scale). Even though the structure of the spines is rather similar, the different anatomy of bipeds and quadrupeds leads to an entirely different loading by gravity and movement.

Medical imaging currently cannot resolve the trabecular microstructure of bones *in vivo*, so the diagnosis of osteoporosis is not possible at microscale. Bone mineral density (BMD) or bone mineral content (BMC) are usually assessed using quantitative computed tomography (QCT), peripheral QCT (pQCT), or dual X-ray absorptiometry (DXA) [21]. Usefulness of these techniques has been studied in *ex vivo* studies where direct measurements are available [219, 218, 112]. Other studies [227, 268, 228, 197, 359] conclude mechanical properties directly from image data. Connections between geometric and mechanical anisotropy were examined using measures such as star volume distribution, star length distribution, volume orientation [159, 89, 265, 323, 191] and morphometric analysis [133, 165].

Treatment techniques for vertebral fractures include fixation devices [292], interbody fusion cages [192, 370], and vertebroplasty and kyphoplasty [130, 79, 206] for vertebral fractures or special implant types for osteoporotic and normal trabecular bone [125, 76]. In *vertebroplasty*, polymethylmethacrylate (PMMA) is injected into a vertebral body in which typically the trabecular microstructure is no longer intact. This is an application we have in mind for elasticity with discontinuous material properties. Moreover, polymerization of PMMA is an exothermic process, also motivating heat diffusion simulations with discontinuous coefficients.

Due to the limited availability of human bones, many biomechanical experiments are performed using animal bones such as bovine, canine, ovine or porcine ones. Different studies [373, 374, 371, 8] have investigated to which extent these are comparable concerning biomechanical properties, despite the obvious anatomical differences between bipeds and quadrupeds, see Figure 1.2. The *craniocaudal axis* (skull to tail in quadrupeds or skull to feet in bipeds) coincides roughly with the direction of gravity in bipeds, but not in quadrupeds.

Numerous studies have dealt with macroscopic mechanic properties of trabecular bone performing mechanical experiments with bone specimens [238, 98, 22, 249, 372, 337], to name a few. Micromechanic stiffness properties of trabecular bone have been examined at trabecular level using microindentation [381] and at sub-trabecular lamellar level using nanoindentation [291]. Finite element (FE) methods are frequently used to simulate the behavior of trabecular bone specimens [118, 253, 345, 346, 136, 250, 78, 382] and larger biological functional units [322, 358, 193, 365, 386, 343, 259, 215, 175, 6, 278, 277, 342, 42, 51], where the two lists of references are by no means meant to give a complete overview. These studies have different aims and in parts compare numerical results to mechanical ones. [202] discusses how sensitive elastic moduli resulting from FE simulations are with respect to typical error-prone parameters.

1.3 Review of Related Simulation Methods

Since about 1950, FE methods have been developed in engineering and in mathematics. They have become a very popular tool for simulation and the numerical treatment of elliptic and parabolic differential equations. This is due to FE being based on variational formulations of boundary and initial value problems and thus their flexibility with respect to geometry and irregularities in solutions. [264] gives a historical overview on the development of FE methods.

Standard Finite Elements. Standard FE methods are capable of dealing with geometric complexities by using geometrically complex and generally unstructured meshes of primitives, most frequently simplices (triangles in 2D, tetrahedra in 3D). The geometry of objects and interfaces can be described explicitly, for example if the object is constructed by computer-aided design (CAD), or implicitly if the object has been scanned in some imaging process, see Section 1.5. *Meshing*, the task of generating an appropriate mesh, is rather well understood in 2D where many methods make use of Voronoi diagrams¹ and Delaunay triangulations² [48, 23, 319, 316]. 3D meshing

¹Named after the Russian mathematician Георгий Феодосьевич Вороной (Georgy Feodosevich Voronoi, sometimes spelled Voronoi) * April 28, 1868 in Zhuravki, † November 20, 1908 in Zhuravki [262].

²Named after the Russian mathematician Борис Николаевич Делоне (Boris Nikolaevich Delone), * March 15, 1890 in St. Petersburg, † July 17, 1980 in Moscow, who used the French transliteration Delaunay in early publications [262].

has been worked on for many years but still is a nontrivial problem [137, 317] which may require substantial user interaction. We refer to [47, 49, 334] for overviews on methods for mesh generation and still challenging problems and to [318] for an overview of mesh quality measures. Different methods for 3D meshing are described, e.g., in [30, 18, 245, 283, 81, 195, 11], mesh quality and mesh improvement is, e.g., discussed in [246, 77, 100, 347].

The main disadvantage of unstructured FE meshes is that (unlike for uniform, e.g., hexahedral meshes) explicit storage of the location of grid points and the connectivity structure is necessary and that there are no canonical coarse versions of the mesh. If the geometry description is given by image data, the voxels immediately define a uniform hexahedral grid. Binary voxel segmentation of complicated domains, see, e.g., [253, 147, 342, 250, 337, 382, 78], suffers from a non-smooth object representation. Subsequent mesh smoothing [52] can remedy this at the possible cost of distorting elements.

Adaptive Methods. A popular strategy with standard FE is to iterate solving a problem on a certain coarse mesh and refining the mesh where a higher resolution is necessary [113, 158]. Typically a posteriori error estimators are used for this purpose [43, 70, 132, 289]. Adaptive quadrilateral or hexahedral refinement strategies [280] permit using efficient data structures such as quadtrees and octrees [122, 300] and avoid unstructured meshes.

Alternative Approaches. Various methods that try to avoid the problems related to meshing have been developed. A general idea is to treat the geometric complexity by adapting finite difference stencils or finite element basis functions. The classical example is the Shortley-Weller approximation [320]. A general term for methods that avoid meshing altogether is *meshless* or *meshfree methods*, we refer to [104, 45, 207, 127] for overviews on these. The following list of different methods for geometric complexities is meant to give an overview on existing methods but is not claimed to be an exhaustive list of publications in this field.

Immersed Interface Methods (IIM) were developed starting in the 1990s and are based on the idea of using Cartesian grids³ and finite differences with stencils adapted near the interface. The IIM for discontinuous coefficients (and possibly singular sources on the interface) can be found in [50, 205] in 1D/2D. [209] is a summary of IIM, they are extended to 3D in [210], and an efficient solver is presented in [211].

The IIM was combined with level set methods [266] in [313]. A multigrid solver for the IIM is introduced in [3, 4]. IIM combined with a finite volume method using ‘capacity functions’ for partially filled cells is presented in [69, 68]. An application to nonlinear 1D problems is shown in [368] and the method is modified to the

³Named after the French philosopher, mathematician, physicist and writer René Descartes, * March 31, 1596 in La Haye en Touraine, Indre-et-Loire, France, † February 11, 1650 in Stockholm, Sweden, who was also known by his Latinized name Renatus Cartesius [1].

Explicit Jump IIM [366, 367, 369, 297], also considering expected singularities in the solution and not only discontinuities of the coefficient. This method has been used for determining effective elasticity properties in [299, 298]. The bridge to the finite element world is built by ‘Immersed Finite Elements’ in 1D and 2D in [212, 214, 208]. An overview of applications of the IIM can be found in [213].

Partition of Unity Methods (PUM) combine the partition of unity subject to a finite cover of the object (classically: supports of FE basis functions) with a priori knowledge about the behavior of the solution at the interface [241, 27].

Generalized Finite Element Methods (GFEM) [240, 101, 28, 29] were also developed under the name *hp clouds* [105, 108, 106, 107, 263] and are per se meshless methods. GFEM use local spaces (of not necessarily polynomial functions) reflecting available information about the unknown solution, thus improving local approximation. They were combined with classical FE to improve their approximation capabilities [328, 102, 329, 103].

Extended Finite Element Methods (XFEM) [99, 46] are classical FE ‘enriched’ by additional basis functions for incorporating discontinuities. The meshes are independent of the location of the discontinuities, but additional degrees of freedom are introduced by the enrichment. An important application of XFEM is simulation of crack growth [247, 90, 327, 26, 325, 331, 177, 128, 354] where XFEM avoids frequent remeshing necessary for classical methods [44, 181].

Fictitious Domain Methods (FDM) go back to [179, 301, 302, 20], see also [135, 286]. They use domain-independent meshes (which are larger than the actual object and easy to mesh) and the PDE under consideration is extended outside the object. This is combined with the p version of FE to the *Finite Cell Method* in 2D [271] and 3D [110].

Weighted Extended B-Splines (WEB splines) [169, 168, 167] use tensor products of splines on uniform grids multiplied by weight functions adapted to the geometric boundary. This method is particularly useful in CAD where splines are also used for object descriptions and allows multigrid solvers [170].

Unfitted Meshes have been introduced and analyzed for problems on curved domains [38, 40, 41, 162] and for discontinuous coefficients across curved interfaces [39, 156, 157]. Here interfaces are not resolved by the computational grid, but accounted for by adapting integration on interfaced elements.

Depending on the method, the ‘complicated domain’ case can be viewed and treated as the limiting case of ‘discontinuous coefficients’ with one degenerate coefficient (zero for resistance-type or infinity for conductance-type parameters). In the CFE context presented here, the two cases are viewed as problems in their own right and treated in separate ways.

The term ‘composite’ has also appeared elsewhere in the FE literature as *Composite Triangles* [148, 336]. These methods also use a virtual subdivision of tetrahedral elements, but not as an adaptation to the geometry of the underlying domains.

1.4 Composite Finite Elements

We will use the method of CFE with the underlying idea of assigning degrees of freedom (DOF) to a computational mesh and using non-standard basis functions that are composed of simpler basis functions on an auxiliary submesh. In short, standard FE treat geometric complexities by ‘simple basis functions on a complicated mesh’, in contrast CFE use ‘complicated basis functions on a simple mesh’. Originally, CFE were developed for more general computational meshes. With the focus on geometry description by images, however, our presentation in this thesis will be restricted to uniform cubic meshes.

The CFE concept was originally introduced for complicated domains in [152, 150, 149]. Dirichlet boundary conditions on complicated domains are treated in [151]. A 1D multigrid method is presented in [126], a 2D one in [324] and a 2-scale CFE method in [289]. A posteriori error estimates are proved in [288]. A CFE approach with adaptive refinement can be found in [290]. CFE for discontinuous coefficients are treated in [364, 304] together with a multigrid strategy, [303] is an overview of CFE for complicated domains and CFE for discontinuous coefficients.

A CFE method on uniform cubic (Cartesian grids) for discontinuous coefficients is presented in [216]. The construction of [216] does not attain optimal orders of convergence in the approximation error. The implementation therein, however, was used as the basis for our implementation. [273] combines CFE for complicated domains and discontinuous coefficients on uniform cubic grids.

Own Contributions. We present the CFE construction for geometrically complicated domains given by 3D voxel datasets in [217, 282] along with a CFE multigrid solver. Our CFE construction for discontinuous coefficients across geometrically complicated interfaces for 3D scalar and vector-valued problems is presented in [310, 281]. In [311] we develop a CFE-based homogenization framework for periodic microstructures in case of complicated domains. We extend this method to statistically periodic complicated domains in [296] and apply the method to specimens of trabecular bone of different species. The cases of periodic and statistically periodic microstructures with discontinuous coefficients are treated in [281]. We moreover use CFE for complicated domains in a biomechanical parameter study [379] for artificial statistical osteoporosis models.

1.5 Image Data Acquisition and Domain Preprocessing

Two types of real specimens are used for the simulations throughout this thesis, these specimens were mostly prepared by Uwe Wolfram (UFB, University of Ulm). On the one hand, we consider aluminum (Al) foams where cuboid specimens were obtained using a band saw, some of these were embedded in polymethylmethacrylate (PMMA). On the other hand, specimens of young human, osteoporotic human, porcine and bovine vertebrae are considered. These were obtained by first extracting individual

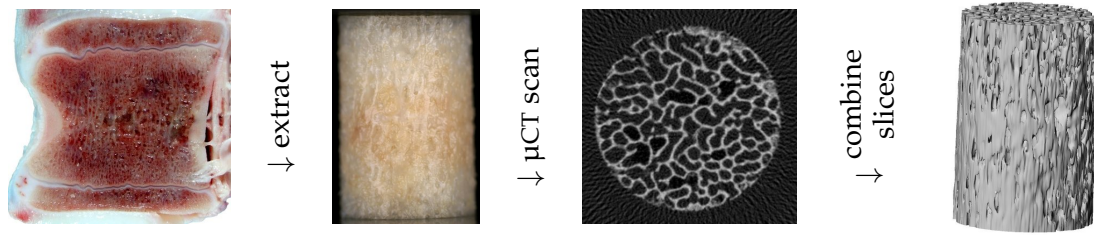


Figure 1.3. Sample and image acquisition workflow for vertebral bone (*from left to right*): After harvesting a vertebra (photograph by Annette Kettler, UFB Ulm), cylindrical specimens are extracted. Specimens are then scanned in μ CT, resulting in a voxel dataset (of which one slice is shown). After denoising and segmentation, the resulting inner structure can be visualized.

vertebrae from the corresponding (frozen) spine, removing top and bottom plates using a band saw and leaving slices of approximately 12 mm thickness. Cylindrical specimens of 8 mm diameter were extracted using a trepan. Bone marrow was then removed using a pulsed water jet device (oral irrigator) and specimens were selected by visual inspection and assessment of structural damage by the sample extraction process. The specimens were then scanned in micro-CT (μ CT), typically at 35 μ m resolution. This workflow is shown in Figure 1.3.

Computed tomography (CT) is an important medical and technical 3D imaging technique that was patented in 1972 [176] based on [87, 88]. In this process, an object is scanned slice by slice by X-rays shot through the object in different directions and measuring the attenuation (depending on the material) along its path. These measurements can then be converted to a voxel dataset of X-ray attenuation values [306]. Different values are subsequently interpreted as different materials. Clinical *in vivo* CT scans with harmless doses of X-ray and tolerable measurement times currently achieve resolutions of several 100 μ m and are thus unable to resolve trabecular structures in human vertebrae.

Another 3D imaging technique is *magnetic resonance imaging* (MRI) [204] that uses strong magnetic fields and is thus less harmful for the patient. MRI is better suited for imaging soft tissues. We refer to [121] for a historical overview of these imaging processes. In situations where μ CT resolution is insufficient, synchrotron radiation has been used [337] to obtain 3D images of trabecular bone structures in undeformed and deformed state.

The image data obtained by these imaging techniques is typically noisy so that an appropriate denoising method has to be applied before segmentation can be performed. Simple denoising techniques include isotropic diffusion or median filtering. An appropriate denoising method should remove noise but not structures, and should not introduce artifacts (structures not present in the physical object). An overview of different denoising techniques can be found in [66]. For our applications, we use simple isotropic diffusion, the edge-preserving Perona-Malik method [275], or an anisotropic method using the implementation from [256].

As for segmentation, we need a method that converts our voxel dataset into a level set representation [266] where, without loss of generality, the interface is the zero level set and negative values correspond to the inside. In the simplest case, this can be achieved by an affine transformation of gray values (subtracting a threshold and possibly flipping the sign), where the threshold can be determined automatically [293, 339, 225], which turned out to be sufficient for our purposes. For reviews on more elaborate segmentation methods, we refer to [270, 276], joint denoising-segmentation include the Mumford-Shah model [254] implemented in [73].

If subsets of the specimen (in case of material/void interfaces) are selected afterwards, they may consist of more than one connected component, typically one main large component and several small pieces of trabeculae actually connected to parts outside the subset. There is no physical coupling between these, so any parts of the domain not connected to the main component (or to faces of the bounding box where we apply boundary conditions) are removed from the dataset.

1.6 A Brief Review of Multilevel and Multigrid Methods

Finite element simulations typically involve three computationally expensive steps:

1. generating a mesh for the object under consideration
2. assembling a system of equations discretizing the PDE which is used to model the physical process under consideration
3. solving the system (possibly multiple times for non-stationary problems)

In many applications, the solution step is most time consuming, so one is particularly interested in efficient solvers.

Multigrid solvers are a class of solvers for linear systems that are of optimal (linear in the number of unknowns) computational complexity for fixed solver accuracy and have turned out to be very efficient in many applications. The main idea is to use iterative methods to reduce high frequency components of the error and, to also reduce lower frequencies, compute corrections on coarsened versions of the problem. Based on ideas in [56, 119, 31, 19], the multigrid algorithm goes back to [59].

Obtaining a coarsened version of the problem is easy for uniform dyadic cubic meshes where 2^3 cubes can be combined to a larger cube of twice the edge length. Coarsening of FE basis functions discretizing the problem is equally straight-forward. An overview on and an introduction to geometric multigrid methods can be found in [258, 153, 383, 61, 360]. Some aspects of convergence are addressed in [34, 226, 33, 388, 389]. This approach will be used for CFE for complicated domains where we also have a uniform cubic computational mesh.

In case of unstructured meshes, coarsening is significantly more difficult, generating a coarser mesh on a subset of nodes is possible but leads to a non-nestedness of the meshes. This problem has been addressed, e.g., in [58, 312, 72, 349, 244, 97].

Multigrid ideas have also been applied to problems where no mesh but only a sparse matrix is explicitly given. In this case, one can interpret the sparsity structure of the matrix as a graph and search for components that are more strongly connected than others to obtain coarse scales in the problem. Such strategies are referred to as *algebraic multigrid* (AMG), in contrast to *geometric multigrid* methods that only make use of the mesh geometry. For an introduction to and an overview on AMG, we refer to [60, 330, 114]. More details on AMG and its implementation can be found in [350, 54, 351, 348, 35, 229, 63, 84, 141, 64, 65]. AMG is typically used as a black box method because it only needs the system matrix, but no information about the underlying problem or discretization. Hybrid methods between purely geometric ('white') and purely algebraic ('black') methods are also possible [123, 120], forming a 'spectrum' in between [74]. Less general, problem-adapted coarsening (e.g., in case of anisotropies) has also been applied [91, 237, 305, 362]. A particular focus on multigrid methods for problems with non-smooth coefficients can be found in [74, 2, 9].

Besides being a solver themselves, multigrid cycles have also been used as a preconditioner [24, 57, 384, 140, 60], e.g., for the conjugate gradients (CG) solver [164].

1.7 Homogenization

The problem of determining effective material properties for a microscopically inhomogeneous but macroscopically (at least statistically) homogeneous material is generally called *upscaling* [15, 352] or *homogenization* [333]. Homogenization can, e.g., be used for two-scale FE simulations [13, 14], or more generally for multiscale simulations [234, 233].

Multigrid coarsening for upscaling [252, 196, 223], using standard geometric coarsening just yields the arithmetic average of the material coefficients [251] ignoring any underlying geometric structure. It is thus difficult to use such techniques in a black-box manner without problem-/geometry-specific knowledge built into the method. We furthermore refer to [16, 17, 62] for overviews on multigrid-based and other upscaling techniques.

We use the method of 'cell problems' [10, Chapter 1] that was introduced in the 1970s by Luc Tartar, whose book chapter [333] gives a review and some theoretical background on this method. The basic idea is to perform few microscopic simulations (using CFE) on a periodic cell of the (exactly) periodic material, computing macroscopic heat flux or stress for a simple macroscopic temperature difference or strain profile, and thus obtain the effective thermal diffusivity or linear elasticity tensor.

In cold chain management, an application we consider for single-scale simulations, one typically has at least three canonical size scales: individual packages, bulk packages or pallets, containers or trucks. Given representative geometry descriptions, material parameters for the goods being transported and the packaging material, and few temperature measurements, an important task here is to estimate possible reduction of shelf life due to temperature abuse, see [12] for a single-scale model.

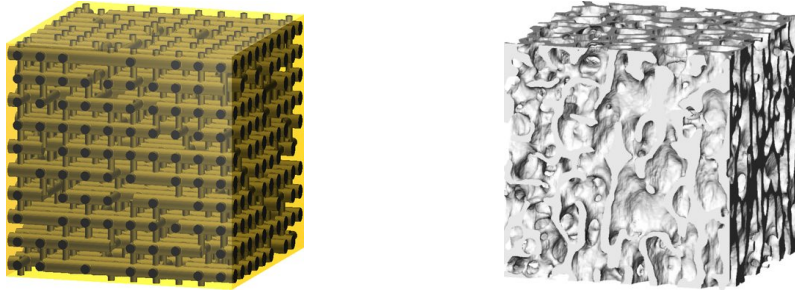


Figure 1.4. The *left* image shows a fundamental cell of an artificial periodic structure of two different materials, the *right* image shows part of a porcine T1 vertebra considered as a statistically representative fundamental cell.

FE models of whole bones require huge amounts of computational resources [343], which makes a full-resolution approach prohibitive for the simulation of larger anatomical structures. Continuum models can be used instead (cf. [160, 185] for their limitations). These, however, rely on a proper knowledge of macroscopic elastic properties. Determining effective elastic properties of cellular solids from unit cells has been of interest for many years [133, 376, 134, 78]. Homogenization techniques using microscopic FE simulations for trabecular bone specimens have been presented in the biomechanics literature, e.g., in [172, 171, 257, 269]. Periodic cells are frequently referred to as ‘representative volume’ [178], ‘representative volume elements’ (RVE) [173, 174] or ‘representative elementary volume’ [144], the term ‘statistical volume element’ (SVE) [267] is used in case of statistical periodicity. A criterion for the size of SVEs for trabecular bone is that they should include 5 inter-trabecular lengths [160]. We will use the term *fundamental cell* to denote exactly periodic or statistically representative cells, cf. Figure 1.4. While [267] distinguishes between microscale (of the microstructure), mesoscale (RVE or SVE), and macroscale (object), our focus lies only on two scales.

Parameterized models for artificial osteoporotic structures have been considered in [284, 321, 393, 385, 341, 147, 199, 279, 95, 96] so that the effect of different variations (e.g., of geometry, material properties) on macroscopic elastic behavior could be studied. In contrast to lattice models, our volume-based CFE approach [379] permits a better resolution of trabecular junctions and is also applicable to voxel scans of physical objects.

1.8 Outline

This dissertation is structured as follows. This chapter presents the background of applications of the CFE methods and a literature overview alternative approaches. A mathematical description of the corresponding model problems is discussed in Chapter 2, along with the respective interfacial coupling conditions. CFE basis functions are then constructed in Chapter 3. Numerical homogenization as a central application framework is addressed in Chapter 4. Chapter 5 deals with multigrid

solver strategies tailored to the CFE methods. Algorithms and their implementation are presented in Chapter 6. The results of different numerical simulations are shown in Chapter 7, concluding with an outlook in Chapter 8.

Many details of the construction are first introduced for the scalar heat diffusion model problem and then generalized to the vector-valued linear elasticity model problem. This will allow us to focus on the CFE peculiarities in the simplest case first and then explain how the construction generalizes to the more technical, vector-valued case.

2 Model Problems and Interfacial Coupling Conditions

RECALLING PHYSICAL AND MATHEMATICAL BACKGROUND and introducing notation, the aim of this chapter is to describe scalar and vector-valued model problems. Since our focus lies on the numerical methods and not on detailed modeling of physical processes, the model problems considered are relatively simple ones: heat diffusion in Section 2.1 and elasticity in Section 2.2. For the case of discontinuous coefficients, coupling conditions across interfaces are derived in Section 2.3 as they will be needed for the CFE construction for discontinuous coefficients.

The model problems discussed here are introduced for a general domain Λ . In the context of complicated domains, this Λ will be the complicated domain, whereas for discontinuous coefficients we assume the interface to divide Λ into two subdomains with different material properties. In this setting, the interface can also be viewed as the jump set of the coefficient function.

2.1 Heat Diffusion

Let us first consider isotropic heat diffusion in 3D with material parameters being constant in time, but not necessarily in space. Let ρ be the *density* (mass per volume), c the *specific heat capacity* (energy difference per mass and temperature difference) and λ *thermal conductivity* (transmitted power times length per temperature difference and cross section area), their SI units are

$$[\rho] = \frac{\text{kg}}{\text{m}^3} \quad [c] = \frac{\text{J}}{\text{K kg}} \quad [\lambda] = \frac{\text{W m}}{\text{K m}^2} = \frac{\text{W}}{\text{K m}}. \quad (2.1)$$

Heat diffusion is governed by continuity of temperature u (with $[u] = \text{K}$) and conservation of energy and expressed in terms of the (physical) *heat flux* $q = \lambda \nabla u$, (with $[q] = \text{W m}^{-2}$):

$$\partial_t(\rho c u) - \text{div}(\lambda \nabla u) = f \quad (2.2)$$

with a source term f in units W m^{-3} . We will often consider the case $f \equiv 0$ for simplicity. All material coefficients are assumed to be constant in time and independent of temperature.

For ρc also being constant in space, we can define the *thermal diffusivity*

$$a = \frac{\lambda}{\rho c} \quad [a] = \frac{\text{m}^2}{\text{s}} \quad (2.3)$$

and rewrite the steady state of Equation (2.2), $\partial_t(\rho c u) \equiv 0$, as the scalar elliptic model problem

$$- \text{div}(a \nabla u) = f, \quad (2.4)$$

where f is meant as a generic right hand side with different units than in (2.2). We will use the simpler form Equation (2.4) for the CFE construction but keep in mind that we need the splitting in λ and ρc in Equation (2.2) for actual simulations. For the sake of simplicity we will also use $q = a\nabla u$ instead of the physical heat flux defined above.

The temperature u is a scalar function $u: \mathbb{R}^d \rightarrow \mathbb{R}$. In the more general anisotropic case, a is a symmetric and positive definite second-order tensor, the isotropic case can also be viewed as the special case $a \simeq a\text{Id}$.

The weak form of (2.4) (for zero Dirichlet boundary values for a domain Λ) is obtained as usual (see, e.g., [335]) by testing with functions in the Sobolev space¹ $H_0^{1,2}(\Lambda)$ and integration by parts.

Problem 2.1. Find $u \in H_0^{1,2}(\Lambda)$ such that

$$\int_{\Lambda} \langle a\nabla u, \nabla v \rangle = \int_{\Lambda} f v \quad \forall v \in H_0^{1,2}(\Lambda). \quad (2.5)$$

For a detailed discussion of Sobolev spaces, we refer to [7].

2.2 Linear Elasticity

A *deformation* is a sufficiently smooth mapping $\Phi: \Lambda \rightarrow \mathbb{R}^d$ with $\det \nabla \Phi > 0$ where $\Lambda \subset \mathbb{R}^d$ is referred to as the *reference configuration*. This reflects the physical understanding that deformations are locally injective and positivity of volumes is preserved. Writing $\Phi = \text{Id} + u$ we can define the *displacement* $u: \mathbb{R}^d \rightarrow \mathbb{R}^d$ which we will usually work with throughout this thesis. For a detailed mathematical description of 3D elasticity we refer to [83].

Define the (second-order) *strain tensor* ϵ as the symmetrized gradient of the displacement

$$\epsilon[u] = \frac{1}{2} [\nabla u + (\nabla u)^T]. \quad (2.6)$$

The skew-symmetric part $\frac{1}{2} [\nabla u - (\nabla u)^T]$ is not considered in the strain because it describes infinitesimal rotations. Then *stress* σ is obtained via

$$\sigma(u) = C\epsilon[u] \quad (2.7)$$

with the (fourth order) *elasticity tensor* C satisfying the symmetry relations

$$C_{ijkl} = C_{jikl} = C_{ijlk} = C_{klij} \quad (2.8)$$

and the ellipticity estimate

$$\sum_{ijkl} C_{ijkl} \tilde{\zeta}_{ij} \tilde{\zeta}_{kl} \geq \alpha > 0 \quad (2.9)$$

¹Named after the Russian mathematician Сергей Львович Соболев (Sergei Lvovich Sobolev), * October 6, 1908 in St. Petersburg, † January 3, 1989 in Moscow [262].

for all $\zeta \in \mathbb{R}^{3 \times 3}$ with $\|\zeta\|_F = 1$. Here, $\|A\|_F = (\sum_{ij} A_{ij}^2)^{1/2}$ is the Frobenius norm² of a square matrix A .

The second order tensors ϵ and σ are symmetric, hence it is convenient to write relation (2.7) in matrix-vector form, called *Voigt's notation* [356, 92]³. In 3D, it can be written as

$$\begin{bmatrix} \sigma_{xx} \\ \sigma_{yy} \\ \sigma_{zz} \\ \sigma_{yz} \\ \sigma_{xz} \\ \sigma_{xy} \end{bmatrix} = \begin{bmatrix} C_{00} & C_{01} & C_{02} & C_{03} & C_{04} & C_{05} \\ C_{10} & C_{11} & C_{12} & C_{13} & C_{14} & C_{15} \\ C_{20} & C_{21} & C_{22} & C_{23} & C_{24} & C_{25} \\ C_{30} & C_{31} & C_{32} & C_{33} & C_{34} & C_{35} \\ C_{40} & C_{41} & C_{42} & C_{43} & C_{44} & C_{45} \\ C_{50} & C_{51} & C_{52} & C_{53} & C_{54} & C_{55} \end{bmatrix} \begin{bmatrix} \epsilon_{xx} \\ \epsilon_{yy} \\ \epsilon_{zz} \\ 2\epsilon_{yz} \\ 2\epsilon_{xz} \\ 2\epsilon_{xy} \end{bmatrix} \quad (2.10)$$

where other forms (without the factor 2) are also common in the literature. The 6×6 matrix in this notation is always symmetric and the tensor is hence described by at most 21 independent material constants. Equation (2.19) illustrates the structure of the elasticity tensor for orthotropic materials.

The *elastic energy* in a body Λ subject to a volume force $f: \Lambda \rightarrow \mathbb{R}^d$ (e.g., gravity) is

$$E_{\text{elast}}[u] = \frac{1}{2} \int_{\Lambda} C\epsilon[u] : \epsilon[u] - \int_{\Lambda} \langle f, u \rangle. \quad (2.11)$$

The elasticity model problem is to find the displacement u satisfying given boundary conditions and minimizing the elastic energy. Using vanishing first variation of (2.11),

$$\begin{aligned} 0 &= \left. \frac{d}{d\vartheta} E_{\text{elast}}(u + \vartheta v) \right|_{\vartheta=0} \\ &= \left. \frac{d}{d\vartheta} \frac{1}{2} \int_{\Lambda} C\epsilon[u + \vartheta v] : \epsilon[u + \vartheta v] - \int_{\Lambda} \langle f, u + \vartheta v \rangle \right|_{\vartheta=0} \\ &= \frac{1}{2} \int_{\Lambda} C\epsilon[v] : \epsilon[u] + \epsilon[u] : C\epsilon[v] - \int_{\Lambda} \langle f, v \rangle \\ &= \int_{\Lambda} C\epsilon[v] : \epsilon[u] - \int_{\Lambda} \langle f, v \rangle, \end{aligned} \quad (2.12)$$

we obtain the weak form of the elasticity problem.

Problem 2.2. Find $u \in H^{1,2}(\Lambda; \mathbb{R}^3)$ such that

$$\int_{\Lambda} C\epsilon[u] : \epsilon[v] = \int_{\Lambda} \langle f, v \rangle \quad \forall v \in H^{1,2}(\Lambda; \mathbb{R}^3). \quad (2.13)$$

²Named after the German mathematician Ferdinand Georg Frobenius, * October 26, 1849 in Berlin-Charlottenburg, † August 3, 1917 in Berlin [1, 262].

³Named after the German Physicist Woldemar Voigt, * September 2, 1850 in Leipzig, † December 13, 1919 in Göttingen.

Note that (2.13) is also the weak form of the problem

$$-\operatorname{div} C\epsilon[u] = f \quad (2.14)$$

in Λ with suitable boundary conditions. We will typically use Dirichlet boundary conditions on part of $\partial\Lambda$ (and transform these to zero ones) and zero Neumann boundary conditions on the remaining boundary.

The volume force (source) term f could, e.g., represent *gravity*. Given the material stiffnesses (where forces on the order of 10 N are applied for typical displacements) and the weight of the specimens (on the order of 10^{-3} N for masses on the order of 100 mg), gravity can be neglected and source terms will typically be set to zero.

Physical Interpretation. Deformations and displacements have unit $[\Phi] = [u] = \text{m}$ and strains have unit $[\epsilon] = 1$, therefore strains are often given in percent (of the respective length). Elasticity tensors and stresses are measured in $\text{N m}^{-2} = \text{Pa}$. Typical elasticity coefficients are in the range of GPa.

Isotropic materials can be described by *Young's modulus*⁴ (uniaxial compressive stiffness) $E > 0$, and *Poisson's ratio*⁵ (bulging ratio under uniaxial compression) $\nu \in [-1, 0.5]$ (see, e.g., [221, Section 3.3]) where

$$\begin{aligned} E &= \frac{\text{force}}{\text{area}} \cdot \frac{\text{length}}{\text{elongation}} \\ \nu &= \frac{\frac{\text{radial bulging}}{\text{radius}}}{\frac{\text{elongation}}{\text{length}}} = \frac{\text{radial bulging} \cdot \text{length}}{\text{elongation} \cdot \text{radius}} \\ [E] &= \frac{\text{N}}{\text{m}^2} = \text{Pa} & [\nu] &= 1. \end{aligned} \quad (2.15)$$

$\nu = 0$ thus means no bulging and $\nu = 0.5$ means volume preservation (incompressibility), most solids have $\nu \in (0, 0.5)$. Materials with $\nu < 0$ are called *auxetic*, examples are certain foam structures [203].

For $\nu \in (-1, 0.5)$, these parameters can be converted to the *Lamé-Navier parameters*⁶ λ and μ [83, Section 3.8]

$$\begin{aligned} \lambda &= \frac{E\nu}{(1+\nu)(1-2\nu)} & \mu &= \frac{E}{2(1+\nu)} \\ [\lambda] &= [\mu] = \frac{\text{N}}{\text{m}^2} \end{aligned} \quad (2.16)$$

and the elasticity tensor has the form

$$C_{ijkl} = \lambda\delta_{ij}\delta_{kl} + \mu(\delta_{il}\delta_{jk} + \delta_{ik}\delta_{jl}) \quad (2.17)$$

⁴Named after the English physicist (and expert in other fields) Thomas Young, * June 13, 1773 in Milverton, Somerset, † May 10, 1829 in London [1].

⁵Named after the French mathematician, geometer, and physicist Siméon-Denis Poisson, * June 21, 1781 in Pithiviers, Loiret, † April 25, 1840 in Sceaux, Hauts-de-Seine [1].

⁶Named after the French mathematician Père de Gabriel Léon Jean Baptiste Lamé, * July 22, 1795 in Tours, † May 1, 1870 in Paris [262] and the French engineer and physicist Claude Louis Marie Henri Navier, * February 10, 1785 in Dijon, † August 21, 1836 in Paris [262].

where δ_{ij} is the usual *Kronecker symbol*⁷ ($\delta_{ij} = 1$ if $i = j$, $\delta_{ij} = 0$ otherwise). In this case, we can write

$$C\epsilon = \lambda(\text{tr } \epsilon)\text{Id} + 2\mu\epsilon. \quad (2.18)$$

Orthotropic Materials. For an orthotropic material, only the upper left block and the lower right diagonal of the elasticity tensor in Voigt's notation (2.10) are nonzero. It can be described by Young's moduli E_i , shear moduli G_{ij} and Poisson's ratios ν_{ij} , the inverse of the elasticity tensor in Equation (2.10) can be written as

$$\begin{bmatrix} \epsilon_{xx} \\ \epsilon_{yy} \\ \epsilon_{zz} \\ 2\epsilon_{yz} \\ 2\epsilon_{zx} \\ 2\epsilon_{xy} \end{bmatrix} = \begin{bmatrix} 1/E_x & -\nu_{xy}/E_x & -\nu_{xz}/E_x & 0 & 0 & 0 \\ -\nu_{yx}/E_y & 1/E_y & -\nu_{yz}/E_y & 0 & 0 & 0 \\ -\nu_{zx}/E_z & -\nu_{zy}/E_z & 1/E_z & 0 & 0 & 0 \\ 0 & 0 & 0 & 1/G_{yz} & 0 & 0 \\ 0 & 0 & 0 & 0 & 1/G_{zx} & 0 \\ 0 & 0 & 0 & 0 & 0 & 1/G_{xy} \end{bmatrix} \begin{bmatrix} \sigma_{xx} \\ \sigma_{yy} \\ \sigma_{zz} \\ \sigma_{yz} \\ \sigma_{zx} \\ \sigma_{xy} \end{bmatrix}. \quad (2.19)$$

Due to symmetry, only three of the Poisson's ratios ν_{ij} are independent. Due to the block structure, the elasticity tensor for orthotropic materials has the same sparsity structure as its inverse: The upper left block and the lower right diagonal are nonzero.

Forces. For any section A through the object, the force F acting on A is given by

$$F = \int_A \langle \sigma(x), n(x) \rangle \, dA(x) \quad (2.20)$$

where $n(x)$ is the normal to A at x (in a defined direction). In particular, 'actio = reactio' implies that it does not matter where we cut the body to compute the force for a deformation. Forces are measured in $[F] = \text{N}$ which fits to planar integration of stress.

Von Mises Stress. Let σ be the 3×3 symmetric second order stress tensor and $\lambda_{0,1,2}$ its eigenvalues. Then the *von Mises stress*⁸ [357, 36] is defined and computed as

$$\begin{aligned} \sigma_{\text{vM}} &:= \sqrt{\frac{1}{2} \left[(\lambda_0 - \lambda_1)^2 + (\lambda_0 - \lambda_2)^2 + (\lambda_1 - \lambda_2)^2 \right]} \\ &= \sqrt{\sigma_{00}^2 + \sigma_{11}^2 + \sigma_{22}^2 - \sigma_{00}\sigma_{11} - \sigma_{00}\sigma_{22} - \sigma_{11}\sigma_{22} + 3(\sigma_{01}^2 + \sigma_{02}^2 + \sigma_{12}^2)}. \end{aligned} \quad (2.21)$$

Due to symmetry of σ , the eigenvalues are real and σ_{vM} is also real. The von Mises stress is used in materials science as a fictitious uniaxial stress with similar wear as for real multiaxial loading and obviously has the same physical units as σ .

⁷Named after the German mathematician and logician Leopold Kronecker, * December 7, 1823 in Liegnitz, † December 29, 1891 in Berlin [1].

⁸Named after the Austrian mathematician Richard Edler von Mises, * April 19, 1883 in Lemberg (now Lviv, Ukraine), † July 14, 1953 in Boston, U.S.A. [1].

To become familiar with the quantities defined above, let us consider a few simple displacements in the Lamé-Navier setting in 3D. Shifting an object, $u(x) = c$, clearly does not require elastic energy

$$\epsilon[u] = 0, \quad \sigma = 0, \quad \sigma_{\text{vM}} = 0.$$

Isotropic compression is described by $u(x) = \alpha x$

$$\epsilon[u] = \begin{pmatrix} \alpha & & \\ & \alpha & \\ & & \alpha \end{pmatrix}, \quad \sigma = \begin{pmatrix} (3\lambda + 2\mu)\alpha & & \\ & (3\lambda + 2\mu)\alpha & \\ & & (3\lambda + 2\mu)\alpha \end{pmatrix}, \quad \sigma_{\text{vM}} = 0$$

where the von Mises stress is not a meaningful quantity. Uniaxial *compression* (which will be simulated frequently later on) is described by $u(x) = (\alpha x_0, 0, 0)$

$$\epsilon[u] = \begin{pmatrix} \alpha & & \\ & 0 & \\ & & 0 \end{pmatrix}, \quad \sigma = \begin{pmatrix} \lambda\alpha & & \\ & \lambda\alpha & \\ & & (\lambda + 2\mu)\alpha \end{pmatrix}, \quad \sigma_{\text{vM}} = 2\mu\alpha.$$

One case of *shearing* is described by the displacement $u(x) = (\alpha x_1, 0, 0)$

$$\epsilon[u] = \begin{pmatrix} 0 & \frac{1}{2}\alpha & \\ \frac{1}{2}\alpha & 0 & \\ & & 0 \end{pmatrix}, \quad \sigma = \begin{pmatrix} 0 & \mu\alpha & \\ \mu\alpha & 0 & \\ & & 0 \end{pmatrix}, \quad \sigma_{\text{vM}} = \sqrt{6}\mu\alpha.$$

Rigid Body Motions and Linearization. Note that linear elasticity is a simplified model of reality: rigid body motions are not necessarily stress-free and stress-free deformations are not necessarily rigid body motions. More precisely, an affine displacement $u(x) = Sx + b$ is

1. a rigid body motion $\iff S + \text{Id} =: Q \in \text{SO}(d)$, i.e., the deformation $\Phi(x)$ is the sum of a rotation and a translation, $\Phi(x) = Qx + b$. Consider a rotation by α around the x_2 axis, which is not stress-free in the isotropic linear setting:

$$S = \begin{pmatrix} \cos(\alpha) - 1 & \sin(\alpha) & \\ -\sin(\alpha) & \cos(\alpha) - 1 & \\ & & 0 \end{pmatrix}, \quad \epsilon[u] = \begin{pmatrix} \cos(\alpha) - 1 & 0 & \\ 0 & \cos(\alpha) - 1 & \\ & & 0 \end{pmatrix},$$

$$\sigma = \begin{pmatrix} 2(\lambda + \mu)(\cos(\alpha) - 1) & & \\ & 2(\lambda + \mu)(\cos(\alpha) - 1) & \\ & & 2\lambda(\cos(\alpha) - 1) \end{pmatrix},$$

$$\sigma_{\text{vM}} = 2\mu(\cos(\alpha) - 1),$$

2. stress-free $\iff S$ is skew-symmetric (hence $\epsilon = 0$), e.g., the stretching rotation described by

$$S = \begin{pmatrix} 0 & \beta & \\ -\beta & 0 & \\ & & 0 \end{pmatrix}, \quad \epsilon[u] = 0, \quad \sigma = 0, \quad \sigma_{\text{vM}} = 0.$$

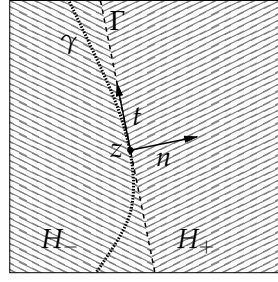


Figure 2.1. The planar approximation Γ of an interface γ at a point z divides the full space in two half-spaces H_{\pm} and defines a normal direction n and a tangential direction t . In 3D, there is an additional tangential direction s .

2.3 Coupling Conditions Across Interfaces

The construction of CFE basis functions for discontinuous coefficients later on in Section 3.3.2 will be such that typical profiles of physical quantities can be well approximated at interfaces. This requires first of all knowing the behavior of such profiles. Based on physical conservation principles, continuity of physical quantities and discontinuity of the material parameters leads to a nondifferentiability in the physical quantity.

In this section, we discuss these coupling conditions depending on both interface geometry and material coefficients. The case of isotropic heat diffusion is the most basic one where the coupling results in a kink of the temperature profile in normal direction to the interface. This allows to understand the coupling without technical complications due to anisotropy. In the anisotropic case, the coupling involves both normal and tangential components and thus becomes more technical and cannot be understood as a simple kink. In the linear elasticity case, we will encounter additional technicalities due to the vector-valued nature of the problem.

Geometric Setting

Consider the following geometric situation. Let z be a point on an interface γ between two domains Ω_- and Ω_+ with different material properties, forming, cf. Equation (3.1), $\Omega = \Omega_- \cup \gamma \cup \Omega_+$. For simplicity of the presentation, we only consider a planar approximation Γ of the interface γ at z , so that Γ defines two half-spaces H_{\pm} . Let n be normal and s, t tangential to the interface γ such that n, s and t are pairwise orthogonal and normalized, in particular $H_{\pm} = \{x | \langle x - z, n \rangle \gtrless 0\}$, cf. Figure 2.1.

Definition 2.3. For g piecewise continuous on Ω_{\pm} , we define the *jump* across the interface γ as

$$[g]_{\gamma} := g^+(z) - g^-(z) \quad \text{where } g^{\pm}(z) := \lim_{x \rightarrow z} g(x). \quad (2.22)$$

More generally, define the restriction to a subdomain as

$$g^{\pm} = g|_{\Omega_{\pm}}. \quad (2.23)$$

For a scalar function u , we can convert between directional derivatives and the Euclidean gradient⁹

$$\begin{pmatrix} n_0 & n_1 & n_2 \\ s_0 & s_1 & s_2 \\ t_0 & t_1 & t_2 \end{pmatrix} \begin{pmatrix} \partial_0 u \\ \partial_1 u \\ \partial_2 u \end{pmatrix} = \begin{pmatrix} \partial_n u \\ \partial_s u \\ \partial_t u \end{pmatrix} \Leftrightarrow \begin{pmatrix} \partial_0 u \\ \partial_1 u \\ \partial_2 u \end{pmatrix} = \underbrace{\begin{pmatrix} n_0 & s_0 & t_0 \\ n_1 & s_1 & t_1 \\ n_2 & s_2 & t_2 \end{pmatrix}}_{=:G} \begin{pmatrix} \partial_n u \\ \partial_s u \\ \partial_t u \end{pmatrix}, \quad (2.24)$$

where we used the property that $G \in \text{SO}(3)$ so that $G^{-1} = G^T$.

Applying a fourth-order tensor H with entries H_{ijkl} to a second-order tensor M with entries M_{kl} can be written using *Einstein summation convention*¹⁰ (summation over indices appearing twice in a term of a product) as

$$(HM)_{ij} = H_{ijkl}M_{kl} = \sum_k \sum_l H_{ijkl}M_{kl}. \quad (2.25)$$

Similar to (2.24), the symmetrized gradient $\epsilon[u]$ of a vector-valued function u can be expressed in terms of directional derivatives using the fourth-order tensor H in

$$\epsilon(u) = \frac{1}{2}(\nabla u + \nabla u^T) =: H \begin{pmatrix} \partial_n u_0 & \partial_s u_0 & \partial_t u_0 \\ \partial_n u_1 & \partial_s u_1 & \partial_t u_1 \\ \partial_n u_2 & \partial_s u_2 & \partial_t u_2 \end{pmatrix} \quad (2.26)$$

with $H_{ijkl} = \frac{1}{2}(\delta_{ik}G_{jl} + \delta_{jk}G_{il})$ with the second-order tensor G as in (2.24), see Section 2.3.2 for an explicit form in 2D.

2.3.1 Heat Diffusion Model Problem

Isotropic Heat Diffusion

Conservation of energy at the interface implies continuous heat flux across the interface, that is

$$a^+ \partial_n u^+(z) = a^- \partial_n u^-(z), \quad (2.27)$$

which in case of isotropic heat diffusion, i.e., scalar and positive a^\pm , translates to the *coupling condition*

$$\begin{aligned} \partial_n u^+(z) &= \frac{a^-}{a^+} \partial_n u^-(z) \\ \partial_{s,t} u^+(z) &= \partial_{s,t} u^-(z) \end{aligned} \quad (2.28)$$

where the continuity of the directional derivatives in the tangential directions is also accounted for. This continuity is sufficient for the temperature to be continuous along the interface.

⁹Named after the ancient Greek mathematician Εὐκλείδης (Euclid of Alexandria), * around 300 BC in Alexandria, Egypt [1].

¹⁰Named after the physicist Albert Einstein, * March 14, 1879 in Ulm, Germany, † April 18, 1955 in Princeton, U.S.A. [1].

Definition 2.4. The *kink ratio* is the scalar factor $\kappa := \frac{a^-}{a^+}$ in Equation (2.28).

It describes the kink of the (continuous) temperature profile perpendicular to the interface. For physical reasons (strictly positive diffusivity coefficients), κ is strictly positive and finite.

Remark 2.5. For a continuous and piecewise continuously differentiable function, a kink in the function corresponds to a jump in its derivative.

Equation (2.28) implies that any locally (in a neighborhood of z) admissible temperature profile has a first order *Taylor approximation*¹¹ in directions n , s , and t (as explained at the beginning of this section)

$$u: x \mapsto \begin{cases} \kappa b \langle x - z, n \rangle + c_s \langle x - z, s \rangle + c_t \langle x - z, t \rangle + d & \text{for } x \in H_+ \\ b \langle x - z, n \rangle + c_s \langle x - z, s \rangle + c_t \langle x - z, t \rangle + d & \text{for } x \in H_- \end{cases} \quad (2.29)$$

with $b, c_s, c_t, d \in \mathbb{R}$. Such functions form a four-dimensional vector space.

Lemma 2.6. The space of piecewise affine functions of the form (2.29) is spanned by the *prototype functions*

$$\begin{aligned} \eta^0(x) &= \begin{cases} \kappa \langle x - z, n \rangle & \text{for } x \in H_+ \\ \langle x - z, n \rangle & \text{for } x \in H_- \end{cases} \\ \eta^1(x) &= \langle x - z, t \rangle \\ \eta^2(x) &= \langle x - z, s \rangle \\ \eta^3(x) &= 1. \end{aligned} \quad (2.30)$$

Even though those η^i obviously form a basis of their span, we prefer the term ‘prototype’ functions to distinguish them from CFE basis functions.

Anisotropic Heat Diffusion

In the anisotropic heat diffusion case where the diffusivity coefficient is second-order tensor-valued (matrix-valued), a more general coupling condition holds, not merely interpretable as a kink. We again have continuous heat flux across the interface (in normal direction) and continuously differentiable temperature along the interface (in tangential directions):

$$\begin{aligned} \langle a^+ \nabla u^+(z), n \rangle &= \langle a^- \nabla u^-(z), n \rangle \\ \partial_{s,t} u^+(z) &= \partial_{s,t} u^-(z) \end{aligned} \quad (2.31)$$

¹¹Named after the English mathematician Brook Taylor, * August 18, 1685 in Edmonton, Middlesex, † December 29, 1731 in London [1].

where the first condition translates to

$$\langle a^+ G \begin{pmatrix} \partial_n u^+ \\ \partial_s u^+ \\ \partial_t u^+ \end{pmatrix}, n \rangle = \langle a^- G \begin{pmatrix} \partial_n u^- \\ \partial_s u^- \\ \partial_t u^- \end{pmatrix}, n \rangle. \quad (2.32)$$

Substituting G defined in (2.24), we obtain

$$a_{ij}^+ n_j n_i \partial_n u^+ + a_{ij}^+ s_j n_i \partial_s u^+ + a_{ij}^+ t_j n_i \partial_t u^+ = a_{ij}^- n_j n_i \partial_n u^- + a_{ij}^- s_j n_i \partial_s u^- + a_{ij}^- t_j n_i \partial_t u^-$$

which, combined with the tangential coupling conditions, results in the system

$$\begin{aligned} \underbrace{\begin{pmatrix} a_{ij}^+ n_j n_i & a_{ij}^+ s_j n_i & a_{ij}^+ t_j n_i \\ 0 & 1 & 0 \\ 0 & 0 & 1 \end{pmatrix}}_{=:K^+} \begin{pmatrix} \partial_n u^+ \\ \partial_s u^+ \\ \partial_t u^+ \end{pmatrix} &= \underbrace{\begin{pmatrix} a_{ij}^- n_j n_i & a_{ij}^- s_j n_i & a_{ij}^- t_j n_i \\ 0 & 1 & 0 \\ 0 & 0 & 1 \end{pmatrix}}_{=:K^-} \begin{pmatrix} \partial_n u^- \\ \partial_s u^- \\ \partial_t u^- \end{pmatrix} \\ \Rightarrow \begin{pmatrix} \partial_n u^+ \\ \partial_s u^+ \\ \partial_t u^+ \end{pmatrix} &= (K^+)^{-1} K^- \begin{pmatrix} \partial_n u^- \\ \partial_s u^- \\ \partial_t u^- \end{pmatrix} =: \underbrace{\begin{pmatrix} K^n & K^s & K^t \\ 0 & 1 & 0 \\ 0 & 0 & 1 \end{pmatrix}}_{=:K} \begin{pmatrix} \partial_n u^- \\ \partial_s u^- \\ \partial_t u^- \end{pmatrix} \end{aligned} \quad (2.33)$$

where K^+ is invertible because a^+ is positive definite, hence $a_{ij}^+ n_j n_i \neq 0$. Let us point out that the entries of the coupling matrix K depend on both the thermal diffusivity tensor a and the local geometry (n, s, t) . Note that for the isotropic case (a being a multiple of Id), (2.33) simplifies to (2.27) with $K^n = \kappa$, $K^s = K^t = 0$. Furthermore note that the coupling now involves all directional derivatives, not only the one in normal direction. In summary, we obtain the following lemma.

Lemma 2.7. The space of piecewise affine functions satisfying (2.31) is spanned by the *prototype functions*

$$\begin{aligned} \eta^0(x) &= \begin{cases} K^n \langle x - z, n \rangle & \text{for } x \in H_+ \\ \langle x - z, n \rangle & \text{for } x \in H_- \end{cases} \\ \eta^1(x) &= \begin{cases} K^s \langle x - z, n \rangle + \langle x - z, s \rangle & \text{for } x \in H_+ \\ \langle x - z, s \rangle & \text{for } x \in H_- \end{cases} \\ \eta^2(x) &= \begin{cases} K^t \langle x - z, n \rangle & + \langle x - z, t \rangle & \text{for } x \in H_+ \\ \langle x - z, t \rangle & \text{for } x \in H_- \end{cases} \\ \eta^3(x) &= 1. \end{aligned} \quad (2.34)$$

2.3.2 Linear Elasticity Model Problem

The coupling condition in the elasticity caes is given by local *equilibrium of force* (continuity of normal stress) across the interface (in normal direction)

$$C^+ \epsilon[u^+] (z) n = C^- \epsilon[u^-] (z) n \quad (2.35)$$

besides continuous differentiability in the tangential directions.

Using G defined in (2.26), we can express this condition in terms of the directional derivatives of the displacement u

$$C_{ijkl}^+ H_{klpq} \begin{pmatrix} \partial_n u_0^+ & \partial_s u_0^+ & \partial_t u_0^+ \\ \partial_n u_1^+ & \partial_s u_1^+ & \partial_t u_1^+ \\ \partial_n u_2^+ & \partial_s u_2^+ & \partial_t u_2^+ \end{pmatrix}_{pq} n_j = C_{ijkl}^- H_{klpq} \begin{pmatrix} \partial_n u_0^- & \partial_s u_0^- & \partial_t u_0^- \\ \partial_n u_1^- & \partial_s u_1^- & \partial_t u_1^- \\ \partial_n u_2^- & \partial_s u_2^- & \partial_t u_2^- \end{pmatrix}_{pq} n_j. \quad (2.36)$$

Together with continuity of $\partial_s u$ and $\partial_t u$, we can substitute H , expand (2.36) to a 9×9 system in block structure and rewrite it in the form

$$\begin{aligned} \underbrace{\begin{pmatrix} L^{n+} & L^{s+} & L^{t+} \\ 0 & \text{Id} & 0 \\ 0 & 0 & \text{Id} \end{pmatrix}}_{=:L^+} \begin{pmatrix} \partial_n u^+ \\ \partial_s u^+ \\ \partial_t u^+ \end{pmatrix} &= \underbrace{\begin{pmatrix} L^{n-} & L^{s-} & L^{t-} \\ 0 & \text{Id} & 0 \\ 0 & 0 & \text{Id} \end{pmatrix}}_{=:L^-} \begin{pmatrix} \partial_n u^- \\ \partial_s u^- \\ \partial_t u^- \end{pmatrix} \\ \Rightarrow \begin{pmatrix} \partial_n u^+ \\ \partial_s u^+ \\ \partial_t u^+ \end{pmatrix} &= (L^+)^{-1} L^- \begin{pmatrix} \partial_n u^- \\ \partial_s u^- \\ \partial_t u^- \end{pmatrix} =: \underbrace{\begin{pmatrix} L^n & L^s & L^t \\ 0 & \text{Id} & 0 \\ 0 & 0 & \text{Id} \end{pmatrix}}_{=:L} \begin{pmatrix} \partial_n u^- \\ \partial_s u^- \\ \partial_t u^- \end{pmatrix}. \end{aligned} \quad (2.37)$$

Equation (2.36) can indeed be rewritten in this form.

Lemma 2.8. The matrix L^{n+} in (2.37) is invertible.

Proof. This can be shown by proving that, given the coupling conditions, $\nabla u^- = 0$ implies that $\nabla u^+ = 0$. First observe that $\partial_s u^+ = \partial_t u^+ = 0$ because of $\partial_s u^- = \partial_t u^- = 0$. Hence we can write $\nabla u^+(x) = wn^T$ for some $w = w(x) \in \mathbb{R}^3$. Continuity of the normal stress implies $C^- \epsilon[u^-] = 0$, and scalar multiplication by w leads to

$$\begin{aligned} 0 &= \langle C^- \epsilon[u^-] n, w \rangle = \sum_i \left(\sum_{jkl} C_{ijkl}^+ \epsilon[u^+]_{kl} n_j \right) w_i \\ &= \sum_i \left(\sum_{jkl} C_{ijkl}^+ (\nabla u^+)_{kl} n_j \right) w_i = \sum_{ijkl} C_{ijkl}^+ w_k n_l w_i n_j \geq \alpha \|wn^T\|_{\mathbb{F}}^2, \end{aligned} \quad (2.38)$$

where we used symmetry and ellipticity (2.9) of the elasticity tensor. Hence $wn^T = 0$, from which $w = 0$ and thus $\nabla u^+ = 0$ immediately follow. \square

In summary, we obtain the following lemma.

Lemma 2.9. The space of piecewise affine vector-valued functions that satisfy (2.35) is spanned by the *prototype functions* $\{\eta^{i,j}\}_{i=0,\dots,3,j=0,1,2}$ defined by

$$\begin{aligned}
 \eta^{0,j}(x) &:= \begin{cases} \langle x - z, n \rangle L_j^n & \text{for } x \in H_+ \\ \langle x - z, n \rangle e_j & \text{for } x \in H_- \end{cases} \\
 \eta^{1,j}(x) &:= \begin{cases} \langle x - z, n \rangle L_j^s + \langle x - z, s \rangle e_j & \text{for } x \in H_+ \\ \langle x - z, s \rangle e_j & \text{for } x \in H_- \end{cases} \\
 \eta^{2,j}(x) &:= \begin{cases} \langle x - z, n \rangle L_j^t + \langle x - z, t \rangle e_j & \text{for } x \in H_+ \\ \langle x - z, t \rangle e_j & \text{for } x \in H_- \end{cases} \\
 \eta^{3,j}(x) &:= e_j
 \end{aligned} \tag{2.39}$$

where the index i corresponds to the same index as in the scalar case (2.34) whereas j refers to the j th vector component. Here, L_j^\bullet denotes the j th column of the matrix $L^\bullet = (L_{ij}^\bullet)_{i,j=0,1,2}$.

Remark 2.10. The $\eta^{i,j}$ can also be written in a different form. Let

$$\begin{aligned}
 L^{0,j}(x) &= \begin{cases} \begin{pmatrix} L_{0j}^n & 0 & 0 \\ L_{1j}^n & 0 & 0 \\ L_{2j}^n & 0 & 0 \end{pmatrix} & \text{for } x \in H_+ \\ \begin{pmatrix} \delta_{0j} & 0 & 0 \\ \delta_{1j} & 0 & 0 \\ \delta_{2j} & 0 & 0 \end{pmatrix} & \text{for } x \in H_- \end{cases} \\
 L^{1,j}(x) &= \begin{cases} \begin{pmatrix} L_{0j}^s & \delta_{0j} & 0 \\ L_{1j}^s & \delta_{1j} & 0 \\ L_{2j}^s & \delta_{2j} & 0 \end{pmatrix} & x \in H_+ \\ \begin{pmatrix} 0 & \delta_{0j} & 0 \\ 0 & \delta_{1j} & 0 \\ 0 & \delta_{2j} & 0 \end{pmatrix} & x \in H_- \end{cases} \\
 L^{2,j}(x) &= \begin{cases} \begin{pmatrix} L_{0j}^t & 0 & \delta_{0j} \\ L_{1j}^t & 0 & \delta_{1j} \\ L_{2j}^t & 0 & \delta_{2j} \end{pmatrix} & x \in H_+ \\ \begin{pmatrix} 0 & 0 & \delta_{0j} \\ 0 & 0 & \delta_{1j} \\ 0 & 0 & \delta_{2j} \end{pmatrix} & x \in H_- \end{cases}
 \end{aligned} \tag{2.40}$$

then we can write

$$\begin{aligned}
 \eta^{i,j}(x) &= L^{i,j}(x) \begin{pmatrix} \langle x - z, n \rangle \\ \langle x - z, s \rangle \\ \langle x - z, t \rangle \end{pmatrix} & i = 0, 1, 2, j = 0, 1, 2, \\
 \eta^{3,j}(x) &= e_j & j = 0, 1, 2.
 \end{aligned} \tag{2.41}$$

Explicit Formulas for Isotropic Lamé-Navier Elasticity in 2D

As an example, let us explicitly state the form of the elasticity coupling conditions for the isotropic case in 2D [310] where the elasticity tensor is given as in Equation (2.17). Let us first determine an explicit form of the tensor H in Equation (2.26). For $n = \begin{pmatrix} n_0 \\ n_1 \end{pmatrix}$ and $t = \begin{pmatrix} t_0 \\ t_1 \end{pmatrix}$, we can write

$$\nabla u \begin{pmatrix} n_0 & t_0 \\ n_1 & t_1 \end{pmatrix} = \begin{pmatrix} \partial_0 u_0 & \partial_1 u_0 \\ \partial_0 u_1 & \partial_1 u_1 \end{pmatrix} \begin{pmatrix} n_0 & t_0 \\ n_1 & t_1 \end{pmatrix} = \begin{pmatrix} \partial_n u_0 & \partial_t u_0 \\ \partial_n u_1 & \partial_t u_1 \end{pmatrix} \quad (2.42)$$

so that

$$\begin{aligned} \nabla u &= \begin{pmatrix} \partial_n u_0 & \partial_t u_0 \\ \partial_n u_1 & \partial_t u_1 \end{pmatrix} \begin{pmatrix} n_0 & t_0 \\ n_1 & t_1 \end{pmatrix}^{-1} = \begin{pmatrix} \partial_n u_0 & \partial_t u_0 \\ \partial_n u_1 & \partial_t u_1 \end{pmatrix} \begin{pmatrix} n_0 & n_1 \\ t_0 & t_1 \end{pmatrix} \\ &= \begin{pmatrix} n_0 \partial_n u_0 + t_0 \partial_t u_0 & n_1 \partial_n u_0 + t_1 \partial_t u_0 \\ n_0 \partial_n u_1 + t_0 \partial_t u_1 & n_1 \partial_n u_1 + t_1 \partial_t u_1 \end{pmatrix}, \end{aligned} \quad (2.43)$$

$$\operatorname{div} u = \operatorname{tr} \nabla u = n_0 \partial_n u_0 + n_1 \partial_n u_1 + t_0 \partial_t u_0 + t_1 \partial_t u_1.$$

Hence

$$\begin{aligned} 2H \begin{pmatrix} \partial_n u_0 & \partial_t u_0 \\ \partial_n u_1 & \partial_t u_1 \end{pmatrix} &= 2\epsilon(u) = \nabla u + \nabla u^T \\ &= \begin{pmatrix} 2n_0 \partial_n u_0 + 2t_0 \partial_t u_0 & n_1 \partial_n u_0 + t_1 \partial_t u_0 + n_0 \partial_n u_1 + t_0 \partial_t u_1 \\ n_0 \partial_n u_1 + t_0 \partial_t u_1 + n_1 \partial_n u_0 + t_1 \partial_t u_0 & 2n_1 \partial_n u_1 + 2t_1 \partial_t u_1 \end{pmatrix}. \end{aligned} \quad (2.44)$$

If we use $G = \begin{pmatrix} n_0 & t_0 \\ n_1 & t_1 \end{pmatrix}$, then the entries of the fourth-order tensor H are given as $H_{ijkl} = \frac{1}{2} (\delta_{ik} G_{jl} + \delta_{jk} G_{il})$.

Now let us collect the terms arising in $C\epsilon[u]n$:

$$\begin{aligned} (\nabla u + \nabla u^T) n &= \begin{pmatrix} (2n_0^2 + n_1^2) \partial_n u_0 + (n_0 n_1) \partial_n u_1 + (2n_0 t_0 + n_1 t_1) \partial_t u_0 + (n_1 t_0) \partial_t u_1 \\ (n_0 n_1) \partial_n u_0 + (n_0^2 + 2n_1^2) \partial_n u_1 + (n_0 t_1) \partial_t u_0 + (n_0 t_0 + 2n_1 t_1) \partial_t u_1 \end{pmatrix}, \\ (\operatorname{div} u) n &= \begin{pmatrix} n_0^2 \partial_n u_0 + n_0 n_1 \partial_n u_1 + n_0 t_0 \partial_t u_0 + n_0 t_1 \partial_t u_1 \\ n_0 n_1 \partial_n u_0 + n_1^2 \partial_n u_1 + n_1 t_0 \partial_t u_0 + n_1 t_1 \partial_t u_1 \end{pmatrix}. \end{aligned} \quad (2.45)$$

Due to orthonormality of n and t ($n_0^2 + n_1^2 = t_0^2 + t_1^2 = 1$, $n_0 t_0 + n_1 t_1 = 0$) and using Equation (2.17) we obtain

$$C\epsilon[u]n = \begin{pmatrix} [\lambda n_0^2 + \mu(1 + n_0^2)] \partial_n u_0 + [\lambda n_0 n_1 + \mu n_0 n_1] \partial_n u_1 + \dots \\ \dots + [\lambda n_0 t_0 + \mu n_0 t_0] \partial_t u_0 + [\lambda n_0 t_1 + \mu n_1 t_0] \partial_t u_1 \\ [\lambda n_0 n_1 + \mu n_0 n_1] \partial_n u_0 + [\lambda n_1^2 + \mu(1 + n_1^2)] \partial_n u_1 + \dots \\ \dots + [\lambda n_1 t_0 + \mu n_0 t_1] \partial_t u_0 + [\lambda n_1 t_1 + \mu n_1 t_1] \partial_t u_1 \end{pmatrix}. \quad (2.46)$$

Hence the coupling condition (2.36) across the interface is given by the linear system of equations

$$\begin{pmatrix} L^{n+} & L^{t+} \\ 0 & 1 \end{pmatrix} \begin{pmatrix} \partial_n u^+ \\ \partial_t u^+ \end{pmatrix} = \begin{pmatrix} L^{n-} & L^{t-} \\ 0 & 1 \end{pmatrix} \begin{pmatrix} \partial_n u^- \\ \partial_t u^- \end{pmatrix} \quad (2.47)$$

with

$$\begin{aligned} L^{n\pm} &= \begin{pmatrix} \lambda^\pm n_0^2 + \mu^\pm(1 + n_0^2) & \lambda^\pm n_0 n_1 + \mu^\pm n_0 n_1 \\ \lambda^\pm n_0 n_1 + \mu^\pm n_0 n_1 & \lambda^\pm n_1^2 + \mu^\pm(1 + n_1^2) \end{pmatrix}, \\ L^{t\pm} &= \begin{pmatrix} \lambda^\pm n_0 t_0 + \mu^\pm n_0 t_0 & \lambda^\pm n_0 t_1 + \mu^\pm n_1 t_0 \\ \lambda^\pm n_1 t_0 + \mu^\pm n_0 t_1 & \lambda^\pm n_1 t_1 + \mu^\pm n_1 t_1 \end{pmatrix}. \end{aligned} \quad (2.48)$$

We can in fact proceed as in Equation (2.37) because L^{n+} is nonsingular because the analogon of Lemma 2.8 is true in 2D.

Let us point out that the derivative in normal direction is coupled to the derivatives in the tangential directions via (2.47) even for $v^\pm = 0$ (which implies $\lambda^\pm = 0$) and a jump only in E .

3 Construction of Composite Finite Elements

ADAPTED BASIS FUNCTIONS are the heart of CFE methods. When dealing with a complicated domain, CFE basis functions will be constructed as standard affine FE basis functions on a Cartesian grid (not resolving the domain boundary) restricted by the boundary. For discontinuous coefficients across a geometrically complicated interface, basis functions are constructed such that they are able to interpolate the expected nondifferentiability in the solution.

Starting from voxel data implicitly describing the domain boundary, a local auxiliary submesh \mathcal{G}^Δ approximating the interface is defined. In case of complicated domains, this \mathcal{G}^Δ is used to construct standard affine FE basis functions restricted to the interior. Figure 3.1 (left column) sketches the idea for this construction in 1D. The 2D and 3D case are conceptually not more complicated, except that ‘complicated’ no longer means ‘disconnected’ as in 1D.

For discontinuous coefficients, the coupling conditions across the interface discussed in Section 2.3 are exploited to construct CFE basis functions. For this purpose, we consider local approximation (or interpolation) problems from nodes of the regular cubic grid to nodes of \mathcal{G}^Δ . Their solutions are used to compose CFE basis functions from a standard affine FE basis on \mathcal{G}^Δ by linear combination with appropriate coefficients (composition weights). This construction is sketched for the scalar 1D case in Figure 3.1 (right column). Generalized to 2D and 3D, this will no longer mean that basis functions themselves satisfy the coupling condition across the interface.

Notice that the construction of local auxiliary meshes depends solely on the interface geometry. Hence also CFE basis functions for complicated domains only depend on the interface geometry. In contrast, the coupling conditions of Section 2.3 and thus

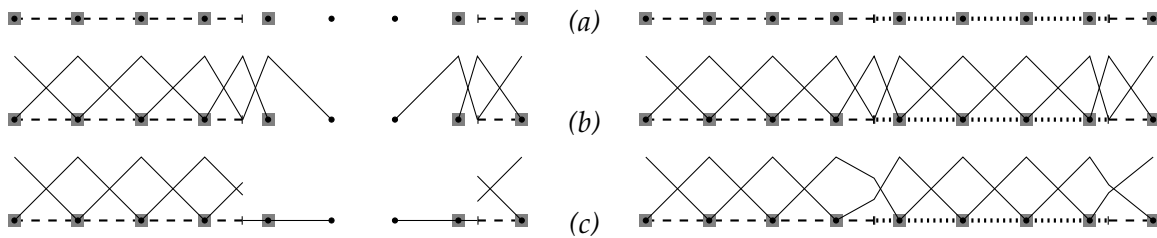


Figure 3.1. Sketch of the scalar 1D CFE construction. *Left column:* Basis functions for a complicated domain, *right column:* basis functions for discontinuous coefficients with kink ratio $\kappa = 3$ between two domains (dashed and dotted). (a) shows the uniform Cartesian grid that does not resolve the geometry. Nodes with degrees of freedom assigned are marked by gray squares. (b) shows a standard basis on a local auxiliary (sub-)mesh approximately resolving the geometry, and (c) shows the resulting CFE basis functions.

the construction of CFE basis functions for discontinuous coefficients also depend on the material coefficients. Actual simulations moreover depend on boundary values and source terms.

The construction of the local auxiliary submesh is discussed in Section 3.1. Section 3.2 describes the construction of CFE basis functions for complicated domains. As for discontinuous coefficients, the isotropic and anisotropic scalar cases and the general vector-valued case are treated in Section 3.3 where composition weights are determined based on the interfacial coupling conditions discussed in Section 2.3. Boundary conditions in the CFE context are discussed in Section 3.4. Finally matrices arising the CFE discretization are addressed in Section 3.5.

The geometric preliminaries and the CFE method for complicated domains are mainly the one in [216] and have been adapted to our CFE framework. It has been published in [217, 282]. The CFE constructions for discontinuous coefficients for both scalar and vector-valued problems have been developed as part of this thesis and has been published and submitted for publication in [310, 281].

3.1 Hexahedral Voxel Grids and Local Auxiliary Meshes

We will explain the CFE construction for the unit cube $\Omega := (0, 1)^3$ as a computational domain which is decomposed in two subdomains Ω_{\pm} and an interface γ described by

$$\begin{aligned}\Omega_+ &:= \{x \in \Omega \mid \varphi(x) > 0\} & \Omega_- &:= \{x \in \Omega \mid \varphi(x) < 0\} \\ \gamma &:= \{x \in \Omega \mid \varphi(x) = 0\}\end{aligned}\tag{3.1}$$

where the *level set function* [266] $\varphi: \Omega \rightarrow \mathbb{R}$ is assumed to be continuously differentiable almost everywhere and non-degenerate in the sense that $\nabla\varphi(z) \neq 0$ for $z \in \gamma$. Note that we require non-degeneracy only for the zero level set.

The *interface* γ represents either the boundary of the geometrically complicated domain Ω_- or the interface between two regions with different material properties. The level set function φ is typically given as voxel image data on a uniform cubic mesh, canonically with piecewise multilinear interpolation.

We will restrict the presentation to the case of two subdomains (i.e., Ω_- is a single, not necessarily connected subdomain, so is Ω_+) even though a single level set function allows for multiple subdomains without triple junctions. The extension to more general Ω or multiple subdomains is possible, as well as the combination of both a complicated domain and an interface with discontinuous coefficients [273].

3.1.1 Regular Tetrahedral Mesh

Definition 3.1. Let \mathcal{G}^{\square} , the *regular cubic grid*, be a uniform cubic mesh discretizing Ω , and let \mathcal{G}^{\boxtimes} , the *regular tetrahedral mesh*, be obtained by dividing each cubic element in six tetrahedra in the way shown in Figure 3.2. Let \mathcal{N}^{\square} be set of *regular nodes* corresponding to \mathcal{G}^{\square} and let $\mathcal{I}^{\square} \subset \mathbb{N}$ be an index set for \mathcal{N}^{\square} with index map $j: \mathcal{N}^{\square} \rightarrow \mathcal{I}^{\square}$.



Figure 3.2. Subdivision of a cube into 6 tetrahedra. The diagonals on the left and right, top and bottom, and front and back faces are pairwise consistent with the neighboring cube, hence the resulting tetrahedral mesh \mathcal{G}^{\boxtimes} is admissible in the usual sense (see, e.g., [55]), in particular there are no hanging nodes. The angles of the regular tetrahedra lie in $\arccos\{0, 1/2, 1/\sqrt{3}, 1/\sqrt{2}, \sqrt{2}/\sqrt{3}\} \approx \{90^\circ, 60^\circ, 54.74^\circ, 45^\circ, 35.26^\circ\}$.

The division of cubic elements is performed in such a way that each cube is split in the same way and such that the (face) diagonals introduced are consistent with neighboring cubes. Note that this introduces a certain anisotropy in the mesh, similar to ‘criss’ (\boxtimes -type division of squares in triangles) or ‘cross’ (\boxtimes -type) meshes in 2D. Note moreover that the node sets \mathcal{N}^{\square} and \mathcal{N}^{\boxtimes} (corresponding to \mathcal{G}^{\boxtimes}) coincide, and we will consistently use \mathcal{N}^{\square} . We will typically use r and s as variables for regular nodes.

Two obvious other choices are not preferable for our application, also in their 3D analogs. Criss-cross (\boxtimes -type) meshes introduce additional nodes. Alternating between criss and cross subdivision of neighboring elements does not allow to treat all elements in the same way and would make the whole construction technically more involved.

Upper case Φ will denote the piecewise affine approximant of the level set function φ and Γ the zero level set of Φ , i.e., a piecewise planar approximation of γ . Moreover, Ω_{\pm}^{Δ} denotes the piecewise tetrahedral approximation of Ω_{\pm} for which Γ forms the interface (the triangle symbol matches \mathcal{G}^{Δ} defined below in Definition 3.3).

Definition 3.2. Let E be a cubic element of \mathcal{G}^{\square} with a fixed ordering of the vertices (e.g., inversely lexicographical ordering of the nodes as explained in Definition 6.1) and φ be the level set function. Then the *signature* $\zeta(E) \in \{-1, 1\}^8$ is defined to be the sign pattern of φ at the vertices. Similarly we define the signature of a simplex $T \in \mathcal{G}^{\boxtimes}$, $\zeta(T) \in \{-1, 1\}^4$, as the sign pattern of its vertices.

3.1.2 Virtual (Tetrahedral) Mesh

Now let us consider a single simplex intersected by the interface (non-intersected simplices require no modification). For this construction we assume that the interface does not pass exactly through any node of \mathcal{G}^{\boxtimes} , see below for a discussion of this issue. In 2D, we can only have a 2 : 1 splitting of the vertices, cutting one regular triangle in one virtual triangle and one quadrilateral q . Subdividing the q in two further virtual triangles is automatically consistent with neighboring regular triangles because no new objects of codimension 2 are introduced. We can hence define the local auxiliary mesh consisting of the virtual triangles.

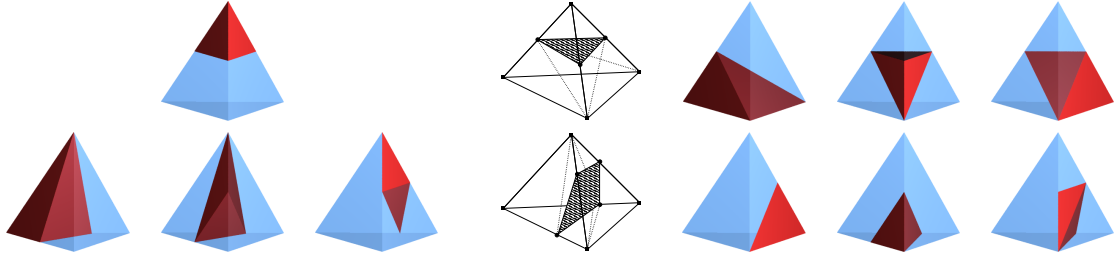


Figure 3.3. Splitting a tetrahedron into one pentahedron and one tetrahedron (*top*) or two pentahedra (*bottom*) by the interface Γ . The dashed lines in the *middle* column show the resulting subdivision in local auxiliary tetrahedra which are visualized individually on the *left* and *right*. Each pentahedron has two triangular faces and three quadrilateral faces for which the subdivision of two neighboring polyhedra needs to be consistent.

Note that our goal is again to use the same subdivision in every square/cube, which may lead to badly shaped simplices as discussed below in Remark 3.6.

In 3D, there are two possibilities how an interface can cut a regular tetrahedron T , see Figure 3.3. Either (top row in Figure 3.3) the vertices of T are split 1 : 3, cutting it into one virtual tetrahedron and one pentahedron which is subdivided in three virtual tetrahedra. Or (bottom row) its vertices are split 2 : 2, cutting T in two pentahedra, each of which is subdivided in three virtual tetrahedra. In both cases, the subdivision of neighboring regular tetrahedra needs to be performed in a consistent way. This is not trivially satisfied because the subdivision introduces new edges (of codimension 2). The virtual tetrahedra finally form the *local auxiliary (sub-)mesh*. By construction, the union of all virtual tetrahedra in one regular tetrahedron equals this regular tetrahedron.

Definition 3.3. Let \mathcal{G}^Δ be the *virtual mesh* obtained by this subdivision procedure with node set $\mathcal{N}^\Delta = \mathcal{N}^\square \dot{\cup} \mathcal{N}^{\text{virt}}$ consisting of *regular nodes* and *purely virtual nodes*. Let \mathcal{N}^Δ be indexed by $j: \mathcal{N}^\Delta \rightarrow \mathcal{I}^\Delta \subset \mathbb{N}$.

Since the meaning of j will always be clear from the context, we do not distinguish notationally between indexing different node sets. Moreover, we will often identify nodes and their indices (and thus, e.g., use nodes as indices for the associated basis functions) to keep notation simple. We will typically use z or y as variables for nodes in \mathcal{N}^Δ .

Lemma 3.4. The meshes and node sets are nested (\succ) in the following way:

$$\begin{aligned} \mathcal{G}^\square &\succ \mathcal{G}^\boxtimes \succ \mathcal{G}^\Delta, \\ \mathcal{N}^\square &= \mathcal{N}^\boxtimes \subset \mathcal{N}^\Delta \supset \mathcal{N}^{\text{virt}}, \quad \mathcal{N}^{\text{virt}} \cap \mathcal{N}^\square = \emptyset. \end{aligned} \tag{3.2}$$

Proof. This follows immediately from the definitions. \square

Notice the resemblance between this subdivision strategy and the marching cubes algorithm [220] and the marching tetrahedra algorithm (see, e.g., [307, Section 6.2]). In particular splitting cubes in regular tetrahedra is performed in the same way for each cube E , which is also true for the subdivision of regular in virtual tetrahedra.

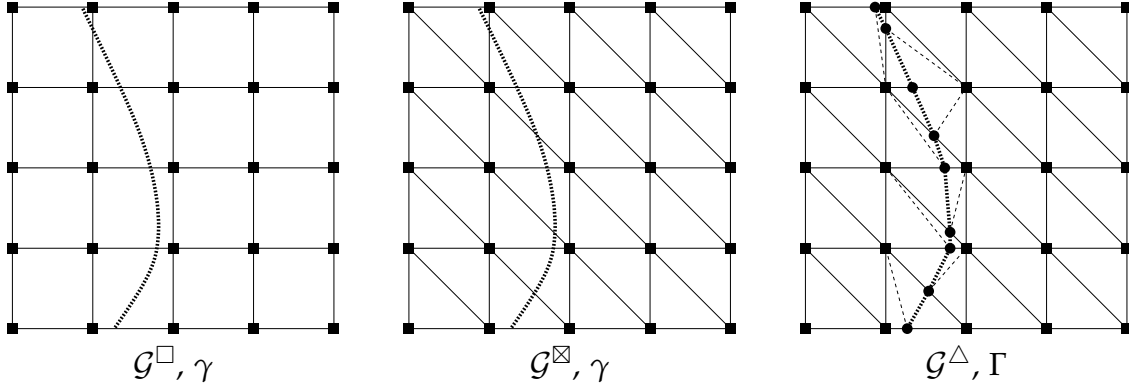


Figure 3.4. The regular (Cartesian) grid \mathcal{G}^{\square} and the regular tetrahedral mesh \mathcal{G}^{\diamond} for a 2D example do not resolve the interface (dotted line) and have the same set of nodes $\mathcal{N}^{\square} = \mathcal{N}^{\diamond}$ shown as \blacksquare . The virtual mesh \mathcal{G}^{\triangle} additionally has purely virtual nodes $\mathcal{N}^{\text{virt}}$ shown as \bullet .

Remark 3.5. The *topology* of the virtual mesh for one cubic element E only depends on the signature $\zeta(E)$ whereas the *geometry* depends on the values of Φ (for which we use piecewise affine interpolation).

If we used a piecewise trilinear approximation of φ to find its zeroes (which is the canonical interpretation of voxel data), we would have to deal with ambiguities for certain $\zeta(E)$ (cf. the ambiguities of marching cubes/tetrahedra, [260, 236, 338]). Along face and space diagonal edges, multilinear means second and third order polynomial, respectively. So the same sign of φ at both end vertices may mean zero or two roots on the edge, and a sign change may be due to one or three roots. Using a piecewise affine interpolation on the tetrahedral subdivision explained above, the topology of the interface approximation is uniquely determined, but due to the mesh anisotropy it is not invariant under rotation or flipping of the data set. Figure 3.5 shows the complete classification of signatures in 128 troublesome and 128 non-ambiguous cases (see also [260]). In the troublesome cases, more than one connected component of the interface cuts through the cube so that the regular tetrahedral subdivision is not topologically invariant under rotation of the dataset. In the other cases, the difference between multilinear and affine approximation is $O(h^2)$ for grid spacing h , thus the location of the interface is determined up to sub-pixel shift, and this error can be neglected compared to inaccuracies in the image acquisition.

Remark 3.6. The virtual tetrahedra can have arbitrarily bad *aspect ratio* (radius of the smallest containing sphere divided by the radius of the largest contained sphere, cf. [77]). For geometric reasons, only certain types of badly shaped tetrahedra [77] can occur in the virtual mesh, see Figure 3.6. As the virtual mesh is not used as a computational mesh, this is no immediate numerical problem in the CFE context.

However, to avoid numerical instabilities due to extremely small virtual tetrahedra, we require the virtual nodes to lie away from the regular nodes by at least a certain fraction of the respective edge length. If there is a lower and upper bound on the gradient of Φ , this can also be achieved by shifting Φ away from zero. For

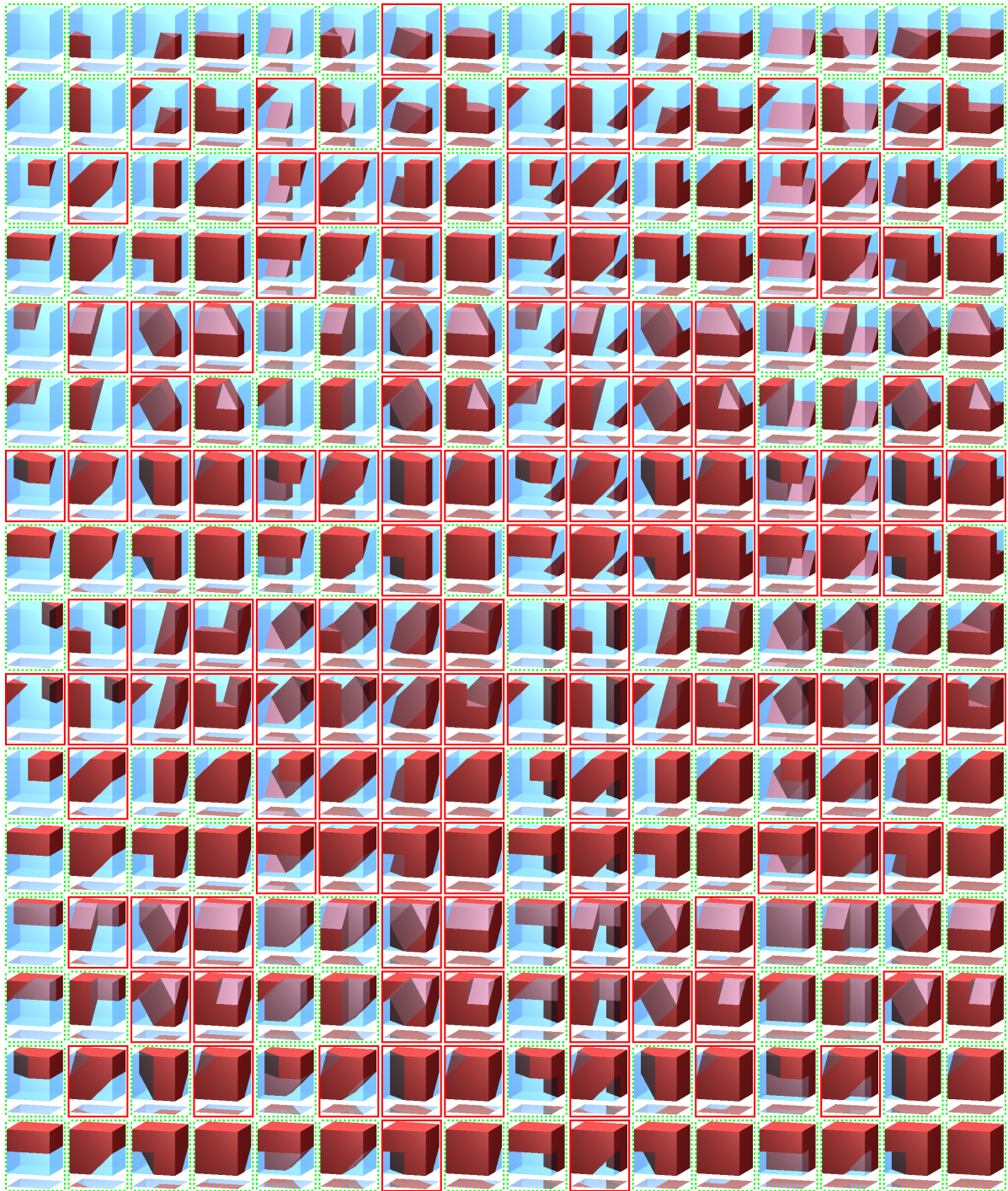


Figure 3.5. For each possible signature (sign pattern of the level set function), the topology of the corresponding local auxiliary mesh is shown. Solid red frames indicate ambiguous cases in a marching cubes approach (the interface cuts the element more than once) for which the topology of the local auxiliary mesh (and thus also \mathcal{G}^Δ) is not invariant under rotation or mirroring of the dataset. Dashed green frames show the invariant cases. A mirror is placed below each cube to show all corners of the element.

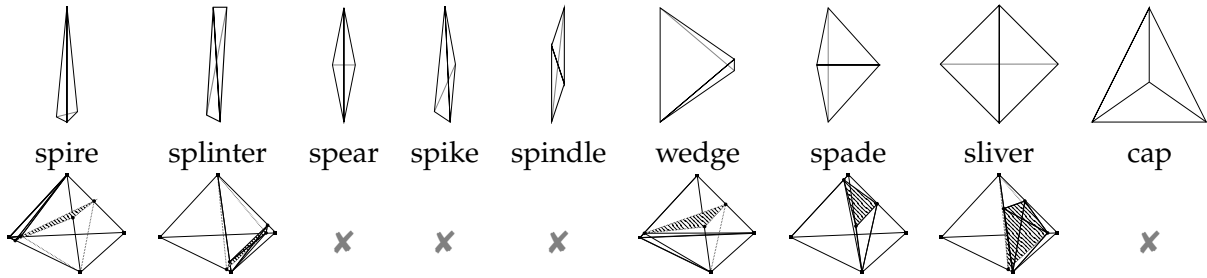


Figure 3.6. The classification of badly shaped tetrahedra (with small aspect ratio) according to [77]. The bottom row shows examples for those types that can occur in the CFE construction, \times indicates those types that cannot occur due to geometric reasons.

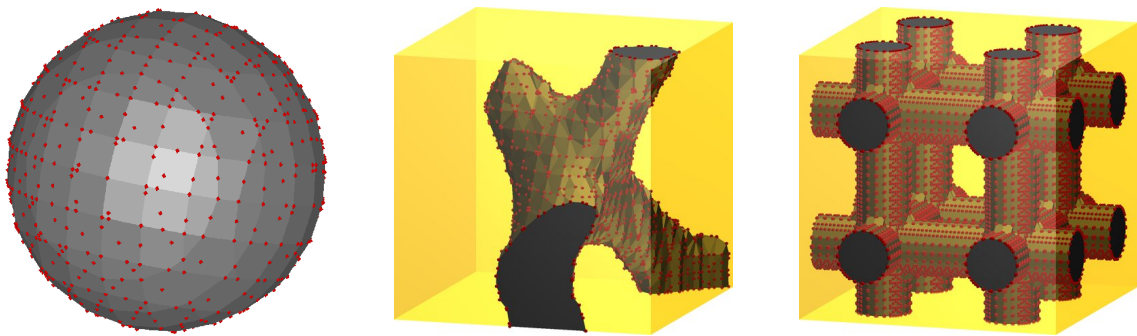


Figure 3.7. Virtual nodes are shown as small red dots for three different interfaces, a sphere (viewed and visualized as a complicated domain), part of an aluminum foam and an artificial trabecular structure (*left to right*, both viewed as domains with discontinuous coefficients). The geometric locations of the virtual nodes (on edges of the regular tetrahedral mesh \mathcal{G}^{\boxtimes}) and the (flat) shading of the faces reflects the cubic structure of \mathcal{G}^{\boxtimes} .

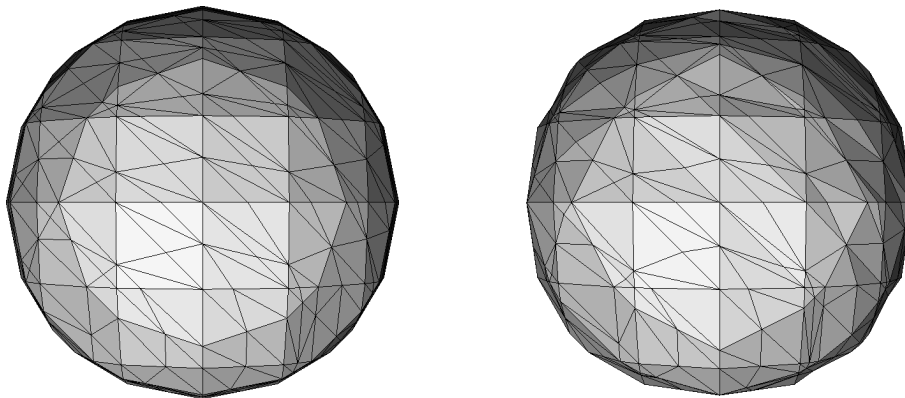


Figure 3.8. The two balls are CFE-reconstructed zero level sets of a floating point voxel dataset (*left*) and a 7 bit (to pronounce the effect) quantized version of the same dataset (*right*), showing that quantization leads to non-smooth interfaces.

appropriate correction parameters this modification shifts the interface only by a negligible amount compared to image acquisition inaccuracies. Note that this correction can also handle the case $\Phi(r) = 0$, i.e., the case of an interface passing precisely through a regular grid point $r \in \mathcal{G}^{\boxtimes}$ (the only decision in this case being whether to use a positive or negative shift).

Examples of the interface reconstruction along with the location of virtual nodes are shown in Figure 3.7 for three different interfaces. Artificial interfaces are typically given by analytically computed signed distance functions, whereas actual physical specimens are described by quantized image data. Figure 3.8 illustrates how quantization of the voxel data (which are often only 8 bit images) leads to less smooth appearance of the reconstructed interface.

3.1.3 General Composite Finite Element Notation

For future use, let us introduce the following notation.

Definition 3.7. If a virtual node z lies on the edge $[r, s]$ in \mathcal{G}^{\boxtimes} between two regular nodes $r, s \in \mathcal{N}^{\square}$, these two nodes are referred to as *geometrically constraining nodes*, $\mathbb{P}^{\setminus}(z) = \{r, s\}$. Conversely, z will also be written as $\hat{r}\hat{s}$.

Definition 3.8. Let $\mathbb{A}(z) = \{T \in \mathcal{G}^{\boxtimes} \mid z \in T\}$ be the set of regular tetrahedra containing z (simplices adjacent to z , *patch* or *star* around z). Furthermore, let $\mathbb{P}^{\boxplus}(z)$ be the set of all vertices of regular tetrahedra in $\mathbb{A}(z)$, which clearly satisfies $\mathbb{P}^{\setminus}(z) \subset \mathbb{P}^{\boxplus}(z)$. These constraint sets are shown in Figure 3.9 for a 2D example.

Definition 3.9. Let $\mathcal{N}^{\text{DOF}} \subset \mathcal{N}^{\square}$ be the set of nodes (on the Cartesian grid) that are assigned a DOF. In case of complicated domains, \mathcal{N}^{DOF} will be a proper subset of \mathcal{N}^{\square} . In case of discontinuous coefficients, the two sets will coincide.

Let $(\psi_z^{\Delta})_{z \in \mathcal{N}^{\Delta}}$ be a standard nodal tent basis on \mathcal{G}^{Δ} (*virtual basis*). The CFE basis functions $(\psi_r^{\text{CFE}})_{r \in \mathcal{N}^{\text{DOF}}}$ will be composed of the virtual basis functions as a linear combination

$$\psi_r^{\text{CFE}} = \sum_{z \in \mathbb{D}(r)} \mathfrak{w}_{z,r} \psi_z^{\Delta} \quad (3.3)$$

with the set of *constrained nodes* $\mathbb{D}(r) \subset \mathcal{N}^{\Delta}$ and *composition weights* $\mathfrak{w}_{z,r}$ to be determined in detail in the following sections. In the complicated domain case, Equation (3.3) holds only inside the object. Conversely, we define a set $\mathbb{P}(z)$ of regular nodes constraining a virtual node z

$$\mathbb{P}(z) := \{r \in \mathcal{N}^{\text{DOF}} \mid z \in \mathbb{D}(r)\} \quad (3.4)$$

where the notation reflects an $m : n$ parent/descendant (child) relation, hence the symbols \mathbb{P} and \mathbb{D} .

Note that one could view this composition (3.3) as a 0th (multigrid) coarsening step. This interpretation, however, is misleading because the virtual mesh considered here is never used as a computational mesh.

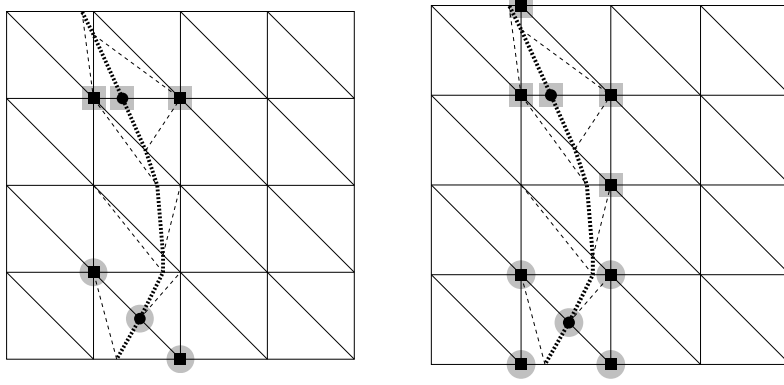


Figure 3.9. The sets $\mathbb{P}^\setminus(\bullet)$ of geometrically constraining regular nodes for two virtual nodes are shown on the *left*, the sets $\mathbb{P}^\boxplus(\bullet)$ for the same nodes are shown on the *right*.

CFE basis functions to be constructed later in this section will be denoted by ψ^{CFE} (scalar) and Ψ^{CFE} (vector-valued basis functions). The corresponding function spaces are defined to be

$$\begin{aligned} \mathcal{V}^{\text{CFE}} &= \text{span} \{ \psi_r^{\text{CFE}} \mid r \in \mathcal{N}^{\text{DOF}} \} && \text{in the scalar case, and} \\ \mathcal{V}^{\text{CFE}} &= \text{span} \{ \Psi_{r;\alpha}^{\text{CFE}} \mid r \in \mathcal{N}^{\text{DOF}}, \alpha \in \{0, 1, 2\} \} && \text{in the vector-valued case.} \end{aligned} \quad (3.5)$$

3.2 CFE for Complicated Domains

Let, for an arbitrary set M ,

$$\begin{aligned} \chi_M: M &\rightarrow \mathbb{R} \\ x &\mapsto \chi_M(x) = \begin{cases} 1 & \text{for } x \in M \\ 0 & \text{otherwise} \end{cases} \end{aligned} \quad (3.6)$$

be the *characteristic function* of M .

Definition 3.10. Scalar CFE basis functions for complicated domains are the standard basis functions $(\psi_r^{\boxtimes})_{r \in \mathcal{N}^{\square}}$ on the regular tetrahedral mesh \mathcal{G}^{\boxtimes} , restricted to the interior of the domain approximation $\Omega_{\triangle}^{\Delta}$:

$$\psi_r^{\text{CFE}} = \chi_{\Omega_{\triangle}^{\Delta}} \psi_r^{\boxtimes}. \quad (3.7)$$

The constraint sets in this case are $\mathbb{P}(z) = \mathbb{P} \setminus (r)$ for all virtual nodes $z \in \mathcal{N}^{\text{virt}}$ and $\mathbb{P}(r) = \{r\}$ for all regular nodes $r \in \mathcal{N}^{\square}$.

Let us put this construction in the general CFE context introduced above. This will allow us to use general CFE methods for assembling FE matrices rather than adapted quadrature to capture the influence of the characteristic function $\chi_{\Omega_{\triangle}^{\Delta}}$. Let $z \in \mathcal{N}^{\text{virt}}$ be a virtual node lying on the edge $[r_0, r_1]$ in \mathcal{G}^{\boxtimes} between two regular nodes $r_0, r_1 \in \mathcal{N}^{\square}$. Then we define

$$\begin{aligned} \mathfrak{w}_{z,r_0} &:= \frac{\|r_1 - z\|_2}{\|r_1 - r_0\|_2}, \\ \mathfrak{w}_{z,r_1} &:= \frac{\|z - r_0\|_2}{\|r_1 - r_0\|_2} = 1 - \mathfrak{w}_{z,r_0}, \\ \mathfrak{w}_{r,r} &:= 1 \quad \text{for any } r \in \mathcal{N}^{\square}, \\ \mathfrak{w}_{p,r} &:= 0 \quad \text{for any } r \in \mathcal{N}^{\square} \text{ and any other (regular or virtual) node } p \in \mathcal{N}^{\Delta}. \end{aligned} \quad (3.8)$$

We can compute the geometric location of z in terms Φ with piecewise affine interpolation along the edge as

$$\begin{aligned} 0 &= \Phi(z) = \frac{z - r_0}{r_1 - r_0} \Phi(r_1) + \frac{r_1 - z}{r_1 - r_0} \Phi(r_0) \\ \Leftrightarrow z &\cdot \frac{\Phi(r_1) - \Phi(r_0)}{r_1 - r_0} = \frac{-r_0 \Phi(r_1) - r_1 \Phi(r_0)}{r_1 - r_0} \\ \Leftrightarrow z &= \frac{-r_0 \Phi(r_1) - r_1 \Phi(r_0)}{\Phi(r_1) - \Phi(r_0)} \end{aligned} \quad (3.9)$$

and substitute these expressions in (3.8).

With these definitions, the CFE basis functions for complicated domains can be expressed in the following way.

Lemma 3.11. Basis functions can be expressed as

$$\psi_r^{\text{CFE}} = \sum_{z \in \mathcal{D}(r)} w_{z,r} \psi_z^{\Delta} \chi_{\Omega_-^{\Delta}}, \quad (3.10)$$

and the set of DOF is $\mathcal{N}^{\text{DOF}} = \{r \in \mathcal{N}^{\square} \mid \psi_r^{\text{CFE}} \not\equiv 0\}$, i.e., the set of nodes for which the corresponding CFE basis function does not vanish on whole Ω_-^{Δ} .

This construction in 1D is illustrated in Figure 3.10.

Remark 3.12. This definition of ψ^{CFE} does not depend on isotropy or anisotropy of coefficients in the problem to be considered. In vector-valued problems, each spatial component of the quantity under consideration is discretized separately, that is $\Psi_{r;\alpha}^{\text{CFE}} = \psi_r^{\text{CFE}} e_{\alpha}$.

Remark 3.13. For assembling CFE matrices, multiplication by the characteristic function $\chi_{\Omega_-^{\Delta}}$ is implemented by restricting the integration to Ω_-^{Δ} .

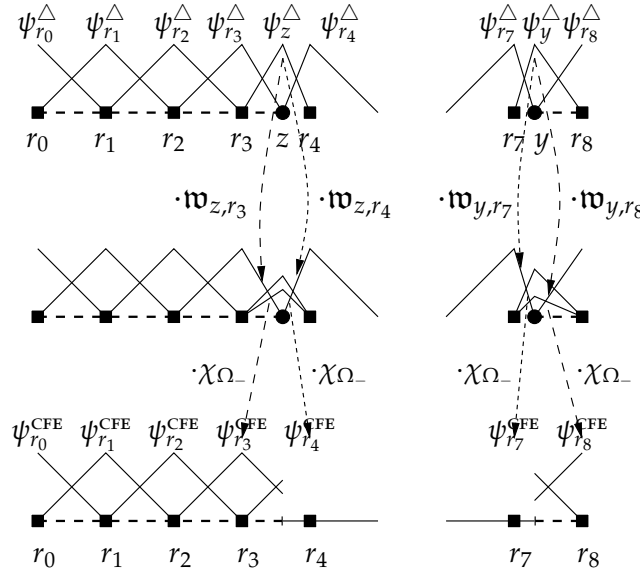


Figure 3.10. For a complicated domain in 1D, CFE basis functions ψ^{CFE} (bottom row) are standard affine tent functions restricted to the interior. In the general CFE context and for the implementation, the ψ^{CFE} are constructed as linear combinations (with weights shown next to the arrows) of the virtual basis functions ψ^{Δ} (middle row) restricted to the interior Ω_- . The virtual basis functions for the regular nodes all contribute to the CFE basis functions with weight 1, for which arrows in the figure are omitted.

Proposition 3.14. The CFE basis functions for complicated domains $(\psi_r^{\text{CFE}})_{r \in \mathcal{N}^{\text{DOF}}}$ satisfy the following properties:

1. The ψ_r^{CFE} are piecewise affine on Ω_-^Δ .
2. The ψ_r^{CFE} form a partition of unity inside Ω_-^Δ .
3. The ψ_r^{CFE} are nodal for regular nodes $r \in \mathcal{N}^\square$ inside Ω_-^Δ .
4. For $r \in \mathcal{N}^\square$ being inside Ω_- with $\mathbb{D}(r) = \{r\}$ (far from the interface), ψ_r^{CFE} is simply the standard tent function ψ_r^Δ .
5. For $r \in \mathcal{N}^\square$ (on either side) with $\mathbb{D}(r) \cap \mathcal{N}^{\text{virt}} \neq \emptyset$ (near the interface), ψ_r^{CFE} is modified and has smaller support than ψ_r^Δ .
6. For any $r \in \mathcal{N}^\square$, the number of nodes $s \in \mathcal{N}^\square$ with overlapping support of their basis functions, $\text{supp}(\psi_r^{\text{CFE}}) \cap \text{supp}(\psi_s^{\text{CFE}}) \neq \emptyset$, is bounded by 15.

Proof. ad 1. This follows immediately from ψ_r^{CFE} being a linear combination of piecewise affine ψ_z^Δ .

ad 2. This is because the ψ_z^Δ do and because for any $z \in \mathcal{N}^\Delta$,

$$\begin{aligned} \sum_{r \in \mathbb{P}(z)} \mathfrak{w}_{z,r} &= \begin{cases} \mathfrak{w}_{z,r_0} + \mathfrak{w}_{z,r_1} & \text{for } z \in \mathcal{N}^{\text{virt}} \Rightarrow \mathbb{P}(z) = \{r_0, r_1\} \\ \mathfrak{w}_{r,r} & \text{for } z = r \in \mathcal{N}^\square \Rightarrow \mathbb{P}(z) = \{r\}. \end{cases} \\ &= 1 \end{aligned} \quad (3.11)$$

ad 3. This is due to nodality of ψ_z^Δ , i.e., $\psi_z^\Delta(y) = \delta_{yz}$ for all $y, z \in \mathcal{N}^\Delta$, the partition of unity property 2, and the fact that $\mathfrak{w}_{r,s} = \delta_{rs}$ for all $r, s \in \mathcal{N}^\square$.

The remaining properties follow from the construction by observing that no constraints other than the geometric ones are used, thus CFE node neighborhoods are contained in standard affine FE neighborhoods. \square

Remark 3.15. Item 3 of Proposition 3.14 implies linear independence of the $(\psi_r^\Delta)_{r \in \mathcal{N}^\square}$, so they indeed form a basis of \mathcal{V}^{CFE} .

Nodes $r \in \mathcal{N}^\square$ being inside Ω_+ with $\mathbb{D}(r) = \emptyset$ (nodes outside and far from the interface) are not assigned a degree of freedom, thus there is no corresponding CFE basis function. Figure 3.11 shows a 2D example of CFE basis functions for complicated domains.

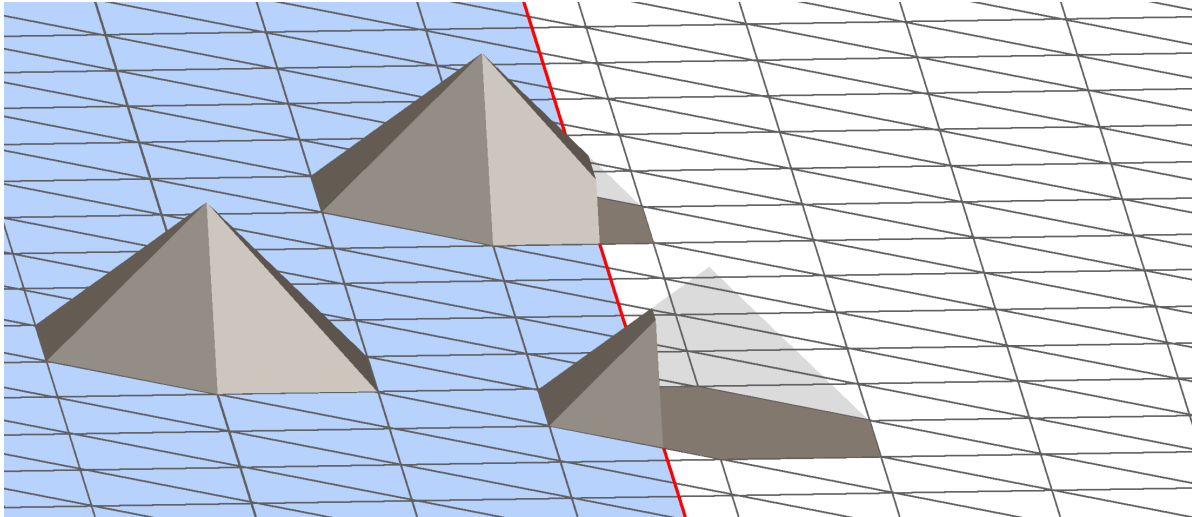


Figure 3.11. 2D CFE basis function example. *Left:* Inside the domain Ω_- (blue region, equals $\Omega_{\triangle}^{\triangle}$ for this straight line interface) and away from the interface (red line), the CFE basis function equals a standard tent function on the cross mesh (gray lines). *Middle two:* At the interface, the standard basis functions are set to zero outside the domain (the light gray tents indicate the standard basis functions). *Right* (no tent function): Nodes outside the domain and far from the interface do not have degrees of freedom or basis functions.

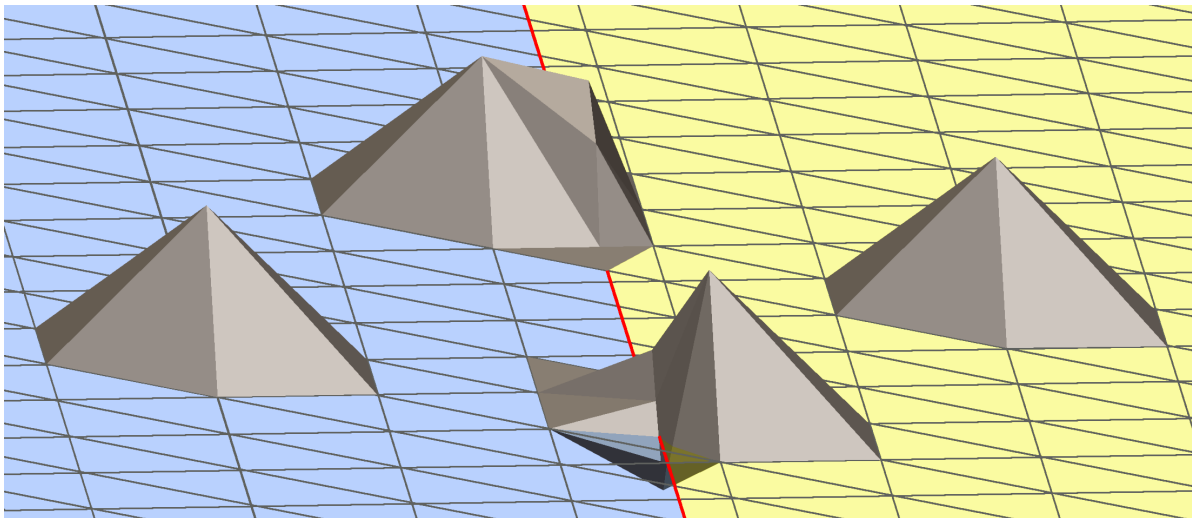


Figure 3.12. 2D CFE basis function example for discontinuous coefficients, isotropic scalar case with a kink ratio $\kappa = 10$. *Left:* In the Ω_- domain (blue region) and away from the interface (red line), the CFE basis function equals a standard tent function on the cross mesh (gray line). *Middle two:* At the interface, CFE basis functions are modified so that locally admissible functions can be approximated correctly. This enlarges their support compared to standard tent functions and allows negative values. *Right:* In the Ω_+ domain (yellow region) and away from the interface, we again obtain standard tent functions.

3.3 CFE for Discontinuous Coefficients

For the construction of CFE basis functions for discontinuous coefficients, the introductory 1D example in Figure 3.1 is partially instructive but may also be misleading. In d space direction, the interface has one normal and $d - 1$ tangential directions which makes the 1D case (without tangential directions) rather special. The CFE basis functions are constructed in such a way that they are capable of a first-order approximation of locally admissible functions as discussed in Section 2.3. This means in particular that the construction is problem-specific. It will turn out that this interpolation property cannot be satisfied if only the two $\mathbb{P}^1(z)$ nodes are used for interpolation and that, in the vector-valued case, spatial components cannot be discretized separately at the interface.

The construction of CFE basis functions for discontinuous coefficients is based on interpolation operators $\mathcal{I}: C^0 \rightarrow \mathcal{V}^\Delta$, the space of piecewise affine functions on \mathcal{G}^Δ , evaluating functions at regular grid nodes and determining values at the virtual nodes on the interface. Interpolation here needs to be consistent with the interfacial coupling conditions (2.28), (2.32), or (2.36).

Degrees of freedom will be assigned to each node of the regular cubic grid, i.e., $\mathcal{N}^{\text{DOF}} = \mathcal{N}^\square$.

In this section, we will first discuss the CFE construction for the scalar model problem (Section 3.3.1), then extend it to the vector-valued model problem in Section 3.3.2. Details about whether the local problems arising in the construction are uniquely solvable or not and examples for specific properties of the resulting CFE basis functions are finally presented in Section 3.3.3.

Geometric Situation. Consider a piecewise planar interface cutting through a regular tetrahedron T with vertices r_0, r_1, r_2, r_3 and one particular virtual node z . For z , consider directions n normal and s and t tangential to the interface such that n, s , and t are pairwise orthogonal and normalized and n is the outer normal to Ω_- .

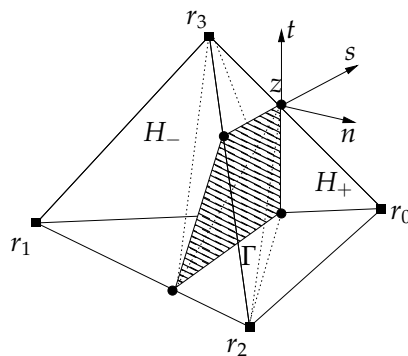


Figure 3.13. Example of a piecewise planar interface approximation cutting through one regular tetrahedron. At one virtual node z , the normal direction n and the tangential directions s, t are shown. A local interpolation scheme from the regular nodes r_i to the virtual node z will be constructed by local Taylor expansion of admissible functions.

For a general, curved interface, n approximates the outer normal to Ω_- at the node z . We compute n by summing the gradient of the level set function over all $T \in \mathcal{A}(z)$ (adjacent tetrahedra, cf. Definition 3.8) and then normalizing the sum. One may be able to improve the approximation of the interface normal by different choice of averaging weights, but this does not necessarily improve the overall approximation.

3.3.1 Heat Diffusion Model Problem

Using the planar interface approximation on T and the corresponding division of \mathbb{R}^3 into $H_{\pm} = \{x | \langle x - z, n \rangle \gtrless 0\}$, we define the space of locally admissible functions $\mathcal{V}^{\text{local}}[T, z, n]$ to be the span of the local prototype functions η^k defined in (2.30) for the isotropic case or (2.34) for the anisotropic case. As an example, we consider the case shown in Figure 3.13, $r_0, r_2 \in H_+$ and $r_1, r_3 \in H_-$, throughout the different constructions. Other sign patterns $\zeta(T)$ are treated similarly.

CFE Construction based on Local Approximation

First let us define the set of coefficients yielding a suitable approximation of a function $u \in C^0$ in $\mathcal{V}^{\text{local}}[T, z, n]$.

Problem 3.16. Let $\mathcal{M}_{T,z,n}[u]$ be the set of coefficient vectors $(\tilde{\alpha}^0, \dots, \tilde{\alpha}^3)$ minimizing

$$\sum_{i=0,\dots,3} \left(u(r_i) - \sum_{k=0,\dots,3} \tilde{\alpha}^k \eta^k(r_i) \right)^2 \quad (3.12)$$

where the r_i are the vertices of the tetrahedron T . There is not necessarily a unique minimizer, so to select a unique coefficient vector, we define

$$(\alpha^0, \dots, \alpha^3) := \operatorname{argmin}_{(\tilde{\alpha}^k)_{k=0,\dots,3} \in \mathcal{M}_{T,z,n}[u]} \sum_{k=0,\dots,3} (\tilde{\alpha}^k)^2. \quad (3.13)$$

Remark 3.17. The set $\mathcal{M}_{T,z,n}[u]$ is an affine subspace of \mathbb{R}^4 , in particular $\mathcal{M}_{T,z,n}[u]$ is nonempty. Its dimension does not depend on u , so the existence of a unique minimizer of (3.12) is independent of u . Equation (3.13) always has a unique solution because we minimize the Euclidean norm of $(\tilde{\alpha}_0, \dots, \tilde{\alpha}_3)$ over the affine subspace $\mathcal{M}_{T,z,n}[u]$.

In Section 3.3.3 we will see that in the isotropic case there exists a unique interpolation of any set of nodal values $u(r_0), \dots, u(r_3)$ in $\mathcal{V}^{\text{local}}[T, z, n]$. Thus the minimum in (3.12) is zero and the minimizer is unique. In contrast, for anisotropic tensors a^{\pm} there may exist an affine solution space of dimension at least 1, and correspondingly not every set of nodal values $u(r_0), \dots, u(r_3)$ can be interpolated appropriately by a function in $\mathcal{V}^{\text{local}}[T, z, n]$.

The local evaluation of this approximation of u at the interface point z is then defined as

$$\mathcal{P}_{T,z,n}[u] := \sum_{k=0,\dots,3} \alpha^k \eta^k(z). \quad (3.14)$$

Now that we have defined $\mathcal{P}_{T,z,n}$ for each regular tetrahedron T intersected by the interface, we can construct a global interpolation operator via local averaging near the interface.

Definition 3.18. Let $\mathcal{I}[\bullet]: C^0 \rightarrow \mathcal{V}^\Delta$ be the *interpolation operator* defined by

$$\mathcal{I}[u](p) := \begin{cases} \frac{1}{\#\mathbb{A}(z)} \sum_{T \in \mathbb{A}(p)} \mathcal{P}_{T,p,n(p)}[u] & \text{for } p \in \mathcal{N}^{\text{virt}}, \\ u(p) & \text{for } p \in \mathcal{N}^\square \end{cases} \quad (3.15)$$

and piecewise affine interpolation on \mathcal{G}^Δ .

Note that the set $\mathbb{A}(z)$ is non-empty and its cardinality is bounded by 8. By construction, $\mathcal{I}[u](p)$ is determined solely by values of u at regular nodes $r \in \mathcal{N}^\square$.

For curved interfaces, using an approximate interface and interface normal for each virtual node causes the interpolation $\mathcal{I}[\bullet]$ to satisfy the interfacial isotropic coupling condition (2.28) or the anisotropic one (2.32) only in an approximate way.

Definition 3.19. The *CFE basis functions for discontinuous coefficients* and the corresponding CFE space are now defined based on the interpolation $\mathcal{I}[\bullet]$ as

$$\psi_r^{\text{CFE}} := \mathcal{I}[\psi_r^\boxtimes] \quad \forall r \in \mathcal{N}^\square, \quad \mathcal{V}^{\text{CFE}} := \text{span} \{ \psi_r^{\text{CFE}} \mid r \in \mathcal{N}^\square \}. \quad (3.16)$$

We will see in Equation (3.22) how the ψ^{CFE} are actually composed of the ψ^\boxtimes .

Reinterpretation of the Construction as Based on Local Interpolation

For this section let us assume that the local approximation problem (3.12) has a unique solution. Then the minimum set $\mathcal{M}_{T,z,n}[u]$ consists of a single coefficient vector corresponding to the minimum zero, and we can equivalently consider a local interpolation problem in $\mathcal{V}^{\text{local}}[T, z, n]$. For any set of r_i -nodal values y_i there exists a unique $u \in \mathcal{V}^{\text{local}}[T, z, n]$ with $u(r_i) = y_i$ and we determine interpolation weights $\mathfrak{w}_{z,r_i;T}$ satisfying

$$\mathcal{P}_{T,z,n}[u] = u(z) = \sum_{i=0,\dots,3} \mathfrak{w}_{z,r_i;T} u(r_i). \quad (3.17)$$

In other words, the $\mathfrak{w}_{z,r_i;T}$ are used to compute the value of any locally admissible function u satisfying the coupling condition (2.28) at a virtual node z as a linear combination of the values of u at the regular nodes of the tetrahedron $T \in \mathbb{A}(z)$. This is done by solving the following problem.

Problem 3.20. Solve the system of equations

$$[\eta^i(r_j)]_{i,j} [\mathfrak{w}_{z,r_j;T}]_j = [\eta^i(z)]_i \quad (3.18)$$

where the η^i are the prototype functions defined in Equation (2.30) or (2.34) spanning the space of locally admissible functions have been substituted in Equation (3.17).

The 4×4 system matrix, called B for later use, obviously depends on $\kappa = \kappa(a)$ and the geometry (r_i, z, n, s, t) . If (3.12) has a unique solution with minimum zero, the system (3.18) is also uniquely solvable. Let us point out that the last line of the system (3.18) implies $\sum_j \mathfrak{w}_{z,r_j;T} = 1$, but the $\mathfrak{w}_{z,r_0;T}$ may be negative or greater than 1, so Equation (3.17) is not necessarily a convex combination (see Section 3.3.4 for 2D examples for $\mathfrak{w} \notin [0, 1]$).

Example 3.21. For the splitting case shown in Figure 3.13 ($r_0, r_2 \in H_-, r_1, r_3 \in H_+$), the system (3.18) becomes

$$\begin{pmatrix} \kappa \langle r_0 - z, n \rangle & \langle r_1 - z, n \rangle & \kappa \langle r_2 - z, n \rangle & \langle r_3 - z, n \rangle \\ \langle r_0 - z, s \rangle & \langle r_1 - z, s \rangle & \langle r_2 - z, s \rangle & \langle r_3 - z, s \rangle \\ \langle r_0 - z, t \rangle & \langle r_1 - z, t \rangle & \langle r_2 - z, t \rangle & \langle r_3 - z, t \rangle \\ 1 & 1 & 1 & 1 \end{pmatrix} \begin{pmatrix} \mathfrak{w}_{z,r_0;T} \\ \mathfrak{w}_{z,r_1;T} \\ \mathfrak{w}_{z,r_2;T} \\ \mathfrak{w}_{z,r_3;T} \end{pmatrix} = \begin{pmatrix} 0 \\ 0 \\ 0 \\ 1 \end{pmatrix}, \quad (3.19)$$

$$\begin{pmatrix} \langle r_0 - z, K^n n \rangle & \langle r_1 - z, n \rangle & \langle r_2 - z, K^n n \rangle & \langle r_3 - z, n \rangle \\ \langle r_0 - z, K^s n + s \rangle & \langle r_1 - z, s \rangle & \langle r_2 - z, K^s n + s \rangle & \langle r_3 - z, s \rangle \\ \langle r_0 - z, K^t n + t \rangle & \langle r_1 - z, t \rangle & \langle r_2 - z, K^t n + t \rangle & \langle r_3 - z, t \rangle \\ 1 & 1 & 1 & 1 \end{pmatrix} \begin{pmatrix} \mathfrak{w}_{z,r_0;T} \\ \mathfrak{w}_{z,r_1;T} \\ \mathfrak{w}_{z,r_2;T} \\ \mathfrak{w}_{z,r_3;T} \end{pmatrix} = \begin{pmatrix} 0 \\ 0 \\ 0 \\ 1 \end{pmatrix}$$

for the isotropic and anisotropic cases, respectively.

Local Interpolation Operator. In case of a globally planar interface, the interpolation scheme obtained above is exact for any other $T \in \mathbb{A}(z)$. The weights $\mathfrak{w}_{z,r;T_0}$ and $\mathfrak{w}_{z,r;T_1}$ for the same pair of a virtual and a regular node with respect to different simplices T_0 and T_1 , however, cannot be expected to be the same. In general, the interface is curved (and a planar approximation is considered inside each regular tetrahedron), so the interpolation scheme Equation (3.17) only yields an approximation. There is no general preference measure for the adjacent tetrahedra, so we use the arithmetic mean of all possible weights.

Definition 3.22. Let (r_0, r_1, r_2, r_3) be the vertices of $T \in \mathbb{A}(z)$ and $\mathfrak{w}_{z,r_j;T}$ be the weights obtained by Equation (3.19), then the *averaged interpolation weights* are obtained as

$$\mathfrak{w}_{z,r} = \frac{1}{\#\mathbb{A}(z)} \sum_{T \in \mathbb{A}(z)} \mathfrak{w}_{z,r;T} \quad (3.20)$$

where $\mathfrak{w}_{z,s;T} = 0$ if s is not a vertex of T .

This averaging preserves the property $\sum_r \mathfrak{w}_{z,r} = 1$ and yields a correct interpolation scheme for a planar interface.

Definition 3.23. Let $\mathbb{P}(z) = \{r \in \mathcal{N}^\square \mid \mathfrak{w}_{z,r} \neq 0\} \subset \mathbb{P}^\boxplus(z)$, then we define the *interpolation operator* $\mathcal{J}[\bullet]: C^0 \rightarrow \mathcal{V}^\Delta$ by

$$\mathcal{J}[u](z) := \sum_{r \in \mathbb{P}(z)} \mathfrak{w}_{z,r} u(r) \quad (3.21)$$

and piecewise affine interpolation on \mathcal{G}^Δ .

3 Construction of Composite Finite Elements

As in Definition 3.10, let $\mathbb{P}(r) = \{r\}$ and $w_{r,r} = 1$ and $w_{p,r} = 0$ for any remaining (regular or virtual) node p not covered by (3.20).

In the implementation (Section 6.2.3) it will turn out that we have a (binary) preference measure and exclude certain ‘unreliable’ tetrahedra from $\mathbb{A}(z)$ based on whether the numerical solution of Equation (3.19) is satisfactory. As long as $\mathbb{A}(z)$ remains non-empty, the stated properties of the construction above still hold.

Composition of CFE Basis Functions. Let us now reinterpret this interpolation to use it for the construction of CFE basis functions. For a fixed regular node $r \in \mathcal{N}^\square$, consider a function $B_r \in \mathcal{V}^\Delta$ with values $B_r(s) = \delta_{rs}$ at all $s \in \mathcal{N}^\square$. Even though such B_r does not globally satisfy Equation (2.28), we can interpolate B_r via (3.21). The value $w_{z,r} = \mathcal{J}[B_r](z)$ is then the value which a composite finite element basis function ψ_r^{CFE} should have at the virtual node z , or in other words the composition weight with which the virtual basis function ψ_z^Δ contributes to ψ_r^{CFE} .

Lemma 3.24. CFE basis functions ψ^{CFE} defined in Equation (3.16) are composed of virtual basis functions ψ^Δ by

$$\psi_r^{\text{CFE}}(x) = \sum_{z \in \mathbb{D}(r)} w_{z,r} \psi_z^\Delta(x). \quad (3.22)$$

This construction is (in 1D) illustrated in Figure 3.14.

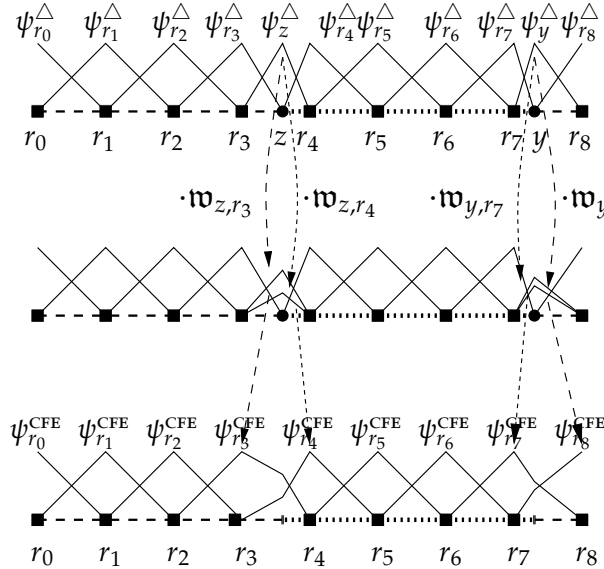


Figure 3.14. For discontinuous coefficients in 1D for kink ratio $\kappa = 3.5$, CFE basis functions ψ^{CFE} are constructed as linear combinations of the virtual basis functions ψ^Δ . The virtual basis functions for the regular nodes all contribute to the CFE basis functions with weight 1, for which arrows are omitted in the figure.

Proposition 3.25. The CFE basis functions for discontinuous coefficients in the scalar case $(\psi_r^{\text{CFE}})_{r \in \mathcal{N}^{\text{DOF}}}$ satisfy the following properties:

1. The ψ_r^{CFE} are piecewise affine on Ω_-^Δ .
2. The ψ_r^{CFE} form a partition of unity if constructed by solving the interpolation problem (3.18).
3. The ψ_r^{CFE} are nodal on \mathcal{N}^\square if constructed by solving the interpolation problem (3.18).
4. For $r \in \mathcal{N}^\square$ with $\mathbb{D}(r) = \{r\}$ (far from the interface), ψ_r^{CFE} is simply the standard tent function ψ_r^Δ .
5. For $r \in \mathcal{N}^\square$ with $\mathbb{D}(r) \cup \mathcal{N}^{\text{virt}} \neq \emptyset$ (near the interface), a ψ_r^{CFE} may have larger support than ψ_r^\square . For such a node z , $\text{supp}(\psi_z^\Delta) \not\subset \text{supp}(\psi_r^\square)$, and thus $\text{supp}(\psi_r^{\text{CFE}}) = \text{supp}(\psi_r^\Delta) \cup \bigcup_{z \in \mathbb{D}(r)} \text{supp}(\psi_z^\Delta)$.
6. Neighborhoods in the sense of overlapping support of basis functions are now larger than for standard affine FE. They are, however, contained in a ball with diameter $6h$ (in 3D) with respect to the maximum norm. Their cardinality is thus bounded by $7^3 = 343$.

Proof. ad 1. This follows immediately from ψ_r^{CFE} being a linear combination of the piecewise affine ψ_z^Δ .

ad 2. This is because the ψ_z^Δ do and because for any $z \in \mathcal{N}^\Delta$, $\sum_{r \in \mathbb{P}(z)} \mathfrak{w}_{z,r} = 1$.

ad 3. Nodality follows from nodality of ψ_z^Δ (i.e., $\psi_z^\Delta(y) = \delta_{yz}$ for each $y \in \mathcal{N}^\Delta$), the partition of unity property 2, and the facts that $\mathfrak{w}_{r,s} = \delta_{rs}$ for all $r, s \in \mathcal{N}^\square$. If ψ_r^{CFE} is not constructed via (3.18), we still obtain $\psi_r^{\text{CFE}}(s) = 0$ for any $s \in \mathcal{N}^\square$ with $s \neq r$.

ad 6. For two nodes in the support the distance can be at most two times the distance between regular and virtual node plus the maximal distance between two virtual nodes of the same local auxiliary tetrahedron.

The remaining properties follow from the construction and the observation that regular nodes far from the interface do not constrain virtual nodes but regular nodes near the interface may constrain more virtual nodes than they constrain geometrically. \square

Additional properties of the basis functions are summarized in the following remark. Figure 3.12 shows a visualization of 2D CFE basis functions for discontinuous coefficients.

Remark 3.26. 1. Near the interface, ψ_r^{CFE} may attain negative values or values greater than 1, which follows from the possible existence of construction weights outside $[0, 1]$, see below in Section 3.3.4.

2. The ψ_r^{CFE} themselves do not necessarily satisfy the interfacial coupling conditions (2.28) or (2.32), in particular \mathcal{V}^{CFE} has a proper subspace of functions (approximately) satisfying the interfacial coupling conditions, see Figure 3.12.

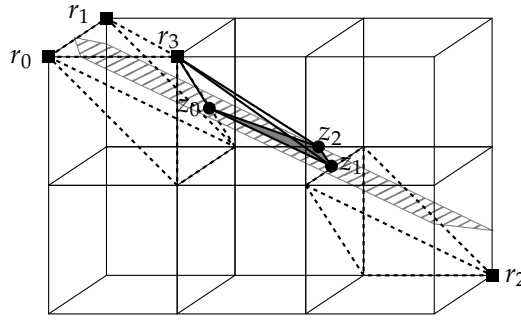


Figure 3.15. For the interface (shaded plane) cutting through the regular grid \mathcal{G}^\square , an example is shown where 3D CFE basis functions have larger support than the corresponding ψ^\boxtimes . The virtual node z_0 is constrained by the nodes r_0 and r_1 (among others) and the node z_1 is constrained by the node r_2 (among others), because z_0 lies in a regular tetrahedron (dashed) containing r_0 and r_1 and z_2 lies in a regular tetrahedron containing r_2 . Furthermore, there is a local auxiliary tetrahedron T (solid) of \mathcal{G}^Δ with nodes r_3, z_0, z_1, z_2 . Hence, $T \subset \text{supp } \psi_{\{0,1\}}^{\text{CFE}} \cap \text{supp } \psi_2^{\text{CFE}}$ which implies that the supports of the CFE basis functions corresponding to the nodes r_0 and r_2 (on the same side of the interface) and r_1 and r_2 (on different sides of the interface) overlap.

3. Again, item 3 in Proposition 3.25 implies linear independence of the ψ_r^{CFE} which thus indeed form a basis of \mathcal{V}^{CFE} .
4. It turns out that the neighborhoods mentioned in item 6 of the previous proposition have cardinality up to 89. The ℓ^∞ diameter (or radius) bound is sharp as illustrated by the example in Figure 3.15. Note that for this distance to occur, a virtual simplex needs to have two virtual nodes on opposite faces of codimension 1 of the Cartesian grid cell. This is not possible for triangles in 2D, where the bound on the diameter is $4h$.

3.3.2 Linear Elasticity Model Problem

In the linear elasticity case, we have seen that coupling condition (2.37) implies a coupling of normal and tangential directional derivatives in locally admissible functions. The prototype functions $\eta^{i,j}$ defined in Equation (2.30) have contributions in all three space directions.

Let us again consider the geometric situation for an interfaced tetrahedron as shown in Figure 3.13.

CFE Construction based on Local Approximation

In analogy to the scalar case (Problem 3.16), consider the following problem.

Problem 3.27. Let $\mathcal{M}_{T,z,n}[u]$ be the set of coefficient vectors $(\tilde{\alpha}^{k,j})_{k=0,1,2,j=0,\dots,3} \in \mathbb{R}^{12}$

minimizing (cf. (3.12))

$$\sum_{i=0,\dots,3} \left| u(r_i) - \sum_{\substack{k=0,1,2 \\ j=0,\dots,3}} \tilde{\alpha}^{k,j} \eta^{k,j}(r_i) \right|^2. \quad (3.23)$$

To select a unique coefficient vector, let

$$(\alpha^{k,j})_{k=0,1,2, j=0,\dots,3} := \operatorname{argmin}_{(\tilde{\alpha}^{k,j}) \in \mathcal{M}_{T,z,n}[u]} \sum_{\substack{k=0,1,2 \\ j=0,\dots,3}} |\tilde{\alpha}^{k,j}|^2. \quad (3.24)$$

Remark 3.28. For the same reason as in Remark 3.17, $\mathcal{M}_{T,z,n}[u]$ is nonempty and an affine subset of \mathbb{R}^{12} . The existence of a unique minimizer of (3.23) does not depend on u and (3.24) always has a unique minimizer.

We will see in Section 3.3.3 that (3.23) is guaranteed to have a unique minimizer with zero minimum only in the special case $\nu = 0$ (no bulging).

The associated approximation of a function $u \in (C^0)^3$ in $\mathcal{V}^{\text{local}}[T, z, n]$ at the interface point z can be evaluated as (cf. (3.14))

$$\mathcal{P}_{T,z,n}[u] := \sum_{\substack{k=0,1,2 \\ j=0,\dots,3}} \alpha^{k,j} \eta^{k,j}. \quad (3.25)$$

Based on the evaluation $\mathcal{P}_{T,z,n}[u]$ of the local approximation, we proceed as in the scalar case and define the global interpolation $\mathcal{I}[u]: (C^0)^3 \rightarrow (\mathcal{V}^\Delta)^3$ as in formula (3.15), now obtaining a vector-valued interpolant.

Definition 3.29. The CFE basis functions for discontinuous coefficients in the vector-valued case and the corresponding CFE space are again defined based on the interpolation $\mathcal{I}[u]$ (cf. Definition 3.19) as

$$\begin{aligned} \Psi_{r;\alpha}^{\text{CFE}} &:= \mathcal{I}[\psi_r^\boxtimes e_\alpha] \quad \forall r \in \mathcal{N}^\square, \alpha = 0, 1, 2, \\ \mathcal{V}^{\text{CFE}} &:= \operatorname{span} \{ \Psi_{r;\alpha}^{\text{CFE}} \mid r \in \mathcal{N}^\square, \alpha = 0, 1, 2 \}. \end{aligned} \quad (3.26)$$

Remark 3.30. A single $\psi_r^\boxtimes e_k$ discretizes the displacement in only one space direction whereas $\Psi_{r;\alpha}^{\text{CFE}}$ (near the interface) may have contributions in all space directions.

Reinterpretation of the Construction as Based on Local Interpolation

Local Interpolation Scheme. Again, if the minimum set $\mathcal{M}_{T,p,n(p)}[u]$ defined in (3.23) consists of a single coefficient vector with zero minimum, we can equivalently consider the interpolation problem in $\mathcal{V}^{\text{local}}[T, z, n]$ of finding 3×3 matrix-valued interpolation weights $\mathfrak{W}_{z,r_i;T}$ such that

$$\mathcal{P}_{T,z,n}[u](z) = u(z) = \begin{pmatrix} u_0(z) \\ u_1(z) \\ u_2(z) \end{pmatrix} = \sum_{i=0}^3 \mathfrak{W}_{z,r_i;T} \begin{pmatrix} u_0(r_i) \\ u_1(r_i) \\ u_2(r_i) \end{pmatrix}. \quad (3.27)$$

We again substitute the prototype functions η (as written in Equation (2.41)) in Equation (3.27) and obtain the following problem.

Problem 3.31. Solve the system

$$\begin{aligned} \begin{pmatrix} 0 \\ 0 \\ 0 \end{pmatrix} &= \sum_{i=0}^3 \mathfrak{W}_{z,r_i;T} L^{j,k} \begin{pmatrix} \langle r_i - z, n \rangle \\ \langle r_i - z, s \rangle \\ \langle r_i - z, t \rangle \end{pmatrix} \quad j, k = 0, \dots, 2 \\ \begin{pmatrix} \delta_{0j} \\ \delta_{1j} \\ \delta_{2j} \end{pmatrix} &= \sum_{i=0}^3 \mathfrak{W}_{z,r_i;T} \begin{pmatrix} \delta_{0j} \\ \delta_{1j} \\ \delta_{2j} \end{pmatrix} \quad j = 0, \dots, 2 \end{aligned} \quad (3.28)$$

of 12×3 equations in 4×9 unknowns (entries of the construction weights $\mathfrak{W}_{z,r_i;T}$).

The bottom three equations imply that the resulting construction weights sum up to a 3×3 identity matrix. As before, if Equation (3.23) has a unique minimizer with zero minimum, also the system (3.28) has a unique minimizer.

The 36×36 system matrix, called B for later use, again depends on L (i.e., the coefficient function) and the geometry (r_i, z, n, s, t) , where L is the matrix from (2.37) encoding the coupling conditions, used for defining the prototype functions η in (2.39). Solving the system, we obtain the local CFE construction weights $\mathfrak{W}_{z,r_i;T}$.

Local Interpolation Operator. The weights are averaged, as before, over the set of all adjacent tetrahedra $\mathbb{A}(z)$ to a virtual node z (cf. Definition 3.22)

$$\mathfrak{W}_{z,r} = \frac{1}{\#\mathbb{A}(z)} \sum_{T \in \mathbb{A}(z)} \mathfrak{W}_{z,r;T} \quad (3.29)$$

and the interpolation operator is defined in analogy to Definition 3.23.

Definition 3.32. Let $\mathbb{P}(z) = \{r \in \mathcal{N}^\square \mid \mathfrak{W}_{r,z} \neq 0\} \subset \mathbb{P}^\square(z)$, then we define the *interpolation operator* $\mathcal{J}[\bullet]: (C^0)^3 \rightarrow (\mathcal{V}^\Delta)^3$ by

$$\mathcal{J}[u](z) = \begin{pmatrix} \mathcal{J}[u]_0(z) \\ \mathcal{J}[u]_1(z) \\ \mathcal{J}[u]_2(z) \end{pmatrix} = \sum_{r \in \mathbb{P}(z)} \mathfrak{W}_{z,r} \begin{pmatrix} u_0(r) \\ u_1(r) \\ u_2(r) \end{pmatrix} \quad (3.30)$$

and piecewise affine interpolation on \mathcal{G}^Δ .

As before, let $\mathbb{P}(r) = \{r\}$ for all $r \in \mathcal{N}^\square$. For construction weights involving only regular nodes, we now need the appropriate one and zero: $\mathfrak{W}_{r,r} = \text{Id}_{\mathbb{R}^{3 \times 3}}$ and $\mathfrak{W}_{n,r} = 0_{\mathbb{R}^{3 \times 3}}$ for any regular node r and any other (virtual or regular) node n not covered by (3.29).

Remark 3.33. The interpolation in Equation (3.30) is *not* separated in space directions.

We now obtain the analog results of Lemma 3.24 and Proposition 3.25.

Lemma 3.34. If we let $\Psi_{z;\alpha}^\Delta := \psi_z^\Delta e_\alpha$ (standard tent functions ‘in a single space direction α'), the CFE basis functions for discontinuous coefficients in the vector-valued case defined in Equation (3.26) are composed of the $\Psi_{z;\alpha}^\Delta$ by

$$\Psi_{r;\alpha}^{\text{CFE}}(x) = \sum_{z \in \text{ID}(r)} \mathfrak{W}_{z,r} \Psi_{z;\alpha}^\Delta(x) = \sum_{z \in \text{ID}(r)} \psi_z^\Delta(x) \mathfrak{W}_{z,r} e_\alpha. \quad (3.31)$$

Proposition 3.35. The CFE basis functions for discontinuous coefficients in the vector-valued case $(\Psi_{r;\alpha}^{\text{CFE}})_{r \in \mathcal{N}^{\text{DOF}}, \alpha \in \{0,1,2\}}$ satisfy the following properties:

1. The $\Psi_{r;\alpha}^{\text{CFE}}$ are piecewise affine on Ω_{-}^{Δ} .
2. The $\Psi_{r;\alpha}^{\text{CFE}}$ form a partition of unity if constructed by solving the interpolation problem (3.28).
3. The $\Psi_{r;\alpha}^{\text{CFE}}$ are nodal on \mathcal{N}^{\square} if constructed by solving the interpolation problem (3.28).
4. For $r \in \mathcal{N}^{\square}$ with $\mathbb{D}(r) = \{r\}$ (far from the interface), $\Psi_{r;\alpha}^{\text{CFE}}$ is simply the standard tent function ψ_r^{Δ} only having contributions in one space direction α .
5. For $r \in \mathcal{N}^{\square}$ with $\mathbb{D}(r) \cap \mathcal{N}^{\text{virt}} \neq \emptyset$ (near the interface), $\Psi_{r;\alpha}^{\text{CFE}}$ may have larger support than ψ_i^{\square} with the same neighborhood structures as in Proposition 3.25.

Proof. ad 1. This follows immediately from $\Psi_{r;\alpha}^{\text{CFE}}$ being a linear combination of the piecewise affine $\Psi_{z;\alpha}^{\Delta}$.

ad 2. This is because the $\Psi_{z;\alpha}^{\Delta}$ do and because for any $z \in \mathcal{N}^{\Delta}$ the last triple of equations in Equation (3.28) implies $\sum_{r \in \mathbb{P}(z)} \mathfrak{W}_{z,r} = \text{Id}_{\mathbb{R}^{3 \times 3}}$.

ad 3. Nodality follows from nodality of $\Psi_{z;\alpha}^{\Delta}$, i.e., $\Psi_{z;\alpha}^{\Delta}(y) = \delta_{yz} e_{\alpha}$ for all $y \in \mathcal{N}^{\Delta}$, the partition of unity property 2, and $\mathfrak{W}_{r,s} = \delta_{rs} \text{Id}_{\mathbb{R}^{3 \times 3}}$ for all $r, s \in \mathcal{N}^{\square}$. If $\Psi_{r;\alpha}^{\text{CFE}}$ is not constructed via (3.28), we still obtain $\Psi_{r;\alpha}^{\text{CFE}}(s) = 0$ for any $s \in \mathcal{N}^{\square}, s \neq r$.

As before, the remaining properties follow from the construction and the observation that regular nodes far from the interface do not constrain virtual nodes but regular nodes near the interface constrain may more virtual nodes than they constrain geometrically. \square

Additional properties of the basis functions are summarized in the following remark.

Remark 3.36. 1. Near the interface, $\Psi_{r;\alpha}^{\text{CFE}}$ may have negative entries and entries larger than 1 and they typically have contributions in all three space directions.
 2. Once again, nodality in item 3 of Proposition 3.35 implies linear independence of the $\Psi_{r;\alpha}^{\text{CFE}}$ which thus form a basis of \mathcal{V}^{CFE} .

In the elasticity case, the decision about reliability and exclusion of tetrahedra in $\mathbb{A}(z)$ is twofold. The numerical solution of Equation (2.37) to determine the coupling condition and the numerical solution of Equation (3.28) to determine the construction weights both need to be considered satisfactory. For details, we again refer to the discussion of implementation in Section 6.2.3.

3.3.3 Unique Solvability of the CFE Construction Systems

Let us now discuss under which circumstances the optimization problems (3.12) and (3.23) in the CFE construction have a unique solution, i.e., the system of equations (3.18) and (3.28) to determine the CFE construction weights in the discontinuous

coefficients case have a unique solution. They do if a piecewise affine function w satisfying the coupling condition across the interface is uniquely determined by its values $w(r_i)$ at the vertices $r_i \in \mathcal{N}^\square$ of the regular tetrahedron.

In the scalar isotropic case, an angle condition on the regular tetrahedra ensures unique solvability whereas there are counterexamples in the anisotropic case. In the isotropic elasticity case, unique solvability can be proved if there is no bulging (Poisson's ratio $\nu = 0$, i.e., $\lambda = 0$) and only a discontinuity in the stiffness (Young's modulus E), otherwise there are counterexamples.

Heat Diffusion Model Problem

An affine function is determined uniquely by its values at the vertices of a geometrically non-degenerate tetrahedron. This is not necessarily true if the tetrahedron is interfaced by H , the local planar interface approximation, and the function is only piecewise affine satisfying one of the coupling conditions (2.28) across H .

Proposition 3.37. In the scalar isotropic case, Problem 3.16 has a unique solution.

Proof. Consider the evaluation mapping $I: \mathcal{V}^{\text{local}} \rightarrow \mathbb{R}^4, u \mapsto (u(r_i))_i$. Preimage and image space have the same dimension (as $\mathcal{V}^{\text{local}}$ is spanned by four linearly independent functions η_i), so the desired uniqueness follows from linearity and injectivity of I , i.e., $u \equiv 0$ being the only piecewise affine function with zero nodal values at the r_i .

Without loss of generality let us assume that the tetrahedron $T = (r_i)_i$ has vertices $r_0, r_1 \in H_-$ and $r_3 \in H_+$, r_2 may be on either side of H . Let w be a piecewise affine function satisfying the respective coupling condition across H and define the zero level sets $Z_\pm := [w^\pm = 0] \subset H_\pm$ of w on both sides of the interface. Moreover let z_2, z_3 be two points on the interface intersected with the edges of T such that the (virtual) tetrahedron (r_0, r_1, z_2, z_3) also is not geometrically degenerate. If I is not injective, then there exists $0 \neq w \in \mathcal{V}^{\text{local}}$ with $w(r_i) = 0$ for each i , without loss of generality with $w(z_2) \neq 0$. In this case, the Z_\pm are of codimension 1, i.e., planes parallel to H or half-planes on each side of the interface not containing z_2 . In the parallel case, $z_2 + \mathbb{R}n$ (the straight line through z_2 in normal direction n) clearly intersects Z_- and Z_+ , which implies a sign change of $\partial_n w$ at z_2 , contradicting the coupling condition (2.28) in the scalar isotropic case. In the non-parallel case, continuity implies that $Z_- \cap H = Z_+ \cap H$ is a line. Since the angles of the edges of the regular tetrahedron (r_0, r_1, r_2, r_3) are bounded from above by 90° (see Figure 3.2) and its vertices lie in $Z_- \cup Z_+$, also the angle between Z_- and Z_+ is bounded by 90° . This implies that $z_2 + \mathbb{R}n$ in fact intersects the half-planes Z_- and Z_+ , leading to the same contradiction as before. \square

Remark 3.38. The 90° condition is crucial for the proof to work. Without this bound on the regular tetrahedra, we can construct a counterexample in the following way. In 2D, we have two rays Z_\pm starting at the origin and containing three vertices r_i of a

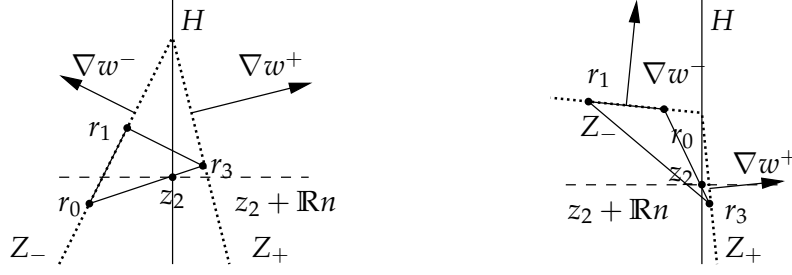


Figure 3.16. The *left* figure shows a setting where, for an anisotropic diffusivity tensor, nodal evaluation does not uniquely identify a piecewise affine function satisfying the coupling condition (2.32). On the *right*, a counterexample for the isotropic case is shown if angles greater than 90° are allowed (which is not the case in \mathcal{G}^\boxtimes).

geometrically non-degenerate triangle, two scalar diffusivities a^\pm and a piecewise affine function $w \not\equiv 0$ satisfying the coupling condition (2.28). Clearly, $\nabla w^\pm \perp Z_\pm$. Consider the data $a^- = 10$, $a^+ = 1$, $H = [x = 0]$, $n = \begin{pmatrix} 1 \\ 0 \end{pmatrix}$, $t = \begin{pmatrix} 0 \\ 1 \end{pmatrix}$, and the functions $w^-(x, y) = 0.1x + y$, $w^+(x, y) = x + y$.

Continuity of w across H and of its derivatives in tangential direction is clearly satisfied and the coupling condition $a^- \partial_n w^- = 10 \cdot 0.1 = 1 \cdot 1 = a^+ \partial_n w^+$ holds. Figure 3.16 (right) shows that a geometrically non-degenerate triangle (r_0, r_1, r_3) with vertices in Z_\pm and intersected by H exists, but clearly $w \not\equiv 0$. Constant extension in the third space direction and r_2 lying above r_0 (or any other of the two vertices) turns this into a 3D counterexample. This type of counterexample can be found as soon as T has one angle greater than 90° .

Example 3.39. In the scalar anisotropic case, the angle condition does not guarantee unique solvability. Consider the tensors $a^- = \begin{pmatrix} 14 & 32 \\ 32 & 86 \end{pmatrix}$ and $a^+ = \begin{pmatrix} 1 & 0 \\ 0 & 1 \end{pmatrix}$ for which positive definiteness is easily verified. Again let $H = [x = 0]$, $n = \begin{pmatrix} 1 \\ 0 \end{pmatrix}$, $t = \begin{pmatrix} 0 \\ 1 \end{pmatrix}$, and consider the functions $w^-(x, y) = -2x + y$, $w^+(x, y) = 4x + y$. w and its tangential derivatives are clearly continuous across H and the coupling condition is also satisfied since

$$\begin{aligned} \langle a^- \nabla w^-, n \rangle &= \left\langle \begin{pmatrix} 14 & 32 \\ 32 & 86 \end{pmatrix} \begin{pmatrix} -2 \\ 1 \end{pmatrix}, \begin{pmatrix} 1 \\ 0 \end{pmatrix} \right\rangle = \left\langle \begin{pmatrix} 4 \\ 22 \end{pmatrix}, \begin{pmatrix} 1 \\ 0 \end{pmatrix} \right\rangle = 4, \\ \langle a^+ \nabla w^+, n \rangle &= \left\langle \begin{pmatrix} 1 & 0 \\ 0 & 1 \end{pmatrix} \begin{pmatrix} 4 \\ 1 \end{pmatrix}, \begin{pmatrix} 1 \\ 0 \end{pmatrix} \right\rangle = \left\langle \begin{pmatrix} 4 \\ 1 \end{pmatrix}, \begin{pmatrix} 1 \\ 0 \end{pmatrix} \right\rangle = 4. \end{aligned} \quad (3.32)$$

$Z^\pm = [w^\pm = 0]$ are two rays starting at the origin perpendicular to ∇w^\pm . Due to $\angle(\nabla w^-, \nabla w^+) > 90^\circ$ and $\angle(Z^-, Z^+) < 90^\circ$, a triangle (r_0, r_1, r_3) with $r_0, r_1 \in Z^+$ and $r_3 \in Z^-$ with a 90° angle and catheti of the same length exists, see Figure 3.16 (left). Let $z_2 = \overline{r_0 r_3} \cap H$, then $w(z_2) \neq 0$ because w is zero at the origin but nowhere else on H . A 3D counterexample is obtained in the same manner as before. Notice that we use the notation \overline{pq} for the straight line (not the line segment) through two points p and q .

Linear Elasticity Model Problem

In the elasticity case we consider vector-valued w with piecewise affine components. We still consider the vertices r_i of a non-degenerate tetrahedron on which w vanishes, and without loss generality $r_0, r_1 \in H_-, r_3 \in H_+$. $w(r) = 0$ implies w being zero in each component. $w(z) \neq 0$ is satisfied if, without loss of generality, at least the first component of w does not vanish at z .

Lemma 3.40. The zero level sets of w^\pm, Z_\pm , can be determined as the zero level sets of the first component of w , i.e., its other components are scalar multiples of the first component.

Proof. Any component $w_i \equiv 0$ is clearly a scalar multiple of w_0 . For all other w_i we distinguish the following cases:

1. $r_2 \in H_-$. In this case, we have three non-collinear points r_0, r_1, r_2 in $[w_i^- = 0]$ for all i , hence $Z_- = [w_i^- = 0]$ for each i . Now we distinguish the cases
 - a) $Z_- \parallel H$, where continuity of w implies $H \parallel Z_+ = [w_i^+ = 0]$ for each i as they have r_3 in common, or
 - b) $Z_- \cap H$ is a straight line L , where continuity of w implies $L = [w_i^+ = 0] \cap H$ for all i , and $r_3 \in [w_i^- = 0] \setminus L$ implies $Z_+ = [w_i^+ = 0]$ for each i .
2. $r_2 \in H_+$. Here, distinguish the cases
 - a) $\overline{r_0 r_1} \cap H = \emptyset = \overline{r_2 r_3} \cap H$. If $[w_i^- = 0] \cap H = L$ is a straight line, then continuity implies $[w_i^+ = 0] \cap H = L$, so $\overline{r_0 r_1} \parallel L \parallel \overline{r_2 r_3}$, hence all r_i are coplanar and T is degenerate, contradiction. So $[w_i^- = 0] \parallel H$ and we proceed as in case 1a.
 - b) $\overline{r_0 r_1} \cap H = \{p\}, \overline{r_2 r_3} \cap H = \{q\}$. We can assume $p \neq q$, else r_i are coplanar, contradiction. Then r_0, r_1, q are not collinear and contained in $Z_- = [w_i^- = 0]$ for each i , similarly r_2, r_3, p are not collinear and contained in $Z_+ = [w_i^+ = 0]$ for each i .
 - c) $\overline{r_0 r_1} \cap H = \{p\}, \overline{r_2 r_3} \cap H = \emptyset$. Here, r_2, r_3, p are not collinear and contained in $Z_+ = [w_i^+ = 0]$ for each i , and there exists a point $q \in [w_i^- = 0] \cap H \setminus \{p\}$ such that r_0, r_1, q are not collinear and contained in $Z_- = [w_i^- = 0]$ for each i .
 - d) $\overline{r_0 r_1} \cap H = \emptyset, \overline{r_2 r_3} \cap H = \{q\}$. This case is treated by obvious modification of the previous case. \square

Proposition 3.41. For isotropic elasticity with Poisson's ratio $\nu = 0$, problem (3.23) has a unique solution.

Proof. If there is no bulging, that is Poisson's ratio $\nu = 0 \Rightarrow \lambda = 0$, we have $C^\pm \epsilon[w^\pm] = E^\pm \epsilon[w^\pm]$. Let us consider the 2D case where $H = [x = 0]$, $n = \begin{pmatrix} 1 \\ 0 \end{pmatrix}$, $t = \begin{pmatrix} 0 \\ 1 \end{pmatrix}$, and mention that the extension to 3D and general planes H is straightforward.

Building in the continuity of w and its derivatives in tangential direction, general w^\pm are of the form

$$w^\pm(x, y) = \begin{pmatrix} w_{00}^\pm & w_{01} \\ w_{10}^\pm & w_{11} \end{pmatrix} \begin{pmatrix} x \\ y \end{pmatrix} \quad (3.33)$$

so that

$$C^\pm \epsilon[w^\pm] n = E^\pm \begin{pmatrix} w_{00}^\pm & \frac{1}{2}(w_{01} + w_{10}^\pm) \\ \frac{1}{2}(w_{01} + w_{10}^\pm) & w_{11} \end{pmatrix} \begin{pmatrix} 1 \\ 0 \end{pmatrix} = \begin{pmatrix} E^\pm w_{00}^\pm \\ E^\pm w_{01} + E^\pm w_{10}^\pm \end{pmatrix} \quad (3.34)$$

leads to the coupling condition

$$E^+ w_{00}^+ = E^- w_{00}^- \quad (3.35a)$$

$$E^+ w_{01} + E^+ w_{10}^+ = E^- w_{01} + E^- w_{10}^-. \quad (3.35b)$$

We now wish to extend the proof from the scalar isotropic case to this vector-valued case. So let again $r_0, r_1 \in H_-$, $r_3 \in H_+$, and Z and its geometric properties restricted to 2D as before. If $w(r_i) = 0$ but component j of w does not vanish (the assumption that this may be taken as the first component does no longer hold as we have possibly rotated our frame of reference) and the other one is a multiple of it, we know as in the scalar case that $\partial_n w_j^-$ and $\partial_n w_j^+$ have different sign and do not vanish. We can distinguish the following cases:

1. $j = 0 \Rightarrow w_{00}^+ \neq 0$. Since E^+ and E^- are both strictly positive, we have a contradiction to the coupling condition (3.35a).
2. $j \neq 0 \Rightarrow w_{00}^+ = 0$. Then Equation (3.35a) implies $w_{00}^- = 0$ and w_1 is the non-vanishing component with $w_{10}^+ \cdot w_{10}^- < 0$. The fact shown before that w_0 is a multiple of w_1 then implies that $w_{01} = 0$, so Equation (3.35b) reads $E^+ w_{10}^+ = E^- w_{10}^-$, so that positivity of E^\pm implies $w_{10}^+ \cdot w_{10}^- > 0$, contradiction.

□

Example 3.42. If Poisson's ratio $\nu \neq 0$, there is again a counterexample for unique solvability of Problem 3.27. Consider the elasticity constants $E^- = 1, \nu^- = 0.4$ and $E^+ = 25, \nu^+ = 0.35$, then we have

$$\begin{aligned} \lambda^- &= \frac{E^- \nu^-}{(1 + \nu^-)(1 - 2\nu^-)} = \frac{10}{7} & \mu^- &= \frac{E^-}{2(1 + \nu^-)} = \frac{1750}{81} \\ \lambda^+ &= \frac{E^+ \nu^+}{(1 + \nu^+)(1 - 2\nu^+)} = \frac{5}{14} & \mu^+ &= \frac{E^+}{2(1 + \nu^+)} = \frac{250}{27} \end{aligned}$$

and the piecewise affine functions w^\pm with

$$\nabla w^-(x, y) = \begin{pmatrix} \frac{3211}{1500} & \frac{7}{10} \\ \frac{3211}{1050} & 1 \end{pmatrix} \quad \nabla w^+(x, y) = \begin{pmatrix} -\frac{67993}{175000} & \frac{7}{10} \\ -\frac{67993}{122500} & 1 \end{pmatrix}$$

where continuity and continuity of the derivative in tangential direction $t = \begin{pmatrix} 0 \\ 1 \end{pmatrix}$ are obvious. Moreover, we have

$$\epsilon[w^-] = \begin{pmatrix} \frac{3211}{1500} & \frac{1973}{1050} \\ \frac{1973}{1050} & 1 \end{pmatrix} \quad \epsilon[w^+] = \begin{pmatrix} -\frac{67993}{175000} & \frac{17757}{245000} \\ \frac{17757}{245000} & 1 \end{pmatrix}$$

so that the coupling condition (2.36)

$$\begin{aligned} C^- \epsilon[w^-] n &= \lambda^- \operatorname{tr} \epsilon[w^-] n + 2\mu^- \epsilon[w^-] n = \begin{pmatrix} \frac{4211}{700} \\ \frac{1973}{1470} \end{pmatrix} \\ &= \lambda^+ \operatorname{tr} \epsilon[w^+] n + 2\mu^+ \epsilon[w^+] n = C^+ \epsilon[w^+] n \end{aligned}$$

is satisfied for $n = \begin{pmatrix} 1 \\ 0 \end{pmatrix}$. The angle between the two gradients is

$$\begin{aligned} \left[\angle(\nabla w_1^-, \nabla w_1^+) = \right] \angle(\nabla w_0^-, \nabla w_0^+) &= \arccos \frac{\left\langle \begin{pmatrix} \frac{3211}{1500} \\ \frac{7}{10} \end{pmatrix}, \begin{pmatrix} -\frac{67993}{175000} \\ \frac{7}{10} \end{pmatrix} \right\rangle}{\left\| \begin{pmatrix} \frac{3211}{1500} \\ \frac{7}{10} \end{pmatrix} \right\| \left\| \begin{pmatrix} -\frac{67993}{175000} \\ \frac{7}{10} \end{pmatrix} \right\|}} \\ &= \arccos \frac{89\,700\,523}{\sqrt{11\,413\,021} \sqrt{19\,629\,298\,049}} \approx 100.9244^\circ \end{aligned}$$

and hence greater than 90° , thus the angle between the two zero level sets (to which the gradients are perpendicular) is smaller than 90° . Therefore there exists a regular triangle with one 90° angle so that its vertices lie in $Z_- \cup Z_+$.

3.3.4 Construction Weights in 2D leading to a Non-Convex Combination

The fact that the CFE basis functions may attain negative values or values greater than 1 (equivalent to interpolation weights $w_{z,r} \notin [0, 1]$) can be observed even in 2D and for the isotropic scalar problem. Let us consider the two examples shown in Figure 3.17 where the cell shown is assumed to be the unit square.

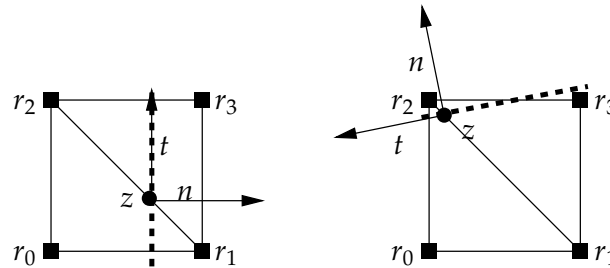


Figure 3.17. Geometric configurations in 2D for which kink ratios $\kappa = 10$ (left) and $\kappa = 40$ (right) lead to CFE construction weights outside $[0, 1]$ so that the corresponding CFE basis functions attain values $[0, 1]$.

Example 3.43. In the left case of Figure 3.17 (which is the underlying construction for Figure 3.12), we use $\kappa = 10$, $z = \begin{pmatrix} 2/3 \\ 1/3 \end{pmatrix}$, $n = \begin{pmatrix} 1 \\ 0 \end{pmatrix}$ and $t = \begin{pmatrix} 0 \\ 1 \end{pmatrix}$. The systems of equations corresponding to the CFE construction on $T_0 := (r_0, r_1, r_2)$ and $T_1 := (r_1, r_2, r_3)$ (with r_i being the vertices of the unit square) are

$$\begin{aligned} T_0 : \quad \begin{pmatrix} 0 \\ 0 \\ 1 \end{pmatrix} &= \begin{pmatrix} \langle r_0 - z, n \rangle & \kappa \langle r_1 - z, n \rangle & \langle r_2 - z, n \rangle \\ \langle r_0 - z, t \rangle & \langle r_1 - z, t \rangle & \langle r_2 - z, t \rangle \\ 1 & 1 & 1 \end{pmatrix} \begin{pmatrix} \mathfrak{w}_{z,r_0;T_0} \\ \mathfrak{w}_{z,r_1;T_0} \\ \mathfrak{w}_{z,r_2;T_0} \end{pmatrix} \\ &= \begin{pmatrix} -2/3 & 10/3 & -2/3 \\ -1/3 & -1/3 & 2/3 \\ 1 & 1 & 1 \end{pmatrix} \begin{pmatrix} \mathfrak{w}_{z,r_0;T_0} \\ \mathfrak{w}_{z,r_1;T_0} \\ \mathfrak{w}_{z,r_2;T_0} \end{pmatrix} \\ T_1 : \quad \begin{pmatrix} 0 \\ 0 \\ 1 \end{pmatrix} &= \begin{pmatrix} \kappa \langle r_1 - z, n \rangle & \langle r_2 - z, n \rangle & \kappa \langle r_3 - z, n \rangle \\ \langle r_1 - z, t \rangle & \langle r_2 - z, t \rangle & \langle r_3 - z, t \rangle \\ 1 & 1 & 1 \end{pmatrix} \begin{pmatrix} \mathfrak{w}_{z,r_1;T_1} \\ \mathfrak{w}_{z,r_2;T_1} \\ \mathfrak{w}_{z,r_3;T_1} \end{pmatrix} \\ &= \begin{pmatrix} 10/3 & -2/3 & 10/3 \\ -1/3 & 2/3 & 2/3 \\ 1 & 1 & 1 \end{pmatrix} \begin{pmatrix} \mathfrak{w}_{z,r_1;T_1} \\ \mathfrak{w}_{z,r_2;T_1} \\ \mathfrak{w}_{z,r_3;T_1} \end{pmatrix} \end{aligned}$$

so that

$$\begin{pmatrix} \mathfrak{w}_{z,r_0;T_0} \\ \mathfrak{w}_{z,r_1;T_0} \\ \mathfrak{w}_{z,r_2;T_0} \end{pmatrix} = \begin{pmatrix} 1/2 \\ 1/6 \\ 1/3 \end{pmatrix}, \quad \begin{pmatrix} \mathfrak{w}_{z,r_1;T_1} \\ \mathfrak{w}_{z,r_2;T_1} \\ \mathfrak{w}_{z,r_3;T_1} \end{pmatrix} = \begin{pmatrix} 2/3 \\ 5/6 \\ -1/2 \end{pmatrix} \quad \Rightarrow \quad \begin{pmatrix} \mathfrak{w}_{z,r_0} \\ \mathfrak{w}_{z,r_1} \\ \mathfrak{w}_{z,r_2} \\ \mathfrak{w}_{z,r_3} \end{pmatrix} = \begin{pmatrix} 1/4 \\ 5/12 \\ 7/12 \\ -1/4 \end{pmatrix}$$

and we obviously obtain a negative interpolation (and construction) weight \mathfrak{w}_{z,r_3} .

Example 3.44. In the right case in Figure 3.17, we use the kink ratio $\kappa = 40$, the point $z = \begin{pmatrix} 0.1 \\ 0.9 \end{pmatrix}$, $n = \begin{pmatrix} -0.2 \\ \sqrt{0.96} \end{pmatrix}$, and $t = \begin{pmatrix} -\sqrt{0.96} \\ -0.2 \end{pmatrix}$ to obtain weights greater than 1. Now only r_2 lies in Ω_+ , resulting in the term $\kappa \langle r_2 - z, n \rangle$ while the other entries have no factor κ , and a short calculation yields

$$\begin{pmatrix} \mathfrak{w}_{z,r_0;T_0} \\ \mathfrak{w}_{z,r_1;T_0} \\ \mathfrak{w}_{z,r_2;T_0} \end{pmatrix} \approx \begin{pmatrix} 0.5862 \\ 0.2504 \\ 0.1634 \end{pmatrix}, \quad \begin{pmatrix} \mathfrak{w}_{z,r_1;T_1} \\ \mathfrak{w}_{z,r_2;T_1} \\ \mathfrak{w}_{z,r_3;T_1} \end{pmatrix} \approx \begin{pmatrix} 2.2130 \\ 0.4687 \\ -1.6817 \end{pmatrix} \quad \Rightarrow \quad \begin{pmatrix} \mathfrak{w}_{z,r_0} \\ \mathfrak{w}_{z,r_1} \\ \mathfrak{w}_{z,r_2} \\ \mathfrak{w}_{z,r_3} \end{pmatrix} \approx \begin{pmatrix} 0.2932 \\ 1.2317 \\ 0.3160 \\ -0.8408 \end{pmatrix}.$$

This shows that also weights greater than 1 (in this case \mathfrak{w}_{z,r_1}) are possible. Since the sum of all construction weights for one virtual node needs to be equal to 1, this implies that at least one weight needs to be negative (in this case \mathfrak{w}_{z,r_3}). Both cases also occur in the 3D scalar case and for entries of the weights in the vector-valued cases.

Let us point out that negative weights imply a change of sign in the directional derivative of an admissible function along the edge—which does not conflict with the coupling condition Equation (2.28) in normal direction.

3.4 Boundary Conditions

In the CFE method derived so far, we have the usual homogeneous Neumann boundary conditions¹ on the boundary of the bounding box Ω and, in case of complicated domains, also on the interface γ .

Focussing on the applications we have in mind, it will be necessary to implement Dirichlet boundary conditions² on a subset of $\partial\Omega$, the faces of the bounding box. This reflects temperature or displacement boundary conditions applied to the outside of a specimen but not its microstructure. Periodic boundary conditions (for the numerical homogenization procedures) on $\partial\Omega$ will also be discussed and are treated in a way similar to Dirichlet boundary conditions. Nonzero Neumann boundary conditions on $\partial\Omega$ or γ and Dirichlet boundary conditions on γ as treated for CFE in general [289] will not be discussed here.

Dirichlet Boundary Conditions

Since virtual nodes $z \in \mathcal{N}^{\text{virt}}$ do not have assigned DOF, we cannot prescribe Dirichlet boundary conditions for them, merely for regular nodes. In case of complicated domains, any virtual node $z_b \in \partial\Omega$ is constrained by two regular nodes $r_b, s_b \in \partial\Omega$, so implicitly any function evaluated at z_b yields the appropriate interpolation of Dirichlet boundary values at r_b and s_b .

Near the edges of $\partial\Omega$ we may encounter $z \notin \partial\Omega$ constrained by r_b on one face and s_b on a different face of $\partial\Omega$. Regardless of whether r_b and s_b are both Dirichlet nodes or only one of them is, the influence of the Dirichlet boundary extends only to an $O(h)$ layer near the boundary.

In case of discontinuous coefficients, in principle there may be virtual nodes $z_b \in \partial\Omega$ constrained also by inner regular nodes. This may result in an interpolation with z_b not satisfying the Dirichlet boundary condition. This, however, is not a problem of the discretization: if the interface γ and the outer boundary $\partial\Omega$ intersect, boundary conditions and interfacial coupling conditions need to be compatible already for the continuous function.

Periodic Boundary Conditions

For our numerical homogenization method for periodic structures, we need to run simulations satisfying periodic boundary conditions on opposite faces of Ω . These boundary conditions are implemented by identifying DOF at different nodes that are viewed as periodic copies of one another. Along with the DOF, the corresponding basis functions are also combined. Details of the treatment of periodic boundary conditions are discussed in Section 4.3.

¹Named after the German mathematician Carl Gottfried Neumann, * May 7, 1832 in Königsberg (now Kaliningrad, Russia), † March 27, 1925 in Leipzig [262].

²Named after the German mathematician Johann Peter Gustav Lejeune Dirichlet, * February 13, 1805 in Düren, † May 5, 1859 in Göttingen [1].

For complicated domain CFEs, this clearly only works if the structure is exactly periodic. Otherwise, there are nodes in \mathcal{N}^{DOF} on one face and nodes of \mathcal{N}^{\square} without DOF on the other side, making the identification clearly impossible. In the discontinuous coefficient CFE case, this identification is always possible because all nodes in \mathcal{N}^{\square} have DOF assigned. However, they may lie in different subdomains (Ω_- and Ω_+), so the naïve identification is obviously not appropriate.

3.5 CFE Discretization and Matrices

Let us now discuss how the CFE basis functions constructed before are used to discretize our model problems. This leads to CFE variants of the usual FE mass, stiffness and elasticity matrices. Their sparsity and block structures are visualized in Figure 3.18. Also, we will briefly present the transformation to zero Dirichlet boundary conditions and the corresponding matrix modifications, and implicit Euler time discretization of heat diffusion.

Throughout this section we identify grid nodes r and their indices $j(r)$ to simplify notation.

3.5.1 Heat Diffusion Model Problem

As usual, continuous temperature profiles $u: \Omega \rightarrow \mathbb{R}$ will be approximated by

$$u(x) \approx U(x) = \sum_{r \in \mathcal{N}^{\text{DOF}}} \psi_r^{\text{CFE}}(x) u(r) \quad (3.36)$$

where we use the notation $U_r = U(r) = u(r)$ where it will be clear from the context whether U is the discrete function (with CFE interpolation) or the vector of nodal values.

The CFE matrices of the previous section arise in the spatial discretization of Problem 2.1 if the unknown quantities are discretized as in Equation (3.36) and test functions are also in \mathcal{V}^{CFE} . In the scalar steady state case, we obtain

$$\begin{aligned} & \int \langle a \nabla u, \nabla v \rangle = \int f v \\ \rightsquigarrow & \int \langle a \nabla \left(\sum_{r \in \mathcal{N}^{\square}} U_r \psi_r^{\text{CFE}} \right), \nabla \psi_s^{\text{CFE}} \rangle = \int \left(\sum_{r \in \mathcal{N}^{\square}} E_r \psi_r^{\text{CFE}} \right) \psi_s^{\text{CFE}} \quad \forall s \in \mathcal{N}^{\square} \quad (3.37) \\ \Leftrightarrow & \sum_{r \in \mathcal{N}^{\square}} \left(\int \langle a \nabla \psi_r^{\text{CFE}}, \nabla \psi_s^{\text{CFE}} \rangle \right) U_r = \sum_{r \in \mathcal{N}^{\square}} \left(\int \psi_r^{\text{CFE}} \psi_s^{\text{CFE}} \right) E_r \quad \forall s \in \mathcal{N}^{\square}. \end{aligned}$$

This can be written in the usual form $LU = MF$ if we use Definition 3.45 and observe symmetry of M and L .

Definition 3.45. The CFE mass matrix M and (weighted) stiffness matrix L are defined in the usual way by their entries

$$\begin{aligned} M_{rs} &= M_{rs}^{\text{CFE}} := \int \psi_r^{\text{CFE}} \psi_s^{\text{CFE}} \\ L_{rs} &= L_{rs}^{\text{CFE}} := \int \langle a \nabla \psi_r^{\text{CFE}}, \psi_s^{\text{CFE}} \rangle \end{aligned} \quad (3.38)$$

where the domain of integration will be specified below.

Using the expressions in Lemma 3.10 and 3.24 for CFE basis functions, M and L can be computed as described in the following lemmas.

Lemma 3.46. In case of CFE for complicated domains, basis functions are restricted to the domain Ω_- so that the CFE matrices are computed as follows:

$$\begin{aligned} M_{rs}^{\text{CFE}} &= \int_{\Omega_-} \psi_r^{\text{CFE}} \psi_s^{\text{CFE}} = \sum_{z \in \mathbb{D}(r)} \sum_{y \in \mathbb{D}(s)} \mathfrak{w}_{z,r} \mathfrak{w}_{y,s} \int_{\Omega_-} \psi_z^\Delta \psi_y^\Delta \\ L_{rs}^{\text{CFE}} &= \int_{\Omega_-} a(x) \langle \nabla \psi_r^{\text{CFE}}, \nabla \psi_s^{\text{CFE}} \rangle = \sum_{z \in \mathbb{D}(r)} \sum_{y \in \mathbb{D}(s)} \mathfrak{w}_{z,r} \mathfrak{w}_{y,s} \int_{\Omega_-} a \sum_i \partial_i \psi_z^\Delta \partial_i \psi_y^\Delta \end{aligned} \quad (3.39)$$

for all $r, s \in \mathcal{N}^{\text{DOF}}$ where a may vary spatially.

Lemma 3.47. In case of discontinuous coefficients, the sets $\mathbb{D}(r)$ and the weights $\mathfrak{w}_{z,r}$ are different from the complicated domain case and integration is performed over the whole domain Ω :

$$\begin{aligned} M_{rs}^{\text{CFE}} &= \int_{\Omega} \psi_r^{\text{CFE}} \psi_s^{\text{CFE}} = \sum_{z \in \mathbb{D}(r)} \sum_{y \in \mathbb{D}(s)} \mathfrak{w}_{z,r} \mathfrak{w}_{y,s} \int_{\Omega} \psi_z^\Delta \psi_y^\Delta \\ L_{rs}^{\text{CFE}} &= \int_{\Omega} a(x) \langle \nabla \psi_r^{\text{CFE}}, \nabla \psi_s^{\text{CFE}} \rangle = \sum_{z \in \mathbb{D}(r)} \sum_{y \in \mathbb{D}(s)} \mathfrak{w}_{z,r} \mathfrak{w}_{y,s} \int_{\Omega} a(x) \sum_i \partial_i \psi_z^\Delta \partial_i \psi_y^\Delta. \end{aligned} \quad (3.40)$$

for all $r, s \in \mathcal{N}^{\text{DOF}}$.

As the ψ_z^Δ are piecewise affine on \mathcal{G}^Δ , exact integration for constant coefficient a is possible, otherwise quadrature is necessary³, cf. Section 6.3.3. Equations (3.39) and (3.40) show in particular that the virtual grid is used for assembling matrices for DOF on the regular grid but not visible afterwards.

Transformation to Zero Dirichlet Boundary Conditions

In the continuous setting, nonzero Dirichlet boundary values can be transformed to zero Dirichlet boundary conditions in the usual way, see, e.g., [55, Section II.2]. In discrete form, the system matrix L is modified for this purpose such that

³Unlike some authors [248, 86, 222, 85] who prefer the term ‘cubature’, we denote the numerical approximation of integrals by ‘quadrature’ regardless of the space dimension.

1. the rows of L for Dirichlet nodes are set to identity rows (rows containing only a 1 on the diagonal) and the RHS (right hand side) entry is set to zero so that the corresponding node is no longer a degree of freedom, and
2. the columns of L for Dirichlet nodes are set to zero away from the diagonal entry because the corresponding vector entry is already known to vanish.

The resulting modified system matrix is still symmetric and definiteness is not lost either. After solving the system of equations, the boundary conditions are added again. The vector-valued case with a system block matrix is treated similarly.

Implicit Euler Time Discretization

In the time-dependent case (2.2), we first discretize in space and obtain

$$M(\partial_t U) + LU = MF. \quad (3.41)$$

Implicit Euler time discretization⁴ approximates $\partial_t U = \frac{U^{k+1} - U^k}{\tau}$ where U^k is the discrete solution at time τk (time step k) so that, in each time step, we need to solve

$$\begin{aligned} \frac{MU^{k+1} - MU^k}{\tau} + LU^{k+1} &= MF^{k+1} \\ \Rightarrow (M + \tau L)U^{k+1} &= MU^k + \tau MF^{k+1}. \end{aligned} \quad (3.42)$$

3.5.2 Linear Elasticity Model Problem

As for the vector-valued problem, the general discretization is

$$u(x) \approx U(x) = \sum_{\substack{r \in \mathcal{N}^{\text{DOF}} \\ \alpha \in \{0,1,2\}}} \Psi_{r;\alpha}^{\text{CFE}}(x) u_\alpha(r) \quad (3.43)$$

where $U_{r;\alpha} = U_\alpha(r) = u_\alpha(r)$ is the vector of discrete values (that can be thought of as a block vector consisting of three blocks with the discrete values of the x , y , and z components of the displacement, or as a block vector consisting of $\#\mathcal{N}^{\text{DOF}}$ blocks containing the displacement at each DOF). Problem 2.2 is discretized using (3.43), and we obtain

$$\begin{aligned} & \int C\epsilon[u] : \epsilon[v] = \int \langle f, v \rangle \\ \rightsquigarrow & \int C\epsilon \left[\sum_{\substack{r \in \mathcal{N}^{\text{DOF}} \\ \alpha \in \{0,1,2\}}} \Psi_{r;\alpha}^{\text{CFE}} U_{r;\alpha} \right] : \epsilon \left[\Psi_{s;\beta}^{\text{CFE}} \right] = \int \left\langle \sum_{\substack{r \in \mathcal{N}^{\text{DOF}} \\ \alpha \in \{0,1,2\}}} \Psi_{r;\alpha}^{\text{CFE}} F_{r;\alpha}, \Psi_{s;\beta}^{\text{CFE}} \right\rangle \\ \Leftrightarrow & \sum_{\substack{r \in \mathcal{N}^{\text{DOF}} \\ \alpha \in \{0,1,2\}}} \left(\int C\epsilon \left[\Psi_{r;\alpha}^{\text{CFE}} \right] : \epsilon \left[\Psi_{s;\beta}^{\text{CFE}} \right] \right) U_{r;\alpha} = \sum_{\substack{r \in \mathcal{N}^{\text{DOF}} \\ \alpha \in \{0,1,2\}}} \left(\int \langle \Psi_{r;\alpha}^{\text{CFE}}, \Psi_{s;\beta}^{\text{CFE}} \rangle \right) F_{r;\alpha} \end{aligned}$$

for all $s \in \mathcal{N}^{\text{DOF}}$ and $\beta \in \{0,1,2\}$. This can be written in the usual form $EU = MF$ if we use Definition 3.48 and observe symmetry of E and M .

⁴Named after the Swiss mathematician and physicist Leonhard Euler, * April 15, 1707 in Basel, † September 18, 1783 in St. Petersburg, Russia [1].

3 Construction of Composite Finite Elements

Definition 3.48. The CFE block mass matrix M and elasticity matrix E are defined in the usual way by the entries $r, s \in \mathcal{N}^{\text{DOF}}$ of their blocks $\alpha, \beta \in \{0, 1, 2\}$

$$\begin{aligned} (M_{\alpha\beta}^{\text{CFE}})_{rs} &:= \int \langle \Psi_{r;\alpha}^{\text{CFE}}, \Psi_{s;\beta}^{\text{CFE}} \rangle \\ (E_{\alpha\beta}^{\text{CFE}})_{rs} &:= \int C\epsilon[\Psi_{r;\alpha}^{\text{CFE}}] : \epsilon[\Psi_{s;\beta}^{\text{CFE}}] \end{aligned} \quad (3.44)$$

where the domain of integration will be specified below.

Using the expressions in Remark 3.10 and Lemma 3.34 for CFE basis functions, M and E can be computed as described in the following lemmas.

Lemma 3.49. The mass matrix for elasticity problems on complicated domains has block structure with three standard CFE mass matrices (3.39) as diagonal blocks and zero off-diagonal blocks whereas in general all blocks of E^{CFE} are nonzero. The entries of the elasticity block matrix is obtained as

$$(E_{\alpha\beta}^{\text{CFE}})_{rs} = \sum_{z \in \mathbb{D}(r)} \sum_{y \in \mathbb{D}(s)} \mathfrak{w}_{z,r} \mathfrak{w}_{y,s} \sum_{ik} \int_{\Omega_-} C_{i\beta k\alpha} \partial_i \psi_y^\Delta \partial_k \psi_z^\Delta. \quad (3.45)$$

Remark 3.50. For isotropic Lamé-Navier elasticity with C as in (2.17), the integrands for the elasticity matrix in case of complicated domains can be written as

$$\lambda \int_{\Omega_-} \partial_\alpha \psi_r^{\text{CFE}} \partial_\beta \psi_s^{\text{CFE}} + \mu \int_{\Omega_-} \partial_\beta \psi_r^{\text{CFE}} \partial_\alpha \psi_s^{\text{CFE}} + \delta_{\alpha\beta} \sum_{m=0}^2 \mu \int_{\Omega_-} \partial_m \psi_r^{\text{CFE}} \partial_m \psi_s^{\text{CFE}}.$$

This is due to

$$\begin{aligned} \nabla \psi_{r;\alpha}^{\text{CFE}} &= (\partial_0 \psi_r^{\text{CFE}} e^\alpha \quad \partial_1 \psi_r^{\text{CFE}} e^\alpha \quad \partial_2 \psi_r^{\text{CFE}} e^\alpha) \\ &= (\delta_{i\alpha} \partial_j \psi_r^{\text{CFE}})_{ij} \end{aligned} \quad (3.46)$$

so that

$$\begin{aligned} (E_{\alpha\beta}^{\text{CFE}})_{rs} &= \int_{\Omega_-} C\epsilon[\psi_r^{\text{CFE}} e_\alpha] : \epsilon[\psi_s^{\text{CFE}} e_\beta] \\ &= \sum_{ijkl} \int_{\Omega_-} \frac{C_{ijkl}}{4} (\delta_{k\alpha} \partial_l \psi_r^{\text{CFE}} + \delta_{l\alpha} \partial_k \psi_r^{\text{CFE}}) (\delta_{i\beta} \partial_j \psi_s^{\text{CFE}} + \delta_{j\beta} \partial_i \psi_s^{\text{CFE}}) \\ &= \sum_{ik} \int_{\Omega_-} C_{i\beta k\alpha} \partial_k \psi_r^{\text{CFE}} \partial_i \psi_s^{\text{CFE}} \end{aligned}$$

where we used the symmetry (2.8) of the elasticity tensor C in the last step.

Lemma 3.51. In case of discontinuous coefficients, single basis functions may have contributions in all space directions, which implies that also the mass matrix is now filled in all blocks.

The mass and elasticity block matrices are given as

$$\begin{aligned}
 (M_{\alpha\beta}^{\text{CFE}})_{rs} &= \int \Psi_{r;\alpha}^{\text{CFE}} \Psi_{r;\beta}^{\text{CFE}} = \int_{\Omega} \left\langle \sum_{z \in \mathbb{D}(r)} \mathfrak{W}_{z,r} \psi_z^{\Delta} e_{\alpha}, \sum_{y \in \mathbb{D}(s)} \mathfrak{W}_{y,s} \psi_y^{\Delta} e_{\beta} \right\rangle \\
 &= \sum_{z \in \mathbb{D}(r)} \sum_{y \in \mathbb{D}(s)} \underbrace{\sum_k (\mathfrak{W}_{z,r})_{k\alpha} (\mathfrak{W}_{y,s})_{k\beta}}_{= (\mathfrak{W}_{z,r})^T \mathfrak{W}_{y,s}} \int_{\Omega} \psi_z^{\Delta} \psi_y^{\Delta}, \tag{3.47}
 \end{aligned}$$

$$\begin{aligned}
 (E_{\alpha\beta}^{\text{CFE}})_{rs} &= \int_{\Omega} \mathbb{C} \epsilon(\Psi_{r;\alpha}^{\text{CFE}}) : \epsilon(\Psi_{s;\beta}^{\text{CFE}}) \\
 &= \int_{\Omega} \sum_{klmn} \frac{C_{klmn}}{4} [\partial_m(\Psi_{r;\alpha}^{\text{CFE}})_n + \partial_n(\Psi_{r;\alpha}^{\text{CFE}})_m] [\partial_k(\Psi_{s;\beta}^{\text{CFE}})_l + \partial_l(\Psi_{s;\beta}^{\text{CFE}})_k] \\
 &= \sum_{z,y} \sum_{klmn} \frac{C_{klmn}}{4} \left[\begin{aligned}
 &(\mathfrak{W}_{z,r})_{n\alpha} (\mathfrak{W}_{y,s})_{l\beta} \int_{\Omega} \partial_m \psi_z^{\Delta} \partial_k \psi_y^{\Delta} \\
 &+ (\mathfrak{W}_{z,r})_{n\alpha} (\mathfrak{W}_{y,s})_{k\beta} \int_{\Omega} \partial_m \psi_z^{\Delta} \partial_l \psi_y^{\Delta} \\
 &+ (\mathfrak{W}_{z,r})_{m\alpha} (\mathfrak{W}_{y,s})_{l\beta} \int_{\Omega} \partial_n \psi_z^{\Delta} \partial_k \psi_y^{\Delta} \\
 &+ (\mathfrak{W}_{z,r})_{m\alpha} (\mathfrak{W}_{y,s})_{k\beta} \int_{\Omega} \partial_n \psi_z^{\Delta} \partial_l \psi_y^{\Delta} \end{aligned} \right]. \tag{3.48}
 \end{aligned}$$

The sparsity structures of the matrices discussed in this section are visualized in Figure 3.18.

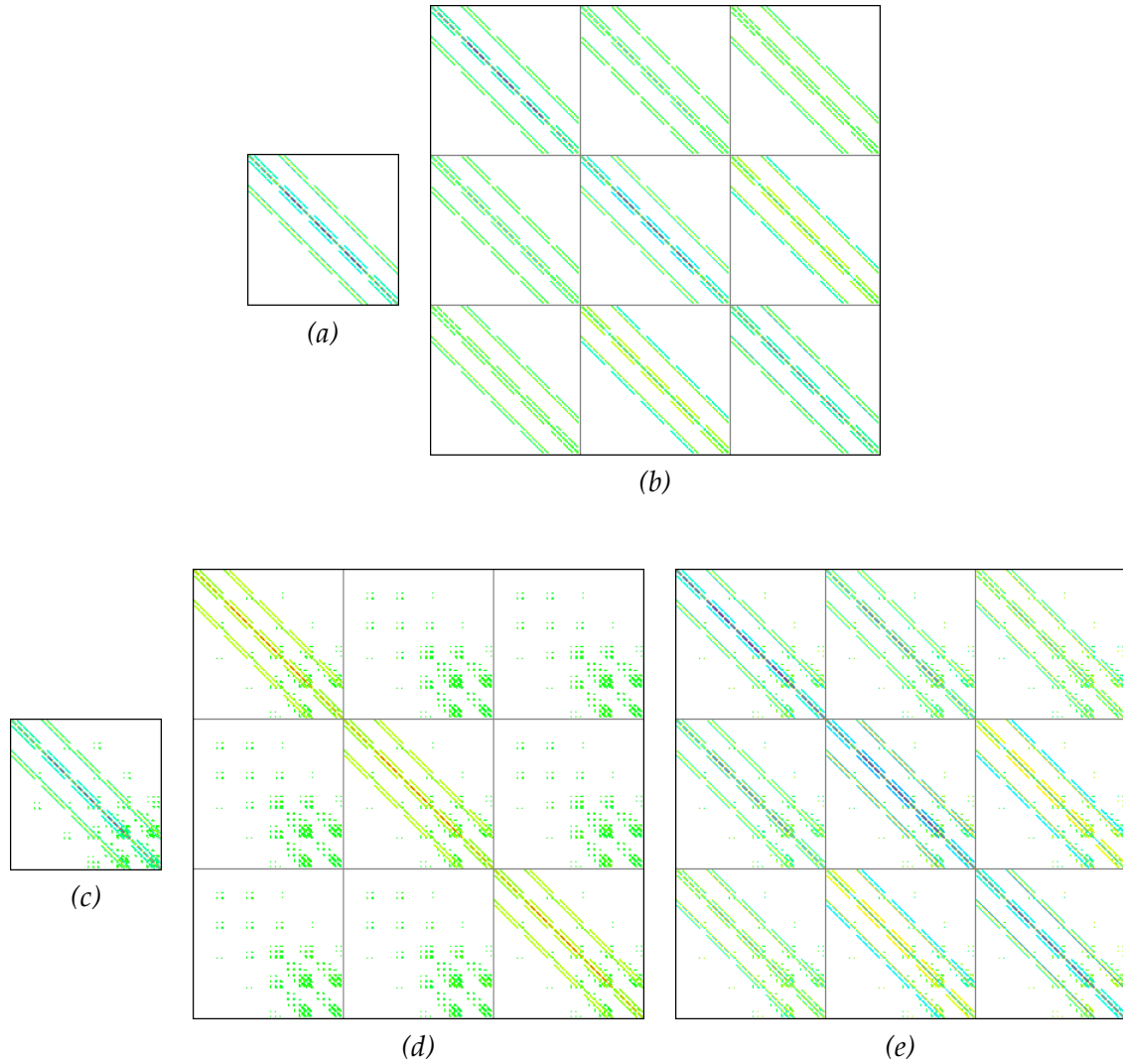


Figure 3.18. Visualization the block and sparsity structure of (a) a stiffness matrix for standard affine FE on \mathcal{G}^{\boxtimes} , (b) a CFE elasticity matrix for a complicated domain and $(E, \nu) = (1.0, 0.3)$, (c) a CFE stiffness matrix for discontinuous thermal diffusivity coefficient with $\kappa = 2$, (d) a CFE block mass matrix and (e) a CFE block elasticity matrix for $(E^-, \nu^-) = (1.0, 0.3)$ and $(E^+, \nu^+) = (1.5, 0.1)$ are shown. A nonlinear HSV blue-to-red color scale represents the values of nonzero entries where green are entries almost equal to zero and white are entries exactly equal to zero. For computational resolution 5^3 , matrices for the scalar problems are of size 125×125 and block matrices for the vector-valued problems are of total size 375×375 , in the complicated domain case (b), 124 of the 125 nodes are DOF nodes.

4 Numerical Homogenization

THE GOAL OF NUMERICAL HOMOGENIZATION is to determine effective, macroscopic material properties. We are interested in finding effective diffusivity or elasticity tensors for periodic or statistically periodic materials. The CFE method, using cubic or brick-shaped computational domains, is well suited for numerical homogenization schemes in which cubic fundamental cells are considered.

In this chapter we first review a numerical homogenization technique for exactly periodic cells (Section 4.1) and extend it to statistical prototype cells in Section 4.2. The CFE discretization is presented in Section 4.3 and suitable solvers for corresponding systems of equations are discussed in Section 4.4. Orthotropy, a special case of anisotropy, of resulting homogenized elasticity tensors is finally addressed in Section 4.5. The two-scale approach presented here distinguishes only between microscale and macroscale, but can easily be iterated to allow for multiscale simulations. Results obtained using the methods of this chapter can be found in Section 7.4.

The application of CFE in homogenization has been published in [311] (for the case of complicated domains and periodic microstructures) and in [296] (for the case of statistically periodic complicated domains), moreover homogenization of (both types of) microstructures with discontinuous coefficients has been treated in [281] (submitted).

Periodic vs. Statistically Periodic Microstructures

In case of exactly periodic structures, we can microscopically simulate simple temperature gradient and loading cases with periodic boundary conditions to obtain macroscopic material properties by computing effective heat fluxes and stresses.

Natural structures are typically only periodic in a statistical sense, so that periodic boundary conditions cannot be imposed. One might be tempted to make specimens periodic by mirroring in all space dimensions as discussed in [269], but this may introduce artificial structural kinks and destroy existing anisotropy as sketched in Figure 4.1. Simply applying periodic boundary conditions in case of non-periodic media does not work either, since this means identifying points on the boundary with different material parameters leading to inconsistent geometric structures or identifying points inside and outside the object. Our approach is to replace periodic boundary conditions by interpolated Dirichlet boundary conditions, clearly introducing boundary artifacts in the microscopic simulation. In case of trabecular microstructures, the influence of boundary artifacts can be diminished by evaluating heat fluxes and stresses only on a centered subdomain, ignoring a boundary layer.

General Notation for Homogenization

We use the notation $\Omega^\#$ for one *fundamental cell* of the microstructure, being either a periodic cell for exactly periodic structures or a representative cell for statistically periodic structures. $\Omega^\#$ is usually assumed to be a cube, the extension to a cuboid, however, is not difficult. Tilings of \mathbb{R}^3 into more complicated $\Omega^\#$ will not be considered in our CFE context.

Let us now pick up the notation from Chapter 2. Let $\Lambda^\#$ be one or more copies of $\Omega^\#$ (intersected with the macroscopic material domain Ω_- in case of complicated domains). $\Lambda^\#$ is referred to as the *periodic domain for computation*. Let us point out that periodic or Dirichlet boundary conditions in the following are only applied to the boundary $\partial^\square \Lambda^\#$ of the bounding box intersected with $\Lambda^\#$, but not the (inner) interface in case of complicated domains. For statistically periodic cells, the *periodic domain for evaluation* $\Lambda^{\#\beta}$ will denote $\Lambda^\#$ minus some boundary layer and will be assumed to contain one or more copies of $\Omega^\#$, see below for the precise definition. We will furthermore use the notation $\bar{\bullet}$ for macroscopic or effective quantities.

Using microscopic periodic source terms in the homogenization may seem surprising at first glance, but if these are not visible at the macroscale one may want to account for them in homogenized material properties. An example for the heat diffusion model problem are heat sources due to electric resistance in conducting components of computer chips. As for the elasticity problem, gravity could be decomposed in a gravity term \bar{f} for the apparent density of the microstructure plus a periodic correction term \tilde{f} being positive inside and negative outside the microstructure. In our applications no such microscopic source terms occur, so they are omitted from the discussion here and we assume $\tilde{f} = 0$. Also macroscopic source terms \bar{f} are assumed to vanish.

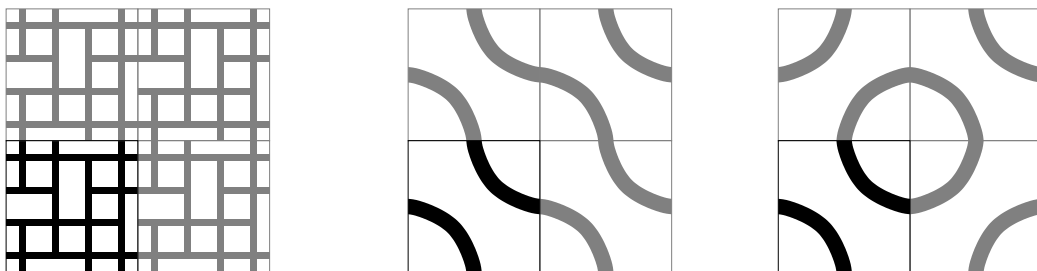


Figure 4.1. The *left* example shows that periodization of merely statistically periodic structures results in artificial interfaces. Mirroring is not an appropriate solution for this problem (*middle* and *right*) as it changes structural anisotropy and connectivity.

4.1 Homogenization for Periodic Specimens

Let us first consider the case of geometrically exactly periodic microstructures.

4.1.1 Cell Problems for Periodic Cells

Heat Diffusion Model Problem

The effective heat flux \bar{q} for $\Lambda^\#$ is given in terms of the macroscopic diffusivity tensor \bar{a} by

$$\bar{q} = \bar{a} \overline{\nabla u} = \bar{a} \int_{\Lambda^\#} \nabla u. \quad (4.1)$$

For numerical homogenization via ‘cell problems’ [10, Chapter 1], we now run multiple microscopic simulations. For specific choice of u , we compute \bar{q} so that we obtain enough equations to determine \bar{a} . This is most easily obtained for unit temperature gradients $\nabla \bar{u} = e_i$ for which the corresponding \bar{q} is simply the i th column of \bar{a} .

For given \bar{u} we need to find a periodic correction profile \tilde{u} so that

$$u = \bar{u} + \tilde{u} \quad (4.2)$$

is the actual physical equilibrium profile that has the same average gradient and macroscopic heat flux as \bar{u} . This decomposition is unique only up to addition of a constant, so we additionally require $\int_{\Lambda^\#} \tilde{u} = 0$. Periodicity of a C^1 function u implies $\int_{\Lambda^\#} \nabla \tilde{u} = 0$ due to Fubini’s theorem¹. This decomposition is illustrated in Figure 4.2.

Substituting this condition in the PDE (2.4) describing the steady state of heat diffusion, we obtain the equation for computing \tilde{u} from \bar{u} :

$$\begin{aligned} -\operatorname{div}(a \nabla(\tilde{u} + \bar{u})) &= 0 \quad \text{in } \Lambda^\# \\ \Leftrightarrow -\operatorname{div}(a \nabla \tilde{u}) &= \operatorname{div}(a \nabla \bar{u}) \end{aligned} \quad (4.3)$$

with periodic boundary conditions for \tilde{u} and $\int_{\Lambda^\#} \tilde{u} = 0$. We hence obtain the following weak problem.

Problem 4.1. Find $\tilde{u} \in H_{\#}^{1,2}(\Lambda^\#)$ satisfying

$$\int_{\Lambda^\#} \langle a \nabla \tilde{u}, \nabla v \rangle = - \int_{\Lambda^\#} \langle a \nabla \bar{u}, \nabla v \rangle \quad \forall v \in H_{\#}^{1,2}(\Lambda^\#) \quad (4.4)$$

where $H_{\#}^{1,2}(\Lambda^\#)$ denotes the space $H^{1,2}(\Lambda^\#)$ restricted to functions satisfying periodic boundary conditions on $\partial^{\square} \Lambda^\#$.

¹Named after the Italian mathematician Guido Fubini, * January 19, 1879 in Venice, † June 6, 1943 in New York, U.S.A. [262].

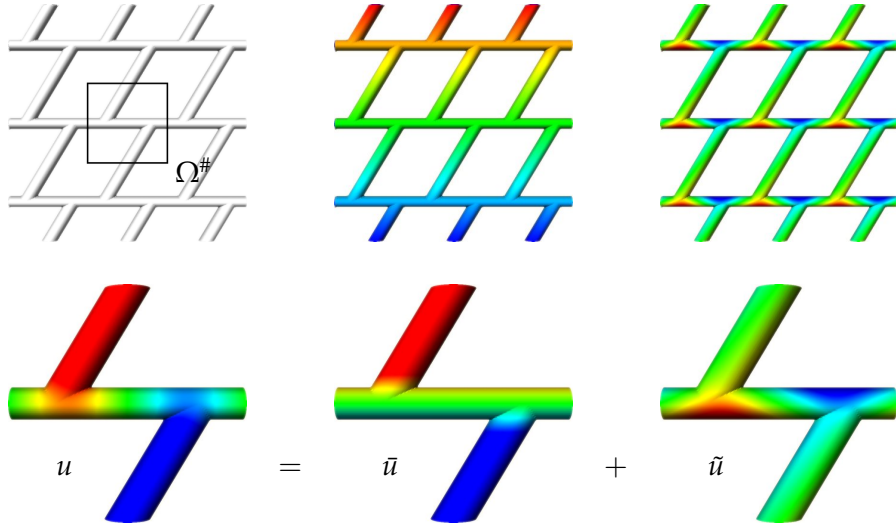


Figure 4.2. For the Z-shaped periodic object (*top left*) with one fundamental cell $\Omega^\#$ highlighted, the decomposition of the equilibrium profile u (*bottom left*) in the smooth macroscopic part \bar{u} (*middle*) and microscopic periodic correction profile \tilde{u} (*right*) is shown on the fundamental cell (*bottom row*) and on a larger part of the domain (*top middle and right*), using different nonlinear color scales for better illustration of the decomposition.

For given \bar{u} we first compute \tilde{u} using (4.4) and then the macroscopic heat flux \bar{q} (cf. (4.1)) by integration over the full domain $\Lambda^\#$ as

$$\bar{q} = \int_{\Lambda^\#} q = \int_{\Lambda^\#} a \nabla u = \int_{\Lambda^\#} a \nabla (\bar{u} + \tilde{u}) . \quad (4.5)$$

Substituting \bar{u} and \bar{q} in (4.1) then yields one equation used for determining the effective diffusivity tensor \bar{a} . Using three linearly independent \bar{u}^i with $\nabla \bar{u}^i = e_i$, $i = 0, 1, 2$, we can determine \bar{a} column by column via

$$\bar{a}_{.i} = \int_{\Lambda^\#} a (\nabla \tilde{u}^i + \nabla \bar{u}^i) = \int_{\Lambda^\#} a (\nabla \tilde{u}^i + e_i) \quad (4.6)$$

where \tilde{u}^i solves (4.3) for given \bar{u}^i .

The effective diffusivity tensor is symmetric due to physical reasons. In the spatially smooth case we will see in Section 4.1.3 that also \bar{a} obtained by the homogenization procedure is symmetric. This is not exactly satisfied in the discrete case, but a violation of symmetry is considered to be a numerical artifact and the tensor is symmetrized.

Linear Elasticity Model Problem

For linear elasticity, the relevant physical quantity is the effective stress $\bar{\sigma}$ which can be expressed in terms of the macroscopic elasticity tensor as

$$\bar{\sigma} = \bar{C} \overline{\epsilon[u]} = \bar{C} \int_{\Lambda^\#} \epsilon[u] . \quad (4.7)$$

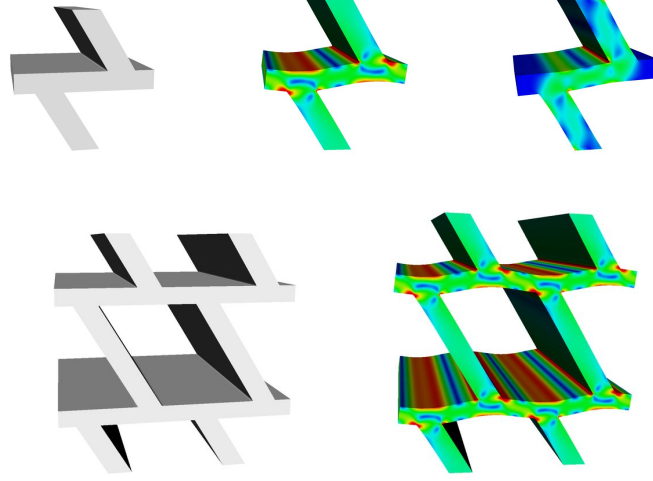


Figure 4.3. *Top row:* The Z-shaped geometry (*left*) is deformed under tensile loading with affine-periodic boundary conditions (*middle*). For comparison, tensile loading with no displacement boundary conditions enforced on the side faces is shown on the *right*. Color (same  color scale for all plots) encodes the von Mises stress at the surface of the structures. The *bottom row* shows a larger part of the periodic domain.

Similar to the scalar case, for given \bar{u} we need to find a periodic correction profile \tilde{u} so that

$$u = \bar{u} + \tilde{u} \quad (4.8)$$

is the actual physical equilibrium profile that has the same average gradient and macroscopic stress as \bar{u} . Compared to (4.2), the functions u are now vector-valued displacements. Again, for a C^1 displacement \tilde{u} , Fubini's theorem implies $\int_{\Lambda^\#} \epsilon[\tilde{u}] = 0$.

This decomposition is unique only up to addition of $v(x) = Sx + b$, with a constant b and a skew-symmetric matrix S . Periodic boundary conditions on $\partial^\square \Lambda^\#$ only allow $S = 0$, and the additional requirement $\int_{\Lambda^\#} \tilde{u} = 0$ only allows $b = 0$, thus making decomposition (4.8) unique. This decomposition of displacements is illustrated in Figure 4.3.

Substituting this in (2.14) we obtain

$$\begin{aligned} -\operatorname{div} C\epsilon[\tilde{u} + \bar{u}] &= 0 \\ \Leftrightarrow -\operatorname{div} C\epsilon[\tilde{u}] &= \operatorname{div} C\epsilon[\bar{u}] \end{aligned} \quad (4.9)$$

with periodic boundary conditions for \tilde{u} . We hence obtain the following weak problem.

Problem 4.2. Find $\tilde{u} \in H_{\#}^{1,2}(\Lambda^\#, \mathbb{R}^3)$ satisfying

$$\int_{\Lambda^\#} C\epsilon[\tilde{u}] : \epsilon[v] = - \int_{\Lambda^\#} C\epsilon[\bar{u}] : \epsilon[v] \quad \forall v \in H_{\#}^{1,2}(\Lambda^\#, \mathbb{R}^3). \quad (4.10)$$

For given \bar{u} , we again first compute \tilde{u} via (4.10) and then the effective stress (cf. (4.7)) via

$$\bar{\sigma} = \int_{\Lambda^\#} \sigma = \int_{\Lambda^\#} C\epsilon[u] = \int_{\Lambda^\#} C\epsilon[\bar{u} + \tilde{u}] . \quad (4.11)$$

Substituting \bar{u} and $\bar{\sigma}$ in (4.7) yields one equation for determining \bar{C} .

Using six linearly independent \bar{u}^{ij} with $\epsilon[\bar{u}^{ij}] = e_{ij} := \frac{1}{2}(e_i \otimes e_j + e_j \otimes e_i)$, where $i \leq j \in \{0, 1, 2\}$, we can determine \bar{C} via

$$\bar{C}_{..ij} = \int_{\Lambda^\#} C \left(\epsilon[\bar{u}^{ij}] + e_{ij} \right) \quad (4.12)$$

where \bar{u}^{ij} solves (4.9) for given \bar{u}^{ij} .

4.1.2 Variational Formulation of the Cell Problems

It turns out to be mathematically more convenient to consider—in the spatially continuous case equivalent—variational formulations for the correction profiles \tilde{u} .

Heat Diffusion Model Problem

For the scalar model problem we consider the following problem.

Problem 4.3. Find the minimizer \tilde{u} in

$$\int_{\Lambda^\#} \langle \bar{a} \nabla \tilde{u}, \nabla \tilde{u} \rangle = \inf_{\tilde{v} \in H_{\#}^{1,2}(\Lambda^\#)} \int_{\Lambda^\#} \langle a \nabla(\tilde{u} + \tilde{v}), \nabla(\tilde{u} + \tilde{v}) \rangle \quad (4.13)$$

for a symmetric tensor a .

This leads to the same Euler–Lagrange equation as (4.4). The minimum in (4.13) is attained by \tilde{u} solving (4.3) for given \bar{u} . Defining $e_{i\pm k} := \frac{1}{2}(e_i \pm e_k)$ and taking into account that

$$a_{ik} = \langle a e_i, e_k \rangle = \langle a e_{i+k}, e_{i+k} \rangle - \langle a e_{i-k}, e_{i-k} \rangle \quad (4.14)$$

holds for symmetric a leads to the following lemma. Recall that a was assumed to be symmetric for physical reasons.

Lemma 4.4. The entries \bar{a}_{ik} of \bar{a} are obtained as

$$\begin{aligned} \bar{a}_{ik} &= \int_{\Lambda^\#} \langle \bar{a} \nabla \bar{u}^i, \nabla \bar{u}^k \rangle = \int_{\Lambda^\#} \langle a \nabla(\bar{u}^i + \tilde{u}^i), \nabla(\bar{u}^k + \tilde{u}^k) \rangle \\ &= \int_{\Lambda^\#} \langle a \nabla(\bar{u}^{i+k} + \tilde{u}^{i+k}), \nabla(\bar{u}^{i+k} + \tilde{u}^{i+k}) \rangle - \langle a \nabla(\bar{u}^{i-k} + \tilde{u}^{i-k}), \nabla(\bar{u}^{i-k} + \tilde{u}^{i-k}) \rangle \end{aligned} \quad (4.15)$$

for $\nabla \bar{u}^i = e_i$, $\nabla \bar{u}^{i\pm k} = e_{i\pm k}$ and $\tilde{u}^{i\pm k}$ being the corresponding solution of (4.3). The tensor \bar{a} is symmetric.

Proof. The second equality is due to the fact that \tilde{u} solves the cell problem (4.3). The third equation finally uses (4.14) and symmetry of the tensor a . Symmetry of \bar{a} is then verified easily. \square

Linear Elasticity Model Problem

For the linear elasticity model problem we consider the following formulation, cf. Equation (4.3).

Problem 4.5. Find the minimizer \tilde{u} in

$$\int_{\Lambda^\#} \bar{C}\epsilon[\bar{u}] : \epsilon[\bar{u}] = \inf_{\tilde{v} \in H_\#^{1,2}(\Lambda^\#, \mathbb{R}^3)} \int_{\Lambda^\#} C\epsilon[\bar{u} + \tilde{v}] : \epsilon[\bar{u} + \tilde{v}] \quad (4.16)$$

leading to the same Euler–Lagrange equation as (4.10).

The minimum in (4.16) is again obtained by \tilde{u} solving (4.9) for given \bar{u} . Defining $e_{ij\pm kl} := \frac{1}{2}(e_{ij} \pm e_{kl})$ and using

$$C_{ijkl} = Ce_{ij} : e_{kl} = Ce_{ij+kl} : e_{ij+kl} - Ce_{ij-kl} : e_{ij-kl} \quad (4.17)$$

for symmetric C , we obtain the following lemma.

Lemma 4.6. The entries \bar{C}_{ijkl} of the effective elasticity tensor \bar{C} are obtained from

$$\begin{aligned} \bar{C}_{ijkl} &= \int_{\Lambda^\#} \bar{C}\epsilon[\bar{u}^{ij}] : \epsilon[\bar{u}^{kl}] = \int_{\Lambda^\#} C\epsilon[\bar{u}^{ij} + \tilde{u}^{ij}] : \epsilon[\bar{u}^{kl} + \tilde{u}^{ij}] \\ &= \int_{\Lambda^\#} C\epsilon[\bar{u}^{ij+kl} + \tilde{u}^{ij+kl}] : \epsilon[\bar{u}^{ij+kl} + \tilde{u}^{ij+kl}] \\ &\quad - C\epsilon[\bar{u}^{ij-kl} + \tilde{u}^{ij-kl}] : \epsilon[\bar{u}^{ij-kl} + \tilde{u}^{ij-kl}] \end{aligned} \quad (4.18)$$

where $\epsilon[\bar{u}^{ij\pm kl}] = e_{ij\pm kl}$ as defined above and $\tilde{u}^{ij\pm kl}$ is the corresponding solution of (4.9). The tensor \bar{C} hence satisfies the symmetry relation $\bar{C}_{ijkl} = \bar{C}_{klij}$.

Proof. The second equation results from \tilde{u} solving the cell problem (4.10). The third equation uses (4.17) and the symmetry of \bar{C} in the first two and in the last two indices. The symmetry property is then easily verified. \square

4.1.3 Symmetry of the Homogenized Tensors

For physical reasons, the homogenized tensors must be symmetric. Let us show that this is also true for the tensors obtained by our homogenization procedures under smoothness assumptions for the microscopic tensor.

Heat Diffusion Model Problem

Let us first consider the scalar model problem of heat diffusion. Symmetry is first shown for the tensor obtained by the cell problem approach, then we show that the same tensor is obtained by the variational formulation (4.13) which is hence also symmetric.

Proposition 4.7. The effective thermal diffusivity tensor \bar{a} obtained by our cell problem approach (4.3) is symmetric if the microscopic tensor a is sufficiently smooth.

Proof. For \bar{u}^k with $\nabla \bar{u}^k = e_k$, \tilde{u}^k solves (4.3) with periodic boundary conditions for \tilde{u}^k . In coordinates, we can write (using Einstein summation convention and the notation $\bullet_{,i} = \partial_i \bullet$ for partial derivatives

$$-(a_{ij}\tilde{u}_{,j}^k)_{,i} = a_{ik,i}, \quad (4.19a)$$

$$\bar{q}^k = (\bar{a}_{ij}\delta_{jk})_i = (\bar{a}_{ik})_i, \quad (4.19b)$$

$$\bar{a}_{ik} = \bar{q}_i^k = \int_{\Lambda^\#} a_{ij}(\delta_{jk} + \tilde{u}_{,j}^k), \quad (4.19c)$$

where (4.19a) follows from $-\operatorname{div}(a\nabla\tilde{u}) = \operatorname{div} a\nabla\bar{u}^k$, (4.19b) from $q = a\nabla u$ and $\nabla\bar{u}_k = e_k$, and (4.19c) follows from (4.6).

Symmetry can now be seen from

$$\begin{aligned} \bar{a}_{ik} - \bar{a}_{ki} &\stackrel{(a)}{=} \int a_{ij}(\delta_{jk} + \tilde{u}_{,j}^k) - \int a_{kj}(\delta_{ji} + \tilde{u}_{,j}^i) = \int a_{ik} - a_{ki} + a_{ij}\tilde{u}_{,j}^k - a_{kj}\tilde{u}_{,j}^i \\ &\stackrel{(b)}{=} \int a_{ij}\tilde{u}_{,j}^k - a_{kj}\tilde{u}_{,j}^i \stackrel{(c)}{=} \int -a_{ij,j}\tilde{u}^k + a_{kj,j}\tilde{u}^i \\ &\stackrel{(d)}{=} \int -a_{ji,j}\tilde{u}^k + a_{jk,j}\tilde{u}^i \stackrel{(e)}{=} \int (a_{jl}\tilde{u}_{,l}^i)_{,j}\tilde{u}^k - (a_{jl}\tilde{u}_{,l}^k)_{,j}\tilde{u}^i \\ &\stackrel{(f)}{=} \int -a_{jl}\tilde{u}_{,l}^i\tilde{u}_{,j}^k + a_{jl}\tilde{u}_{,l}^k\tilde{u}_{,j}^i \stackrel{(g)}{=} \int -a_{jl}\tilde{u}_{,l}^i\tilde{u}_{,j}^k + a_{lj}\tilde{u}_{,l}^i\tilde{u}_{,j}^k = 0 \end{aligned} \quad (4.20)$$

where, for simplicity, we omit the domain of integration $\Lambda^\#$. Step (a) is due to (4.19c), (b) uses symmetry of the microscopic tensor a , (c) results from integration by parts with periodic boundary conditions, (d) again uses microscopic symmetry, (e) uses (4.19a), (f) once more results from integration by parts, and (g) finally is a renaming of indices. Let us point out that steps (b) and (f) require differentiation of the microscopic tensor a which is not necessarily possible in the discrete setting. \square

Proposition 4.8. The effective thermal diffusivity tensors obtained by the cell problem approach (4.3) and by the variational formulation (4.13) coincide if the microscopic tensor is sufficiently smooth.

Proof. For $\nabla\bar{u}^{i\pm j} = \frac{1}{2}(e_i \pm e_j)$ the periodic function $\tilde{u}^{i\pm j}$ solves

$$\int_{\Lambda^\#} \langle a\nabla\bar{u}^{i\pm j}, \nabla\tilde{v} \rangle = - \int_{\Lambda^\#} \langle a\nabla\tilde{u}^{i\pm j}, \nabla\tilde{v} \rangle \quad (4.21)$$

for all test functions $\tilde{v} \in H_{\#}^{1,2}(\Lambda^\#)$. Making use of the notation above we observe that $\tilde{u}^{i\pm j} = \frac{1}{2}(\tilde{u}^i \pm \tilde{u}^j)$. Moreover,

$$\bar{q}^{i\pm j} = \frac{1}{2}(\bar{q}^i \pm \bar{q}^j) = \int_{\Lambda^\#} a\nabla(\bar{u}^{i\pm j} + \tilde{u}^{i\pm j}), \quad (4.22a)$$

$$0 = \int_{\Lambda^\#} a \nabla (\bar{u}^{i\pm j} + \tilde{u}^{i\pm j}) \nabla \bar{v} \quad (4.22b)$$

for all test functions \bar{v} as above.

Hence, again omitting the domain of integration $\Lambda^\#$,

$$\begin{aligned} \bar{a}_{ij} &= \int \langle \bar{a} e_i, e_j \rangle = \int \langle \bar{a} \nabla u^i, \nabla u^j \rangle \\ &\stackrel{(a)}{=} \int \langle a \nabla (\bar{u}^{i+j} + \tilde{u}^{i+j}), \nabla (\bar{u}^{i+j} + \tilde{u}^{i+j}) \rangle - \langle a \nabla (\bar{u}^{i-j} + \tilde{u}^{i-j}), \nabla (\bar{u}^{i-j} + \tilde{u}^{i-j}) \rangle \\ &\stackrel{(b)}{=} \int \langle a \nabla (\bar{u}^{i+j} + \tilde{u}^{i+j}), \nabla \bar{u}^{i+j} \rangle - \langle a \nabla (\bar{u}^{i-j} + \tilde{u}^{i-j}), \nabla \bar{u}^{i-j} \rangle \\ &\stackrel{(c)}{=} \frac{1}{4} \left(\langle \bar{q}^i + \bar{q}^j, e_i + e_j \rangle - \langle \bar{q}^i - \bar{q}^j, e_i - e_j \rangle \right) \\ &\stackrel{(d)}{=} \frac{1}{4} (\hat{a}_{ii} + \hat{a}_{jj} + \hat{a}_{ij} + \hat{a}_{ji}) - \frac{1}{4} (\hat{a}_{ii} + \hat{a}_{jj} - \hat{a}_{ij} - \hat{a}_{ji}) = \frac{1}{2} (\hat{a}_{ij} + \hat{a}_{ji}) \\ &\stackrel{(e)}{=} \hat{a}_{ij} \end{aligned} \quad (4.23)$$

where \hat{a} denotes the homogenized tensor obtained by the non-variational cell problem formulation above. Here, step (a) follows from Lemma 4.4. Step (b) uses the fact that the \bar{u} are admissible test functions in (4.22b), (c) takes into account (4.22a), (d) uses the property (4.19c) for the tensor \hat{a} , and finally (e) is the result of Proposition 4.7. So the two tensors are equivalent and \bar{a} is also symmetric. \square

Linear Elasticity Model Problem

Microscopic symmetry of stress and strain ensures the symmetries $\bar{C}_{ijkl} = \bar{C}_{jikl} = \bar{C}_{ijlk}$ for the first and second pair of indices separately also for the homogenized elasticity tensor. For physical reasons, the symmetry $\bar{C}_{ijkl} = \bar{C}_{klij}$ also needs to be satisfied. The proof for this works in the same way as above and has been presented in [296], it is given here mainly for completeness.

Proposition 4.9. The effective elasticity tensor \bar{C} obtained by our cell problem approach (4.9) is symmetric if the microscopic tensor C is sufficiently smooth.

Proof. First observe the analog of (4.19)

$$-(C_{ijkl} \tilde{u}_{l,k}^{mn})_{,i} = (C_{ijmn})_{,i} \quad (4.24a)$$

$$\bar{\sigma}^{kl} = (\bar{C}_{ijmn} \epsilon[e_{kl}]_{mn})_{ij} = (\bar{C}_{ijkl})_{ij} \quad (4.24b)$$

$$\bar{C}_{ijkl} = \bar{\sigma}_{ij}^{kl} = \int_{\Lambda^\#} C_{ijkl} (\delta_{ik} \delta_{jl} + \tilde{u}_{j,i}^{kl}) \quad (4.24c)$$

where (4.24a) follows from (4.9) and the symmetry of the microscopic tensor C , (4.24b) follows from $\sigma = C\epsilon[u]$, $\epsilon[\bar{u}^{kl}] = e_{kl}$, and (4.24c) follows from (4.12).

Then the desired symmetry holds due to

$$\begin{aligned}
 \bar{C}_{ijkl} - \bar{C}_{klij} &\stackrel{(a)}{=} \int C_{ijmn}(\delta_{mk}\delta_{nl} + \tilde{u}_{n,m}^{kl}) - \int C_{klmn}(\delta_{mi}\delta_{nj} + \tilde{u}_{n,m}^{ij}) \\
 &= \int C_{ijkl} - C_{klij} + C_{ijmn}\tilde{u}_{n,m}^{kl} - C_{klmn}\tilde{u}_{n,m}^{ij} \stackrel{(b)}{=} \int C_{ijmn}\tilde{u}_{n,m}^{kl} - C_{klmn}\tilde{u}_{n,m}^{ij} \\
 &\stackrel{(c)}{=} \int -C_{ijmn,m}\tilde{u}_n^{kl} + C_{klmn,m}\tilde{u}_n^{ij} \stackrel{(d)}{=} \int -C_{mnij,m}\tilde{u}_n^{kl} + C_{mnkl,m}\tilde{u}_n^{ij} \quad (4.25) \\
 &\stackrel{(e)}{=} \int (C_{mnpq}\tilde{u}_{q,p}^{ij})_{,m}\tilde{u}_n^{kl} - (C_{mnpq}\tilde{u}_{q,p}^{kl})_{,m}\tilde{u}_n^{ij} \\
 &\stackrel{(f)}{=} \int -C_{mnpq}\tilde{u}_{q,p}^{ij}\tilde{u}_{n,m}^{kl} + C_{mnpq}\tilde{u}_{q,p}^{kl}\tilde{u}_{n,m}^{ij} = 0.
 \end{aligned}$$

The domain of integration $\Lambda^\#$ is again left out. Step (a) is due to (4.24c), (b) uses the symmetry of C , (c) results from integration by parts with periodic boundary conditions, (d) again uses symmetry of C , (e) takes into account Equation (4.24a), and (f) is again based on an integration by parts. \square

Proposition 4.10. The effective elasticity tensors obtained by the cell problem approach (4.9) and by the variational formulation (4.16) coincide if the microscopic tensor is sufficiently smooth.

Proof. First,

$$\bar{\sigma}^{ij\pm kl} = \frac{1}{2}(\bar{\sigma}^{ij} \pm \bar{\sigma}^{kl}) = \int_{\Lambda^\#} C\epsilon \left[\bar{u}^{ij\pm kl} + \tilde{u}^{ij\pm kl} \right], \quad (4.26a)$$

$$0 = \int_{\Lambda^\#} C\epsilon \left[\bar{u}^{ij\pm kl} + \tilde{u}^{ij\pm kl} \right] : \epsilon[\tilde{v}] \quad (4.26b)$$

for all test functions $\tilde{v} \in H_\#^{1,2}(\Lambda^\#; \mathbb{R}^3)$. Hence

$$\begin{aligned}
 \bar{C}_{ijkl} &= \int \bar{C}_{ijkl}e_{ij} : e_{kl} = \bar{C}_{ijkl}\epsilon \left[\bar{u}^{ij} \right] : \epsilon \left[\bar{u}^{kl} \right] \\
 &\stackrel{(a)}{=} \int C_{ijkl}\epsilon \left[\bar{u}^{ij+kl} + \tilde{u}^{ij+kl} \right] : \epsilon \left[\bar{u}^{ij+kl} + \tilde{u}^{ij+kl} \right] \\
 &\quad - C_{ijkl}\epsilon \left[\bar{u}^{ij-kl} + \tilde{u}^{ij-kl} \right] : \epsilon \left[\bar{u}^{ij-kl} + \tilde{u}^{ij-kl} \right] \\
 &\stackrel{(b)}{=} \int C_{ijkl}\epsilon \left[\bar{u}^{ij+kl} + \tilde{u}^{ij+kl} \right] : \epsilon \left[\bar{u}^{ij+kl} \right] - C_{ijkl}\epsilon \left[\bar{u}^{ij-kl} + \tilde{u}^{ij-kl} \right] : \epsilon \left[\bar{u}^{ij-kl} \right] \\
 &\stackrel{(c)}{=} \frac{1}{4} \left[(\bar{\sigma}^{ij} + \bar{\sigma}^{kl}) : (e_{ij} + e_{kl}) - (\bar{\sigma}^{ij} - \bar{\sigma}^{kl}) : (e_{ij} - e_{kl}) \right] \quad (4.27) \\
 &\stackrel{(d)}{=} \frac{1}{4} (\hat{C}_{ijij} + \hat{C}_{ijkl} + \hat{C}_{klij} + \hat{C}_{klkl}) - \frac{1}{4} (\hat{C}_{ijij} - \hat{C}_{ijkl} - \hat{C}_{klij} + \hat{C}_{klkl}) \\
 &= \frac{1}{2} (\hat{C}_{ijkl} + \hat{C}_{klij})
 \end{aligned}$$

where \hat{C} denotes the homogenized tensor obtained cell problem formulation (4.12) above and where the domain $\Lambda^\#$ of integration is again left out. Step (a) results from Lemma 4.6, step (b) uses admissibility of the functions \tilde{u} as test functions in (4.26b), step (c) takes into account (4.26a), step (d) uses the property (4.24c) for \hat{C} . \square

4.2 Homogenization for Statistically Periodic Specimens

In case we do not have exact periodicity of the material, the cell problems with the decomposition in macroscopic and correction profiles and the use of periodic boundary conditions can be replaced by enforcing a macroscopic profile via Dirichlet boundary conditions. These boundary conditions are clearly not zero ones, and the term '(in)homogeneous boundary conditions' should—and will—be avoided in the context of homogenization.

Let

$$\Lambda^{\#\beta} := \left\{ x \in \Lambda^{\#} \mid \text{dist}(x, \partial^{\square} \Lambda^{\#}) > \beta \right\}, \quad (4.28)$$

then $\Lambda^{\#}$ is $\Lambda^{\#\beta}$ plus an additional boundary layer used for simulation, but not for evaluation. The choice of β can be tedious because increasing β leads to (desired) reduced influence of the boundary layer but (undesired) computational overhead for fixed $\Lambda^{\#\beta} \subset \Lambda^{\#}$ or decreased representativity for fixed $\Lambda^{\#}$, it will be further investigated below.

The (strong) cell problem formulations (4.3) and (4.9) are now modified to boundary value problems with the same macroscopic profiles \bar{u} as before.

Problem 4.11. For given macroscopic temperature profile \bar{u} , solve

$$\begin{aligned} -\operatorname{div}(a\nabla u) &= 0 && \text{in } \Lambda^{\#} \\ u &= \bar{u} && \text{on } \partial^{\square} \Lambda^{\#}. \end{aligned} \quad (4.29)$$

Problem 4.12. For given macroscopic displacement \bar{u} , solve

$$\begin{aligned} -\operatorname{div}(C\epsilon[u]) &= 0 && \text{in } \Lambda^{\#} \\ u &= \bar{u} && \text{on } \partial^{\square} \Lambda^{\#}. \end{aligned} \quad (4.30)$$

The Dirichlet boundary conditions in Equation (4.30) lead to artificial stiffening (in the elasticity case) near the boundary, as illustrated in Figure 4.4, and to overestimated energy in (4.16). The same effect happens for the scalar model problem and for the

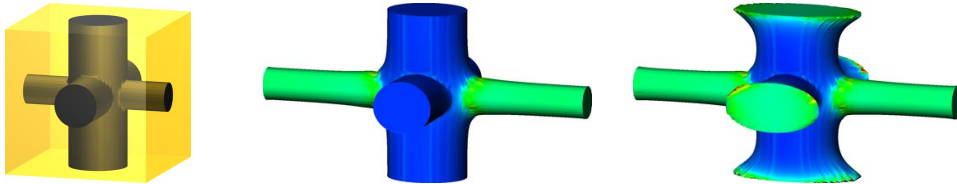


Figure 4.4. For a $1 \times 1 \times 1$ rod dataset, the difference between periodic (*middle*) and Dirichlet (*right*) boundary conditions is shown for one tensile loading case. Dirichlet boundary conditions prevent the longitudinal rods from thinning at the boundary and force the transverse rods to an elliptic cross section at the boundary, leading to higher average stress for the same macroscopic strain. Color  encodes the von Mises stress at the interface.

energy in (4.13) but is less intuitively explained there. To reduce the influence of these boundary artifacts, heat fluxes or stresses are now averaged only over the strict subdomain $\Lambda^{\#\beta}$

$$\bar{q} = \int_{\Lambda^{\#\beta}} q = \int_{\Lambda^{\#\beta}} a \nabla u \quad (4.31)$$

$$\bar{\sigma} = \int_{\Lambda^{\#\beta}} \sigma = \int_{\Lambda^{\#\beta}} C \epsilon[u] \quad (4.32)$$

where u is computed for given \bar{u} by solving (4.29) or (4.30).

The effective thermal diffusivity and elasticity tensors are then obtained as described in the following lemmas.

Lemma 4.13. Using three linearly independent \bar{u}^i with $\nabla \bar{u}^i = e_i$, $i = 0, 1, 2$, the columns $\bar{a}_{\cdot i}$ of the effective thermal diffusivity tensor \bar{a} for statistically representative fundamental cells can be determined via

$$\bar{a}_{\cdot i} = \int_{\Lambda^{\#\beta}} a \nabla u^i \quad (4.33)$$

where u^i solves (4.29) for given \bar{u}^i .

Lemma 4.14. Using six linearly independent macroscopic displacement profiles \bar{u}^{ij} , $i \leq j \in \{0, 1, 2\}$ with $\epsilon[\bar{u}^{ij}] = e_{ij} := \frac{1}{2} (e_i \otimes e_j + e_j \otimes e_i)$, we can determine the effective elasticity tensor \bar{C} for statistically representative fundamental cells via

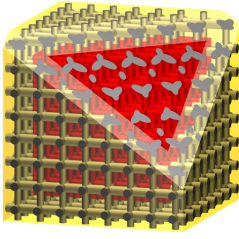
$$\bar{C}_{\cdot ij} = \int_{\Lambda^{\#\beta}} C(\epsilon[u^{ij}]) \quad (4.34)$$

where u^{ij} solves (4.30) for given \bar{u}^{ij} .

For physical reasons the homogenized tensors have to satisfy symmetry conditions which we have proven in the case of periodic fundamental cells and for sufficient smoothness of the microscopic tensor. We hence consider small symmetry defects in the tensors obtained from Lemma 4.13 or 4.14 as numerical artifacts and symmetrize the tensors (unless mentioned otherwise). Figure 7.32 lists the non-symmetrized elasticity tensors for the same object at different computational resolutions and shows that the symmetry defect diminishes for increasing resolution.

Choice of the Boundary Layer

To evaluate the effect of the Dirichlet boundary condition and the parameter β on the homogenized effective elasticity tensor in case of a trabecular microstructure, we performed the following numerical experiment: A structure with $8 \times 8 \times 8$ cylindrical rods of diameter-to-length ratios $d/l = (0.4, 0.35, 0.3)$ (see Section 7.3.2 and Figure 7.22) with microscopically isotropic material properties ($E = 10$, $\nu = 0.1$) embedded in 1 m^3 of material with $E = 1$, $\nu = 0.3$ (see Figure 4.5) at computational resolution 129^3



boundary layer β	0/8	1/8	2/8	3/8
relevant Frobenius difference	0.108	0.045	0.029	0.020
relative DOF usage	1.000	0.422	0.125	0.016

Figure 4.5. For an artificial trabecular structure, the image shows the evaluation subdomain $\Lambda^{\#\beta}$ for $\beta = 1/8$. A larger boundary layer does not yield a significantly better tensor when using the homogenization method for statistically periodic fundamental cells compared to the tensor obtained using the method for periodic cells, but results in a drastic increase of computational resources required.

was first viewed as a periodic fundamental cell. The corresponding homogenization procedure was used to obtain the reference macroscopic tensor in Voigt's notation

$$C = \begin{bmatrix} 2.698 & 0.652 & 0.650 & & & \\ 0.652 & 2.505 & 0.649 & & & \\ 0.650 & 0.649 & 2.314 & & & \\ & & & 0.581 & & \\ & & & & 0.611 & \\ & & & & & 0.642 \end{bmatrix}$$

where entries smaller than 10^{-3} times the maximal entry have been omitted. Considering this domain as a merely statistically representative fundamental cell and applying the corresponding homogenization procedure with Dirichlet boundary values, the following macroscopic tensors were obtained for different values of β

$$C^{\beta=0} = \begin{bmatrix} 2.713 & 0.652 & 0.651 & & & \\ 0.652 & 2.525 & 0.649 & & & \\ 0.651 & 0.649 & 2.337 & & & \\ & & & 0.609 & & \\ & & & & 0.641 & \\ & & & & & 0.673 \end{bmatrix}, \quad C^{\beta=\frac{1}{8}} = \begin{bmatrix} 2.698 & 0.652 & 0.650 & & & \\ 0.652 & 2.505 & 0.649 & & & \\ 0.650 & 0.649 & 2.314 & & & \\ & & & 0.592 & & \\ & & & & 0.624 & \\ & & & & & 0.657 \end{bmatrix}$$

where again small entries have been omitted. Obviously, artificial stiffening near the boundary plays a significant role for the diagonal entries in the Voigt tensor for $\beta = 0$. Leaving out a boundary layer of one trabecular distance size ($\beta = 1/8$ in this case) almost completely eliminates this effect. In fact, choosing larger β only leads to a slight improvement in the Frobenius norm difference of the relevant entries (upper left block and lower right diagonal in Voigt's notation), at the cost of immensely decreasing relative DOF usage (number of DOF used for evaluation, which need to cover one fundamental cell $\Omega^{\#}$, relative to number of DOF used in the simulation), cf. Figure 4.5.

According to [160], the size of a cell should be at least 5 inter-trabecular lengths for the cell to be statistically representative for morphological quantities determined on the cell. This criterion is used also when determining effective elasticity properties, e.g., in [171, 345].

Hence we require $\Lambda^{\#\beta}$ to be of size about 5 inter-trabecular lengths and add a boundary layer of one inter-trabecular length at each side, so that we typically rescale

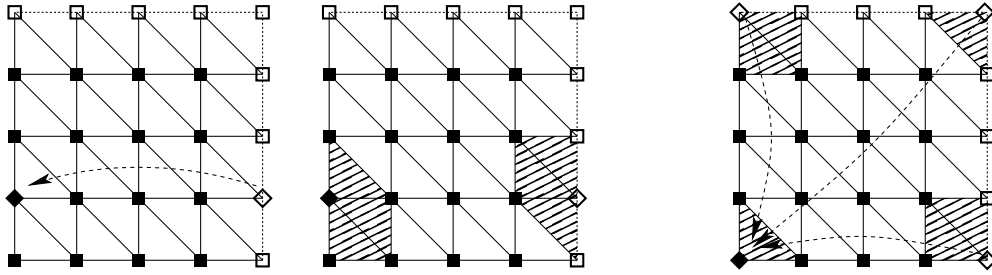


Figure 4.6. The identification of an inactive node \diamond with its active counterpart \blacklozenge is shown on the *left*, correspondingly the support of the associated basis function is disconnected (*middle*), leading to a different node neighborhood structure. For corner nodes (*right*), there are even more components of the support.

our problem to $\Lambda^\# = [0, 1]^3 \supset [1/8, 7/8] = \Lambda^{\#\beta}$, $\beta = 1/8$. Let us point out that $\Lambda^{\#\beta}$ determines the computational cost (where the boundary layer overhead contributes by power 3). This amounts to a computational overhead of about 137% compared to a simulation only on the evaluation domain $\Lambda^\#$.

Table 7.38 indicates that $\beta = 1/8$ is also a useful value for non-artificial trabecular objects. The same thickness of a boundary layer to be ignored is obtained in a similar approach in [340]. The authors of [340] consider cylindrical specimens and model a standard mechanical experiment with stress-free side boundary which leads to artificial softening of the structure compared to its in situ properties.

4.3 Composite Finite Element Discretization

Let us now discuss the peculiarities of the CFE method used for homogenization. Periodic boundary conditions are treated in Section 4.3.1, the constraints of the form $\int U = 0$ are discretized in Section 4.3.2 and an algorithm for cell problems for periodic fundamental cells is given in Section 4.3.3.

4.3.1 Periodic Boundary Conditions

Periodic boundary conditions in the FE context are treated in the standard way by identifying certain degrees of freedom. In this section we describe what these identification means in the CFE context and how it is implemented.

Let us introduce some notation for the nodes involved. A node r is called *inactive node* if, by periodicity assumption, the value of u at r is the value of u at a counterpart node and thus no DOF is associated to r . The node to which we actually associate a DOF and that DOF will be called *active counterpart node* and *active counterpart DOF*, respectively. For an active node, the terms active counterpart node and active counterpart DOF just refer to the node/DOF itself. See Figure 4.6 for an example.

This identification of inactive DOF and their active counterparts also means identifying the associated CFE basis function, implying that the support of such basis functions is disconnected within $\Lambda^\#$ (because it extends to an adjacent cell).

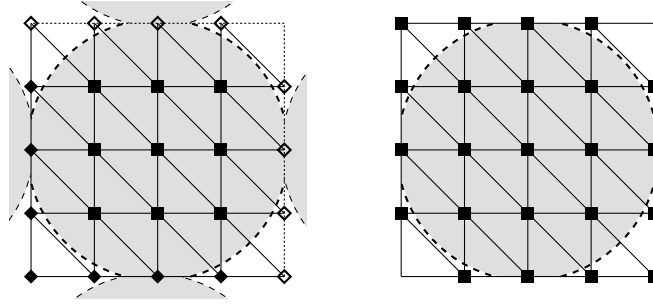


Figure 4.7. The CFE mesh for one periodic cell has the set of DOF shown as filled \blacksquare and \blacklozenge symbols on the *left*. For the same geometric object being the full domain (and not merely one fundamental cell), the set of DOF is shown on the *right*, showing that these two sets are mutually not contained.

In case of complicated domains, counterparts of inactive nodes are not necessarily DOF on the CFE mesh determined only on $\Lambda^\#$, even though periodicity implies the same intersection of the domain with opposing periodic faces of $\Lambda^\#$, see Figure 4.7 for an example. This is not surprising, however, because a CFE mesh for the periodic extension of such domains does have DOF at such positions. In summary, we observe that the sets of CFE DOF and their active counterpart DOF may be distinct in the sense that none is subset of the other, see Figure 4.7 for an example.

Periodicity in data vectors and for matrices must be taken into account when passing between the interpretation of $\Lambda^\#$ as a single cell and a periodic cell. For simplicity (and computational efficiency, albeit at the cost of additional memory requirement), we use data structures for a full discretization of the cell $\Lambda^\#$.

When dealing with vectors containing point values, the point value at an inactive node equals the value at its active counterpart node, so the vector entries corresponding to inactive nodes are ignored in the data vectors and set to zero. We call this operation *periodic restriction* (as opposed to the grid transfer restriction \mathcal{R} in multigrid methods) and denote it by \mathcal{Q} , see below for a precise definition. The inverse \mathcal{Q}^{-1} , filling those entries back in by copying them, will be referred to as *periodic extension*.

Identifying basis functions leads to larger support for those at active boundary nodes. So, when dealing with integrated quantities in data vectors or matrices (containing integrals of basis functions or integrals of their derivatives), this is translated to adding entries at inactive nodes to those at their active counterparts. We call this operation *periodic collapsing* and denote it by \mathcal{S} (as in summation).

For matrices and vectors in these periodized interpretations, we use the notation $\bullet^\#$. It will be clear from the context whether this means $\bullet^\# = \mathcal{Q}(\bullet)$ or $\bullet^\# = \mathcal{S}(\bullet)$. In the vector-valued case, the operators are applied separately to all components of a block vector or all blocks of a block matrix.

The effect of the periodic collapsing \mathcal{S} on a CFE mass matrix for a complicated domain is visualized in Figure 4.8. The visualization shows the effect of DOF removed because they are periodic copies of other nodes and DOF newly introduced as explained above. In particular, using band matrices requires introducing additional

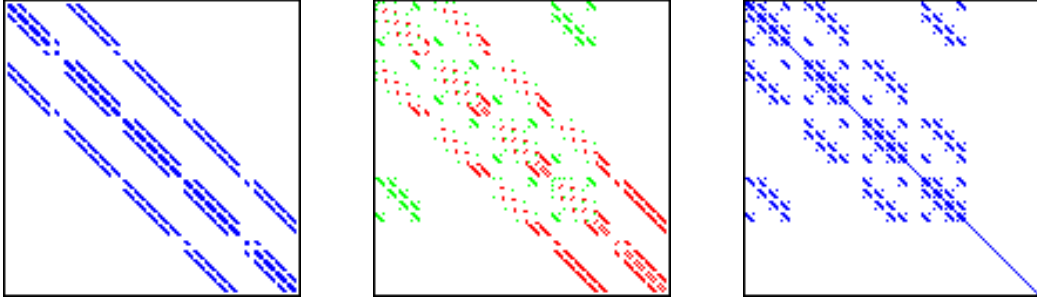


Figure 4.8. The sparsity structure of a CFE mass matrix corresponding to the 3D analogon of the situation in Figure 4.7 (an object similar to the ball in Figure 7.9) is shown before (*left*) and after (*right*) periodic collapshion and writing identity rows for non-DOF nodes. Computational resolution 5^3 implies that the matrices are of size 129×129 . In the *middle*, the difference between the two sparsity structures is shown, red pixels indicate those entries which are no longer DOF after collapshion, green pixels indicate newly introduced DOF. Identity rows for non-DOF nodes have been ignored in the ‘diff’ view in the middle.

full bands of length n^3 containing only $O(n^2)$ nonzero entries and is thus inefficient, in terms of both computational workload and memory.

Definition 4.15. Let $a(r)$ denote the active counterpart of a node r , V be a vector and M be a matrix. Then we define the periodic restriction \mathcal{Q}

$$\begin{aligned} \mathcal{Q}(V)_i &:= \begin{cases} V_i & \text{if } i \text{ is an active node} \\ 0 & \text{otherwise} \end{cases} \\ \mathcal{Q}(M)_{ij} &:= \begin{cases} M_{ij} & \text{if both } i \text{ and } j \text{ are active nodes} \\ 0 & \text{otherwise,} \end{cases} \end{aligned} \quad (4.35)$$

the periodic extension \mathcal{Q}^{-1} (only used for vectors)

$$\mathcal{Q}^{-1}(V^\#)_i := V_{a(i)}^\#, \quad (4.36)$$

and the periodic collapshion \mathcal{S}

$$\begin{aligned} \mathcal{S}(V)_i &:= \sum_{k:a(k)=i} V_k & \mathcal{S}(M)_{ij} &:= \sum_{\substack{k:a(k)=i \\ l:a(l)=j}} M_{kl} \end{aligned} \quad (4.37)$$

4.3.2 Discretization of Equality Constraints

Lemma 4.16. Constraints of the form $f U = 0$ for discretized functions U are canonically discretized as

$$\left\langle \frac{1}{\langle M\vec{1}, \vec{1} \rangle} M\vec{1}, U \right\rangle =: \langle J, U \rangle = 0 \quad (4.38)$$

where M is the CFE mass matrix and $\vec{1}$ is the all-1 vector.

Proof. This follows from

$$\int_{\Lambda^\#} U = \int_{\Lambda^\#} U \mathbb{1} = \frac{1}{\int_{\Lambda^\#} \mathbb{1}} \int_{\Lambda^\#} \mathbb{1} U. \quad (4.39)$$

where $\mathbb{1}$ is the constant-1 function. \square

This constraint is periodized via

$$M^\# = \mathcal{S}(M), \quad \vec{\mathbb{1}}^\# = \mathcal{Q}(\vec{\mathbb{1}}), \quad J^\# = \frac{M^\# \vec{\mathbb{1}}^\#}{\langle M^\# \vec{\mathbb{1}}^\#, \vec{\mathbb{1}}^\# \rangle}. \quad (4.40)$$

The factor $1/\langle M^\# \vec{\mathbb{1}}^\#, \vec{\mathbb{1}}^\# \rangle$ is non-trivial for the case of complicated domains. If $\Lambda^\#$ is simply the unit cube, this factor is 1 and J simplifies to $M\vec{\mathbb{1}}$.

Scalar Problem. The periodic and discretized form of Equation (4.3), the system of equations for determining the temperature correction profile, is obtained by using

$$L^\# = \mathcal{S}(L), \quad B^\# = -\mathcal{S}(L\bar{U}) \quad (4.41)$$

so that we obtain the system

$$\begin{aligned} L^\# \tilde{U}^\# &= B^\# \\ \text{subject to } \langle J^\#, \tilde{U}^\# \rangle &= 0 \end{aligned} \quad (4.42)$$

where the system matrix $L^\#$ is singular and has a one-dimensional kernel (eigenspace to the zero eigenvalue) corresponding to addition of constant functions. The additional condition makes the system (4.42) uniquely solvable for suitable right hand side.

Vector-Valued Problem. In the elasticity case, our constraints for the discrete displacement apply to all spatial components separately, i.e.,

$$\langle J^\#, \tilde{U}_\alpha^\# \rangle = 0 \quad \forall \alpha \in \{0, 1, 2\}. \quad (4.43)$$

In the vector-valued case, the system of equations for determining the displacement correction profile (4.9) is periodized using

$$E^\# = \mathcal{S}(E) \quad B^\# = \mathcal{S}(E\bar{U}) \quad (4.44)$$

so that we obtain

$$\begin{aligned} \begin{pmatrix} E_{00}^\# & E_{01}^\# & E_{02}^\# \\ E_{10}^\# & E_{11}^\# & E_{12}^\# \\ E_{20}^\# & E_{21}^\# & E_{22}^\# \end{pmatrix} \begin{pmatrix} \tilde{U}_0^\# \\ \tilde{U}_1^\# \\ \tilde{U}_2^\# \end{pmatrix} &= \begin{pmatrix} B_0^\# \\ B_1^\# \\ B_2^\# \end{pmatrix} \\ \text{subject to } \left\langle \begin{pmatrix} J^\# \\ 0 \\ 0 \end{pmatrix}, \begin{pmatrix} \tilde{U}_0^\# \\ \tilde{U}_1^\# \\ \tilde{U}_2^\# \end{pmatrix} \right\rangle &= \left\langle \begin{pmatrix} 0 \\ J^\# \\ 0 \end{pmatrix}, \begin{pmatrix} \tilde{U}_0^\# \\ \tilde{U}_1^\# \\ \tilde{U}_2^\# \end{pmatrix} \right\rangle = \left\langle \begin{pmatrix} 0 \\ 0 \\ J^\# \end{pmatrix}, \begin{pmatrix} \tilde{U}_0^\# \\ \tilde{U}_1^\# \\ \tilde{U}_2^\# \end{pmatrix} \right\rangle = 0. \end{aligned} \quad (4.45)$$

Here, the system block matrix $E^\#$ is singular with three-dimensional kernel corresponding to addition of constant displacements (shifts) in the three space directions.

Subspace Projection. Let $s := \{u \mid \int u = 0\}$ be the subspace of all continuous functions satisfying the average-zero constraint. The projection onto s is given by $\Pi_s u = u - (\int u) \mathbb{1}$ for any continuous u .

Remark 4.17. Π_s is indeed a projection because the idempotency $\Pi_s \circ \Pi_s = \Pi_s$ is satisfied.

In discrete form, we consider the subspace $S := \text{span} \{J\}^\perp$ using J defined in (4.38) and obtain the projection

$$\Pi_S(U) = U - \langle J, U \rangle \vec{\mathbb{1}}. \quad (4.46)$$

or

$$\Pi_S(U^\#) = U^\# - \langle J^\#, U^\# \rangle \vec{\mathbb{1}}^\#. \quad (4.47)$$

in periodized form. Again, idempotency is clear, so Π_S is indeed a projection. In the vector-valued case, each spatial component is projected separately.

4.3.3 Algorithms for Cell Problems

Let us now summarize the steps necessary for treating one instance (given \bar{u}) of the cell problems, both for periodic and Dirichlet boundary conditions.

Cell Problems for Periodic Cells. For the scalar model problem, the procedure for determining an effective thermal diffusivity tensor is summarized in Algorithm 4.9.

In the vector-valued case, the procedures in Algorithm 4.10 are almost the same, except we now use block matrices M and E (instead of L), block vectors, and a different CFE construction.

Dirichlet Boundary Conditions/Statistically Periodic Cells. In case of statistically periodic specimens, the macroscopic temperature or displacement profile was enforced by corresponding nonzero Dirichlet boundary conditions. These are transformed to zero Dirichlet boundary conditions and treated in a standard manner as described in Section 3.5.1.

procedure DETERMINEEFFECTIVEHEATFLUX(macroscopic temperature profile \bar{U})

set up $\bar{\mathbf{1}}$ and CFE matrices M, L as usual ▷ depends on $\Lambda^\#$ and microscopic tensor a

$B^\# \leftarrow -\mathcal{S}(L\bar{U})$ ▷ compute the right hand side

$M^\# \leftarrow \mathcal{S}(M)$ ▷ periodize matrices ...

$L^\# \leftarrow \mathcal{S}(L)$

$\bar{\mathbf{1}}^\# \leftarrow \mathcal{Q}(\bar{\mathbf{1}})$ ▷ ... and the all-1 vector

$J^\# \leftarrow M^\# \bar{\mathbf{1}}^\# / \langle M^\# \bar{\mathbf{1}}^\#, \bar{\mathbf{1}}^\# \rangle$ ▷ compute the constraint vector

solve the system (4.42), $L^\# \tilde{U}^\# = B^\#$ subject to $\langle J^\#, \tilde{U}^\# \rangle = 0$, for $\tilde{U}^\#$

$U \leftarrow \mathcal{Q}^{-1}(\tilde{U}^\#) + \bar{U}$ ▷ periodically extend the solution and add macroscopic part

$\bar{Q} \leftarrow \int a \nabla U$ ▷ compute effective heat flux

return \bar{Q}

procedure DETERMINEEFFECTIVETHERMALDIFFUSIVITYTENSOR

for $i \in \{0, 1, 2\}$ **do**

set up vector \bar{U}^i as usual, discretizing \bar{u}^i with $\nabla \bar{u}^i = e_i$

$\bar{Q}^i \leftarrow$ DETERMINEEFFECTIVEHEATFLUX (\bar{U}^i)

$\bar{a}_{ji} \leftarrow \bar{Q}_j^i$ ▷ \bar{Q}^i becomes i^{th} column of a

return effective tensor \bar{a}

Algorithm 4.9. Cell Problems for the scalar model problem

procedure DETERMINEEFFECTIVESTRESS(macroscopic displacement profile \bar{U})

set up $\bar{\mathbf{1}}_k$ and CFE block matrices M, E ▷ depends on $\Lambda^\#$ and microscopic tensor C

$B^\# \leftarrow -\mathcal{S}(E\bar{U})$ ▷ compute the right hand side

$M^\# \leftarrow \mathcal{S}(M)$ ▷ periodize matrices ...

$E^\# \leftarrow \mathcal{S}(E)$

$\bar{\mathbf{1}}_k^\# \leftarrow \mathcal{Q}(\bar{\mathbf{1}}_k)$ ▷ ... and the all-1-block vectors

$J_k^\# \leftarrow M^\# \bar{\mathbf{1}}_k^\# / \langle M^\# \bar{\mathbf{1}}_k^\#, \bar{\mathbf{1}}_k^\# \rangle$ ▷ compute the constraint vectors

solve the system (4.45), $E^\# \tilde{U}^\# = B^\#$ subject to $\langle J_k^\#, \tilde{U}^\# \rangle = 0 \forall k$, for $\tilde{U}^\#$

$U \leftarrow \mathcal{Q}^{-1}(\tilde{U}^\#) + \bar{U}$ ▷ periodically extend the solution and add macroscopic part

$\bar{\sigma} \leftarrow \int C \epsilon[U]$ ▷ compute effective stress

return $\bar{\sigma}$

procedure DETERMINEEFFECTIVEELASTICITYTENSOR

for $i \leq j \in \{0, 1, 2\}$ **do**

set up block vector \bar{U}^{ij} as usual, discretizing \bar{u}^{ij} with $\epsilon[\bar{u}^{ij}] = e_{ij}$

$\bar{\sigma}^{ij} \leftarrow$ DETERMINEEFFECTIVESTRESS (\bar{U}^{ij})

$\bar{C}_{mnij} \leftarrow \bar{\sigma}_{mn}^{ij}$

fill whole \bar{C} by tensor symmetry

return effective tensor \bar{C}

Algorithm 4.10. Cell Problems for the vector-valued model problem

4.4 Solvers for the Constrained Systems

Let us now discuss how to solve the ‘constrained systems of equations’ (4.42) and (4.45). For simplicity of notation, let us omit the periodicity throughout this section and consider the generic problem

$$\begin{aligned} AU &= B \\ \text{subject to } \langle J_i, U \rangle &= 0 \quad \forall i \end{aligned} \tag{4.48}$$

with A standing for L or E . Clearly, this system can only be solved if the right hand side B lies in the image of the A .

This system can be solved using a projecting (preconditioned) conjugate gradient solver where the The projection is performed according to Equation (4.47). The conjugate gradient solver [164] is a Krylov space method² [25] and thus has the desired property that, starting with initial guess in the subspace $S = \text{span}\{J\}^\perp$, all iterates lie in this subspace. As we typically start with zero as the initial guess, the condition is trivially satisfied. However, this property is only true in exact arithmetic, but not using floating point numbers of finite precision.

To prevent the numerical solution from ‘drifting’ away from the desired subspace S , we thus project the iterates back to S if the constraints are violated by more than a given threshold (due to finite precision, we cannot expect it to be satisfied exactly).

This projection makes sense because it does not change the residual (which would clearly interfere with CG convergence).

Lemma 4.18. The projection Π_S defined in Equation (4.46) does not change the residual of the systems $LU = B$ or $EU = B$.

Proof. In the scalar case,

$$\begin{aligned} L(\Pi_S U) - B &= L(U - \langle J, U \rangle \vec{1}) - B \\ &= LU - \langle J, U \rangle \underbrace{L\vec{1}}_{=0} - B = LU - B \end{aligned} \tag{4.49}$$

and in the vector-valued case

$$\begin{aligned} E(\Pi_S U) - B &= E(U - \sum_{\alpha \in \{0,1,2\}} \langle J_\alpha, U \rangle \vec{1}_\alpha) - B \\ &= EU - \sum_{\alpha \in \{0,1,2\}} \langle J_\alpha, U \rangle \underbrace{E\vec{1}_\alpha}_{=0} - B = EU - B \end{aligned} \tag{4.50}$$

where $\vec{1}_\alpha$ is the block vector that is all-1 in the block for space direction α . □

Let us point out that this projection scheme is compatible with preconditioning because this only changes the iterates but not the actual system or the residual computation. The projection can also be combined with our CFE multigrid method, this is discussed in Section 5.3.

²Named after the Russian naval engineer, applied mathematician and memoirist Алексей Николаевич Крылов (Alexei Nikolaevich Krylov), * August 15, 1863 in Simbirsk (today Ulyanovsk), † October 26, 1945 in St. Petersburg [262].

4.5 Orthotropy Directions

Once an effective elasticity tensor for a given microstructure has been determined, an interesting question is whether it corresponds to an orthotropic material. If it does, the axes of orthotropy will typically not be aligned with the coordinate axes, so they also need to be determined. As for trabecular bone, only the craniocaudal axis is rather easy to preserve throughout our sampling and scanning process if the cylindrical specimens are aligned with this axis.

A straightforward idea for checking orthotropy [344, 392] is to determine the rotation $R \in \text{SO}(3)$ that ‘best rotates the effective tensor to an orthotropic one’ in terms of an orthotropy violation measure to be defined below. Such a method also provides a mechanism to check whether the orthotropy assumption was justified: after optimal rotation, the orthotropy violation should be small.

To simplify notation, we will use no bars atop a or C throughout this section even though the methods described here will typically be applied to homogenized tensors.

4.5.1 Rotation of Tensors

Rotations in $Q \in \text{SO}(3)$ can be described as

$$\begin{aligned} Q &= Q(\alpha, \beta, \gamma) = Q_{xy}(\alpha)Q_{xz}(\beta)Q_{yz}(\gamma) \\ &= \begin{pmatrix} \cos(\alpha) & -\sin(\alpha) & 0 \\ \sin(\alpha) & \cos(\alpha) & 0 \\ 0 & 0 & 1 \end{pmatrix} \begin{pmatrix} \cos(\beta) & 0 & -\sin(\beta) \\ 0 & 1 & 0 \\ \sin(\beta) & 0 & \cos(\beta) \end{pmatrix} \begin{pmatrix} 1 & 0 & 0 \\ 0 & \cos(\gamma) & -\sin(\gamma) \\ 0 & \sin(\gamma) & \cos(\gamma) \end{pmatrix} \end{aligned} \quad (4.51)$$

with $\alpha, \beta, \gamma \in [-\pi/4, \pi/4)$ being the rotations in the xy , xz , and yz plane, respectively. These angles are also referred to *roll*, *pitch*, and *yaw angles* and commonly used in computer graphics and aviation, see, e.g. [194]. Note that rotations do not commute, and that the inverse rotation is given by

$$Q_{\text{back}}(\alpha, \beta, \gamma) = Q_{yz}(-\gamma)Q_{xz}(-\beta)Q_{xy}(-\alpha). \quad (4.52)$$

Note moreover that our bounds are chosen such that ambiguities due to switching axes by 90° rotations are ruled out, as we have no preference which of the axes of orthotropy should correspond to which coordinate axis.

Suppose we have a material with orthotropic thermal diffusivity tensor a for which the axes of orthotropy are the coordinate axes rotated by some rotation matrix Q , see Figure 4.11.

Lemma 4.19. Let $Q \in \text{SO}(3)$ be the rotation from an (unknown) aligned configuration to the actual configuration, and let \bullet^* denote quantities in the aligned configuration. Then the thermal diffusivity tensor is rotated according to

$$a_{mn} = Q_{mi}Q_{nj}a_{ij}^*. \quad (4.53)$$

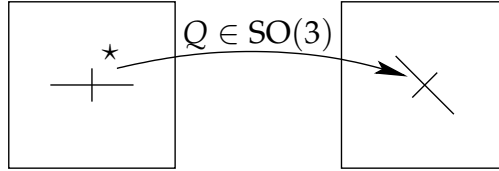


Figure 4.11. Axes of orthotropy in the actual configuration (*right*) are not aligned with the coordinate axes but rotated from a reference configuration (*left*) by some rotation Q . Quantities in the aligned configuration are denoted by \star .

Proof. With gradients written as column vectors, we obtain

$$x^\star = Q^T x, \quad u^\star(x^\star) = u(x), \quad \nabla u^\star(x^\star) = Q^T \nabla u(x), \quad (4.54)$$

so that in the quadratic form assigned to the diffusion problem 2.1 we obtain

$$\begin{aligned} \langle a^\star \nabla u^\star, \nabla u^\star \rangle &= \langle a^\star Q^T \nabla u, Q^T \nabla u \rangle \\ &= \langle Q a^\star Q^T \nabla u, \nabla u \rangle \end{aligned} \quad (4.55)$$

so that $a = Q a^\star Q^T$. This can be written in components as $a_{mn} = Q_{mi} a_{ij}^\star Q_{jn}^T$ from which (4.53) follows. \square

Lemma 4.20. Let $Q \in \text{SO}(3)$ be the rotation as in the previous lemma. Then the elasticity tensor is rotated according to

$$C_{mnpq} = Q_{mi} Q_{nj} Q_{pk} Q_{ql} C_{ijkl}^\star. \quad (4.56)$$

Proof. In the linear elasticity case, also the displacement u needs to be rotated and its component-wise gradients are interpreted as rows of ∇u , hence we obtain

$$\begin{aligned} u(x) &= Q u^\star(x^\star), \quad \nabla u(x) = Q \nabla u^\star(x^\star) Q^T \\ \Rightarrow \epsilon[u] &= \frac{1}{2} (\nabla u + \nabla u^T) = \frac{1}{2} \left(Q \nabla u^\star(x^\star) Q^T + (Q \nabla u^\star(x^\star) Q^T)^T \right) \\ &= \frac{1}{2} \left(Q \nabla u^\star(x^\star) Q^T + Q^{TT} \nabla u^{\star T}(x^\star) Q^T \right) = Q \epsilon[u^\star] Q^T. \end{aligned} \quad (4.57)$$

Hence we obtain in the quadratic form assigned to the elasticity problem 2.2

$$\begin{aligned} C^\star \epsilon[u^\star] : \epsilon[u^\star] &= C^\star Q^T \epsilon[u] Q : Q^T \epsilon[u] Q \\ &= C_{ijkl}^\star Q_{kp}^T \epsilon[u]_{pq} Q_{ql} Q_{im}^T \epsilon[u]_{mn} Q_{nj} \\ &= \left(Q_{mi} Q_{nj} Q_{pk} Q_{ql} C_{ijkl}^\star \right) \epsilon[u]_{pq} \epsilon[u]_{mn} \\ &= C \epsilon[u] : \epsilon[u] \end{aligned} \quad (4.58)$$

with C as in Equation (4.56). \square

4.5.2 Visualization of Elasticity Tensors

A mere listing of macroscopic elasticity tensors is not particularly intuitive, so we use a visualization of such tensors that is common in biomechanics [71, 161] showing them as deformed and colored spheres \mathcal{K}_C . We briefly explain this visualization here and show one example in Figure 4.12.

Deformation. Let n be any unit vector in \mathbb{R}^3 (corresponding to a point on the unit sphere). The sphere is deformed according to compressive stiffness in the respective direction n . For this purpose, compute

$$\begin{aligned} N &= n \otimes n & \text{in components: } N_{ij} &= n_i n_j \\ S &= CN & S_{ij} &= C_{ijkl} N_{kl} \\ \sigma &= N : S & \sigma &= N_{ij} S_{ij} \end{aligned} \tag{4.59}$$

and finally draw the shape $\mathcal{K}_C = \{\sigma(n) \mid \|n\| = 1\}$.

Color. Moreover we compute the bulk modulus $\text{tr } S = \sum_i S_{ii}$ and color the shape \mathcal{K}_C with the resulting values from minimal to maximal value an HSV (hue, saturation, value) color map.

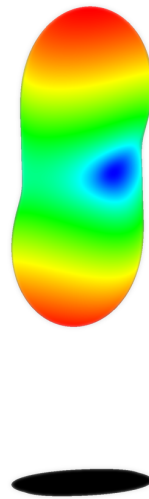


Figure 4.12. Example for the visualization of an elasticity tensor C as a deformed and colored sphere \mathcal{K}_C . The shadow underneath is meant to improve the 3D visual impression.

4.5.3 Determining Orthotropy Directions

Recall Voigt's notation for elasticity tensors (2.10)

$$\begin{bmatrix} \sigma_{xx} \\ \sigma_{yy} \\ \sigma_{zz} \\ \sigma_{yz} \\ \sigma_{xz} \\ \sigma_{xy} \end{bmatrix} = \begin{bmatrix} C_{00} & C_{01} & C_{02} & C_{03} & C_{04} & C_{05} \\ C_{10} & C_{11} & C_{12} & C_{13} & C_{14} & C_{15} \\ C_{20} & C_{21} & C_{22} & C_{23} & C_{24} & C_{25} \\ C_{30} & C_{31} & C_{32} & C_{33} & C_{34} & C_{35} \\ C_{40} & C_{41} & C_{42} & C_{43} & C_{44} & C_{45} \\ C_{50} & C_{51} & C_{52} & C_{53} & C_{54} & C_{55} \end{bmatrix} \begin{bmatrix} \epsilon_{xx} \\ \epsilon_{yy} \\ \epsilon_{zz} \\ 2\epsilon_{yz} \\ 2\epsilon_{xz} \\ 2\epsilon_{xy} \end{bmatrix}. \quad (4.60)$$

We will now switch back and forth between standard tensor notation with four indices and Voigt notation with two indices.

For an orthotropic material whose axes of orthotropy coincide with the coordinate axes, the upper right 3×3 (and, due to symmetry, also the lower left 3×3) block of a is zero and the lower right 3×3 block is diagonal. Symmetry holds independent of orthotropy. A lack of orthotropy can be quantified by

$$F(C) = \frac{\|R_a(C)\|_{\mathbb{F}}^2}{\|R_b(C)\|_{\mathbb{F}}^2} = \frac{2 \sum_{i=0}^2 \sum_{j=3}^5 C_{ij}^2 + 2 \sum_{i=3}^5 \sum_{j=0}^2 C_{ij}^2 + 4 \sum_{i,j=3,i \neq j}^5 C_{ij}^2}{1 \sum_{i,j=0}^5 C_{ij}^2 + 4 \sum_{i=j=3}^5 C_{ij}^2} \quad (4.61)$$

where the function F differs from the one proposed in [344, Equation (4)] in the weighting factors 2 and 4 (the authors of [344] use 1 everywhere) which reflects that entries in the Voigt tensor represent up to four entries of the full fourth order tensor. R_a is the restriction to the entries not present in an orthotropic tensor whereas R_b is the restriction to those present (upper left block and diagonal of lower right block). Small $F(C)$, which is clearly bounded from below by 0, thus corresponds to small undesired entries relative to the desired entries. Then consider the following optimization problem.

Problem 4.21. Determine an optimal rotation minimizing

$$G_C(\alpha, \beta, \gamma) = F(Q_{mi}Q_{nj}Q_{ok}Q_{pl}C_{ijkl}) \quad (4.62)$$

over the admissible set $A := [-\pi/4, \pi/4]^3$ where Q is the matrix $Q_{\text{back}}(\alpha, \beta, \gamma)$.

The objective function G is not convex and may have multiple local minima and also multiple global minimizers. However, G is not highly oscillatory and depends on only three variables, so an inelegant and inefficient minimization method by interval nesting is sufficient: We discretize A with finite angular resolution, evaluate G_C at every point to determine the discrete minimizer and proceed by discretizing a smaller interval there until a fixed accuracy in the angles is attained. As this optimization procedure is typically part of the postprocessing and compared to the main simulation, the workload is not critical.

If the minimal value is sufficiently small so that the rotated tensor can be considered orthotropic, we can use Equation (2.19) to determine compressive and shear moduli, and Poisson's ratios.

5 Multigrid Solvers for Composite Finite Elements

WHILE THE SYSTEMS OF EQUATIONS resulting from CFE discretizations have a nice sparsity structure, the performance of standard iterative solvers still suffers from bad condition numbers (cf. Section 7.1.4) or other effects. The major advantage of the underlying Cartesian grids is that they contain canonical coarse scales, thus permitting the construction of ‘geometric’ multigrid solvers.

In this chapter we first discuss the general framework of multigrid solvers based on geometric coarsening in Section 5.1. Section 5.2 deals with the coarsening procedure for complicated domains. The performance of the CFE multigrid method will later be compared to other solvers in Section 7.1.5. Certain geometric situations severely affect the computational efficiency, which will later be discussed in Section 8.2. In case of discontinuous coefficients (Section 5.4), the multigrid construction cannot be extended in a straightforward manner. Like the CFE construction for complicated domains, the multigrid method is originally the one in [216] and it has been published in [217, 282]. The multigrid method for homogenization applications has been published in [311].

5.1 Geometric Coarsening

Let us briefly recall the basic ideas behind multigrid methods in general. The solution of a system of equations $Ax = b$ resulting from a discretization procedure can be viewed as the iterative reduction of the (Euclidean) norm of the *residual* $r = Ax - b$. Iterative methods such as the Jacobi method¹ [180] or the Gauß–Seidel method² (cf. [387, 315]) are capable of reducing high-frequency components of the residual within a few iterations, even though general convergence is typically slow. Frequency is relative to the resolution of the discretization, so low frequencies for the original problem can be treated efficiently on a coarsened version of the problem.

5.1.1 Basic Multigrid Scheme

The basic multigrid cycle, first stated in this form in [59], is of the form shown in Algorithm 5.1. The *solve* step \sphericalangle can be replaced by multiple recursive calls of the multigrid method on the next coarsest level. In case of one or two recursive calls, the cycles are denoted by *V cycles* and *W cycles*, respectively. V cycles are typically faster in practice whereas certain convergence results are only known for W cycles.

¹Named after the German Mathematician Carl Gustav Jacob Jacobi, * December 10, 1804 in Potsdam, † February 18, 1851 in Berlin [1].

²Named after German mathematicians Johann Carl Friedrich Gauß, * April 30, 1777 in Braunschweig, † February 23, 1855 in Göttingen [1] and Philipp Ludwig von Seidel, * October 24, 1821 in Zweibrücken, † August 13, 1896 in München [262].

```

procedure MULTIGRIDSOLVE(system matrix  $A$ , right hand side  $b$ )
  if  $A$  is on explicit level then
    apply explicit solver:  $x \leftarrow A^{-1}b$ 
  else
     $k \leftarrow 0, x^0 = x$ 
    while  $\|b - Ax^k\| > \text{threshold}$  do
       $x^{k+1/3} \leftarrow \underline{\Delta}^{v_{\text{pre}}}(x^k)$  ▷ perform  $v_{\text{pre}}$  Gauß-Seidel iterations (pre-smoothing)
       $r \leftarrow b - Ax^{k+1/3}$  ▷ compute residual
       $\tilde{r} \leftarrow \mathcal{R}(r)$  ▷ restrict residual
       $\tilde{e} \leftarrow \underline{\square}(\tilde{A}, \tilde{e}) = \text{MULTIGRIDSOLVE}(\tilde{A}, \tilde{e})$  ▷ solve coarse problem ( $\tilde{A} = \mathcal{R}A\mathcal{P}$ )
       $e \leftarrow \mathcal{P}(\tilde{e})$  ▷ prolongate
       $x^{k+2/3} \leftarrow x^{k+1/3} + e$  ▷ coarse grid correction
       $x^{k+1} \leftarrow \underline{\Delta}^{v_{\text{post}}}(x^{k+2/3})$  ▷ perform  $v_{\text{post}}$  Gauß-Seidel iterations (post-smoothing)
    return Solution  $x$ 

```

Algorithm 5.1. Basic Multigrid Algorithm. In the CFE context, pre-smoothing $\underline{\Delta}$ and post-smoothing $\underline{\Delta}$ will be performed by Gauß-Seidel iterations whereas restriction \mathcal{R} and prolongation \mathcal{P} will be developed in this section.

The ‘explicit solver’ in this context can be a direct solver (if the coarsest problem is sufficiently small) or an iterative (e.g., preconditioned conjugate gradient) solver. We will use the notation

$$V_l(v_{\text{pre}}, v_{\text{post}}) \text{ cycles} \tag{5.1}$$

for a multigrid method with coarsening up to level l , v_{pre} pre- and v_{post} post-smoothing steps in a V cycle.

Coarsening Schemes. The typical choice in FE methods is a geometric coarsening procedure with \mathcal{R} being weighted averaging and for $\mathcal{P} = \mathcal{R}^T$ being its transpose (and also an interpolation), see Section 5.2.1. The coarsened system matrix is then obtained as $\tilde{A} = \mathcal{R}A\mathcal{P}$ where the grid-transfer operators are identified with their matrix representation. The coarsening scheme is chosen such that coarsened basis functions resemble those FE basis functions one would obtain for the coarse discretization, thus \tilde{A} resembling the coarse discretization of the problem. Our CFE multigrid methods are based on finding such an appropriate coarsening procedure.

Algebraic Multigrid. Algebraic multigrid (AMG) methods already mentioned in the introduction (Section 1.6) do not consider any underlying mesh geometry for a given system matrix. Instead, they mimic this coarsening procedure purely based on the matrix, interpreting the sparsity structure of the matrix as a graph with matrix entries assigned to the respective edges and replacing the notion of geometric neighborhood by ‘strong’ connectivity of the graph.

For comparison of our CFE multigrid methods to established methods, we will use the boomerAMG [163, 116] (part of the hypre software library [82, 117, 115]) as a black box method³.

5.1.2 Computational Costs

The advantage of multigrid methods compared to other iterative solvers lies in their efficiency. If we have an estimate that, in each iteration, the error norm decreases by a factor $\zeta < 1$, $\|e_{k+1}\| \leq \zeta \|e_k\|$, then the iterative process is guaranteed to reduce the error by a given tolerance ϵ within $O(\log(1/\epsilon))$ iterations. The total computational cost of the solution is determined by the number of iterations times the cost per iteration.

Let us briefly compare the computational costs for the conjugate gradient (CG) method [164] as a ‘classical’ iterative solver and for multigrid methods. We can assume only a limited number b of entries per row in the matrix and let n be the number of unknowns. For CG, each iteration has complexity $O(bn)$ (dominated by one matrix-vector multiplication and a fixed number of vector operations), the constant in the number of iterations can be bounded via the convergence rate $\frac{\sqrt{\kappa}-1}{\sqrt{\kappa}+1}$ for κ being the condition number of the system matrix. Convergence depends on the whole spectrum (distribution of eigenvalues of the matrix) and preconditioning techniques (see, e.g., [154]) can reduce κ and thus improve convergence, but in practice the number of CG iterations tends to be large and grows with problem size. A single multigrid cycle has the same order of complexity, but a larger constant due to multiple smoother steps (typically involving every matrix entry), prolongation and restriction (involving each vector entry on the fine grid multiple times, bounded by the number of neighbors in the coarsening scheme) and operations on the coarse problem (with exponentially less grid points). The convergence rate of the multigrid cycles, however, is not affected directly by large condition numbers and tends to be small in practice (even though there are situations where both the condition number is large and multigrid performance is poor). Roughly speaking: the better the correction obtained from the coarse problem in each step, the faster the convergence.

³This notion is nicely explained in [93]: ‘We refer to this method as black box multigrid not because—as some would have it—multigrid is black magic, but because the code which implements the method acts as a black box for the user.’

5.2 Multigrid Coarsening for Complicated Domains

This section describes how standard multigrid coarsening for affine FE on the regular tetrahedral mesh \mathcal{G}^{\boxtimes} is adapted to a coarsening scheme for CFE for complicated domains. The method is based on [126, 324].

5.2.1 Notation for Cartesian and Regular Grids

The geometric structure of the Cartesian (regular hexahedral) grids \mathcal{G}^{\square} permits a natural octree structure if we assume that the number of nodes in each space direction is $2^L + 1$ for some nonnegative integer *grid depth* L . The same is true for the regular tetrahedral grids \mathcal{G}^{\boxtimes} . Let $(\mathcal{G}^{\square l})_{l=0,\dots,L}, (\mathcal{G}^{\boxtimes l})_{l=0,\dots,L}$ be these grids and $(\mathcal{N}^{\square l} = \mathcal{N}^{\boxtimes l})_{l=0,\dots,L}$ the corresponding node sets.

In a geometric interpretation, we have the obvious inclusion of $\mathcal{N}^{\square l-1}$ in $\mathcal{N}^{\square l}$. If the nodes are indexed in the canonical way $(0, \dots, 2^l$ in each component), a node $n \in \mathcal{N}^{\square l}$ is present on the next coarsest grid if and only if all its components have an even index. Such nodes will also be referred to as *even nodes*. This means that $n \in \mathcal{N}^{\square l-1}$ is geometrically the node $2n \in \mathcal{N}^{\square l}$. As our coarsening procedure is purely discrete, we prefer referring to nodes by their indices rather than geometric location.

Definition 5.1. For a node $n \in \mathcal{N}^{\square l}$, let

$$\mathbb{S}(n) := \{v \in \mathcal{N}^{\square l} \mid v \text{ is a neighbor of } n \text{ considered for coarsening}\}. \quad (5.2)$$

It depends on the CFE scheme which nodes we will consider here. We can then define ‘descendant’ (child) and ‘parent’ relations between nodes $c \in \mathcal{N}^{\square l-1}$ and $f \in \mathcal{N}^{\square l}$

$$\begin{aligned} c \in \mathbb{P}(f) &: \Leftrightarrow f \in \mathbb{S}(2c) \\ f \in \mathbb{D}(c) &: \Leftrightarrow c \in \mathbb{P}(f) \end{aligned} \quad (5.3)$$

which permits interpreting $\mathbb{S}(n)$ as a ‘sibling’ relation.

Consider coarsening weights $\mathfrak{w}_{f,c}$ for $f \in \mathcal{N}^{\square l}$ and $c \in \mathcal{N}^{\square l-1}$ to be determined in such a way that

$$\psi_{\text{coarsened } c}^{\text{CFE}} = \sum_{f \in \mathbb{D}(c)} \mathfrak{w}_{f,c} \psi_{\text{fine } f}^{\text{CFE}} \quad (5.4)$$

is an appropriate approximation of $\psi_{\text{coarse } c}^{\text{CFE}}$. Weights $\mathfrak{w}_{g,c}$ for $g \notin \mathbb{D}(c)$ are set to zero. Then restriction and prolongation operators are defined in terms of these weights. They are only used in a discrete setting, so we define them by their matrix representation

$$\begin{aligned} \mathcal{P}^{l-1 \rightarrow l} &= \mathcal{P} \in \mathbb{R}^{\#\mathcal{N}^{\square l} \times \#\mathcal{N}^{\square l-1}}, \quad \mathcal{P}_{f,c} = \mathfrak{w}_{f,c}, \\ \mathcal{R}^{l \rightarrow l-1} &= \mathcal{R} \in \mathbb{R}^{\#\mathcal{N}^{\square l-1} \times \#\mathcal{N}^{\square l}}, \quad \mathcal{R}_{c,f} = \mathfrak{w}_{f,c}. \end{aligned} \quad (5.5)$$

If A^l is the FE system matrix on grid level l , the coarsened version is obtained by *Galerkin coarsening*⁴ [153] as

$$A^{l-1} = \mathcal{R}^{l \rightarrow l-1} A^l \mathcal{P}^{l-1 \rightarrow l}. \quad (5.6)$$

Remark 5.2. For exact coarsening of basis functions in Equation (5.4) and FE stiffness matrices, this implies the following formula for the entries.

$$\begin{aligned} L_{cd}^{l-1} &= \int_{\Omega} \langle \nabla \psi_{\text{coarse } c}^{\text{CFE}}, \nabla \psi_{\text{coarse } d}^{\text{CFE}} \rangle = \int_{\Omega} \langle \nabla \psi_{\text{coarsened } c}^{\text{CFE}}, \nabla \psi_{\text{coarsened } d}^{\text{CFE}} \rangle \\ &= \int_{\Omega} \langle \nabla \sum_{f \in \mathbb{D}(c)} \mathfrak{w}_{f,c} \psi_{\text{fine } f}^{\text{CFE}}, \nabla \sum_{g \in \mathbb{D}(d)} \mathfrak{w}_{g,d} \psi_{\text{fine } g}^{\text{CFE}} \rangle \\ &= \sum_{f \in \mathbb{D}(c)} \sum_{g \in \mathbb{D}(d)} \mathfrak{w}_{f,c} \int_{\Omega} \langle \nabla \psi_{\text{fine } f}^{\text{CFE}}, \nabla \psi_{\text{fine } g}^{\text{CFE}} \rangle \mathfrak{w}_{g,d} \\ &= \sum_{f,g} \mathcal{R}_{cf}^{l \rightarrow l-1} L_{fg}^l \mathcal{P}_{gd}^{l-1 \rightarrow l} \end{aligned} \quad (5.7)$$

Similar formulas hold for the mass matrix M and the elasticity block matrix E where each block is treated separately.

Notice that Equation (5.7) is based on a similar idea as Equation (3.39) and (3.40): coarse (CFE) basis functions are written as a linear combination of fine (virtual) basis functions. The difference, however, is that the fine grid here is used as a computational grid whereas the virtual mesh in the CFE construction is never used globally for computations.

5.2.2 Coarsening Neighborhoods and Coarsening Weights

Node neighborhoods for coarsening in the complicated domain case $\mathbb{S}(n)$ are simply the standard neighborhoods defined by \mathcal{G}^{\boxtimes} . Given $\mathcal{N}^{\text{DOF } l}$, the set of nodes with assigned DOF on grid level l , $\mathcal{N}^{\text{DOF } l-1}$ is defined as

$$\mathcal{N}^{\text{DOF } l-1} := \left\{ c \in \mathcal{N}^{\square l-1} \mid \mathbb{S}(2c) \cap \mathcal{N}^{\text{DOF } l} \neq \emptyset \right\} \quad (5.8)$$

which means that a coarse node c of $\mathcal{G}^{\boxtimes l-1}$ has a DOF if the corresponding fine node $2c$ of $\mathcal{G}^{\boxtimes l}$ or any other of c 's descendants has a DOF.

In the construction of CFE basis functions ψ^{CFE} for complicated domains, we have seen the peculiarity that we have one layer of DOF outside the actual object. This now also occurs during the coarsening process, and since 'layer' is relative to the current grid (spacing), the coarsening process will introduce coarse DOF at geometric locations where there are no fine DOF.

⁴Named after the Russian mathematician and engineer Борис Григорьевич Галёркин (Boris Grigoryevich Galerkin), * March 4, 1871 in Polozk, Belarus, † July 12, 1945 in Moscow [262].

Definition 5.3. Coarsening weights for $f \in \mathcal{N}^{\boxtimes l}, c \in \mathcal{N}^{\boxtimes l-1}$ are defined to be

$$\mathfrak{w}_{f,c} = \begin{cases} 1 & \text{if } c \in \mathcal{N}^{\text{DOF}^{l-1}}, f \in \mathcal{N}^{\text{DOF}^l} \wedge f = 2c, \\ 1/2 & \text{if } c \in \mathcal{N}^{\text{DOF}^{l-1}}, f \in \mathcal{N}^{\text{DOF}^l} \wedge \mathbb{S}(2c) \ni f \neq 2c, \\ 0 & \text{otherwise.} \end{cases} \quad (5.9)$$

Let us point out that, far from the interface, these coarsening weights are those one uses for piecewise affine FE on \mathcal{G}^{\boxtimes} , and that (unlike for multilinear FE) the value 1/2 is independent of space dimension. Figure 5.2 illustrates this coarsening process for basis functions in 1D.

In Section 3.2, CFE basis functions were constructed from standard basis functions on the virtual mesh \mathcal{G}^{Δ} . This could be viewed as a 0th coarsening step (but should not be interpreted in this manner because \mathcal{G}^{Δ} is no computational mesh), and the ψ^{CFE} inherit certain properties from the ψ^{Δ} . A similar inheritance of properties also holds for the multigrid coarsening process, where coarsened basis functions are obtained as a linear combination of fine basis functions.

Proposition 5.4. The coarsened CFE basis functions for complicated domains satisfy the following properties:

1. They are piecewise affine on Ω_{-}^{Δ} , the piecewise tetrahedral approximation of Ω_{-} on the finest level.
2. They form a partition of unity.
3. They are nodal.
4. Far from the interface, standard affine FE coarsening results in standard coarse basis functions.
5. Near the interface, we obtain modified coarsened basis functions with possibly smaller support than the standard ones.
6. The neighborhood structure of nodes is the same as before (contained in the 15 standard neighbors of affine FE on \mathcal{G}^{\boxtimes}).

Proof. ad 1. This follows immediately from the fact that coarsening is achieved by linear combination of fine basis functions.

ad 2. The partition of unity property is preserved because $\sum_{c \in \mathbb{P}(f)} \mathfrak{w}_{f,c} = 1$ for all fine nodes f .

ad 3. Preservation of nodality follows from $\mathfrak{w}_{2d,c} = \delta_{cd}$.

The remaining properties follow from the construction and the fact that no additional neighbors are introduced. \square

Remark 5.5. The coarsened and coarse basis functions generally do not coincide because the resolution (triangulation) of the interface on the coarse grid is generally different from the one on the fine grid, except for very simple, e.g., hyperplanar interfaces. In particular, if the coarsened grid (especially after several coarsening steps) is too coarse to resolve interface details of Ω_{-} , the coarsened basis functions may still resolve them, see Figure 5.3.

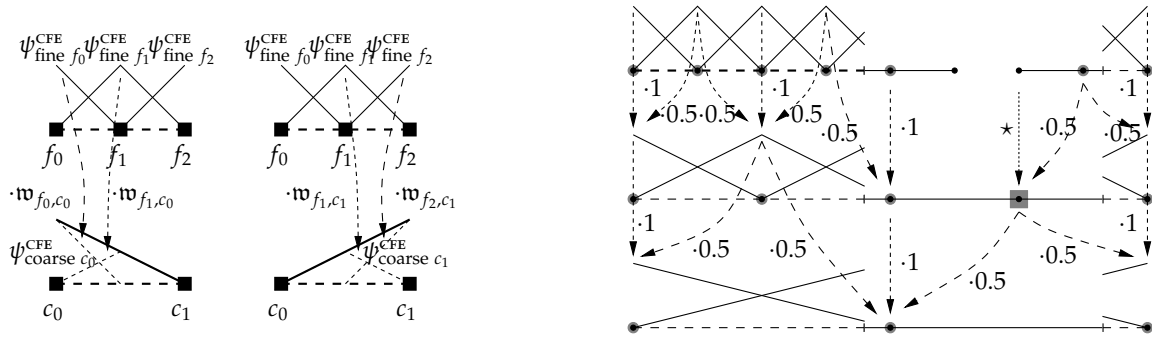


Figure 5.2. The *left* sketch shows how 1D basis functions are coarsened by computing weighted sums of fine grid basis functions using coarsening weights $w_{f,c}$. The *right* sketch shows this coarsening procedure in the 1D complicated domain case and the coarsening weights. The dotted line indicated by \star shows that coarsening from non-DOF nodes on the fine grid can be viewed as using a (non-existing) zero fine grid basis function. In this case, a new DOF (gray square) on the coarsened grid is introduced.

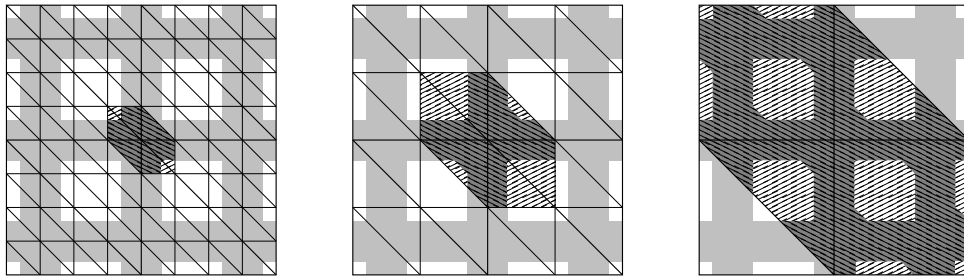


Figure 5.3. Coarsened 2D CFE basis functions contain details that could not be resolved by the construction immediately on the coarse grid. In this geometric case, this may be a desired property. The complicated domain is shown in gray, the support of the basis functions at different coarsening steps is shaded.

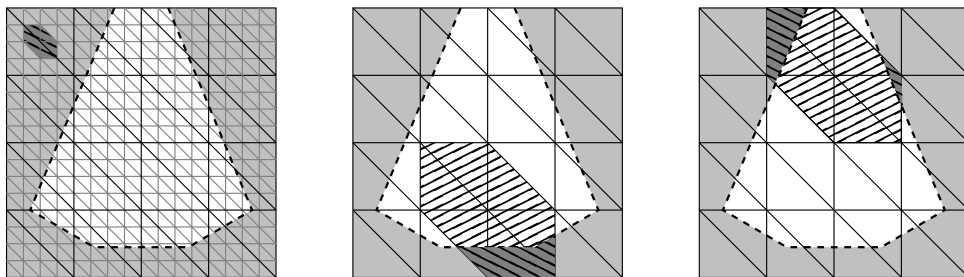


Figure 5.4. On a fine grid (*left*), the gap is sufficiently wide so that no basis function has disconnected support. After coarsening, the support of the basis function shown in the *middle* is still connected, but the one shown on the *right* has two disconnected components, numerically coupling parts of the domain with weak physical coupling of this horseshoe-type geometry.

This effect may be desired, but may also be problematic, in particular if coarsened basis functions turn out to consist of multiple disconnected components. In this case, coarsening introduces an artificial (numerical but unphysical) coupling on the coarse scale, resulting in poor coarse grid corrections and slow overall convergence of the multigrid solver, as illustrated in Figure 5.4. In many cases reported in Chapter 7, we successfully applied the multigrid solver, e.g., convergence rates better than 0.6 were obtained for the elasticity simulations in Figure 7.16. One example where this artificial coupling may introduce problems is shown in Figure 7.10. A possible approach to avoid this type of problem in a multigrid solver is presented in Section 8.2.

5.2.3 Treatment of Dirichlet Nodes

The fact that the coarsening process introduces additional nodes may pose a difficulty if we have Dirichlet boundary conditions and new boundary nodes are introduced. For this purpose we assume the problem to be transformed to zero Dirichlet boundary conditions on the finest level. If Dirichlet boundary conditions are imposed on a whole face of the bounding box Ω , any newly introduced nodes geometrically lying on that face are also Dirichlet nodes. In general, we consider a hierarchy of boundary element faces (objects of codimension 1). A face on the finest grid is labeled ‘D’ (Dirichlet) if at least one of its nodes is a Dirichlet node, ‘N’ (Neumann) otherwise. In a coarsening step, a face is ‘D’ if at least one of its descendant faces is ‘D’, it is ‘N’ otherwise. All vertices of ‘D’ faces are Dirichlet nodes on the coarsened grid. This procedure is illustrated in Figure 5.5.

If a face of the bounding box has nonempty intersection with both the Dirichlet and Neumann boundary, the coarsening above leads to conservative coarse grid corrections, because the Dirichlet boundary on coarsened grids grows. However, shrinking Dirichlet boundary throughout the coarsening process would mean that coarse grid corrections are computed for which the prolongation leads to a violation of the boundary conditions.

5.3 Homogenization Multigrid Solvers (Complicated Domains)

For being able to use a multigrid solver for the problems with periodic boundary conditions for the complicated domain case, recall that periodicity changes neighborhood relations, which also affects multigrid restriction and prolongation schemes, see Figure 5.6.

Coarsening Scheme. As usual, the coarsening weight $w_{f,c}$ from a fine grid node f to a coarse grid node c is simply the value of the coarse grid basis function located at c evaluated at f . These weights, as we know from Section 5.2.2, are 0, $1/2$, and 1. Modified neighborhoods imply that we loop over all coarse nodes which are active DOF nodes or whose active counterpart nodes are active DOF nodes, see Figure 5.6. In either case, we prolongate only to a fine neighbor of the coarse node if the fine node is an active DOF node.

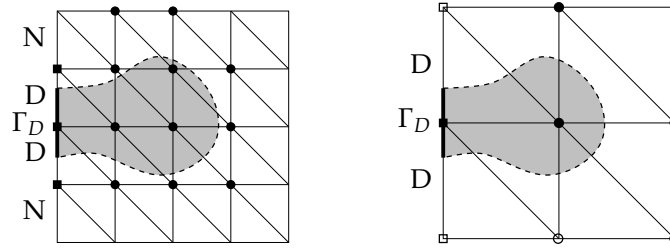


Figure 5.5. Coarsening of Dirichlet boundary conditions (2D CFE complicated domain case): for the jellyfish-shaped domain with DOF and Dirichlet nodes shown as filled circles and squares, respectively, on the *left*, boundary faces are labeled Dirichlet or Neumann. On the *right*, newly introduced DOF and Dirichlet nodes are shown as open circles and squares, boundary faces are again labeled.

As in the non-periodic case, the restriction is the adjoint (transpose) of the prolongation and subject to the same modifications due to periodicity. Coarsening of the system matrices is also performed as in the non-periodic case by pre- and postcomposing with prolongation and restriction, respectively.

Constraints and Projection. The smoothing operations (standard, possibly block-wise, Gauß-Seidel smoothing using the periodized matrices) used in our multigrid solver do not guarantee that we stay inside the subspace satisfying the constraints $\langle J_\alpha, U \rangle = 0$, so the multigrid solver has to perform projections to the space S as shown in (4.46). Our approach is to perform this projection after presmoothing, coarse-grid correction and postsmoothing on each but the coarsest level. On the coarsest level, we use a projecting CG solver (as described in the previous subsection) to make the coarsest problem uniquely solvable. A theoretical justification why the multigrid method can be combined with subspace projection, hence why this approach should work in general, is not known at present.

We thus need coarsened constraints (J_α). These are computed using all-1 vectors (periodically restricted) corresponding to the coarse grid and using coarsened mass matrices (periodically collapsed). For this purpose, we use the same coarsening method as for the system matrices in the scalar case.

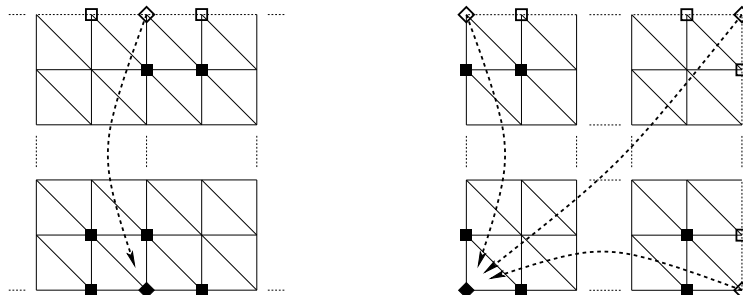


Figure 5.6. Identification of inactive nodes \diamond with their active counterparts \blacklozenge changes standard neighborhoods (\blacksquare) for multigrid prolongation and restriction, see also Figure 4.6.

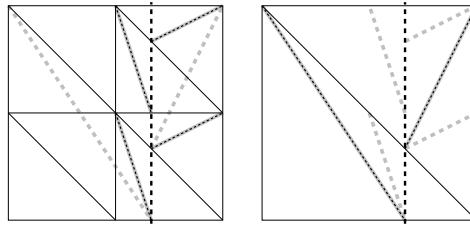


Figure 5.7. Virtual edges (dashed lines) for a planar interface on a fine grid (*left*) do not appear in the construction on a coarse grid (*right*) and vice versa.

This coarsening process accumulates rounding errors in the coarsened system matrices so that constant vectors no longer exactly lie in the kernel. Thus, the projection may destroy convergence of the CG solver. To remedy this, note that a constant vector is an eigenvector to eigenvalue 0 if and only if each row of the matrix has sum zero. If this condition is not satisfied for coarsened system matrices (due to rounding errors), we can reestablish it by modifying the diagonal entry in such rows. This modification is justified because it is of the same magnitude as the rounding errors.

5.4 Multigrid Coarsening for Discontinuous Coefficients

A multigrid coarsening strategy for CFE for discontinuous coefficients cannot be designed as a straightforward generalization of the complicated domain case. Using standard coarsening weights on standard neighborhoods is not a suitable approach because it does not produce an appropriate representation of the coupling conditions on coarsened levels.

In 1D, we are in the special situation that basis functions themselves satisfy the kink property given by the coupling condition. It is thus possible to use a coarsening strategy preserving the kinks at interface positions and not introducing artificial kinks in the coarsened basis functions that would not be present in basis functions constructed on the coarse grid (provided the interface can be resolved there), see Figure 8.3.

In more than one space dimension, this is no longer possible. Due to the tangential directions, CFE basis functions on the fine grid themselves do not satisfy the coupling condition across the interface (and merely need to allow to interpolate functions satisfying it). Moreover, Figure 5.7 shows that virtual edges on the coarse grid do not exist on the fine grid and vice versa. So if we compare coarsened basis functions to those constructed immediately on the coarse grid, depending on the construction weights the coarsened ones may or may not have kinks across the fine virtual edges (note that these are not interface kinks but classical mesh edge kinks of tent functions) but cannot have kinks across coarse virtual edges as the coarse basis functions do.

In Section 8.3 we present some ideas for a coarsening strategy. However, a generally effective multigrid solver could not be developed for CFE for discontinuous coefficients, even in the scalar isotropic case.

6 Algorithms and Implementation

UP-TO-DATE COMPUTERS provide large amounts of memory and computational power and to some extent modern compilers are capable of effective automatic optimization. As one usually aims at running the largest simulations possible on the available hardware, it makes sense to implement methods in an efficient way, both in terms of memory consumption and CPU time. The aim of this chapter is to discuss efficient implementation of the methods presented before. After some technical remarks on global indexing in Section 6.1 we discuss the data structures and algorithms for the CFE construction in Section 6.2. Data vectors and matrices are treated in Section 6.3 and algorithmic aspects concerning multigrid methods are addressed in Section 6.4. Algorithms will be presented in pseudocode notation here. If it helps to keep the presentation of the algorithms simple, some obvious optimizations are omitted in the presentation of the algorithms.

We will encounter the common trade-off in scientific computing between memory and computational efficiency. Keeping in mind that we are particularly interested in what we can compute on standard PCs, today providing about 4 GiB of memory, typically memory efficiency will be considered more important. For current shared-memory multi-core or multi-processor computers, parallelizing code allows significant speed-up at low implementational effort. Parallel reading of the same data is not problematic in this case (except for possible speed and cache issues), but simultaneous write access to the same data must be avoided. As parallelization is not our main focus here, we will only use it where modifications of the algorithms are obvious and where write conflicts can be ruled out. We will not consider distributed computing that may be necessary for even larger problems but where specialized data structures and algorithmic techniques are necessary to avoid extreme communication costs dominating computational costs [32].

In the actual implementation in C++, data structures make use of the standard template library (STL) where appropriate. OpenMP is used for parallelization, making, e.g., matrix-vector multiplications very easy to parallelize automatically.

The implementation described here is based on the one for [216] but has been extended substantially for being able to treat discontinuous coefficients and for making available efficient matrix data structures and multigrid solvers. Parts of the description here are also part of the previous publications listed in the preamble.

6.1 Global Indexing

This section briefly describes global indexing of DOF (necessary for organizing data vectors and matrices) and virtual nodes (as they also need to be stored, see Section 6.2).

Nodes in the regular cubic grid (or in the regular tetrahedral mesh) in 3D are identified by index triples corresponding to their geometric location. Such triples can be assigned a single global index in an inversely lexicographical manner which is commonly used in computer graphics.

Definition 6.1. *Inversely lexicographical index mapping* is achieved by the mapping

$$j: \{0, \dots, N_x - 1\} \times \{0, \dots, N_y - 1\} \times \{0, \dots, N_z - 1\} \rightarrow \mathbb{N}, \quad (6.1)$$

$$(i_0, i_1, i_2) \mapsto j(i_0, i_1, i_2) := N_x \cdot N_y \cdot i_2 + N_x \cdot i_1 + i_0.$$

In our applications, 32 bit integers are sufficiently large for the global indices. For cubic domains, $l = 10$ implies $\#\mathcal{N}^{\text{DOF}} = (2^{2^{10}} + 1)^3 = 1025^3 < 2^{31}$, so 32 bit integers can be used without problems due to the sign bit. This is at the limit of memory capabilities of current hardware because already a data vector in this case takes about 8 GiB if standard IEEE 754 double floating-point numbers are used.

The same indexing can also be used for cubic elements $E \in \mathcal{G}^\square$ if these are identified by their vertex with smallest global node index. Note, however, that certain elements such as $(0, 0, N_z - 1)$ then do not exist. Local vertex indices for an element E are then easily converted to global node indices.

Definition 6.2. A *global index* of a virtual node $z = \widehat{rs}$ is given by

$$j(\widehat{rs}) = \begin{cases} 2^{32}j(r) + j(s) & \text{if } j(r) > j(s), \\ 2^{32}j(s) + j(r) & \text{otherwise.} \end{cases} \quad (6.2)$$

For a virtual node \widehat{rs} , clearly $r \neq s$ so that at most one of them can have global index 0. Hence $j(\widehat{rs}) \geq 2^{32}$ and the ranges of global indices of regular nodes and virtual nodes are disjoint. Note that the definition in Equation (6.2) differs from the one in [217, Section 4.2]. Note moreover that the concatenation of two 32 bit integers results in a 64 bit integer.

Observing that virtual nodes \widehat{rs} only lie on edges between neighboring nodes (and that there is only a very limited number of neighbors for a given node, e.g., 15 in 3D), one could save many bits by defining global indices $j(\widehat{rs})$ in terms of $j(r)$ or $j(s)$ and a neighbor index.

6.2 Virtual Meshes and CFE Basis Functions

Let us first consider the steps necessary to construct the CFE basis functions for complicated domains and for discontinuous coefficients. A lookup table for the topological subdivision of cubic elements based on their signature is constructed

in Section 6.2.1, based on which the actual geometric subdivision is treated in Section 6.2.2. Constraints and CFE construction weights are then determined in Section 6.2.3.

All these steps do not require significant computational time (compared to assembling matrices and solving systems of equations), so parallelization is of little benefit here. Moreover, avoiding write conflicts in the algorithms of this section would not always be trivial.

6.2.1 Topology Lookup

In Section 3.1 we have seen that extracting the object geometry from the level set function can be sped up significantly if topology and geometry of the interface cutting through a cubic element E is determined separately. The topology of the subdivision of E in regular and virtual simplices only depends on the signature $\zeta(E)$ (the sign pattern of the level set function on the vertices of E). The number of possible signatures is 2^{2^d} (256 in 3D) of which 128 are possibly ambiguous (cf. Figure 3.5).

We can compute a lookup table containing the subdivision for each signature which is determined by Algorithm 6.1. Different from [217, Algorithm 1], we here also include positive tetrahedra. In Algorithm 6.1, we use element-local instead of global indices for the vertices r_k .

Computational and Storage Costs. This lookup table could be computed once and for all because it does not depend on any level set function describing an object. However, it only takes a few milliseconds to compute the lookup table, so loading it from a file is of no benefit compared to computing it during each program run. In our implementation for double floating point accuracy, the lookup table requires about 2067 KiB and thus a negligible amount of memory compared to vectors and matrices.

6.2.2 Storage of Virtual Nodes

As we have seen in Sections 3.2 and 3.3, we need to store data associated with virtual nodes. As virtual nodes lying on element faces are part of different elements, a per-element storage of virtual nodes is not feasible. However, during grid traversal, the set of virtual nodes for a given element needs to be easily accessible. Hence an efficient global storage strategy is necessary.

A global index for a virtual node z is defined in Equation (6.2), and these indices can be used as keys in an STL map (without additional hashing) to store virtual nodes and data for them (see Algorithm 6.2), including

- geometric information: the location of the virtual node is stored, additionally an averaged (over adjacent regular tetrahedra) normal to the zero level set at z
- CFE construction information: constraining regular nodes $\mathbb{P}(z)$ and construction weights $w_{z,r}$ for $r \in \mathbb{P}(z)$, and
- administrative information: tetrahedra in which z lies.

procedure CREATETOPOLOOKUPTopoLookup $\leftarrow \emptyset$ **for** $\zeta \in \{-1, 1\}^8$ **do** \triangleright for each signature $\zeta(E)$ of an element**for** $j \in \{0, \dots, 5\}$ **do** \triangleright for each standard tetrahedron T_j of E TopoLookup \leftarrow TopoLookup \cup SPLITTETRAHEDRON($T_j, \zeta(T_j)$)**return** TopoLookup**procedure** SPLITTETRAHEDRON(simplex $T = (r_0, \dots, r_3)$, signature $\zeta = (\zeta_0, \dots, \zeta_3)$) $N_v \leftarrow \emptyset$ \triangleright local virtual nodes**for** $a, b \in \{0, \dots, 3\}, a \neq b$ **do****if** $\zeta_a \neq \zeta_b$ **then** \triangleright if the edge (r_a, r_b) of T is interfaced $N_v \leftarrow N_v \cup \{\widehat{r_a r_b}\}$ \triangleright store local virtual node $N_{\pm} \leftarrow \{r_j \mid \zeta_j = \pm 1\}$ \triangleright positive and negative vertices of T $S_{\pm} \leftarrow \emptyset$ \triangleright positive and negative local virtual simplices**if** $\#N_- = 0$ **then** $\triangleright T$ does not split and lies inside $S_+ \leftarrow S_+ \cup \{(T, T)\}$ \triangleright store pair (regular simplex containing itself, simplex)**else if** $\#N_- = 1$ **then** $\triangleright T$ splits into tetrahedron inside and pentahedron outsidereorder vertices such that $N_- = \{r_0\}, N_+ = \{r_1, r_2, r_3\}$ and $r_1 < r_2 < r_3$ $S_- \leftarrow S_- \cup \{(T, (r_0, \widehat{r_0 r_1}, \widehat{r_0 r_2}, \widehat{r_0 r_3}))\}$ \triangleright tetrahedron inside $S_+ \leftarrow S_+ \cup \{(T, (r_1, r_2, \widehat{r_0 r_2}, \widehat{r_0 r_3}))\}$ \triangleright subdivision of ... $S_+ \leftarrow S_+ \cup \{(T, (r_2, r_3, r_1, \widehat{r_0 r_3}))\}$ \triangleright pentahedron $S_+ \leftarrow S_+ \cup \{(T, (r_1, \widehat{r_0 r_1}, \widehat{r_0 r_2}, \widehat{r_0 r_3}))\}$ \triangleright ... outside**else if** $\#N_- = 2$ **then** $\triangleright T$ splits into two pentahedrareorder vertices such that $N_- = \{r_0, r_1\}, N_+ = \{r_2, r_3\}, r_0 < r_1$ and $r_2 < r_3$ $S_- \leftarrow S_- \cup \{(T, (r_0, r_1, \widehat{r_1 r_3}, \widehat{r_1 r_2}))\}$ \triangleright subdivision of ... $S_- \leftarrow S_- \cup \{(T, (r_0, \widehat{r_0 r_2}, \widehat{r_0 r_3}, \widehat{r_1 r_2}))\}$ \triangleright pentahedron $S_- \leftarrow S_- \cup \{(T, (r_0, \widehat{r_1 r_3}, \widehat{r_0 r_3}, \widehat{r_1 r_2}))\}$ \triangleright ... inside $S_+ \leftarrow S_+ \cup \{(T, (r_2, \widehat{r_1 r_3}, \widehat{r_0 r_3}, \widehat{r_1 r_2}))\}$ \triangleright subdivision of ... $S_+ \leftarrow S_+ \cup \{(T, (r_2, \widehat{r_0 r_2}, \widehat{r_0 r_3}, \widehat{r_1 r_2}))\}$ \triangleright pentahedron $S_+ \leftarrow S_+ \cup \{(T, (r_2, r_3, \widehat{r_0 r_3}, \widehat{r_1 r_3}))\}$ \triangleright ... outside**else if** $\#N_- = 3$ **then** $\triangleright T$ splits into pentahedron inside and tetrahedron outsidereorder vertices such that $N_- = \{r_0, r_1, r_2\}, N_+ = \{r_3\}$ and $r_0 < r_1 < r_2$ $S_- \leftarrow S_- \cup \{(T, (r_0, r_1, \widehat{r_1 r_3}, \widehat{r_2 r_3}))\}$ \triangleright subdivision of ... $S_- \leftarrow S_- \cup \{(T, (r_1, r_2, r_0, \widehat{r_2 r_3}))\}$ \triangleright pentahedron $S_- \leftarrow S_- \cup \{(T, (r_0, \widehat{r_0 r_3}, \widehat{r_1 r_3}, \widehat{r_2 r_3}))\}$ \triangleright ... inside $S_+ \leftarrow S_+ \cup \{(T, (r_3, \widehat{r_0 r_3}, \widehat{r_1 r_3}, \widehat{r_2 r_3}))\}$ \triangleright tetrahedron outside**else** $\triangleright \#N_- = 4, T$ does not split and lies outside $S_- \leftarrow S_- \cup \{(T, T)\}$ **for** $\tilde{T} \in S_- \cup S_+$ **do****if** \tilde{T} does not have positive orientation **then**switch \tilde{T}_0 and \tilde{T}_1 \triangleright make orientation positive by switching two vertices**return** N_v, S_-, S_+ **Algorithm 6.1.** Creating a lookup table for the topological decomposition of cubic elements

```

procedure DETECTVIRTUALNODES(level set function  $\Phi$ )
  VNMap =  $\emptyset$ 
  for  $E = (r_0, \dots, r_7) \in \mathcal{G}^\square$  do ▷ for each (cubic) element in the grid
    for  $S_\pm \in \text{TOPOLOOKUP}(\zeta(E))$  do ▷ lookup table determined by Algorithm 6.1
      for  $(T_p, T) \in S_\pm$  do ▷ virtual tetrahedra for  $E$ 
        for  $z = \widehat{s_0 s_1}$  virtual vertex of  $T$  do ▷ local vertex indices for  $E$ 
           $i \leftarrow e_{s_0}, k \leftarrow e_{s_1}$  ▷ so that  $z = \widehat{r_i r_k}$  are global node indices of regular nodes
          if VNMap[ $j(z)$ ] does not yet exist then
            VNMap[ $j(z)$ ]  $\leftarrow$  global geometric position:  $[\Phi|_{(r_i, r_k)} = 0]$ 
            Add  $E$  and  $T_p$  to set  $\mathbb{A}(z)$  of constraining regular tetrahedra of VNMap[ $j(z)$ ]
        return VNMap

procedure DETECTANDINITVIRTUALNODES(level set function  $\Phi$ , coefficients  $a$ )
  VNMap = DETECTVIRTUALNODES( $\Phi$ )
  for  $z \in \text{VNMap}$  do
     $n \leftarrow 0_{\mathbb{R}^3}$  ▷ for approximate normal of  $[\Phi = 0]$  at  $z$ 
    for  $T_p \in \mathbb{A}(z)$  do ▷ constraining regular tetrahedron of  $z$ 
       $n \leftarrow n + \nabla\Phi|_{T_p}$  ▷ by affine interpolation of vertex values of  $\Phi$ 
     $n \leftarrow n/\|n\|$  ▷ normalization is implicitly also averaging
    store normalized normal  $n$  for  $z$ 
  for  $z \in \text{VNMap}$  do
    DETERMINEWEIGHTSANDCONSTRAINTS( $z, a$ ) ▷ for CFE, cf. Section 6.2.3

```

Algorithm 6.2. Detection and initialization of virtual nodes. The subroutines DETERMINEWEIGHTSANDCONSTRAINTS are described in Algorithms 6.3 and 6.4 for the case of complicated domains and discontinuous coefficients, respectively.

In Algorithm 6.2, the piecewise affine approximation Φ of the continuous level set function φ is used so that the geometric location of the virtual node z on the edge (r_0, r_1) is obtained as in Equation (3.9)

$$z = \frac{r_0\Phi(r_1) + r_1\Phi(r_0)}{\Phi(r_0) - \Phi(r_1)} \quad (6.3)$$

The normalized outer normal to the zero level set is given by $\nabla\Phi(z)/\|\nabla\Phi(z)\|$. As z lies on the edge where the piecewise affine approximation is continuous, but in general not differentiable, the gradient is computed on each adjacent regular tetrahedron (and constant there), added up and finally normalized, implicitly averaging the normals before the normalization. Determining constraints and construction weights for the CFE basis functions is discussed in the next section.

Computational and Storage Costs. The typical memory requirement for the data to be stored for each virtual node is about 250 bytes for the case of complicated domains and about 300 and 750 bytes in the scalar and vector-valued cases of discontinuous coefficients, respectively.

The number of virtual nodes clearly depends on the geometric complexity of a given interface. Typically the interface is a hypersurface (i.e., of dimension 2), so that we have $O(2^{2l})$ virtual nodes compared to $O(2^{3l})$ regular grid points, but with large constant. The resolution is typically limited (e.g., to few grid cells per trabecular diameter) so that our objects may seem to have fractal dimension [37]. In any case, the number of virtual nodes is bounded by a small constant times the number of regular nodes.

The computational cost for Algorithm 6.2 is $O(n)$ in the number of elements and $O(n \log n)$ in the number of virtual nodes (insertion to the STL map VNMap has logarithmic complexity), and takes about 14 seconds for the case of complicated domains and 32 and 943 seconds for the scalar and vector-valued case of discontinuous coefficients for the dataset used in Figure 7.13 with 1 368 973 virtual nodes and on one 3 GHz Opteron processor. The (constant) complexity of the subroutine DETERMINEWEIGHTSANDCONSTRAINTS is discussed in the next section.

6.2.3 Constraints and CFE Construction Weights

The most important ingredient for the CFE construction are the constraints $\mathbb{P}(z)$ and construction weights $w_{z,r}(r) \in \mathbb{P}(z)$ for a virtual node z , see Equation (3.3). We now give an algorithmic description how these are determined for the case of complicated domains (cf. Section 3.2) and discontinuous coefficients in case of isotropic diffusion (cf. Section 3.3.1) and linear elasticity (cf. Section 3.3.2).

Let us point out that we describe the computation of CFE construction weights based on the interpolation Problems 3.20 and 3.31. These are only useful if Problems 3.16 and 3.27 have unique solutions. However, cases where the latter problems do not have unique solutions were tested for and never observed in our computations. This is not only a numerical artifact. For non-uniquely solvable Problems 3.16 and 3.27 we can expect large unreliability values $\varrho \gtrsim 1$ as discussed below for failing numerical matrix inversion. The observed values ϱ , however, are on the order of 10^{-10} , which indicates only accumulated numerical errors.

CFE for Complicated Domains. In case of complicated domains, we know from Equation (3.8) that the constraint set of a virtual node consists only of its geometrically constraining nodes, moreover the construction weights are given by Equation (3.8). The corresponding Algorithm 6.3 is rather straightforward and given here mainly for completeness.

CFE for Discontinuous Coefficients, Isotropic Diffusion. For scalar isotropic diffusion, we determine simplex-wise construction weights for each adjacent regular simplex and average these. On each simplex, the 4×4 matrix B from Equation (3.19) needs to be inverted.

The inversion (yielding the numerically computed inverse denoted by B^{-1}) may be ill-conditioned in certain geometric situations, in which case the resulting construction

```

procedure DETERMINEWEIGHTSANDCONSTRAINTS(virtual node  $z = \widehat{r}s$ )
   $C \leftarrow \{r, s\}$  ▷ geometrically constraining regular nodes
   $W[r] \leftarrow \frac{\|s-z\|_2}{\|s-r\|_2}$ 
   $W[s] \leftarrow \frac{\|z-r\|_2}{\|s-r\|_2}$ 
return  $C, W$ 

```

Algorithm 6.3. Constraints and CFE construction weights for complicated domains

weights may not be useful (and destroy the convergence order of the approximation). We hence define an unreliability measure.

Definition 6.3. For a tetrahedron T and the the matrix $B = B(T)$ in Equation (3.19), the *unreliability measure* is defined as

$$\varrho_s(T) := \|BB^{\sim 1} - \text{Id}\|_F \quad (6.4)$$

where $\|\bullet\|_F$ is the Frobenius norm.

In exact arithmetic we have $\varrho_s(B) = 0$, so large ϱ_s stands for low reliability. If $\varrho_s(B)$ is greater than some threshold, the current tetrahedron is excluded from the averaging process (used with averaging weight 0). The threshold needs to be chosen sufficiently small such that numerical instabilities in the inversion do not result in bad CFE construction weights but also sufficiently large so that each virtual node has at least one adjacent regular tetrahedron from which CFE construction weights can be determined. The corresponding Algorithm 6.4 summarizes the procedure for the CFE construction for discontinuous coefficients.

CFE for Discontinuous Coefficients, Linear Elasticity. In the vector-valued linear elasticity case, the construction is essentially the same for matrix-valued construction weights. The main difference is that determining the local coupling condition as described in Section 2.3.2 also requires inverting the matrix L^+ defined in Equation (2.37), depending on the directions n, s, t and the elasticity coefficient C . This numerical matrix inversion is also considered for the reliability of single adjacent regular tetrahedra for the averaging. The complete construction procedure is summarized in Algorithm 6.4.

Definition 6.4. For a tetrahedron T and the matrices $L^+ = L^+(T)$ defined in Equation (2.37) and $Bx = b$, $B = B(T)$, $b = b(T)$ being the system of equations (3.28), the *unreliability measure* is defined as

$$\varrho_v(T) := \max(\|L^+L^{+\sim 1} - \text{Id}\|_F, \|B(B^{\sim 1}b) - b\|_2). \quad (6.5)$$

Note that we here check the quality of the numerical inverse of the 3×3 matrix L^+ and the norm of the residual for the 36×36 system $Bx = b$ because only L^+ is inverted explicitly.

procedure WEIGHTCONSTRAINTCONSTRUCTION(scalar case; $a, T, W, P, N_{\text{reliab}}, \dots$)
 set up system matrix $B := B(a, r_i, z, n, s, t)$ from Equation (3.19)
 $B^{\sim 1} \leftarrow$ numerically computed inverse of H
 $q_s(T) \leftarrow \|BB^{\sim 1} - \text{Id}\|_{\text{F}}$ ▷ unreliability measure (6.4)
if $q_s(T) <$ reliability threshold **then**
 $N_{\text{reliab}} \leftarrow N_{\text{reliab}} + 1$
 $P \leftarrow P \cup \{r_0, \dots, r_3\}$ ▷ use all vertices of $T_p = (r_i)_i$ as constraints
 $[\mathfrak{w}_{z,r_0;T} \ \mathfrak{w}_{z,r_1;T} \ \mathfrak{w}_{z,r_2;T} \ \mathfrak{w}_{z,r_3;T}]^T \leftarrow B^{\sim 1} [0 \ 0 \ 0 \ 1]^T$ ▷ solve for weights
 $W[r_i] \leftarrow W[r_i] + \mathfrak{w}_{z,r_i;T}$ ▷ store per-tetra weights
else
 do nothing ▷ consider T_p unreliable and ignore it

procedure WEIGHTCONSTRAINTCONSTRUCTION(vector-valued case; $C, T, W, P, N_{\text{reliab}}, \dots$)
 set up matrix $L^{\pm} = L(C, n, s, t)$ from Equation (2.37) for the local coupling condition
 compute $L \leftarrow (L^+)^{\sim 1} L^-$
 set up system block matrix $B = B(L, r_i, z, n, s, t)$ from Equation (3.28): $Bx = b$
 $q_v(T_p) \leftarrow \max(\|L^+(L^+)^{\sim 1} - \text{Id}\|_{\text{F}}, \|B(B^{\sim 1}b) - b\|_2)$ ▷ unreliability measure (6.5)
if $q_v(T_p) <$ reliability threshold **then**
 $n_{\text{reliab}} \leftarrow n_{\text{reliab}} + 1$
 $P \leftarrow P \cup \{r_0, \dots, r_3\}$ ▷ use all vertices of $T_p = (r_i)_i$ as constraints
 $[\mathfrak{W}_{z,r_0;T_p} \ \mathfrak{W}_{z,r_1;T_p} \ \mathfrak{W}_{z,r_2;T_p} \ \mathfrak{W}_{z,r_3;T_p}]^T \leftarrow$ solution of Equation (3.28) using $B^{\sim 1}$
 $W[r_i] \leftarrow W[r_i] + \mathfrak{W}_{z,r_i;T_p}$ ▷ store per-tetra weights
else
 do nothing ▷ consider T_p unreliable and ignore it

procedure DETERMINEWEIGHTSANDCONSTRAINTS(virtual node $z = \widehat{r_k r_l}$, coefficient k)
 $P \leftarrow \emptyset, W \leftarrow \emptyset$ ▷ for constraints and weights
 $N_{\text{reliab}} \leftarrow 0$ ▷ count number of reliable tetrahedra
 $s, t \leftarrow$ tangential directions, orthonormal and orthogonal to n
for $T_p = (r_0, \dots, r_3) \in \mathbb{A}(z)$ **do** ▷ constraining regular tetrahedron of z
 WEIGHTANDCONSTRAINTCONSTRUCTION($k, T_p, W, P, N_{\text{reliab}}, \dots$)
if $N_{\text{reliab}} = 0$ **then**
 return Exception, need to increase threshold
for r_i entry of W **do**
 $W[r_i] \leftarrow W[r_i] / N_{\text{reliab}}$ ▷ average weights
 if $W[r_i] = 0$ **then**
 $P \leftarrow P \setminus \{r_i\}$ ▷ remove constraints with weight 0
return C, W

Algorithm 6.4. Constraints and CFE construction weights for discontinuous coefficients (here denoted by k) are computed using the corresponding subprocedure for the scalar or vector-valued case.

Computational Costs. As the number of tetrahedra adjacent to a virtual node, $\#\mathcal{A}(z)$, is bounded by 8 for geometric reasons, Algorithms 6.3 and 6.4 have constant $O(1)$ computational complexity if the necessary data (including evaluation of the coefficient functions a, C) can be provided in constant time. They produce $O(1)$ data for each virtual node that needs to be stored.

6.3 Data Vectors and Composite Finite Element Matrices

Let us now discuss algorithmic and memory complexity of data vectors (Section 6.3.1), CFE system matrix operations (Section 6.3.2) and assembly (Section 6.3.3).

6.3.1 Data Vectors

Data vectors for CFE simulations contain entries for all nodes of \mathcal{N}^\square in inversely lexicographical ordering as defined in Equation (6.1). In particular, non-DOF nodes in case of complicated domains are *not* left out to preserve the simplicity and efficiency of data structures for uniform hexahedral grids, even though this wastes a certain amount of memory.

For vector-valued problems, we use block vectors containing one (large) vector for each spatial component of the unknown quantity (e.g., displacement). The total memory requirement is thus $O(\#\mathcal{N}^\square) = O(2^{3l})$ with constant 8 for double floating point accuracy times the number of spatial components.

6.3.2 Matrix Data Structures

The sparsity structure of the resulting CFE matrices (see Figure 3.18) is clearly determined by neighborhood structures of regular grid nodes in terms of supports of basis functions, since matrices contain integrals of basis functions or their derivatives. As we have seen before, the number of entries per row is limited to

- 15 for DOF nodes in the complicated domain case (see Section 3.2)
- 89 for nodes near the interface in the scalar isotropic discontinuous coefficients case and 15 far from the interface (see Section 3.3.1)

so the total number of matrix entries is linear in the number of DOF, see also Figure 3.18. As we have already seen for the data vectors, even in case of complicated domains, we wish to store matrix rows also for non-DOF nodes (either as zero rows or as identity rows), so the total number of matrix entries is $O(2^{3l})$. The constant, however, is relatively large (compared to the data vectors) and matrices require most of the memory necessary for a CFE simulation, so it is worth investigating how they can be stored memory-efficiently. There are different possibilities how the matrices can be stored.

General sparse matrix format clearly requires least implementational effort, but is also rather inefficient. In most cases, the sparsity structure is known and need not be stored explicitly (wasting a column index per entry). Moreover, typical row-wise storage does not immediately allow fast access to matrix columns if this is necessary (e.g., for treatment of boundary conditions).

Band matrix format is computationally more efficient, but also wastes memory. For complicated domains and non-DOF nodes, at most a diagonal entry 1 needs to be stored; for discontinuous coefficients, a substantial number of rows only contains 15 entries each (instead of 89). Moreover, additional bands would have to be introduced for periodic boundary conditions but would only be filled for nodes near the boundary.

Mixed row-wise (hybrid) matrix format can be rather efficient if the format is tailored to the CFE application. We use different types of rows, depending on the node to which the row corresponds. For DOF nodes far from the interface, the sparsity structure is the one of standard neighborhoods, thus only the 15 entries need to be stored. For non-DOF nodes, diagonal rows only need to store the diagonal entry. Rows with non-standard sparsity structure (due to nodes near the interface) will be stored as general sparse rows.

If coefficients are constant throughout the whole subdomains, the rows corresponding to nodes far from the interface all contain the same entries (merely in different columns). The same is true for the diagonal rows corresponding to non-DOF nodes. This fact can be exploited by storing single reference rows and marking such rows as column-shifted copies of the corresponding reference row. This approach can reduce the memory requirement dramatically. As matrices are assembled by adding contributions from the individual elements (cf. Section 6.3.3), one needs to make sure that the reference row is written to only once.

Parallelization of matrix-vector multiplications is parallelized in a straightforward manner by splitting the set of row indices, automatically preventing write conflicts.

In block matrices, whose structure obviously needs to be compatible with block data vectors, each block is treated separately. Sharing sparsity structure information which is stored explicitly could slightly reduce memory requirements but makes the implementation more complicated.

6.3.3 Assembling Matrices Element by Element

The entries of CFE matrices need to be computed according to Section 3.5. However, regular nodes constraining a given virtual node are stored, but not vice versa. We hence follow the usual approach of assembling FE matrices by looping over all elements and summing up the local contributions rather than looping over all entries [55, Section II.8].

This way, we can assemble standard local FE matrices on the virtual mesh \mathcal{G}^Δ using the virtual basis functions ψ^Δ , this is denoted by the function COMPUTELOCAL-TETRAMATRIX in Algorithm 6.5 where M can stand for mass or stiffness matrix. In

```

procedure ASSEMBLEADDCFEMATRIX(coefficient  $a$ )
  for  $E = (r_0, \dots, r_7) \in \mathcal{G}^\square$  do                                 $\triangleright$  for each (cubic) element in the grid
    if  $\zeta(E) \in \{(-1, -1, -1, -1, -1, -1, -1, -1), (1, 1, 1, 1, 1, 1, 1, 1)\}$  then
       $\triangleright$  element is not interfaced
      for  $k, l \in \{0, \dots, 7\}$  do                                 $\triangleright$  for each pair of cube vertices
         $M_{\square}^{\text{loc}} \leftarrow \text{COMPUTEHEXAMATRIX}(a)$ 
         $r \leftarrow r_k, s \leftarrow r_l$ 
         $M^{\text{glob}}[j(r), j(s)] \leftarrow M^{\text{glob}}[j(r), j(s)] + M_{\square}^{\text{loc}}[k, l]$ 
      else                                                         $\triangleright$  element is interfaced
        for  $(T_p, T) \in S_{\pm} \in \text{TOPOLOGYLOOKUP}(\zeta(E))$  do
           $(T_0, \dots, T_3) \leftarrow T$ 
           $M_T^{\text{loc}} \leftarrow \text{COMPUTELOCALTETRAMATRIX}(E, T, a)$ 
          for  $k, l \in \{0, \dots, 3\}$  do                                 $\triangleright$  loop over pairs of vertices  $T_k, T_l$ 
            retrieve  $\mathbb{P}(z), \mathbb{P}(y)$  and weights  $\mathfrak{w}_{z,\bullet}, \mathfrak{w}_{y,\bullet}$  from  $\text{VNMAP}[y], \text{VNMAP}[z]$ 
            for  $r \in \mathbb{P}(z)$  do
              for  $s \in \mathbb{P}(y)$  do
                 $M^{\text{glob}}[j(r), j(s)] \leftarrow M^{\text{glob}}[j(r), j(s)] + \mathfrak{w}_{z,r} \mathfrak{w}_{y,s} M_T^{\text{loc}}[k, l]$ 
          return  $M^{\text{glob}}$ 
    
```

Algorithm 6.5. Element-by-element assembling scheme for CFE matrices. Only interfaced elements require special treatment. In the complicated domain case, only elements and virtual tetrahedra in Ω_- , i.e., with negative signature, are considered.

the elasticity case, both the local and global matrices M have block structure and matrix-valued weights $\mathfrak{W}_{z,r}$ are used instead of $\mathfrak{w}_{r,r}$. For the innermost for loops, recall that $\mathbb{P}(r) = \{r\}$ and $\mathfrak{w}_{r,r} = 1$ (or $\mathfrak{W}_{r,r} = \text{Id}_{\mathbb{R}^{3 \times 3}}$) for simplex vertices being regular nodes $r \in \mathcal{N}^{\boxtimes}$.

Let us point out that these local matrices can be obtained from precomputed ones for the reference configuration by an appropriate scaling. For all elements not intersected by the interface, the quadrature is geometrically the same and only differs if the problem coefficient a is not constant, this case is hence treated separately by the function `COMPUTEHEXAMATRIX` in the algorithm. If a (in the scalar case) or C (in the vector-valued case) is constant, these contributions can be precomputed.

For varying coefficient a , the methods `COMPUTELOCALTETRAMATRIX` and `COMPUTEHEXAMATRIX` perform quadrature. For this purpose, constant average a for $E \cap \Omega_{\pm}^{\triangle}$ and $E \cap \Omega_{\mp}^{\triangle}$ are computed as the arithmetic average of the values of a at the corresponding vertices of E .

The assembling procedure is not parallelized because solving the system of equations later on dominates the workload of a CFE simulation even though it is easy (but not trivial) to protect shared data from race conditions in an element-by-element assembling scheme.

6.4 Iterative and Multigrid Solvers

6.4.1 Multigrid Implementation

Most building blocks of the CFE multigrid solver presented in Section 5 are standard and require no further discussion here.

The grid transfer operations (restriction and prolongation) can be implemented explicitly by loops over the coarse grid nodes and their sets of fine grid descendants or by multiplication with appropriate (rectangular) matrices. Due to standard coarsening weights and simple neighborhoods the explicit scheme is more efficient, both in terms of memory and computational workload. This may be different for adapted multigrid schemes as discussed in Section 8.2 and 8.3. Similarly, coarsening of system matrices can be implemented as the multiplication of three matrices or explicitly by loops implementing the sums in Equation (5.7).

The workload for restriction and prolongation is clearly $O(N_{\text{fine}})$ where N_{fine} is the number of nodes on the fine grid. The constant depends on the number of (multigrid coarsening) parent nodes per fine grid node. When coarsening the system matrix, the algorithmic complexity is also $O(N_{\text{fine}})$ and the constant depends on the square of the number of (multigrid coarsening) sibling nodes.

6.4.2 Parallelization

Parallelization of a standard conjugate gradient (CG) solver is easily achieved by parallelizing the matrix-vector multiplication (in the scalar case). In the vector-valued case where block matrices and block vectors are multiplied, it is more beneficial to parallelize at the block level (first—and on the level of individual matrices only if many parallel threads are desired).

For a block diagonal and block SSOR preconditioner, it makes sense to cache the inverses of 3×3 blocks for each DOF node instead of computing them in each iteration. Parallelization of this caching is obvious, but not very beneficial. The (standard and block) SSOR preconditioner itself can be parallelized if our inversely lexicographical ordering of the DOF is adapted to a $2n$ zebra-type ordering [109] for parallelization to n threads, where our typical choice was $n = 2$. The zebra scheme rules out write conflicts. Block preconditioners obviously cannot be parallelized at the block level.

As for the CFE multigrid solver, the individual iterations are inherently sequential, but still parallelization of the steps in each iteration is possible and useful (cf. [184]). The smoother can be parallelized in the same manner as the SSOR preconditioner. Prolongation can be parallelized by partitioning the index set of coarse grid nodes, whereas restriction needs to protect shared data from race conditions. For the vector-valued problem, the grid transfer operations can be parallelized at the block level provided the coarsening process does not involve coupling of the spatial components.

System matrix coarsening could be parallelized but (similar to assembling matrices) one must again ensure protection of shared data from race conditions. Note that this is different for AMG where the coarse grid generation process is expensive and thus also a candidate for parallelization [5, 142, 143].

7 Numerical Results and Applications

RESULTS OF DIFFERENT numerical tests and simulations are presented in this chapter. We start with numerical tests in Section 7.1, proceeding to applications of the CFE methods to heat diffusion and elasticity simulations in Section 7.2 and Section 7.3, respectively. In either case, both artificial objects and specimens of real objects with realistic material parameters are considered. Moreover, we present results of the homogenization procedure in Section 7.4.

Throughout this chapter we will use SI units for the material parameters and results whenever they represent realistic materials, but not for artificial examples. Temperatures (for heat diffusion simulations) and von Mises stresses at the interface (for elasticity simulations) are visualized using a standard HSV (hue, saturation, value) color map, also known as the ‘rainbow color map’. While this is not generally the ideal color map [294, 239], we consider it very intuitive for temperatures and appropriate for showing qualitative results. Most of the results here were already part of previous publications listed in the preamble, references are given in the text.

7.1 Numerical Tests

In this section we present results of numerical tests. For the case of scalar isotropic discontinuous coefficients, we investigate convergence of the CFE approximation of given functions in Section 7.1.1. We moreover consider elliptic BVP for which the analytic solution is known and examine the convergence of the CFE solution. Numerical consistency for both complicated domains and discontinuous coefficients is investigated in Section 7.1.3 for both scalar and vector-valued problems. Furthermore, the influence of geometric degeneracy or increasing discontinuity of the coefficient on the condition numbers of CFE matrices is examined in Section 7.1.4 and the performance of different solvers and preconditioners for CFE example problems (again scalar and vector-valued, for complicated domains and discontinuous coefficients) is measured in Section 7.1.5.

7.1.1 Function Approximation by CFE

Let us first determine the numerical order of convergence when approximating an analytically given function satisfying a given kink condition across an interface by CFE. As an extension of the cases presented in [281], we considered three different interfaces (shown in Figure 7.1) with different test functions and kink ratios $\kappa \in \{2, 32, 1000, 10^6\}$.

1. For the (rotated) planar interface, we used the corresponding rotation of a piecewise affine and continuous function with kink across the interface and non-vanishing derivatives in the tangential directions

$$\nabla u_{\text{planar}}(x) = \begin{cases} (1, 2, 5)^T & \text{for } x \in \Omega_- \\ (\kappa, 2, 5)^T & \text{for } x \in \Omega_+ . \end{cases} \quad (7.1)$$

2. For the cylindrical interface, we used the prototype function shown in Figure 7.1 to build a cylindrically symmetric function intersecting the boundary $\partial\Omega$ of the computational domain. The prototype function was constructed in such a way that it is piecewise second order polynomial, continuous and has the desired kink across the interface for fixed radius $R = 1/3$.

$$u_{\text{prototype}}(r) = \begin{cases} r^2 & \text{for } 0 \leq r < R \\ \kappa r^2 + (1 - \kappa)R^2 & \text{for } r \geq R \end{cases} \quad (7.2)$$

$$u_{\text{cylind}}(x) = u_{\text{prototype}}(r(x)) \quad (7.3)$$

where $r(x) = \text{dist}(x, \text{central axis of the cylinder})$.

3. For the spherical interface, we reused the prototype defined in Equation (7.2) and built a spherically symmetric test function, now multiplied by the tangential modulation term also shown in Figure 7.1 of the form

$$m(x) = \frac{\bar{x}_0 \bar{x}_1 \bar{x}_2}{\sqrt{\bar{x}_0^2 + \bar{x}_1^2} \sqrt{\bar{x}_0^2 + \bar{x}_2^2} \sqrt{\bar{x}_1^2 + \bar{x}_2^2}} \quad (7.4)$$

where $\bar{x} = x - \text{center of the sphere}$, $m(\text{center}) = 0$ and

$$u_{\text{sphere}}(x) = u_{\text{prototype}}(r(x)) \cdot (1 - 0.1m(x)) \quad (7.5)$$

where $r(x) = \text{dist}(x, \text{central axis of the sphere})$.

4. Moreover, a spherically symmetric (and unmodulated) test function $u_{\text{sphere } 0}$ for the cylindrical interface was considered based on the piecewise fourth-order polynomial prototype $u_{\text{prototype } 0}$ shown in Figure 7.1. The function $u_{\text{prototype } 0}$ was constructed in such a way that it is continuous, has the desired kink and vanishing second derivative at $r = R = 0.3$, and has C^2 transition to constant 1 at $r = 0$ and to constant 0 at $r = 0.45$. The last condition ensures that $u_{\text{sphere } 0} = 0$ on $\partial\Omega$.

All these functions were given analytically and their partial derivatives could also be computed in closed form. We computed approximate L^2 and H^1 errors of the CFE approximation of these functions by midpoint quadrature over the tetrahedra of the virtual mesh \mathcal{G}^Δ for increasing computational resolution, divided by the L^2 norm of the function to be approximated. This normalization compensates for scaling effects of κ in the function. An approximate L^∞ error was computed as the maximal

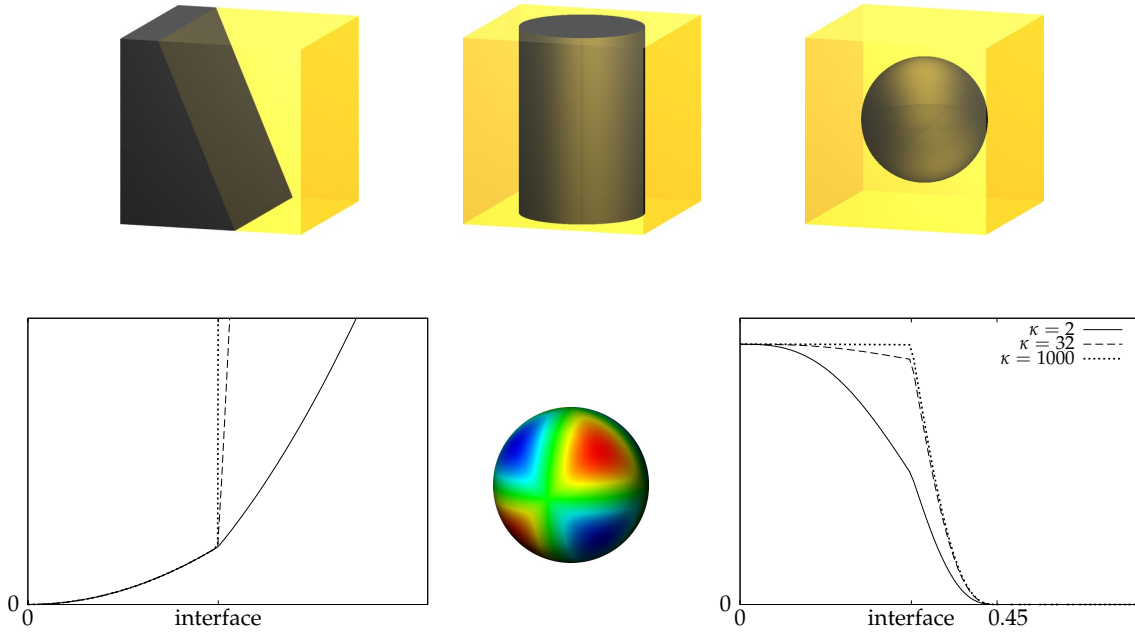


Figure 7.1. The *top row* shows the different interfaces used for numerically testing CFE approximation quality in Figure 7.2. Across the planar interface, a piecewise affine function was used. For the cylindrical interface, cylindrically symmetric functions with kink, based on the prototype function $u_{\text{prototype}}$ (*bottom left*), were used. For the spherical interface, a spherically symmetric function based on the same prototype was multiplied by the tangential modulation $1 - 0.1m(x)$ (*bottom middle*). Moreover, a spherically symmetric function based on the prototype $u_{\text{prototype } 0}$ with zero Dirichlet boundary conditions (*bottom right*) was used for testing the CFE approximation quality both of the function itself and of the solution of an elliptic BVP in Figure 7.3.

difference over all nodes \mathcal{N}^Δ and all quadrature points. For comparison and for using the same quadrature, we also computed these errors for an approximation by standard affine FE (stdFE) which do not resolve the kink.

Figure 7.2 shows that CFE perfectly approximated the piecewise affine function for the planar interface up to machine accuracy. For the cylindrical test case, the CFE approximation error shows second order convergence in the L^∞ and L^2 norms and first order in the H^1 norm. For the spherical test case, second order convergence is lost in the L^∞ norm. These outliers, however, do not affect convergence in L^2 or H^1 , where full second and first order can be observed. In contrast, stdFE exhibit orders 1, 1.5, and 0.5 in the L^∞ , L^2 , and H^1 norm, respectively. The loss of one full order compared to CFE in the L^∞ norm is due to non-representation of the kink in a layer of volume $O(h)$ near the interface of codimension 1. This leads to a loss of half an order in the convergence in L^2 and H^1 norms due to $(\int_{O(h)} O(h)^2)^{1/2} = O(h^{3/2})$.

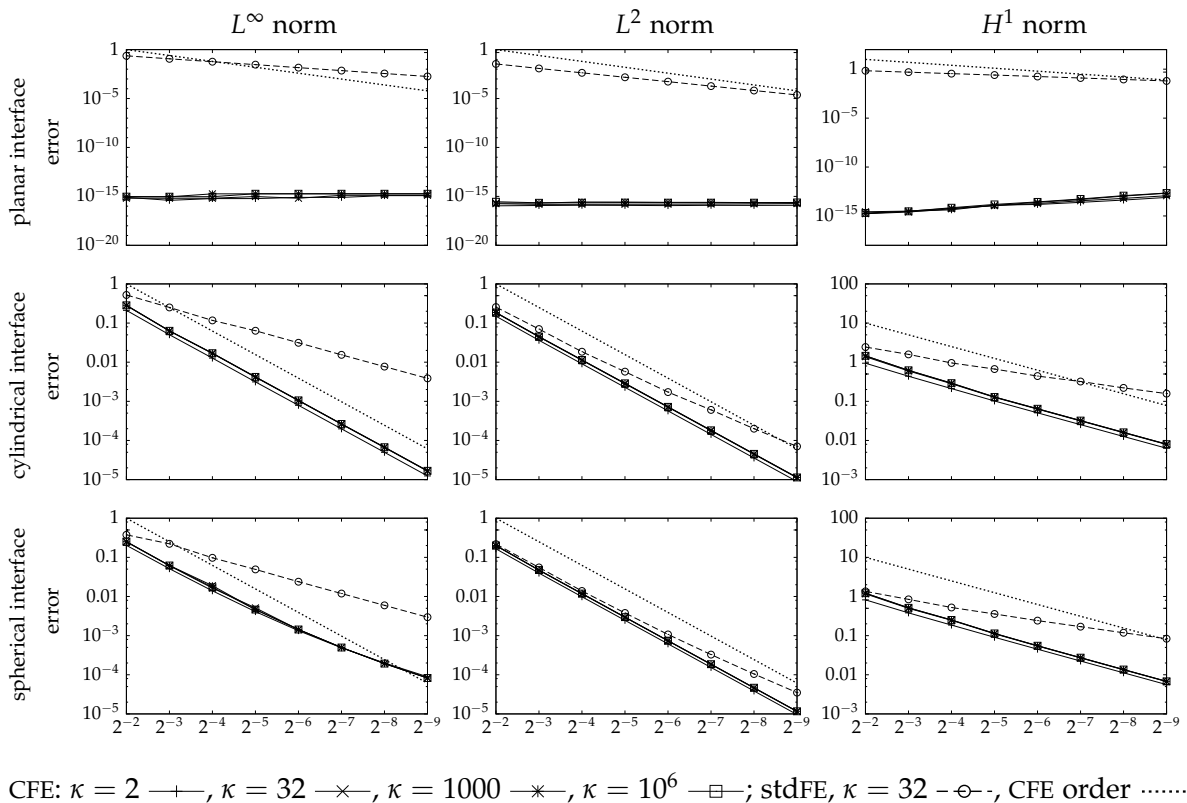
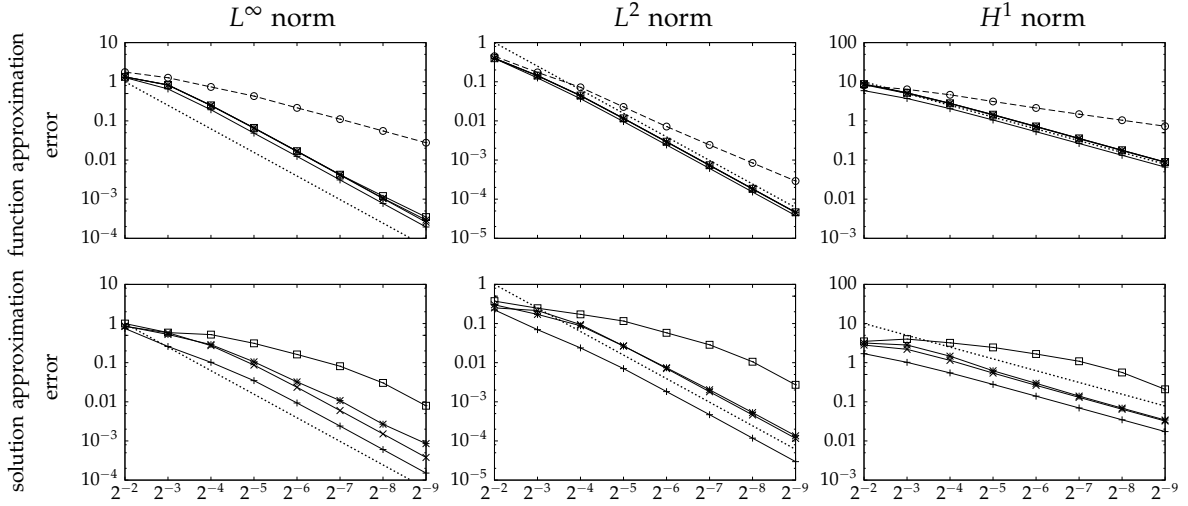


Figure 7.2. For three different interfaces and corresponding test functions with kink, the plots show the decrease of the CFE approximation error (normalized by the L^2 norm of the function considered) as the grid is refined. For a planar interface (*top row*), the approximation is exact up to machine accuracy, otherwise convergence in the L^∞ and L^2 norms is of second order and convergence in the H^1 norm is of first order. This expected order is shown by black dashed lines. For comparison, standard affine FE which do not resolve the kink only attain orders 1, 1.5 and 0.5.

7.1.2 Approximation of the Solution of an Elliptic BVP by CFE

Let us now consider the test function with zero boundary values of item 4. We computed its negative Laplacian¹ $f = -\Delta u_{\text{sphere } 0}$ and subsequently solved the problem $-\Delta u = f$ subject to zero Dirichlet boundary conditions for u using CFE. We then compared the CFE solution to the known analytic solution of the problem. Convergence of both the approximation of $u_{\text{sphere } 0}$ and of the solution of the elliptic boundary value problem are shown in Figure 7.3. The observed orders of convergence for the function approximation are the same as before. The same orders of convergence are achieved for the solution once the asymptotic range is reached. For larger kink ratio, the coarse discretizations lie outside this asymptotic range.

¹Named after the French mathematician and astronomer Pierre Simon, marquis de Laplace, * March 23, 1749 in Beaumont-en-Auge, Normandy, † March 5, 1827 in Paris [1].



CFE: $\kappa = 2$ —+—, $\kappa = 32$ —×—, $\kappa = 1000$ —*—, $\kappa = 10^6$ —□—; stdFE, $\kappa = 32$ —○—, CFE order

Figure 7.3. For a radially piecewise polynomial test function across a spherical interface with inherent zero boundary conditions for the unit cube, the *top row* shows the decrease of the CFE approximation error as in Figure 7.2. The *bottom row* shows the decrease of the error of the CFE solution of a corresponding elliptic boundary value problem with analytically known solution given by the test function.

7.1.3 Numerical Consistency Tests

We now turn to scalar and vector valued boundary value problems for which no analytic solution is given. Here, we investigated how the numerical solutions converge to a reference solution obtained on a very fine grid.

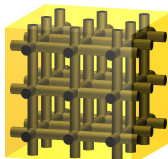
Linear Elasticity on a Complicated Domain. This case was investigated in [379] where two geometric objects of $3 \times 3 \times 3$ trabeculae with diameter-to-length ratios $d/l = (0.2, 0.2, 0.4)$ and $(0.4, 0.4, 0.4)$ were considered (see Figure 7.22). For linear elasticity, Lamé constants $\lambda = 9.779$ GPa and $\mu = 5.038$ GPa were used for the structure, corresponding to Young's modulus $E = 13.4$ GPa [291] and Poisson's ratio $\nu = 0.33$ [291, 201] for trabecular bone. We computed the L^2 norm of the difference between the results obtained at different coarse solutions and the reference solution obtained for a 513^3 grid by midpoint quadrature over the coarse virtual mesh \mathcal{G}^Δ , relative to the imposed displacement of 1% of the edge length. The actual value of the edge length of this artificial object is irrelevant for the relative errors.

The results reported in Table 7.4 show that coarse resolution in this case underestimates the volume of the structures and that the errors decrease with more than order 1. Moreover, a relative L^2 error of about 0.01 is obtained at resolution 33^3 , corresponding to a resolution of 2.13 and 4.26 voxels per trabecular diameter for $d/l = 0.2$ and 0.4, respectively.

Table 7.4. Sample geometries ($3 \times 3 \times 3$ trabeculae) with the same diameter-to-length ratios d/l in all space directions and with thinner transverse trabeculae were resolved at different resolutions. Results obtained on 9^3 to 257^3 grids were compared to the results for a 513^3 grid, considering the fraction of volume segmented, and a relative L^2 error of the displacement for compression and shear simulations, relative to the imposed displacement.

grid	$d/l = (0.2, 0.2, 0.4)$			$d/l = (0.4, 0.4, 0.4)$		
	volume fraction	rel. error (compr.)	rel. error (shear)	volume fraction	rel. error (compr.)	rel. error (shear)
9^3	0.841 816	0.040 175	0.033 242	0.883 848	0.055 986	0.027 218
17^3	0.978 785	0.017 572	0.014 527	0.978 967	0.015 301	0.016 932
33^3	0.992 192	0.006 604	0.010 219	0.992 375	0.007 203	0.011 090
65^3	0.997 183	0.002 943	0.004 587	0.997 552	0.003 150	0.004 636
129^3	0.999 167	0.001 486	0.001 654	0.999 344	0.001 287	0.001 877
257^3	0.999 823	0.000 616	0.000 510	0.999 868	0.000 443	0.000 561

Table 7.5. For numerical consistency tests we considered the domain on the *left*. Results obtained at different resolutions were compared to reference solutions computed on 513^3 and 257^3 grids, respectively, using pointwise ℓ^2 and Frobenius norms for the vector-valued displacement and its derivative.



grid	scalar problem			elasticity problem		
	L^∞ error	L^2 error	H^1 error	L^∞ error	L^2 error	H^1 error
17^3	0.055 279	0.008 245	0.359 515	0.266 884	0.007 583	0.564 360
33^3	0.023 502	0.003 393	0.193 077	0.108 070	0.003 046	0.268 633
65^3	0.009 512	0.001 092	0.097 312	0.051 376	0.000 939	0.121 923
129^3	0.004 850	0.000 348	0.048 578	0.049 559	0.000 230	0.056 526
257^3	0.002 119	0.000 090	0.023 283			

Table 7.6. The numbers of degrees of freedom and the total memory requirement (in MiB) are listed for the complicated domain elasticity simulations for $d/l = (0.2, 0.2, 0.4)$ (*left*) in Table 7.4 as well as for the scalar and elasticity problem with discontinuous coefficients in Table 7.5 (*middle and right*).

grid	Tab. 7.4, $d/l = (0.2, 0.2, 0.4)$		Tab. 7.5, scalar		Tab. 7.5, elasticity	
	# DOF	memory	# DOF	memory	# DOF	memory
9^3	1 395	4				
17^3	8 163	14	4 913	102	14 739	137
33^3	39 789	67	35 937	132	107 811	263
65^3	213 309	327	274 625	262	823 875	822
129^3	1 358 175	1 837	2 146 689	874	6 440 067	3 515
257^3	9 562 185	10 816	16 974 593	3 814	50 923 779	16 307
513^3	71 219 541	73 163	135 005 697	19 656		

Heat Diffusion and Linear Elasticity with Discontinuous Coefficients. Furthermore, we considered the 3^3 rod interface shown in Table 7.5. For this configuration we computed the solutions of a scalar boundary value problem (isotropic coefficient with kink ratio $\kappa = 42$, boundary values 0 and 1 on two opposite faces of the cube) and an elasticity problem (compression by 1 in z direction, which clearly lies far outside the physical range of (even non-)linear elasticity, and material parameters $E = 5, \nu = 0.2$ in the rods and $E = 1, \nu = 0.2$ in the embedding) [281]. The solutions were computed at different resolution and compared to a reference solution obtained on a 513^3 grid (scalar problem) and a 257^3 grid (elasticity problem). We evaluated the L^∞, L^2 , and H^1 norms of the difference by midpoint quadrature now on the finest \mathcal{G}^Δ . In the elasticity case, pointwise ℓ^2 and Frobenius norms were used for differences of the vector-valued quantity and its derivatives, respectively.

We observe in both problems that convergence in L^∞ is far from second order (which is due to outliers at individual quadrature points) whereas convergence in L^2 is closer to order 2 and in H^1 we have almost perfect first order convergence.

Memory Requirements. As in [379] we also list the number of degrees of freedom and the memory requirements for some simulations in this section.

Table 7.6 shows that, unlike in the discontinuous coefficient case, not every node of \mathcal{N}^\square was assigned degrees of freedom for a complicated domain. Moreover, the elasticity problems clearly need 3 DOF per grid node. Even though the interfaces are different in the two cases, one can see that higher density of matrix entries caused by larger parent sets $\mathbb{P}(z)$ of virtual nodes z and the vector-valued CFE construction weights in the discontinuous coefficient case lead to larger memory requirement compared to the complicated domain case.

7.1.4 Condition Numbers of CFE Matrices

Let us now extend the investigation of condition numbers for CFE matrices in [282]. For this purpose and to pronounce the influence of intersected grid cells, we considered an interface perpendicular to the x_1 axis located in $(0.5, 0.75)$ where the computational resolution is 5^3 and with higher sample density near the interval boundaries. A 2D projection of this division of the unit cube in two bricks is shown in Figure 7.7, the extension in the third space direction is constant.

We considered the matrix $M + \tau L$ for $\tau = h$ arising in an implicit Euler scheme for a time-dependent heat diffusion problem and the matrix for an elasticity problem with Dirichlet boundary conditions at the top and bottom. For the complicated domain case, the diffusivity was assumed to be 1 and the material properties for linear elasticity were set to $E = 1$ Pa, $\nu = 0.33$. For the discontinuous coefficients cases, the scalar kink ratio was $\kappa = 42$, in the vector-valued case we used $(E^-, \nu^-) = (70, 0.35)$ and $(E^+, \nu^+) = (3, 0.38)$. With E in GPa, these are realistic values for aluminum and PMMA. Furthermore for the discontinuous coefficient cases, we varied the scalar kink ratio and the stiffness E^- for $(E^-, 0.1)$ and $(E^+, \nu^+) = (1.0, 0.3)$ for fixed geometric location of the interface.

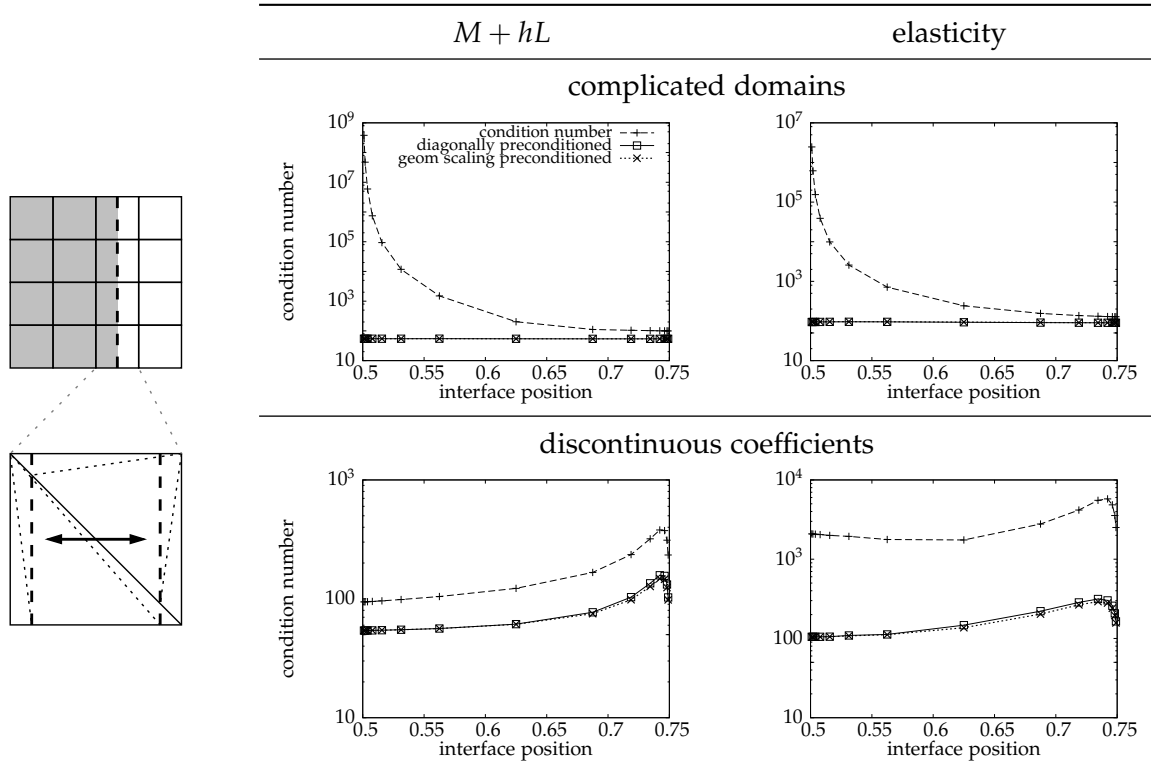


Figure 7.7. For fixed coefficients in the complicated domain cases and fixed discontinuity in the discontinuous coefficients cases, the plots show how changing the geometric location of the interface (shown as a 2D projection on the left) influenced the condition number of CFE matrices in a scalar and vector-valued problem. The plots also show to what extent diagonal and geometric scaling preconditioning are capable of reducing the condition number.

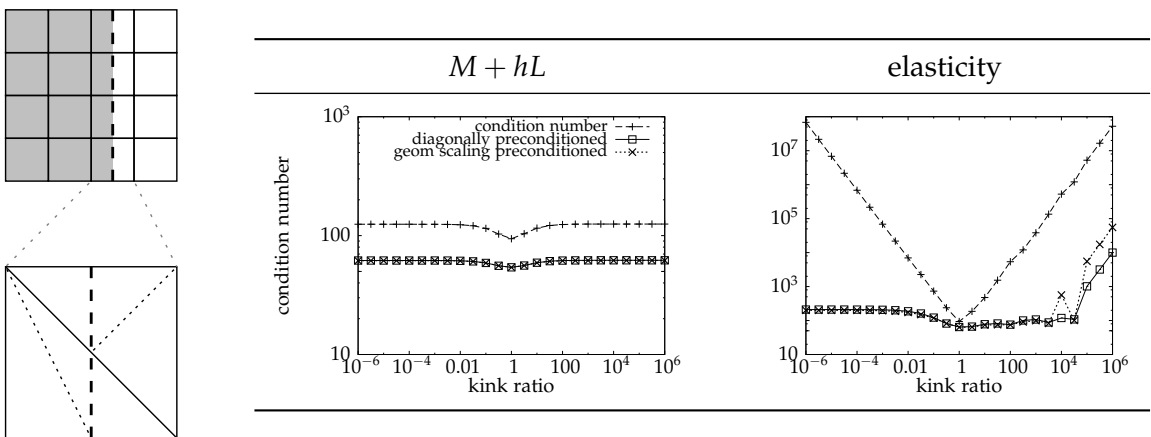


Figure 7.8. For fixed geometric location of the interface, the plots show the influence of the discontinuity in the coefficient on the condition number of CFE matrices for a scalar and vector-valued problem. Again diagonal and geometric scaling preconditioning are capable of reducing the condition number.

The plots in Figures 7.7 and 7.8 then show the condition numbers of the matrices $A = M + hL$ or the elasticity matrix described determined by vector iteration [155, Section 25] for the matrix and its inverse to obtain the largest and smallest eigenvalue. The effect of preconditioning is shown by evaluating the condition number of $D^{1/2}AD^{1/2}$ where D is a diagonal matrix containing the inverses of the diagonal entries of A (diagonal preconditioning [285, Chapter 4]) or the inverses of row-wise l^2 norms of A (preconditioning by geometric scaling [139]).

We observe that bad virtual tetrahedra in the complicated domain case lead to ill-conditioned matrices, which can be remedied by simple diagonal preconditioning. In the discontinuous coefficient cases for fixed discontinuity, the effect of increasingly bad virtual tetrahedra on the condition number of the matrices is marginal. For a fixed location of the interface without bad virtual tetrahedra, varying the scalar kink ratio also has marginal effect on the condition number whereas varying the ratio of Young's moduli (stiffnesses) for discontinuous Poisson's ratio (bulging number) leads to large condition numbers for E^-/E^+ away from 1.

7.1.5 Solver and Preconditioner Performance

For the conjugate gradient (CG) solver [164], smaller condition number of the matrix to be inverted implies a smaller bound on the convergence rate [154], but the actual convergence speed depends on more properties of the system. In the scenarios before, diagonal preconditioning turned out to be capable of reducing the condition number, but this is certainly not the only preconditioning technique.

To investigate the effect of different solvers and preconditioners in CFE simulations of the heat diffusion and elasticity problems above, we considered part of a porcine T1 vertebral trabecular bone dataset at 70 μm resolution and the same physical problems and sets of parameters as before. For the complicated domain example, again $E = 1 \text{ Pa}$, $\nu = 0.33$ were used as elasticity parameters. In case of discontinuous coefficients, the scalar kink ratio and the material parameters were again $\kappa = 42$, $(E^-, \nu^-) = (70, 0.35)$, and $(E^-, \nu^-) = (3, 0.38)$ for the vector-valued problem. The following solvers were used:

1. standard conjugate gradient solver (CG)
2. preconditioned CG solvers [285, Chapter 4] using
 - a) diagonal preconditioning for both physical problems and block-diagonal preconditioning [285, Chapter 4] for the elasticity problem, where the unknowns are (implicitly) ordered in such a way that considering 3×3 blocks along the diagonal simultaneously treats the displacement in all spatial directions at a single node (diag-PCG, blockDiag-PCG)
 - b) geometric scaling preconditioner [139] as described before (geomSca-PCG)
 - c) successive symmetric over-relaxation (SSOR) preconditioning with relaxation parameter $\omega = 1.2$ [154, Chapter 4], again also in a block variant for the elasticity problems (SSOR-PCG)

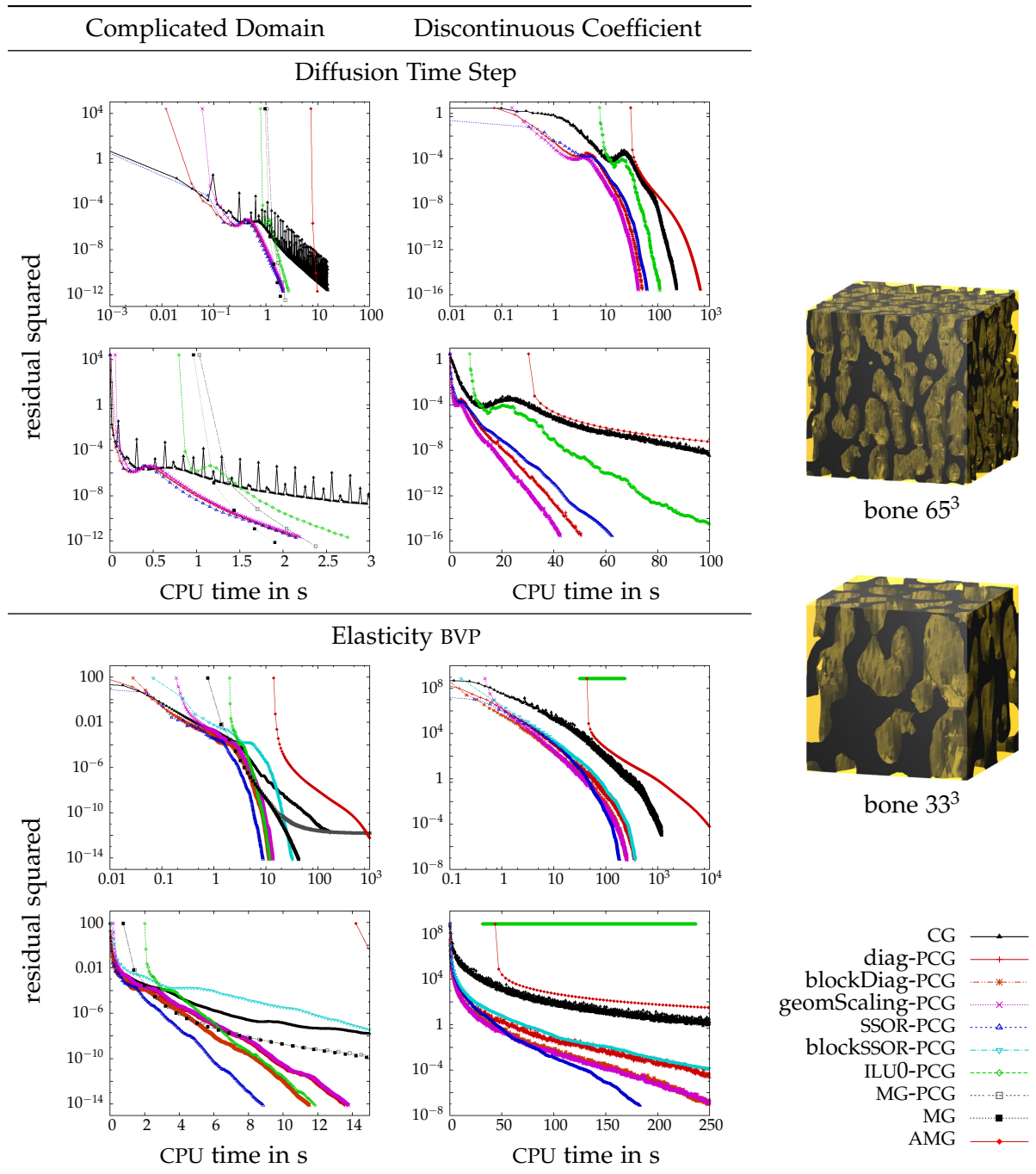


Figure 7.9. The plots show the computational performance of different iterative solvers and preconditioners applied to a scalar (one implicit Euler time step of heat diffusion with time step h using the 65^3 dataset shown on the *right*) and a vector-valued (linear elasticity BVP using the 33^3 dataset shown on the *right*) CFE problem, both for complicated domains and discontinuous coefficients. The *first* and *third row* of plots uses a logarithmic time axis to show the decrease of the squared norm of the residual also for less efficient solvers and to emphasize the different computational workload for setting up the different solvers, whereas the *second* and *fourth row* of plots uses a linear time scale for a better comparison of those solvers that quickly converge for our test problems.

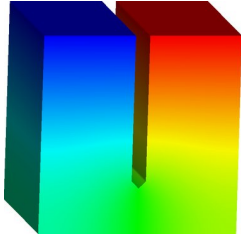
- d) incomplete LU decomposition ILU₀ (see, e.g., [361] or [285, Chapter 4]) as a general-purpose preconditioner which requires conversion of our CFE matrices to some matrix format where all entries are stored (which is not the case for our ‘hybrid’ matrices, cf. Section 6.3.2)
 - e) the CFE multigrid methods described below applied as a preconditioner, using a single V cycle (complicated domains only)
3. the CFE multigrid solvers described in Chapter 5 using $V_2(3,3)$ cycles coarsening up to grid level 2 (5^3 grid), for the case of complicated domains only
 4. the general-purpose algebraic multigrid solver BoomerAMG [163, 116] (part of the HYPRE preconditioner library [82, 117, 115]), viewed as a black box method for our purposes, with Falgout-CLJP coarsening, $V(1,1)$ cycles with hybrid Gauß-Seidel/Jacobi relaxation and which requires converting our CFE matrices to a HYPRE matrix structure

We measured the CPU time on a 3.6 GHz Pentium 4 processor both for setting up the solver and for applying it where the stopping criterion was reduction of the norm of the residual by 8 orders of magnitude or a maximum number of iterations. The total time for applying the solver is then divided by the number of iterations to give an approximate time per iteration. While this is not generally justified, it is a suitable approximation for our purposes. The solvers printed their squared residual after each iteration so we can plot the decrease of the squared residual over approximate CPU time spent. Plotting data points connected by line segments in the plots in Figure 7.9, we can compare the solver performance quantitatively in terms of CPU time and at least qualitatively in terms of iteration count.

This study has some major limitations. The example geometries and problems are chosen arbitrarily without any justification of them being representative for other scenarios. Possibly the parameters of the different solvers can be optimized further for individual scenarios. Moreover, the ILU₀ preconditioner and BoomerAMG solver are general purpose methods and not optimized for the CFE matrix sparsity and data structures, requiring an artificially long setup phase and making them infeasible for larger simulations due to memory consumption. Furthermore we wanted to test a larger (also somewhat arbitrary) selection of solvers by some of which we are restricted to the medium-scale simulations of up to 65^3 . Finally, benefits of parallelization are completely ignored here.

Judging from the examples considered here, preconditioned CG using block-diagonal or standard SSOR as preconditioners seem to be the most robustly efficient solvers. In more detail, the following can be observed:

- Not unexpectedly from the condition numbers determined above, the standard CG converged slowly and preconditioning could significantly improve convergence. Particularly in the scalar problem for complicated domains, standard CG did not converge monotonically but exhibits oscillations.
- Diagonal and geometric scaling preconditioning were comparable in the complicated domain examples whereas geometric scaling was slightly faster in the



l_{expl}	cube with $1/14$ slot		solid cube	
	n_{iter}	final conv. rate	n_{iter}	final conv. rate
6	7	0.106366	7	0.101203
5	8	0.171015	8	0.143673
4	32	0.650487	8	0.152011
3	37	0.696033	8	0.154998
2	39	0.706050	8	0.159531

Figure 7.10. For the geometric object shown on the *left* resolved at grid level 7 corresponding to computational resolution 129^3 , the table lists the number of $V_{l_{\text{expl}}}(3,3)$ multigrid cycles for different explicit levels $l_{\text{expl}} < 7$ and the convergence rate in the final iteration. For comparison, the same numbers are listed for a solid cube without slot. Convergence breaks down as soon as coarse grid corrections involve basis functions supported in both legs of the ‘horseshoe’.

discontinuous coefficient examples. Block-diagonal preconditioning lead to faster convergence even though each iteration had slightly higher workload.

- Standard SSOR preconditioning, in contrast, outperformed block-SSOR preconditioning in terms of CPU time. For the discontinuous coefficient example, this was even true in terms of iteration count.
- The ILUo preconditioner took significant time to set up, which is not surprising as an incomplete LU decomposition needs to be computed. It then performed well in many of the examples but seemed to be ineffective for the discontinuous elasticity examples.
- Our CFE multigrid method needs to perform matrix coarsening. It was fast in the scalar complicated domain example but not in the elasticity examples, both when used as a solver and as a preconditioner.
- The BoomerAMG method was the slowest method when being set up, which is also hardly surprising as it had to copy the matrix and analyze its sparsity structure for algebraic coarsening. Convergence of the AMG afterwards was only comparable to the other efficient methods in the scalar complicated domain example.

Let us finally show one example where the CFE multigrid solver for complicated domains fails for an inappropriate choice of the grid resolution where an explicit solver is applied. For this purpose, consider the horseshoe-type object shown in Figure 7.10 for which we solve the heat equation with Dirichlet boundary data ± 1 at the end plates of the two legs. The gap has width $1/14$, so the coarsest level at which basis functions will extend across the gap will be grid level 4 corresponding to resolution 17^3 . Using different explicit levels in the multigrid solver, we clearly observe that the convergence rate and the number of iterations breaks down at that point.

7.2 Heat Diffusion Simulations

We now consider the scalar model problem of heat diffusion for numerical simulations, both for complicated domains and for discontinuous coefficients, using both artificial and actual physical objects.

7.2.1 Complicated Domains

Let us first consider the case of complicated domains. Artificial objects consisting of an array of cylindrical pillars between two thick plates are shown in Figure 7.11, where a heat source was placed in one corner [217]. $V_2(3,3)$ multigrid cycles were used with a stopping criterion of reducing the norm of the residual by 8 orders of magnitude. For the 4×4 and 32×32 pillar example (leftmost and rightmost picture in Figure 7.11) in (resolved on a 257^3 grid), 12 and 142 iterations with convergence rates 0.251 and 0.944 were necessary, taking and 37 and 40 seconds per iteration, respectively.

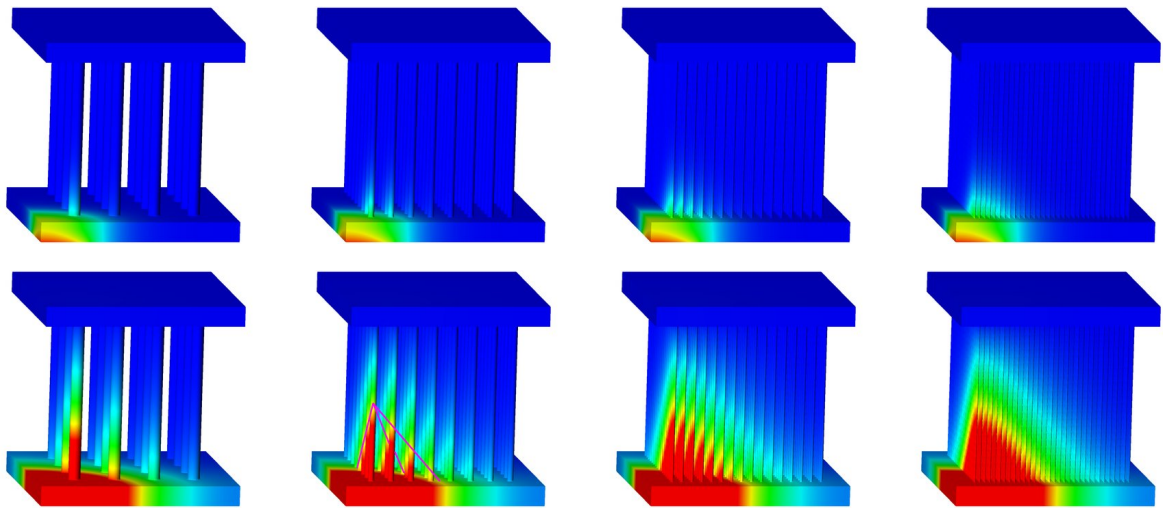
The resulting temperature profiles at time $t = 5$ and $t = 30$ in Figure 7.11 show that the resulting temperature isosurfaces do not resemble spheres as one would observe in a solid object but—due to the geometric structure—a cone as indicated in the 8×8 example.

A realistic geometry is shown in Figure 7.12 where the tissue part of a human liver was considered as computational domain [217]. Blood vessels (where one would also have to deal with advection, see the author's Diplom thesis [309] for a simple coupled 2D model) were not included in the heat diffusion simulation with a local source at 129^3 resolution, making the simulation realistic only to a limited extent.

Again, $V_2(3,3)$ multigrid cycles were used with a stopping criterion of reducing the norm of the residual by 8 orders of magnitude. In the first diffusion time step, the solver requires 12 iterations with convergence rate 0.219 in the final iteration which took 4.3 seconds.

7.2.2 Discontinuous Coefficients

As for the case of discontinuous coefficients, let us consider the specimen of Al/PMMA shown in Figure 7.13 with edge length 7.71 mm resolved at 257^3 [281]. Using realistic volume-specific heat capacities $\rho c = \{2.43, 1.75\} \cdot 10^6 \text{ J/m}^3\text{K}$ and thermal conductivities of $\lambda = \{237.0, 0.19\} \text{ W/m}\cdot\text{K}$ for Al and PMMA, respectively, we here considered a kink ratio of approximately 1247 in λ . The initial condition for the temperature was 293.15 K (room temperature), boundary conditions were set to 194.65 K (sublimation point of CO_2) at the bottom and 373.15 K (boiling point of H_2O) at the top. The results in Figure 7.13 show that an almost steady state was reached significantly faster in the metal than in the plastic.



# pillars	4×4	8×8	16×16	32×32
# DOF	4 350 226	4 545 512	4 990 894	6 010 360
# virtual nodes	1 192 986	1 875 326	3 188 938	5 521 294

Figure 7.11. On an object consisting of parallel pillars of increasing number and thus increasing geometric complexity (4×4 up to 32×32) between two plates, we simulated diffusion of heat from a source in one corner. An HSV colorbar shows the temperatures on the interior at times $t = 5$ (top row) and $t = 30$ (bottom row). The magenta lines in the lower, second to left visualization indicate a temperature isosurface. The table moreover lists the the number of DOF and of virtual nodes.

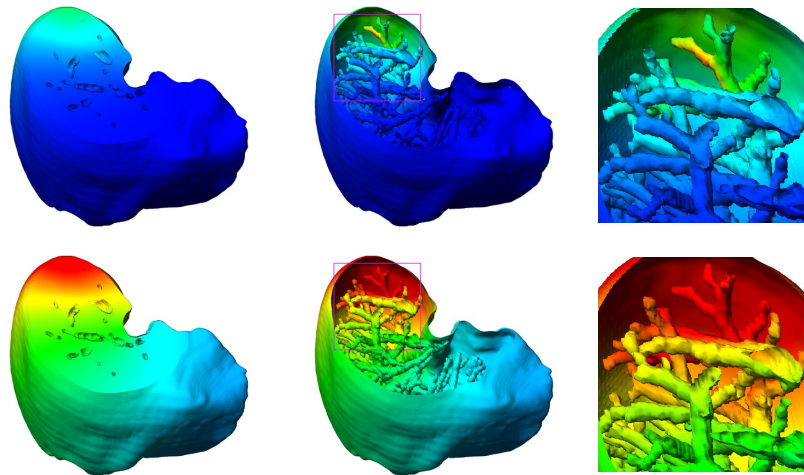


Figure 7.12. Diffusion of heat was simulated on a domain segmented from a CT dataset of a human liver (dataset by Tobias Preusser, Fraunhofer MEVIS), where blood vessels are considered as void. The top row shows the temperature profile at $t = 5$ whereas the bottom row two correspond to $t = 30$. In the left column we show cuts through the computational domain whereas in the middle column the internal vascular structure (which is not part of the computational domain) is shown colored by the temperature on the interface according to an HSV colorbar. The right column shows zooms to the regions indicated.

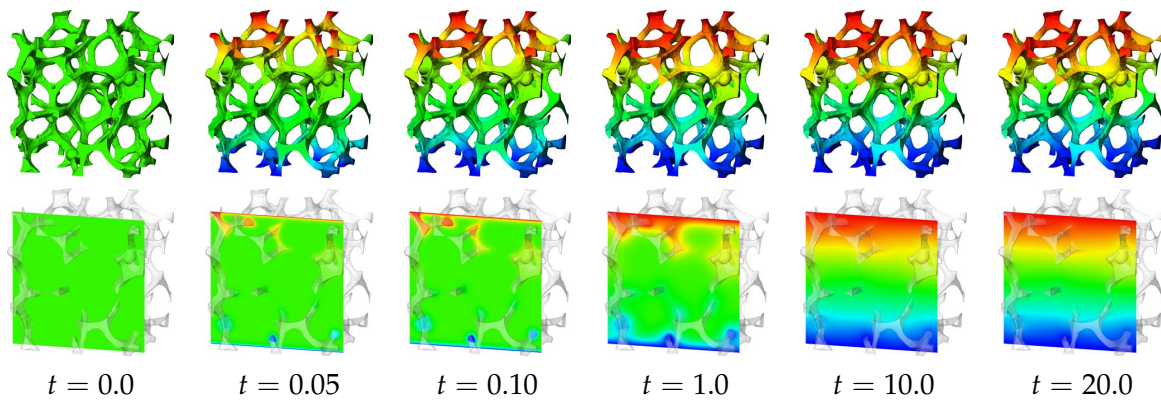


Figure 7.13. On a specimen of Al foam embedded in PMMA with a kink ratio in the thermal diffusivities of $237 : 0.19$, we simulated the diffusion of heat. Temperatures for the given times are visualized on the material interface (*top row*) and on a slice through the composite material (*bottom row*).

7.2.3 Thermal Diffusivity of Meat Specimens

Application Background

An important problem in cold chain management is to estimate temperature profiles in goods being transported depending on environmental influences during transport. For this purpose, different thermal effects such as conductive, convective and radiative heat transfer are included in models that can become rather involved to properly represent the underlying physical processes and material properties.

One application of CFE in this context [295] is a simulation to determine the thermal diffusivity of meat (chicken breast). Let us briefly describe the experiments and models used for this purpose. Figure 7.14 shows the experimental setup used in [355, 295]: a piece of meat is placed in water (inside a *Dewar flask*², an insulating container) which was stirred continuously. Time-dependent temperature curves of the water and at approximately the center of the meat were measured until they reached a steady equilibrium value. This final value yields the specific heat capacity of the meat whereas the temporal evolution depends on and can be used for determining the thermal diffusivity coefficient.

This section summarizes joint work with Judith Kreyenschmidt, Verena Raab, and Annette Rudolf (Cold Chain Management group, Institute of Animal Science, University of Bonn), and Remmer Meyer-Fennekohl (Institute for Applied Physics, University of Bonn). This material has not been published yet and is thus presented here in some detail.

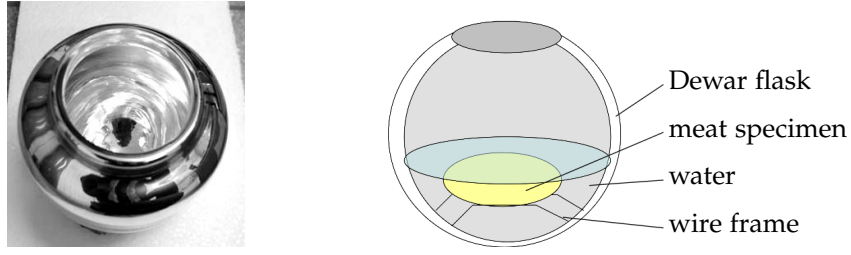


Figure 7.14. The experimental setup for determining thermal diffusivity coefficients of meat is shown on the *right*. Inside an insulating container (Dewar flask, photo on the *left*), a cold piece of meat was placed in water at room temperature. Under constant stirring, temperatures of the water and near the center of the meat were measured. The images were adapted from [295, Figures 3 and 4].

Numerical Model

The heat capacity of the dewar flask was first determined experimentally. The water was then assigned ‘virtual’ material properties, namely a specific heat capacity

$$\rho c_W = 10^3 \frac{\text{kg}}{\text{m}^3} \cdot \left(4.1868 \frac{\text{J}}{\text{gK}} + \frac{C_{\text{Dewar}}}{m_{\text{water}}} \right) \quad (7.6)$$

also accounting for the Dewar flask, and a ‘large’ thermal diffusivity accounting for the stirring process. The equilibrium temperature was used to determine the specific heat capacity ρc_M of the meat.

For the CFE simulation, we chose a cubic water domain of edge length s with specific heat capacity

$$\rho c_V = \frac{\text{real water volume}}{\text{box volume} - \text{meat volume}} \cdot \rho c_W \quad (7.7)$$

in which an ellipsoid with radii $0.4s$, $0.26s$, $0.1s$ represented the piece of meat. These radii approximated the geometry of actual chicken breasts as measured in [355]. The edge length s was chosen such that the volume of the ellipsoid was the same as the (measured) volume of the specimen. Since we did not have scans of each specimen used and since the exact position of the temperature probe was unknown, this simple approximation is sufficient. The temperature sensor inserted into the meat was ignored for the diffusion process.

Artificial thermal diffusivity values were set to $a_M = 1 \text{ m}^2/\text{time unit}$ for the meat and $a_V = 100 \text{ m}^2/\text{time unit}$ for the virtual water. What matters here is that the ‘virtual’ water has large thermal diffusivity compared to the meat to account for the stirring process. A rescaling of the units of time was later used in a parameter fitting to obtain a value of a_M in SI units (see below).

The initial temperature profile throughout water and meat cannot be modelled to be discontinuous if we use (globally) continuous FE for the simulation, instead

²Named after the British chemist and physicist James Dewar, * September 20, 1842 in Kincardine-on-Forth, Scotland, † March 27, 1923 in London [1].

nodal values are interpolated continuously at the meat/water interface. To start with correct initial energy contained in the meat, we corrected its specific heat capacity as follows

$$\rho C_M \leftarrow \rho C_M \cdot \frac{\int_{\Omega} I^{\text{CFE}} \chi_{\text{meat}}}{\text{volume of meat}}. \quad (7.8)$$

This effect was neglected for the water domain.

Our usual implicit Euler time stepping scheme was used for numerically solving the time-dependent heat equation. In this case, however, using the standard CFE mass matrix lead to violation of the maximum principle, more precisely an unphysical decrease of the central meat temperature was observed in the simulation. This well-known effect can be remedied by using lumped mass matrices [335]. Computational resolution was 65^3 and the time step was 1 in the artificial units. For each time step, the temperature value at the center of the (meat) ellipsoid was evaluated.

Parameter Fitting

Suppose temperatures inside the meat were measured with time step τ_v and its values are given in a value vector V of length K , the computation was performed with time step τ_u and values are stored in a vector in U . If we assume that in both cases initial conditions were given at $t = 0$ and temperature remained constant after the last measurement/sample, we can interpolate (and extrapolate) the temperature via

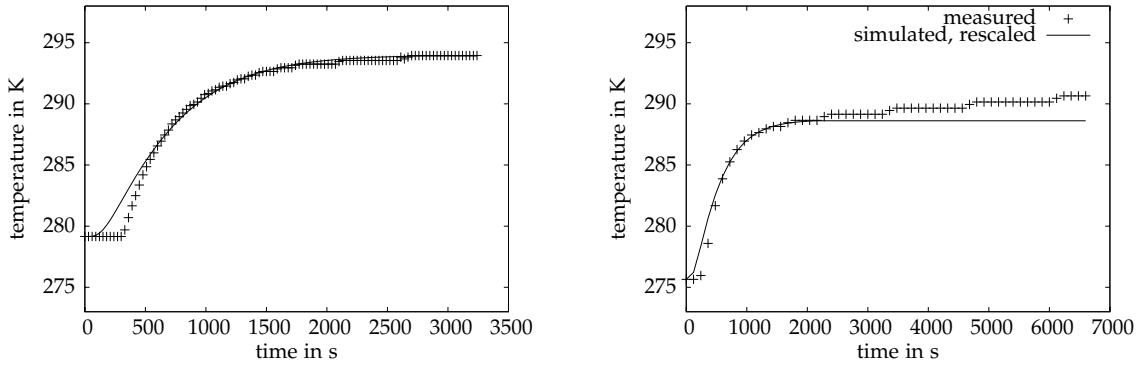
$$\begin{aligned} v(t) &= \mathcal{I}^{\text{lin}}[V] \left(\frac{t}{\tau_v} - t_{\text{shift}} \right) && \text{(measured)} \\ u[\theta](t) &= \mathcal{I}^{\text{lin}}[U] \left(\frac{\theta t}{\tau_u} \right) && \text{(simulated)} \end{aligned} \quad (7.9)$$

where θ is the unknown factor by which $\lambda = 1$ needs to be scaled to obtain λ_M , this is the inverse scaling of τ_u . u and v are extended to the left and right by the initial and terminal temperatures, respectively. Moreover, t_{shift} is an unknown time offset due to variable beginning of the measurement. \mathcal{I}^{lin} is the piecewise linear interpolation of the discrete values, constantly extended outside the considered time intervals.

We determined θ and t_{shift} by parameter fitting, more precisely by minimizing the squared error between measurement and simulation over θ over an appropriate time interval $[t_{\text{minF}}, t_{\text{maxF}}]$,

$$\begin{aligned} E(\theta, t_{\text{shift}}) &= \int_{t_{\text{minF}}}^{t_{\text{maxF}}} |u[\theta](t) - v(t - t_{\text{shift}})|^2 \\ &\approx \sum_{k=K_{\text{minF}}}^{K_{\text{maxF}}} \left| \mathcal{I}^{\text{lin}}[U] \left(\frac{\theta k \tau_v}{\tau_u} \right) - V_{k-K_s} \right|^2 \rightarrow \min! \end{aligned} \quad (7.10)$$

where $t_{\text{minF}} = \tau_v K_{\text{minF}}$, $t_{\text{maxF}} = \tau_v K_{\text{maxF}}$, $t_{\text{shift}} = \tau_v K_s$ and $V_k = V_0$ for $k < 0$.



experiment #	20080819V1	20090508V1
size of bounding box s in m	0.1438	0.1193
water volume in m^3	$5.80 \cdot 10^{-4}$	$2.95 \cdot 10^{-4}$
initial temperature water in K	296.45	290.65
initial temperature meat in K	279.15	275.65
meat ρC_M in $\text{J}/\text{K}\cdot\text{m}^3$	$3.4215 \cdot 10^6$	$2.9235 \cdot 10^6$
virtual water ρC_V in $\text{J}/\text{K}\cdot\text{m}^3$	$4.5282 \cdot 10^6$	$4.7700 \cdot 10^6$
rescaling factor θ	0.4069	0.3141

Figure 7.15. Results of the parameter fit for computing thermal diffusivities of chicken meat for two measurements in [355] (left) and [295] (right).

We used a simple interval nesting scheme for the minimization in θ and fixed discrete possibilities for minimization in t_{shift} because $E(\theta, t_{\text{shift}})$ is sufficiently non-oscillatory but not necessarily convex (thus we need a global optimization strategy) and the objective function depends on only two variables. For the results in Figure 7.15 we used the time interval $t_{\text{minF}} = 500$ s, $t_{\text{maxF}} = 2500$ s.

The table in Figure 7.15 lists the parameters of two measurements and the rescaling factor θ which is also the value of λ in $\text{W}/\text{m}\cdot\text{K}$. For 4 experiments in [355], $\lambda = 0.354 \pm 0.064$ $\text{W}/\text{m}\cdot\text{K}$ (mean \pm standard deviation) was obtained, for 5 experiments in [295], we obtained $\lambda = 0.361 \pm 0.045$ $\text{W}/\text{m}\cdot\text{K}$. These values compare quantitatively to those obtained for turkey (processed and emulsified meat) in [230, Fig 1] which can be extrapolated to around 0.3 $\text{W}/\text{m}\cdot\text{K}$ in our temperature range, the authors of [375] obtain $\lambda = 0.477$ $\text{W}/\text{m}\cdot\text{K}$ by measurements using a guarded hot plate.

While the authors of [230] consider a temperature range of 293 to 353 K (20 to 80 °C) and find a dependence of λ on the temperature, we assumed that in our lower temperature range (below 295 K), λ does not change significantly with temperature.

For the matches shown in Figure 7.15, we observed an increase of temperature of both meat and water at the end of the measurements (and not the simulations). This is probably due to an influence of the environment and thus ignored for matching simulated and measured curves.

7.3 Linear Elasticity Simulations

For the linear elasticity simulations described in this section, we considered both artificial objects and scans of actual physical specimens. For most of the artificial objects we simulate large deformations that, in reality, would lie far outside the range of linear elasticity but allow unscaled visualization.

7.3.1 Individual Artificial Objects

Complicated Domains

Again let us start with simulations for complicated domains. We first considered compression of solid domains with spherical holes shown in Figure 7.16 [217, 282]. The bottom of the objects was fixed and we impose a downward displacement at the top by 1% of the edge length. Material parameters are $E = 1$, $\nu = 0.33$. The deformed objects are colored according to the von Mises stress at the interface.

For the left and middle objects shown in Figure 7.16, $3 \cdot 258\,064 = 774\,192$ and $3 \cdot 16\,458\,648 = 49\,375\,944$ DOF were used, and the simulations required 534 MiB and 28 GiB, respectively. The first simulation could thus be run on a standard PC, taking 193 seconds (about three minutes) on a 3.6 GHz Pentium 4 processor for the multigrid solver with the usual stopping criterion (reduction of the norm of the residual by 8 orders of magnitude) and achieving convergence rate 0.548 in the last iteration. The second simulation was run on a compute server and the solver took 10 411 seconds (less than three hours) on one 1.8 GHz Opteron processor, achieving convergence rate 0.552 in the last iteration. For the right object, $3 \cdot 16\,482\,675 = 49\,448\,025$ DOF were used. The multigrid solver using $V_2(3,3)$ cycles needed 19 iterations taking 579 seconds (less than ten minutes) each and achieved a convergence rate 0.580 in the last iteration.

A second compression scenario (again by 1%) was simulated on the artificial trabecular objects shown in Figure 7.17. These are 3D grids of $20 \times 20 \times 20$ rods resolved at 257^3 , and the same geometry with 10 percent (up to integer rounding) of the trabeculae removed at random (see below for details). These simulations

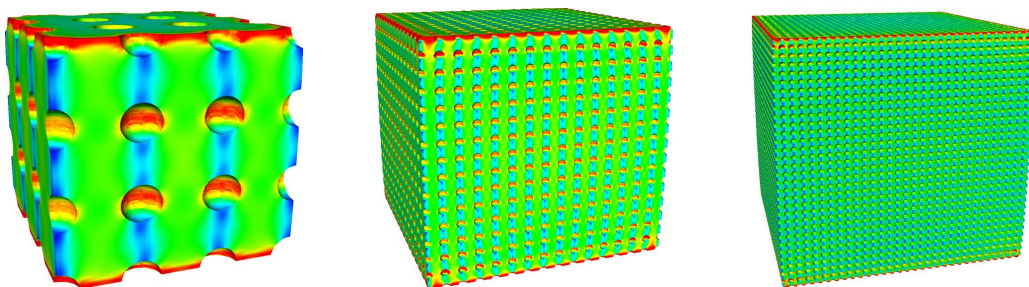


Figure 7.16. Results of a compression simulation for a solid domain with 8^3 spherical holes at resolution 65^3 and 16^3 and 32^3 spherical holes at resolution 257^3 (from left to right). The HSV colorbar indicates the von Mises stress at the interface.

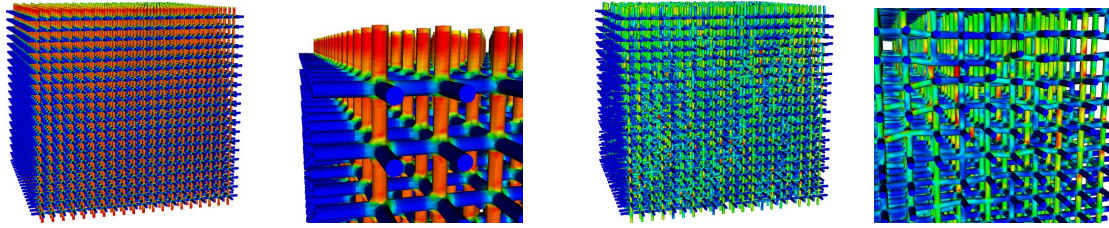


Figure 7.17. From *left to right*, compression of $20 \times 20 \times 20$ rods and zoom to the top left corner, the same object minus 10 percent of the trabeculae (chosen randomly) removed, and zoom to an ‘interesting’ region are shown.

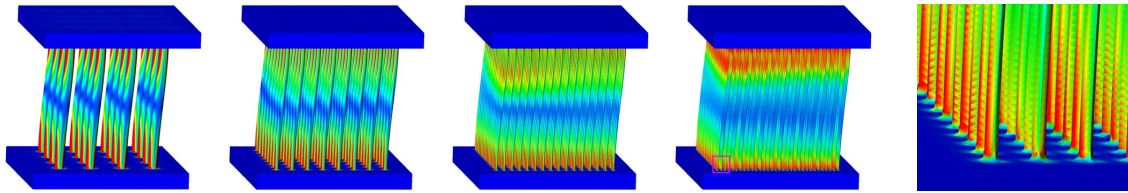


Figure 7.18. The elastic deformation of artificial objects under shearing displacement is shown. From *left to right* the number of pillars increases from 4×4 to 32×32 , again resolved on a 257^3 computational grid. For the 32×32 case we additionally show a zoom to the lower left corner. The HSV colorbar indicates the von Mises stress at the interface.

used $3 \cdot 5\,028\,836 = 15\,086\,508$ and $3 \cdot 4\,653\,815 = 13\,961\,445$ DOF, they required about 30 GiB of memory and about 1.4 and 4 days of CPU time on one Opteron 1.8 GHz processor, respectively. Poor final multigrid convergence rates of approximately 0.977 and 0.996 were observed in this case, which is not surprising for this type of microstructure.

As other examples of artificial objects we reused the objects shown in Figure 7.11. We there simulated shearing by fixing the bottom of the object and imposing a displacement of the top to the right [217]. The same type of visualization as before is used to show the results in Figure 7.18.

Discontinuous Coefficients

As a first toy example for discontinuous coefficients, we considered a spherical stiff sphere of radius 0.3 ($E_{\circ} = 10$ and $\nu_{\circ} = 0.1$) embedded in a softer cube [310] of edge length 1 m ($E_{\square} = 1$ and $\nu_{\square} = 0.3$), cf. Figure 7.19. For a compression simulation by 20% of the edge length, the bottom face was fixed and the top face was shifted in downward direction. Figure 7.19 shows the undeformed and deformed object and a visualization of the displacement. A resolution of 65^3 was used for this simulation, resulting in a memory requirement of about 550 MiB.

Let us furthermore study the influence of a spatially varying elasticity tensor. For this purpose, we considered a circular column embedded in a softer material

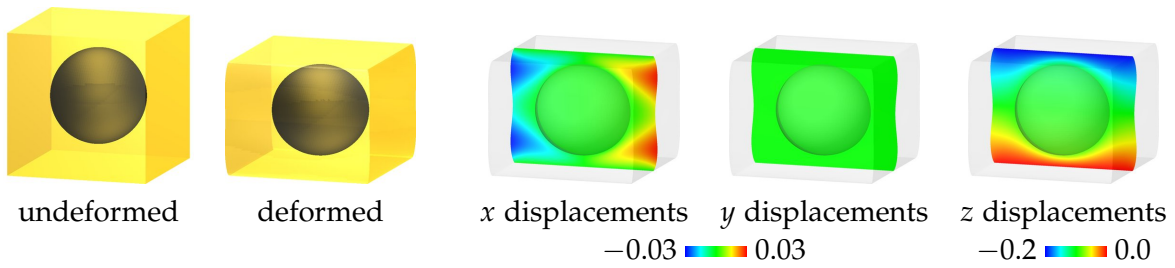


Figure 7.19. Results of an elasticity simulation (compression by 20%) with discontinuous coefficients. The effect of the 10-fold stiffness of the sphere becomes visible both in the deformed object and in the displacements.

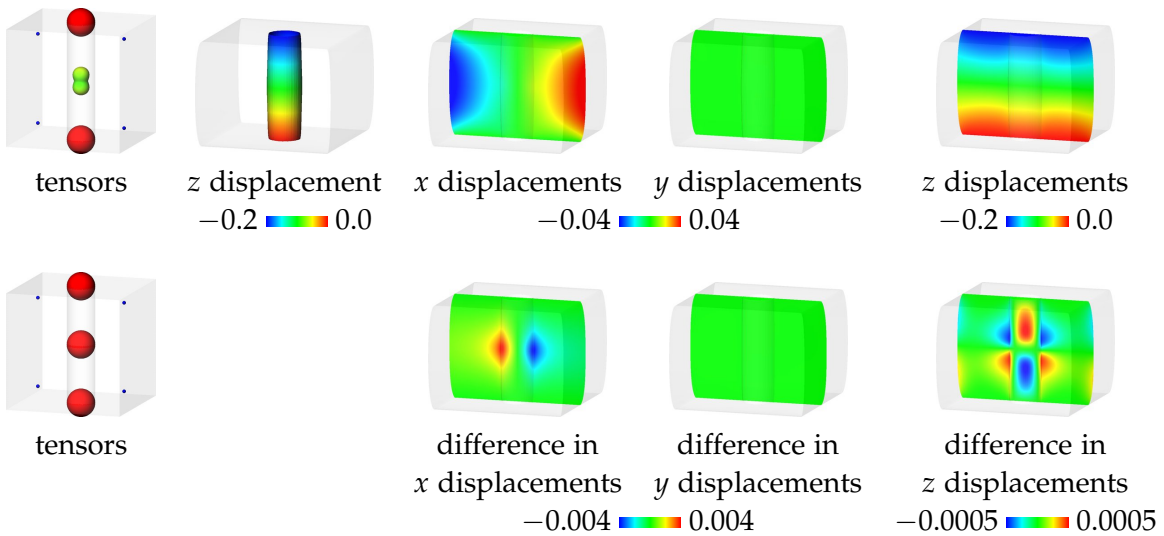


Figure 7.20. A comparison of piecewise constant and spatially varying material properties for a stiff column embedded in a softer material is shown. On the *very left*, the elasticity tensors are visualized for different geometric locations within the object. The *top row* visualizes the displacement of the object subject to compression on the material interface and on a slice at $y = 0.5$ through the object, the bottom row shows the difference to displacements obtained for constant elasticity tensor in the column.

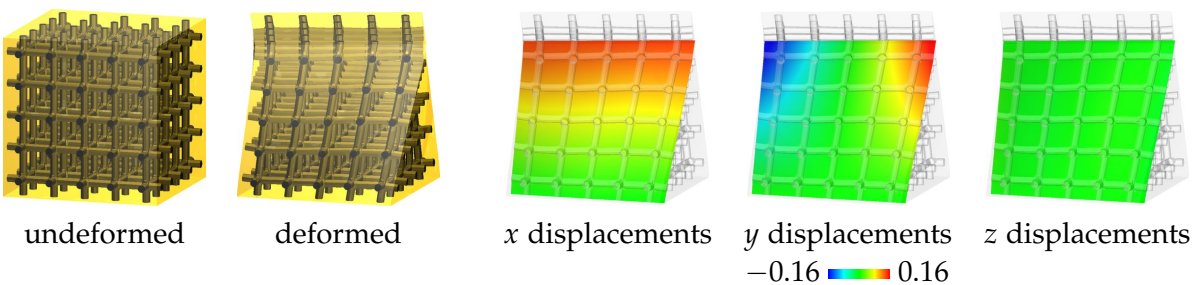


Figure 7.21. Results of a torsion by 20° simulation for an artificial trabecular dataset with varying transverse isotropy in the trabeculae are shown. On a slice through the object, the three spatial components of the displacement are visualized.

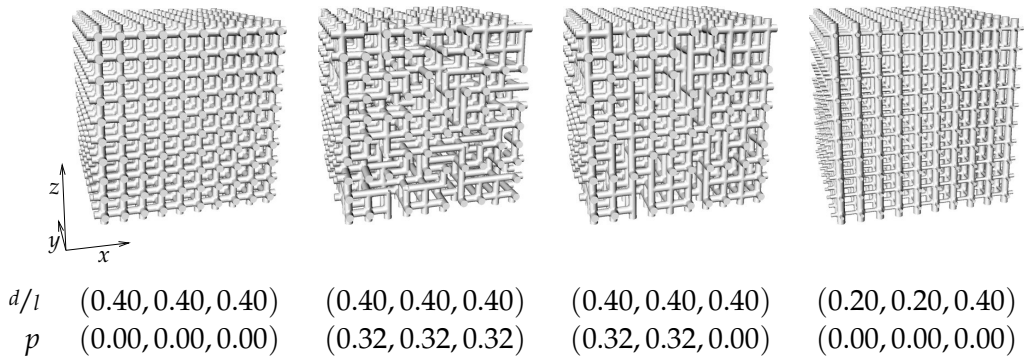


Figure 7.22. Artificial $10 \times 10 \times 10$ trabecular datasets are parameterized by the diameter-to-length ratios d/l of the trabeculae and the degradation ratios p (up to integer rounding) in the three space directions.

as shown in Figure 7.20. We first simulated compression for constant material parameters $E_{\square} = 1$ and $\nu_{\square} = 0.38$ in the surrounding material and $E_{\circ} = 10$ and $\nu_{\circ} = 0.33$ in the column (results not shown). Then the material parameters of the column were modified in such a way that it has only half Young's modulus $E_{\circ}(z = 0.5) = 5$ in the middle with linear transition to $E_{\circ}(z \in \{0, 1\}) = 10$ at the top/bottom. In Figure 7.20 we show the resulting displacements for this second case and the difference to the case of piecewise constant stiffness tensor for compression by 20%. Combined with the surrounding material, the spatially varying material parameter in the column (being softer on average) lead to slightly more bulging.

A more complicated example for spatially varying elasticity tensor is shown in Figure 7.21. In this example from [310], we considered a $5 \times 5 \times 5$ grid of circular rods. Using the transversely isotropic elasticity tensor

$$C = \begin{bmatrix} 19.7785 & 8.4190 & 8.4190 & & & \\ 8.4190 & 16.1824 & 7.6152 & & & \\ 8.4190 & 7.6152 & 16.1824 & & & \\ & & & 8.5671 & & \\ & & & & 9.4713 & \\ & & & & & 9.4713 \end{bmatrix}$$

in GPa for human vertebral trabecular bone [381], we assigned this tensor C (rotated appropriately for the trabeculae so that the longitudinal axis was assigned the more stiff x direction in C) to the center of the trabeculae and interpolate trilinearly in between. The surrounding material was assigned the isotropic properties of PMMA ($E = 3$ GPa, $\nu = 0.38$). Figure 7.21 shows the results of simulation of 20° torsion.³ In reality this lies far outside the range of linear elasticity but enhances the visualization of the effect here.

³Notice that, in linearized elasticity, torsion by 20° is *not* the same as torsion by 1° scaled by 20.

7.3.2 Statistical Osteoporosis Models

In [379], a wider selection of artificial trabecular objects was considered, selected results are reported here. For compression and shearing simulations, the effect of different degradation scenarios (thinning or removal of trabeculae) on the macroscopic stiffness was investigated. These objects are characterized by a *diameter-to-length ratio* d/l of the trabeculae and a *removal percentage* p , see Figure 7.22. Both are triples whose entries correspond to the trabeculae in the different space directions. If all entries are the same, p and d/l are also given as a scalar and referred to as ‘isotropic’. Trabeculae to be removed were chosen randomly using a pseudo random number generator based on the *Mersenne twister*⁴ [235].

The objects considered consisted of $10 \times 10 \times 10$ rods with circular cross section of diameter 0.134 mm [165] for the reference configuration $d/l = 0.4$, resulting in 9×9 internal trabeculae in each space direction and 10×10 free trabecular ends on each face at the outside. The bottom face was clamped (zero Dirichlet boundary conditions), for the top face we imposed a displacement in longitudinal (downward; compression in z direction) or transverse direction (to the right; shear in x direction). We did not impose displacement boundary conditions on the remaining side faces. Microscopically we assumed Young’s modulus $E = 13.4$ GPa [291] and Poisson’s ratio $\nu = 0.33$ [291, 201] for the structures, corresponding to $\lambda \approx 9.779$ GPa, $\mu \approx 5.038$ GPa.

After computation of the displacements for the given boundary conditions and in order to evaluate the macroscopic stiffness, we evaluated the corresponding forces acting on the elastic object. For this purpose, we considered cutting planes A parallel to the fixation plane through the object. Consider one such cutting plane passing through grid points and a virtual CFE tetrahedron T for which one face $T \cap A$ lies in the cutting plane. Then the displacement u is affine within T , thus the local stress tensor

$$\sigma(T) = \mu \left[\nabla u(T) + (\nabla u(T))^T \right] + \lambda [(\operatorname{div} u(T))\mathbb{1}] \quad (7.11)$$

is constant in T and we can compute the force distribution $\int_{T \cap A} \langle \sigma(x), n(x) \rangle$ on the local facets $T \cap A$. For each facet in the interior we average the two forces evaluated on the two adjacent tetrahedra. Hence, the total force on A can be approximated by

$$F(A) = \sum_T \langle \sigma(T), n \rangle \cdot \operatorname{area}(T \cap A) \quad (7.12)$$

where we sum over all faces $T \cap A$ lying in the cutting plane. Let us emphasize that due to static equilibrium, the exact value for the resulting total force is independent of the cutting plane. To avoid numerical artifacts at specific slices, we chose a larger set of lattice planes and computed mean and standard deviation of the forces obtained for each of these planes. For each configuration of d/l and p , we considered six different specimens, the plots show the corresponding six mean values and six standard deviations corresponding to the per-specimen averaging.

⁴Named after the French theologian, philosopher, mathematician, and music theorist Marin Mersenne, * September 8, 1588 near near Oizé, Maine, † September 1, 1648 in Paris [1].

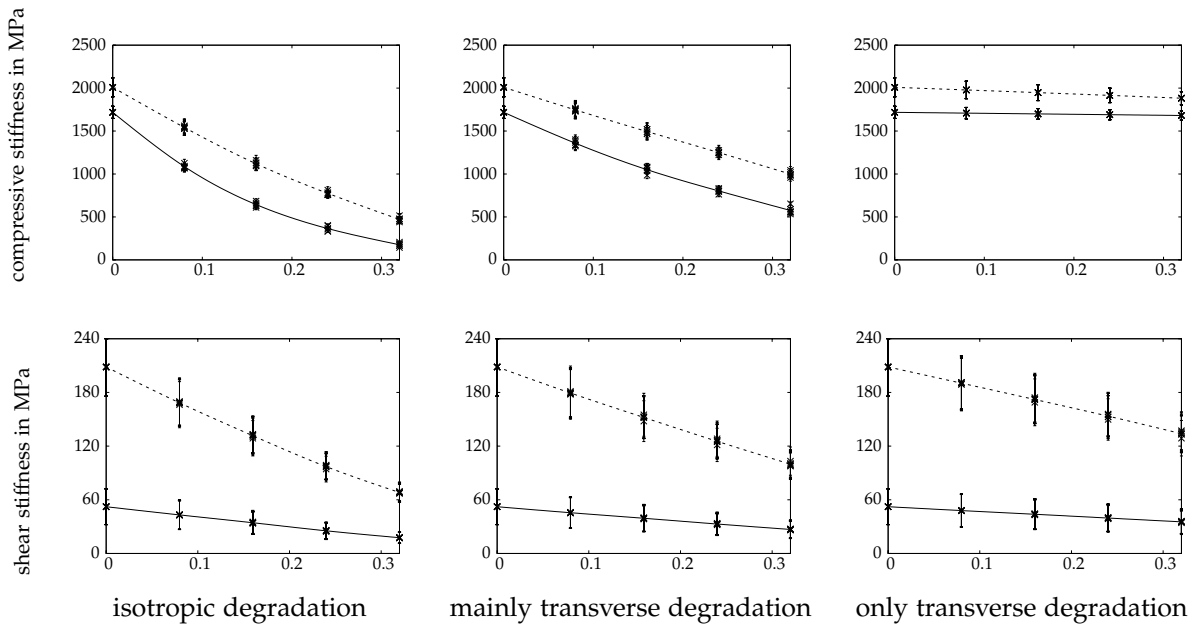


Figure 7.23. For specimens with $d/l = (0.4, 0.4, 0.4)$ (*dashed lines*) and $d/l = (0.2, 0.2, 0.4)$ (*solid lines*, thinner transverse trabeculae), we consider isotropic ($p = (\beta, \beta, \beta)$, *left*), mainly transverse ($p = (\beta, \beta, \beta/2)$, *middle*) and only transverse ($p = (\beta, \beta, 0)$, *right*) degradation. The plots show the decrease of compressive (*top row*) and shear (*bottom row*) stiffness for $\beta \in [0, 0.32]$. The standard deviations shown by error bars in the plot are those obtained for each specimen when computing the compressive forces for different cutting planes through the object.

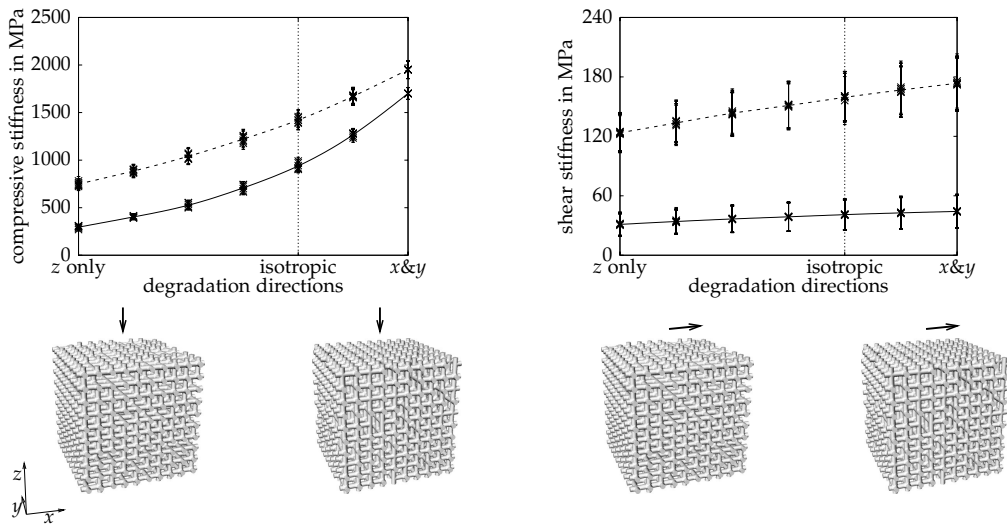


Figure 7.24. For specimens with $d/l = (0.4, 0.4, 0.4)$ (*dashed lines*) and $d/l = (0.2, 0.2, 0.4)$ (*solid lines*, thinner transverse trabeculae), we fixed a total degradation of 10%. The plots show how varying the degradation anisotropy according to $p = (0.5\beta, 0.5\beta, 0.3 - \beta)$, $\beta \in [0.0, 0.3]$, from degradation in longitudinal direction z to degradation in the transverse directions x and y (*left to right* in the plots) influences macroscopic compressive (*left plot*) and shear (*right plot*) stiffness.

Table 7.25. The relative loss of compressive *top table* and shear *bottom table* stiffness for isotropic up to 32% degradation of specimens with different d/l is listed averaged over 6 different specimens, along with the average (intra-specimen) standard deviations for the force computation process.

p	$d/l = 0.4$	$d/l = 0.3$	$d/l = 0.2$	$d/l = (0.2, 0.2, 0.4)$
0.00	0.000 ± 0.055	0.000 ± 0.074	0.000 ± 0.113	0.000 ± 0.041
0.08	0.233 ± 0.040	0.267 ± 0.051	0.317 ± 0.074	0.368 ± 0.026
0.16	0.443 ± 0.028	0.494 ± 0.034	0.563 ± 0.045	0.625 ± 0.015
0.24	0.615 ± 0.019	0.669 ± 0.021	0.737 ± 0.026	0.788 ± 0.009
0.32	0.766 ± 0.011	0.812 ± 0.012	0.865 ± 0.013	0.898 ± 0.005

p	$d/l = 0.4$	$d/l = 0.3$	$d/l = 0.2$	$d/l = (0.2, 0.2, 0.4)$
0.00	0.000 ± 0.156	0.000 ± 0.259	0.000 ± 0.529	0.000 ± 0.382
0.08	0.192 ± 0.125	0.184 ± 0.210	0.174 ± 0.436	0.175 ± 0.310
0.16	0.369 ± 0.097	0.355 ± 0.168	0.339 ± 0.348	0.343 ± 0.242
0.24	0.534 ± 0.071	0.522 ± 0.121	0.507 ± 0.258	0.516 ± 0.175
0.32	0.673 ± 0.050	0.663 ± 0.084	0.652 ± 0.181	0.663 ± 0.120

In Figure 7.23 we considered a reference configuration of $d/l = 0.4$ in each space direction and an object with thinner transverse trabeculae subject to different degradation scenarios. We observe that the trabeculae in longitudinal direction play an important role for shear stiffness and even more so for compressive stiffness. Loss of transverse trabeculae, however, has a significantly smaller influence on the macroscopic stiffness.

Isotropic degradation for different d/l is considered in Table 7.25 where we computed the loss of compressive and shear stiffness relative to the full $10 \times 10 \times 10$ structure. We here observe that the loss of compressive stiffness varies more with varying diameter of the trabeculae than the shear stiffness does.

We moreover investigated how anisotropy of the degradation (for a fixed total degradation percentage) influences the macroscopic compressive and shear stiffness. Figure 7.24 shows that the macroscopic compressive stiffness is more sensitive to degradation anisotropy than shear stiffness.

For the specimen with radii $d/l = (0.2, 0.2, 0.4)$ and isotropic degradation ratios $p = (0.16, 0.16, 0.16)$, the following computational profile was observed: For a volume fraction of 0.131 resolved at 129^3 , $3 \times 647\,728 = 1\,943\,184$ DOF were used (corresponding to a DOF fraction of 0.302). The computation required 2408 MiB of memory for data vectors, matrices and the solver. Computation times on a 3.6 GHz Pentium 4 processor are listed in Table 7.26, where for this parameter study we used $V_2(3, 3)$ cycles and a stopping criterion of reducing the norm of the the residual by 7 orders of magnitude. The solver took 50 multigrid iterations in these cases, the convergence rates in the last step were 0.877 and 0.879, respectively, and one iteration took approximately 42 and 41.5 seconds, respectively. So an additional order of magnitude in the solver accuracy takes about 12 min 15 s.

Table 7.26. Computational profiles for two of the statistical osteoporosis models

simulation	compression	shear
generating level set representation of specimen	16.01 s	15.86 s
setting up CFE grid	6.96 s	6.04 s
setting up system of equations (assembling matrices and enforcing boundary conditions)	130.98 s	131.22 s
solving system of equations	2220.14 s	2187.03 s
postprocessing (force computation)	109.39 s	109.40 s

7.3.3 Simulations on Real Specimens

Complicated Domains

In Figure 7.27 we show the elastic deformation of the different specimens of the internal trabecular structure (spongiosa) of a porcine T1 vertebra [217]. Again we imposed a displacement shearing the upper boundary of the bone volume to the right while the lower boundary plate was kept fixed. Here we chose material parameters $E = 10.9$ GPa, $\nu = 0.3$. Again, the deformed objects are colored according to the von Mises stress at the interface. The numbers of DOF and virtual nodes are

resolution	33^3	65^3	129^3	257^3
# DOF	27 921	243 477	1 847 286	10 124 160
# virtual nodes	16 887	142 234	1 004 417	5 606 274

For the 33^3 and 129^3 (left and second to right) specimens, 71 and 384 $V_2(3,3)$ multi-grid cycles taking 0.5 and 56 seconds each were required to achieve a reduction of the norm of the residual by 8 orders of magnitude achieving convergence rates of 0.860 and 0.978 seconds in the final iteration.

Discontinuous Coefficients

Finally, we simulated linear elasticity for objects with discontinuous coefficients. For this purpose we again considered an Al/PMMA specimen [281] with realistic stiffness parameters $E = 70$ GPa, $\nu = 0.35$ and $E = 3$ GPa, $\nu = 0.38$, subject to 1° torsion. The object was now resolved at $120 \mu\text{m}$ resolution on a 65^3 computational mesh and shown in Figure 7.28. This was the same object as previously used in Figure 7.13 but at different resolution and visualized from a different perspective.

Figure 7.28 also shows a specimen extracted from a porcine T1 vertebra with parameters $E = 13$ GPa and $\nu = 0.32$ for the trabecular microstructure. These values are realistic for human vertebral trabecular bone [380] whose inter-trabecular spacing, however, is larger than the one in pigs. The specimen is assumed to be filled with PMMA with the same parameters as before. The corresponding computational mesh was $143 \times 143 \times 214$ for a scan resolution of $35 \mu\text{m}$. Results of the simulation of compression in longitudinal direction are shown in Figure 7.28.

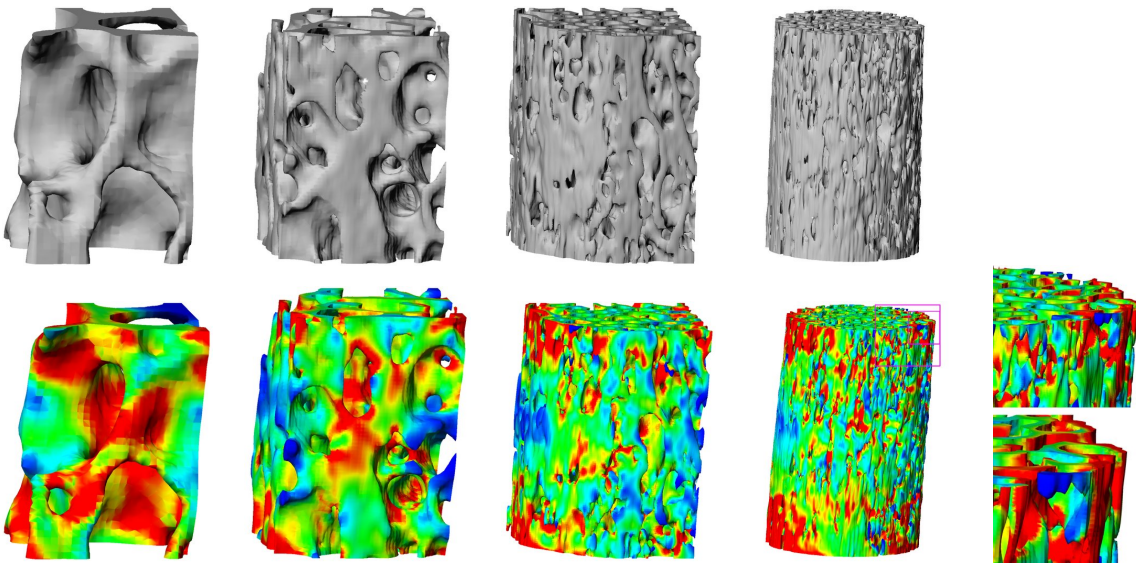


Figure 7.27. The plots visualize shearing of specimens of a porcine T1 vertebra. The elastic deformation of the internal structure of a porcine vertebral bone is depicted. From *left to right* the resolution increases from 33^3 to 257^3 . The *top row* shows the original undeformed structures whereas the *bottom row* shows the deformed structures where a HSV colorbar visualizes the von Mises stress at the interface. For the object of highest complexity, we also show a zoom to the regions indicated by magenta boxes.

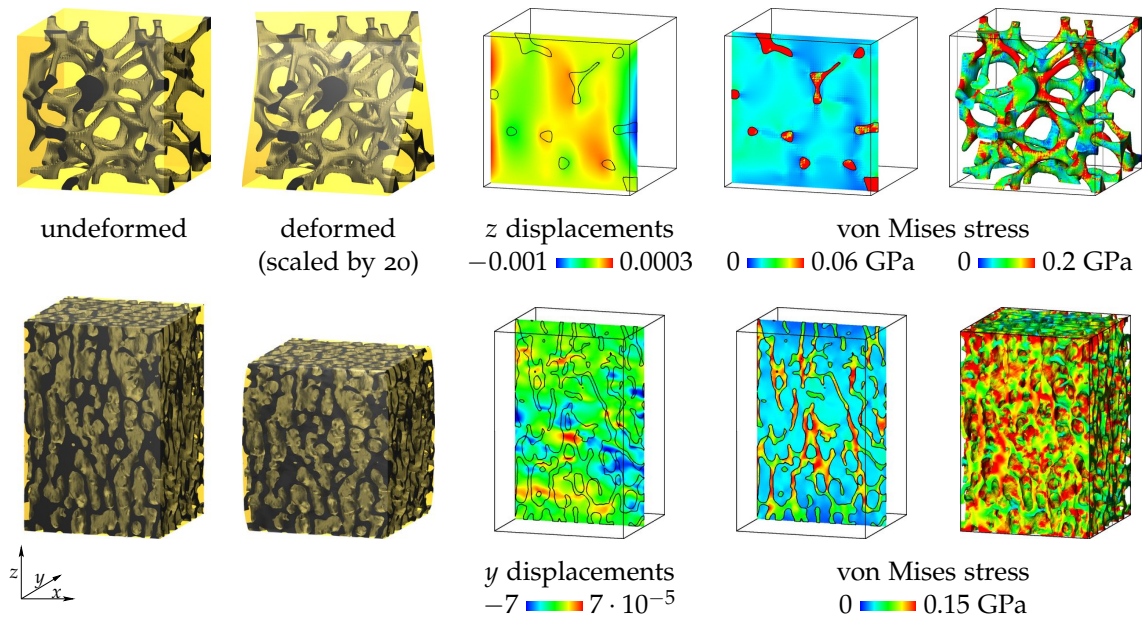


Figure 7.28. The *top row* shows torsion of an Al/PMMA specimen. Besides the undeformed and deformed object, we show the z displacements and von Mises stresses on a slice ($y = 1/6$) through the object and on the material interface (stresses only). The *bottom row* shows compression of a porcine trabecular bone specimen embedded in PMMA, where y displacements and von Mises stresses are visualized on the slice $y = 1/2$ through the object and on the material interface (stresses only). Both displacements are given relative to the specimen height. In both cases, the effect of the higher stiffness of the trabecular microstructure becomes visible in the displacements induced by the microstructure.

7.4 Homogenization

Let us now present results obtained by our homogenization method. Results of heat diffusion (Section 7.4.1) and elasticity (Section 7.4.2) homogenizations for artificial object geometries are presented to show the capabilities of our method for both periodic and merely statistically representative fundamental cells. In Section 7.4.3 the method is applied to actual specimens of trabecular bone.

7.4.1 Heat Diffusion in Artificial Objects

For the scalar case of heat diffusion, we first considered the fundamental cells shown in Figure 7.29 consisting of $10 \times 10 \times 10$ cylindrical rods, an example from [281]. These objects have different d/l ratios and removal percentages where the removal of trabeculae was performed in such a way that these structures are periodic fundamental cells. The chosen ratio of 237 : 0.19 between the two diffusivity coefficients reflects realistic values for aluminum and PMMA. The figure also reports the resulting homogenized diffusivity tensors.

To further investigate how the finite resolution introduces slight anisotropy for objects that appear to have isotropic macroscopic properties, we considered a geometrically simpler structure and the resulting homogenized thermal diffusivity tensors in Figure 7.30, also from [281]. Indeed, for this structure we expect to have isotropic macroscopic properties, and the off-diagonal entries in the tensor diminish for increasing computational resolution.

7.4.2 Linear Elasticity of Artificial Objects

Aligned Orthotropic Objects

As a first artificial elastic object, we considered the one shown in Figure 7.32 from [311], $1 \times 1 \times 1$ cylinders with $d/l = (0.4, 0.3, 0.2)$. This was assumed to be a complicated domain with material parameters $E = 1$, $\nu = 0.33$ and edge length of $\Omega^\#$ of 1 m. The figure also shows the visualization of the homogenized tensor as described in Section 4.5.2. Different from later tensor listings, the tensors obtained by our homogenization method is listed here without symmetrizing them as described in Section 4.1.3. We observe that, for increasing computational resolution, the roll, pitch and yaw angles (obtained by our optimization procedure to check for orthotropy, cf. Section 4.5) decrease as well as the final orthotropy violation.

In [311] we furthermore compared the homogenization results from Figure 7.32 to compressive and shearing stiffnesses obtained for $n \times n \times n$ fundamental cells $\Omega^\#$ as in Figure 7.32 (see [379]) subject to the corresponding boundary conditions (two opposite faces of the bounding cube were displaced by a fixed value, no boundary conditions were imposed on the side faces). Microscopic elasticity parameters were set to $E = 1$, $\nu = 0.33$. A $5 \times 5 \times 5$ such structure is shown in Figure 7.31. In this geometric situation, compressive stiffnesses for individual specimens are almost the same as those obtained by homogenization (periodic and natural Neumann boundary

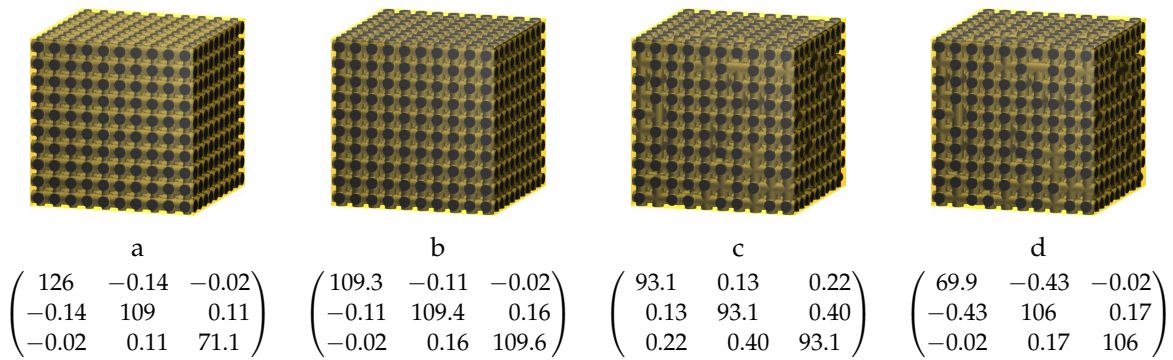


Figure 7.29. For different artificial objects, homogenized thermal diffusivity tensors are listed. Specimen (a) is a $10 \times 10 \times 10$ structure of cylindrical rods with $d/l = (0.38, 1/3, 0.24)$, whereas specimens (b), (c), (d) have diameter/length ratios $1/3$ in each space direction where (a), (b) are full structures, (c) has removal percentages $p = (0.1, 0.1, 0.1)$ and (d) has $p = (0.3, 0, 0)$.

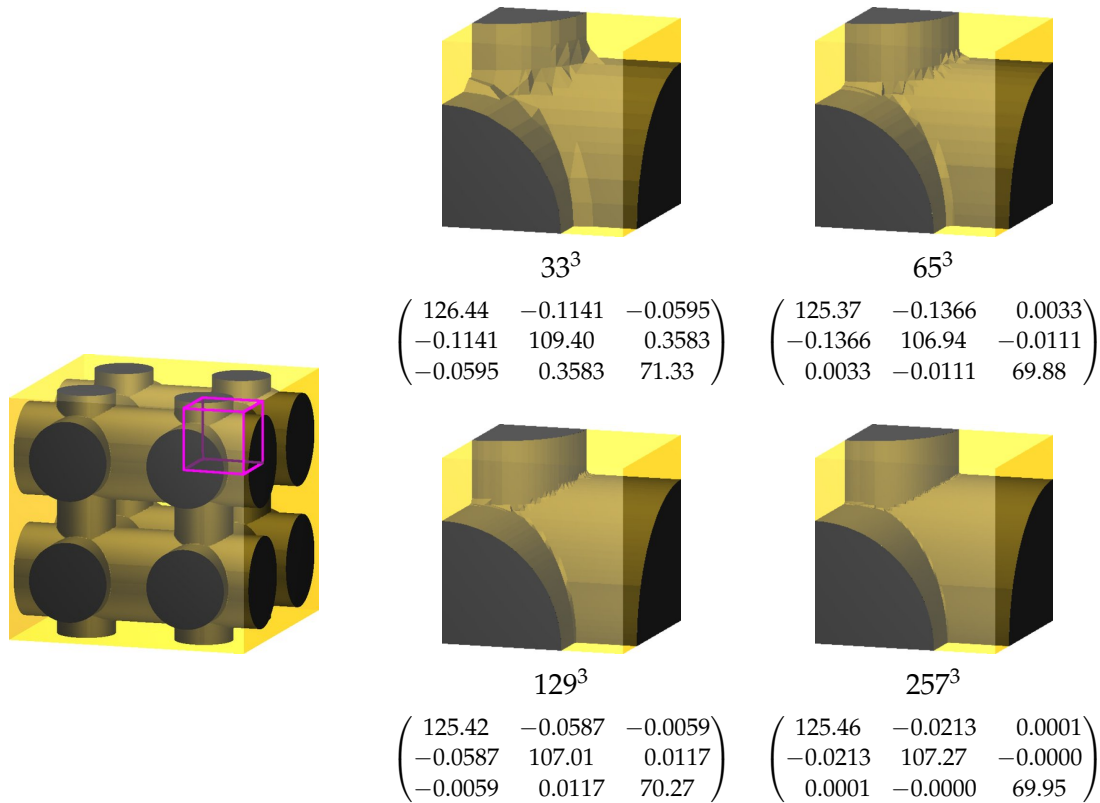
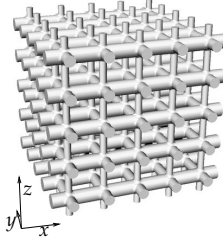


Figure 7.30. For $2 \times 2 \times 2$ rods with $d/l = (0.38, 0.33, 0.24)$ (left), the zoom to one trabecular crossing (magenta box) at different computational resolution is shown, along with the numerically homogenized thermal diffusivity tensors obtained at the respective resolution.

n	resolution	compressive stiffness (x)
1	129^3	0.133939 Pa
5	129^3	0.133248 Pa
10	129^3	0.132871 Pa
15	257^3	0.132860 Pa
20	257^3	0.132436 Pa



displacement	stiffness
x compression	0.132726 Pa
y compression	0.082275 Pa
z compression	0.039549 Pa
xy shear	0.0021291, 0.0020593 Pa
xz shear	0.0029628, 0.0026015 Pa
yz shear	0.0072422, 0.0068263 Pa

Figure 7.31. For artificial trabecular specimens consisting of $n \times n \times n$ circular rods with $d/l = (0.4, 0.3, 0.2)$ (middle image for $n = 5$), the left table lists the compressive stiffness in x direction for different values of n and different computational resolutions. The right table lists compressive and shear stiffnesses for the $10 \times 10 \times 10$ specimen at computational resolution 257^3 .

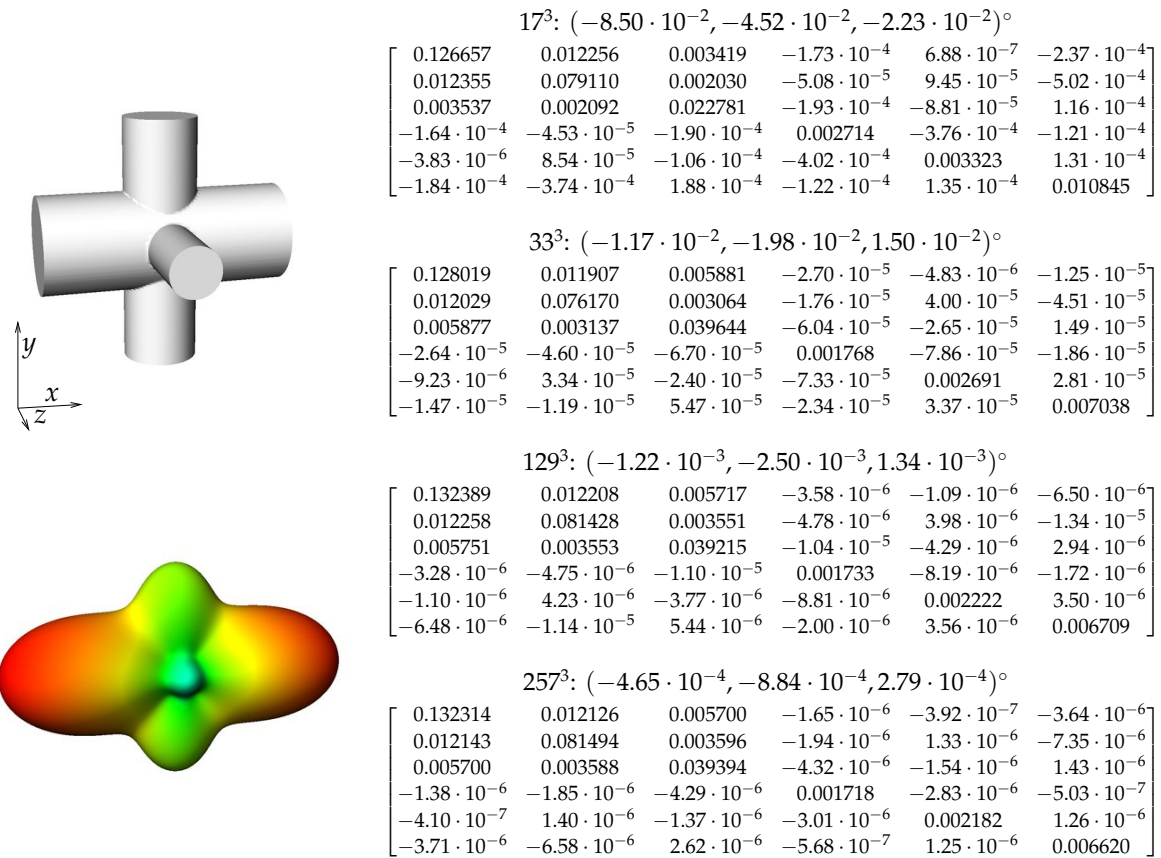


Figure 7.32. For a $1 \times 1 \times 1$ artificial trabecular crossing with $d/l = (0.4, 0.3, 0.2)$, the corresponding homogenized orthotropic elasticity tensor is visualized (left). For different computational resolution, roll, pitch, and yaw angles yielding the best rotation to an aligned orthotropic tensor are listed along with the homogenized tensors in Voigt's notation. To show the convergence behavior, the tensors have not been symmetrized and small entries have not been omitted, instead those entries not present in a perfectly aligned orthotropic tensor have been listed in exponential notation and in units of GPa.

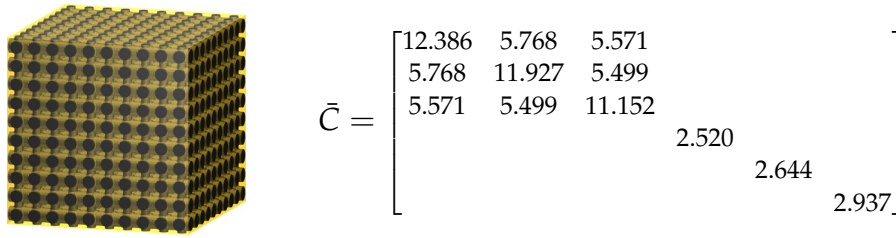


Figure 7.33. For the specimen shown on the *left*, the homogenized elasticity tensor \bar{C} is listed where entries smaller than 10^{-3} times the maximal entry have been omitted.

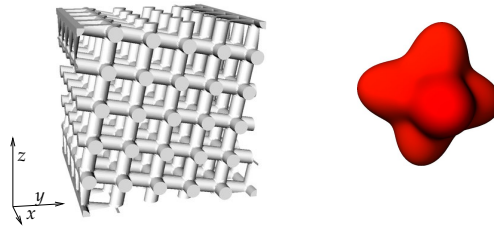


Figure 7.34. A periodic rotated $5 \times 5 \times 5$ rod sample with constant $d/l = (0.4, 0.4, 0.4)$ is shown, along with a visualization of the corresponding macroscopic orthotropic elasticity tensor. The axes of orthotropy match the geometric axes of the structure and are identified correctly by our optimization procedure.

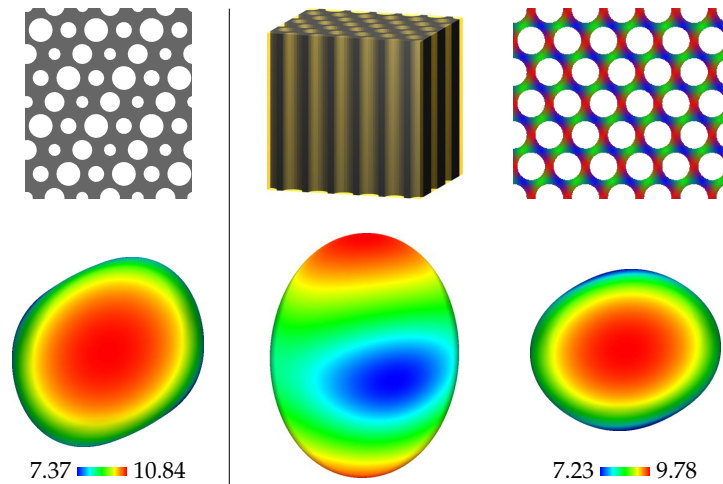


Figure 7.35. On the *top left* a cross section through a honeycomb structure viewed as a complicated domain is shown. For constant isotropic material properties with Young's modulus $E = 8$, the geometric symmetry axes lead to a non-orthotropic macroscopic elasticity tensor visualized on the *bottom left* where the color bar shows the range of the bulk modulus. In the *top middle* a honeycomb structure with constant radii is visualized where the microscopically isotropic elasticity tensor varies in the structure and is constant 1 in the cylinders visualized in yellow. The variation is shown on a cross section through the structure on the *top right* where red corresponds to a Young's modulus of 4, green to 8, blue to 12 and values are interpolated in between. The corresponding macroscopic elasticity tensor is again non-orthotropic and visualized *bottom middle and right*. The perspectives for the visualizations in the bottom row matches those for the visualizations above.

Non-Orthotropic Objects

Non-orthotropy can be caused, e.g., by lack of geometric symmetry or by non-constant microscopic material parameters. Let us consider one example for each of these cases to show that our method also treats this case correctly. A geometric non-orthotropy can be obtained for the pattern of radii shown on the left side of Figure 7.35 which shows the constant cross section of a 3D object viewed as a complicated domain. Isotropic microscopic elasticity parameters were set to $E = 8$, $\nu = 0.38$ in the structure and the computational resolution was $56 \times 64 \times 64$ for the object of size 1 m in z direction. Moreover, we considered a 2D honeycomb structure with constant radii, shown on the right side of Figure 7.35. Here we assumed microscopically isotropic material with varying Young's modulus in one subdomain. In the cylinders, we assume $E = 1$, $\nu = 0.25$, whereas the honeycomb structures are assumed to have $\nu = 0.38$ and E varying between 4 and 12, according to position as visualized in the figure. Computational resolution here was $65 \times 57 \times 65$. The homogenized elasticity tensors \bar{C}^G for the complicated domain and \bar{C}^M for the discontinuous and varying coefficient were (in Voigt's notation)

$$\bar{C}^G = \begin{bmatrix} 4.172 & 1.899 & 2.307 & 1.22 \cdot 10^{-10} & -7.58 \cdot 10^{-10} & 0.125 \\ 1.899 & 3.451 & 2.033 & 4.53 \cdot 10^{-10} & -3.57 \cdot 10^{-10} & -0.051 \\ 2.307 & 2.033 & 6.499 & 4.20 \cdot 10^{-10} & -1.32 \cdot 10^{-09} & 0.028 \\ 1.22 \cdot 10^{-10} & 4.53 \cdot 10^{-10} & 4.20 \cdot 10^{-10} & 1.179 & 0.036 & 1.22 \cdot 10^{-13} \\ -7.58 \cdot 10^{-10} & -3.57 \cdot 10^{-10} & -1.32 \cdot 10^{-09} & 0.036 & 1.337 & 8.44 \cdot 10^{-11} \\ 0.125 & -0.051 & 0.028 & 1.22 \cdot 10^{-13} & 8.44 \cdot 10^{-11} & 1.085 \end{bmatrix}$$

$$\bar{C}^M = \begin{bmatrix} 4.362 & 1.711 & 2.140 & -1.02 \cdot 10^{-05} & 5.73 \cdot 10^{-06} & -0.030 \\ 1.711 & 3.652 & 1.868 & 1.49 \cdot 10^{-06} & 4.69 \cdot 10^{-07} & 0.051 \\ 2.140 & 1.868 & 5.769 & 2.03 \cdot 10^{-06} & -3.21 \cdot 10^{-06} & 0.008 \\ -1.02 \cdot 10^{-05} & 1.49 \cdot 10^{-06} & 2.03 \cdot 10^{-06} & 1.111 & 0.015 & 1.12 \cdot 10^{-06} \\ 5.73 \cdot 10^{-06} & 4.69 \cdot 10^{-07} & -3.21 \cdot 10^{-06} & 0.015 & 1.351 & 5.47 \cdot 10^{-07} \\ -0.030 & 0.051 & 0.008 & 1.12 \cdot 10^{-06} & 5.47 \cdot 10^{-07} & 1.043 \end{bmatrix}$$

after symmetrization and optimal rotation to an aligned orthotropic tensor. The resulting tensors obviously show the expected lack of orthotropy.

7.4.3 Linear Elasticity for Real Specimens

Complicated Domains

In [296] specimens of trabecular bone of different specimens were compared in terms of their homogenized elasticity tensors. Specimens were harvested from a young male (*human-y*; T11–L2 vertebrae) and an osteoporotic elderly female Caucasian human donor (*human-o*; T10–T12), and from a porcine (T1–T6) and a bovine (L1–L2) spine. As described in the introduction in Section 1.5, we obtained cylindrical specimens from different vertebrae by removing top and bottom end plates and then extracting cylinders by a trepan so that the cylinder axis coincides with the craniocaudal anatomical axis (up to orientation) but the other axes are no longer known and differ between different cylinders. A segmentation threshold was determined based on the gray value histogram [293] and two cubes of 129^3 voxels (corresponding to 5.16 mm edge length) were extracted at the bottom and top of the cylindrical dataset. Thereby, the z axis in the datasets is the craniocaudal anatomical axis (up to orientation)

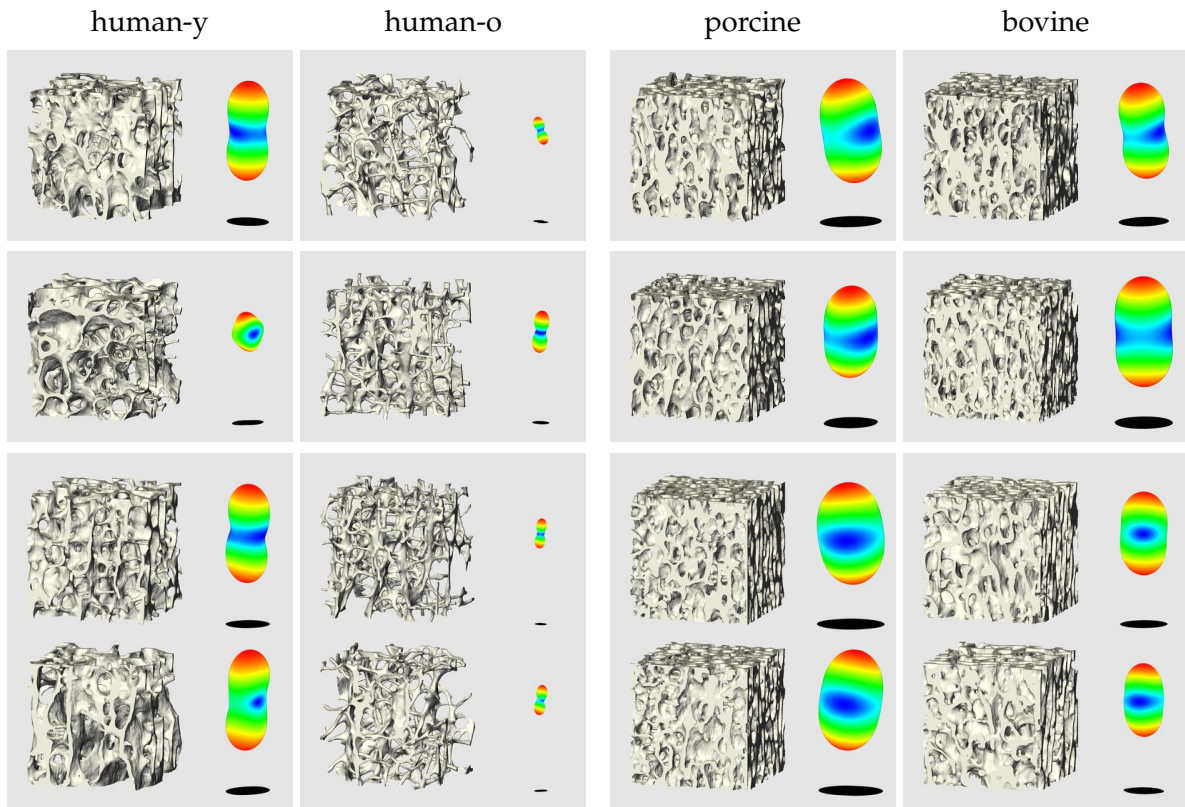


Figure 7.36. Four specimens of trabecular bone are visualized for each species along with the resulting effective elasticity tensors (from the same perspective, i.e., before optimizing axis alignment). The scale of the tensor visualization is the same for all human specimens (*left two columns*) and four times bigger than for all animal specimens (*right two columns*). The *lower two rows* show specimens from the same vertebra per species, spaced apart about 2 mm (visualized approximately to scale).

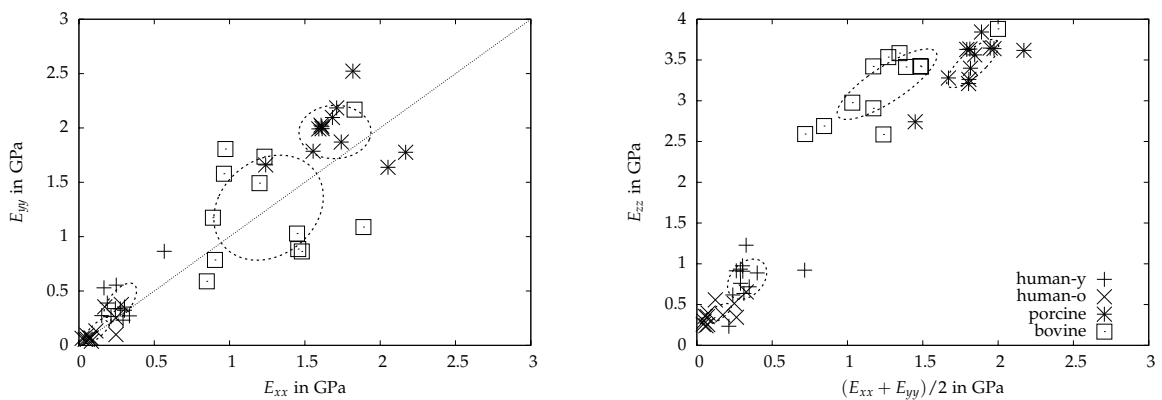


Figure 7.37. The *left* plot shows scattering of the compressive stiffnesses in the transverse directions for different species (after determining the axes of orthotropy). On the *right*, the compressive stiffness in craniocaudal direction is plotted against the average transverse compressive stiffness (again after determining the axes of orthotropy). The ellipses in both cases show one standard deviation obtained by a principle component analysis [183] for each species.

whereas the dorsoventral and dextrosinistral axes are no longer known and differ between specimens (but are the same for each pair of cubes from the same cylinder).

For the trabecular structures, we assume Young's modulus $E = 13$ GPa and Poisson's ratio $\nu = 0.32$ which are realistic values for human trabecular bone [380] but slightly questionable for the animals. While the constituents of bone tissue are the same across mammals [243], the sub-microscopic setup could be different, possibly resulting in different microscopic material properties for the different species.

Trabecular separation (Tb.Sp) was determined via the identification of the largest sphere that includes the point of interest and that fits completely in the pore [166]. For a boundary layer of thickness $\beta = 1/8$, the evaluation domain $\Lambda^{\#\beta}$ then had size 4.22 Tb.Sp and 3.65 Tb.Sp for the human-y and human-o specimens, respectively, so the human specimens do not fully satisfy the criterion of [160]. For the animal specimens, $\Lambda^{\#\beta}$ had size 9.08 Tb.Sp and 7.90 Tb.Sp for the porcine and bovine specimens, respectively, so these specimens are sufficiently large.

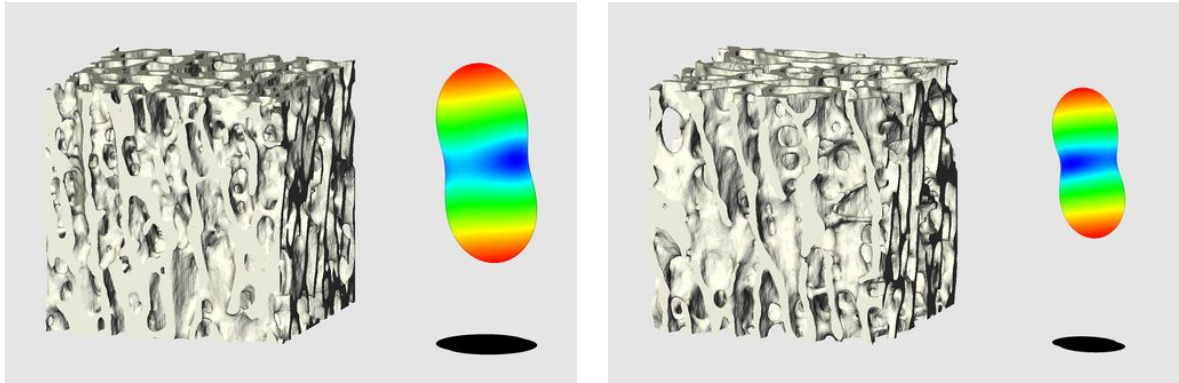
Four specimens for each species and the resulting homogenized elasticity tensors are visualized in Figure 7.36. For the top one in each column, we examined the influence of the parameter β on the compressive stiffnesses in the three space directions. Table 7.38 shows that $\beta = 1/8$ is a good choice if we use the same β for all species.

As only the craniocaudal axis can still be identified as the z axis in the specimens, we assume transverse isotropy and average the compressive stiffnesses in the remaining two directions. The scatter plots in Figure 7.37 show the differences between the species concerning whether this assumption is justified (left plot) and to what extent the structures are anisotropic measured as craniocaudal over average transverse compressive stiffness (right plot).

The human osteoporotic specimens in our study have about half the compressive stiffness of the non-osteoporotic ones in craniocaudal direction and an anisotropy that is about 1.6 times as large. The bovine specimens have slightly smaller craniocaudal compressive stiffness than the porcine ones, but a higher anisotropy ratio (approximately 1.9 vs. 2.6). Comparing the bovine to the non-osteoporotic human specimens, craniocaudal compressive stiffness is about four times as large and the anisotropy ratio is slightly larger.

Table 7.38. For one specimen of each species (those in the top row of Figure 7.36), the resulting compressive stiffnesses (in units of GPa) in direction of the optimal axes of orthotropy are listed. These are computed from the effective elasticity tensors obtained by evaluation over different $\Lambda^{\#\beta}$.

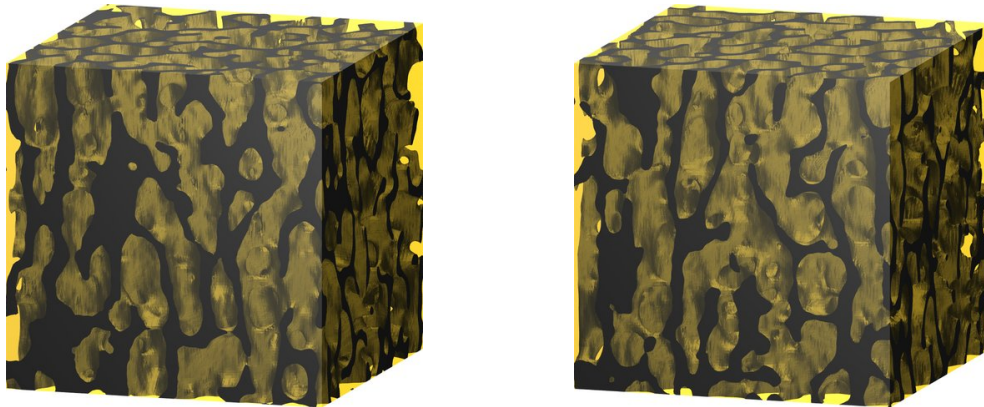
β	human-y			human-o			porcine			bovine		
	E_{xx}	E_{yy}	E_{zz}									
0/16	0.389	0.368	1.024	0.107	0.151	0.300	1.812	2.101	3.628	1.392	1.858	3.519
1/16	0.255	0.298	0.975	0.064	0.105	0.283	1.656	1.959	3.568	1.218	1.735	3.438
2/16	0.293	0.231	0.914	0.053	0.092	0.254	1.613	2.012	3.635	1.232	1.735	3.426
3/16	0.258	0.197	0.886	0.052	0.083	0.232	1.585	2.012	3.620	1.238	1.741	3.364
4/16	0.309	0.194	0.953	0.043	0.086	0.231	1.663	2.005	3.747	1.238	1.741	3.364



roll = -7.52° , pitch = 9.44° , yaw = -18.22°
 $E_{xx} = 1.199$, $E_{yy} = 1.492$, $E_{zz} = 3.584$ GPa

roll = -12.27° , pitch = 10.75° , yaw = -26.27°
 $E_{xx} = 0.903$, $E_{yy} = 0.786$, $E_{zz} = 2.690$ GPa

Figure 7.39. For two specimens from the same bovine vertebra (spaced apart approximately 2 mm in craniocaudal direction), the resulting axes of orthotropy and macroscopic elasticity tensors differ significantly.



$$\bar{\mathbf{C}} = \begin{bmatrix} 8.369 & 4.585 & 4.575 & -0.012 & 0.061 \\ 4.585 & 8.424 & 4.587 & -0.017 & 0.075 \\ 4.575 & 4.587 & 9.040 & -0.059 & 0.018 \\ -0.012 & -0.057 & 1.996 & 0.033 & -0.020 \\ 0.061 & 0.075 & 0.018 & -0.020 & 1.897 \end{bmatrix}$$

$$\bar{\mathbf{C}} = \begin{bmatrix} 7.929 & 4.433 & 4.427 & & 0.030 \\ 4.433 & 8.072 & 4.442 & & 0.053 \\ 4.427 & 4.442 & 8.629 & -0.029 & \\ & -0.029 & 1.879 & 0.021 & \\ 0.030 & 0.053 & & 0.021 & 1.863 & -0.012 & 1.783 \end{bmatrix}$$

roll = 3.82° , pitch = 7.26° , yaw = -25.12°

roll = 7.37° , pitch = 2.16° , yaw = -40.99°

$$\bar{\mathbf{C}}^* = \begin{bmatrix} 8.250 & 4.594 & 4.560 & & & \\ 4.594 & 8.519 & 4.598 & -0.012 & -0.098 & -0.014 \\ 4.560 & 4.598 & 9.055 & & & \\ & -0.012 & & 2.025 & & \\ & -0.098 & & & 1.958 & \\ & -0.014 & & & & 1.903 \end{bmatrix}$$

$$\bar{\mathbf{C}}^* = \begin{bmatrix} 7.902 & 4.422 & 4.424 & & & \\ 4.422 & 8.120 & 4.444 & & & \\ 4.424 & 4.444 & 8.633 & & & \\ & & & 1.890 & 0.009 & \\ & & & 0.009 & 1.851 & \\ & & & & & 1.772 \end{bmatrix}$$

Figure 7.40. Two cubic specimens of a porcine T1 vertebra, embedded in PMMA, are shown in the *top row*. For the homogenized elasticity tensors $\bar{\mathbf{C}}$ in GPa, we determine rotation angles to an optimally aligned orthotropic tensor $\bar{\mathbf{C}}^*$, obtaining rather similar tensors.

Figure 7.39 emphasizes that the interior of vertebral bodies (spongiosa) does not have constant macroscopic properties throughout one vertebral body and indicates that a full two-scale model should be employed for simulations on a whole vertebra (which additionally contains the compact outer shell). This spatial variation of effective properties is even more important in other bones where the geometry of the trabecular microstructure is strongly adapted to the shape of the bone and stresses for typical anatomical loading⁵.

For the simulations for the leftmost (human-y) specimen in Figure 7.36 at resolution 129^3 , the CFE discretization resulted in a 3×3 block matrix using 1158.6 MiB of memory, where the solver took 6755.6 seconds of CPU time on a 3 GHz Opteron processor on average for each of the six different settings of boundary conditions and a reduction of the norm of the residual by 8 orders of magnitude. For the (more dense) rightmost (bovine) specimen, matrix memory consumption was 1808.8 MiB and solver CPU time was 14 426.5 seconds.

Discontinuous Coefficients

As real specimens in the case of discontinuous coefficients we considered two cubic specimens from the same porcine T₁ vertebra shown in Figure 7.40 at 35 μm resolution and on a 129^3 computational mesh [281]. The dataset is part of the one used in Figure 7.28. We assumed the same bone/PMMA parameters as before, $E = 13$ GPa, $\nu = 0.32$ in the bone, $E = 3$ GPa, $\nu = 0.38$ in the PMMA. The specimens are sufficiently large (trabecular separation is 0.432 and 0.438 mm, respectively) so that $\Lambda^{\#\beta}$ for $\beta = 1/8$ covers more than five inter-trabecular lengths in each space direction, and thus the criterion of [160] for a representative cell is satisfied.

The homogenized tensors for these two specimens listed in Figure 7.40 are in fact quite similar and exhibit small orthotropy violation. The z axis in the specimens is roughly parallel to the craniocaudal axis of the pig, its orientation and the alignment of x and y axes, however, is unknown but the same for both cubes.

⁵This has been known at least since the 1870s [378]: ‘... dass in der That das spongiöse Knochengefüge nicht ein regelloses und gleichgültiges Gewirre von Knochenbälkchen und Hohlräumen ist, wie man das bisher geglaubt hat, dass ihm vielmehr wirklich jene „wohlmotivirte Architectur“ eigen ist, durch die jedem seiner Bälkchen eine statische Bedeutung, und, so zu sagen, eine bestimmte Rolle als zweckmässig angelegter Baustein in dem grossartigen Gesamtbauengerüst des Knochens zugewiesen ist.’

8 Conclusions and Outlook

STARTING WITH a summary of what has been achieved and which points require further investigation, Section 8.1 is intended to suggest questions for future research. Section 8.2 summarizes some ideas how the multigrid solver in the complicated domain case can possibly be improved and Section 8.3 presents ideas for a multigrid coarsening strategy for discontinuous coefficients. Both these have not lead to success so far.

8.1 Summary and Open Problems

Implementation of CFE. The CFE for complicated domains presented in this thesis have been implemented except for the case of spatially varying elasticity parameters. This, however, will not require much effort. The corresponding multigrid method has also been implemented successfully with the limitations presented in Section 5.2.2. Some ideas for improvement of the multigrid method are presented below in Section 8.2.

As for the case of discontinuous coefficients, the scalar isotropic and the general linear elasticity cases have been implemented (but not the scalar anisotropic case). The development of a corresponding multigrid coarsening strategy has not been successful, some first ideas are discussed below in Section 8.3.

Both methods have not only been applied to simple artificial geometries but also to scans of actual trabecular structures with high geometric complexity.

Homogenization. Homogenization procedures have been implemented and applied for all combinations of {complicated domains, discontinuous coefficients} and {periodic, statistically periodic} fundamental cells. For complicated domains, an appropriate multigrid solver for both types of fundamental cells has also been implemented successfully, with the same limitations as before.

Again, the homogenization methods have been applied successfully to artificial geometries and samples of real trabecular bone.

Generalization of the CFE Concept. First of all, it would be useful to have a 2D CFE implementation for the cases discussed here in the same C++ framework as our 3D implementation. This should not involve methodical difficulties and would allow for easier testing of further extensions.

While we only consider 3D non-adaptive cubic meshes, a similar construction of CFE for general hexahedral, non-hexahedral or adaptive meshes is possible. This certainly requires using efficient and well-known methods for not globally uniform meshes.

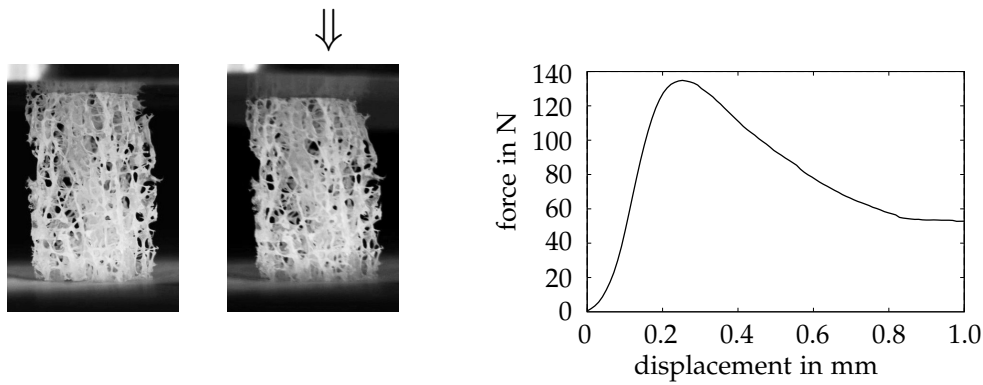


Figure 8.1. For an experimental validation of the CFE elasticity simulations for complicated domains, specimens of trabecular bone are tested in mechanical compression experiments and force is measured as a function of strain. Stiffness in the linearly elastic range (here for about 1% of the specimen height of 12 mm) is then compared to simulation results.

If domains are described by image data, one typically uses the corresponding voxel grid and adaptivity is obtained by coarsening (unlike adaptive refinement if one starts with a coarse geometry approximation).

For 2D complicated domains, CFE for not uniformly hexahedral meshes have already been discussed in [290] and an extension to 3D should not be difficult. In contrast, CFE for discontinuous coefficients on non-uniform meshes require an appropriate interface approximation, identification of coupling conditions across the approximated interface, and finally composition of basis functions, which can be expected to be significantly more technical.

Validation. Validation of the methods used here for the elasticity case is work in progress. First, the segmentation of the image data needs to be compared to specimen volumes measured, e.g., using Archimedes' principle¹ by *helium micro-pycnometry*, cf. [75, 332]. The elasticity method can be validated by comparing simulated macroscopic stiffnesses to those measured in compression experiments (for which the range of linearly elastic behavior needs to be identified, see Figure 8.1).

First experiments indicate that the thresholding according to [293] works well. This method determines the segmented volume by counting voxels with gray value above or below a fixed value. It seems to be unnecessary to use the CFE segmentation instead, which makes finding the threshold more than two orders of magnitude more expensive in terms of CPU time. Denoising or resampling of the dataset, however, needs to be performed with care since the structures are only a few voxels in diameter and biased errors in the segmentation will not only result in incorrect segmented volume but also in incorrect simulated mechanical results.

¹Named after the Greek mathematician and scientist Ἀρχιμήδης (Archimedes) who lived in the third century BC, * and † in Syracuse, Sicily [1].

8.2 Ideas for Improved Coarsening for Complicated Domains

As we have seen in Figure 7.10, some geometric situations may lead to poor multigrid convergence because coarse-grid correction introduces artificial numerical coupling. Stopping the coarsening process globally is a simple remedy (cf. Figure 7.10) which drastically decreases the efficiency of the multigrid solver. The following ideas on how this problem could be overcome are meant as suggestions for future research.

Let us propose a geometric criterion for troublesome situations in the multigrid coarsening where numerical coupling is introduced between parts of the structure whose physical coupling is only weak. Note, however, that this geometric criterion is necessary but not sufficient for a weak physical coupling of the components.

Detour-Connectedness. Recalling Figure 5.4 we observe that the support of a coarsened basis function consists of disconnected components if those components are part of disjoint subsets of the structure Ω_- or if the geodesic distance (minimal distance along paths inside Ω_-) between the components is greater than the Euclidean distance. Let us introduce the term *detour-connected* (relative to Ω_-) for sets where, between any two points, the geodesic distance (with respect to Ω_-) is not larger than the Euclidean distance plus a maximal detour ζ . If $\zeta = 0$, the set is convex.

If the imaging resolution is sufficiently high, we can assume that all supports of basis functions on the finest level are detour-connected. We can now attempt standard CFE coarsening and check whether the coarsened basis functions still have detour-connected support. If one basis function does not, a troublesome case has been detected. We can then stop the coarsening process globally and mark the current fine level as the explicit level.

We could instead stop the coarsening process only locally. This means modifying restriction and prolongation operators such that rows in the restriction matrices are left out and the coarsened problem has less DOF and no correction is prolonged from the coarse grid correction—instead of an unphysical coarse grid correction. This might make sense if detour-disconnectedness occurs only at few geometric locations and the overall convergence is not impeded by this ‘better be safe than sorry’ coarse grid correction. At those points, coarse grid correction could be replaced by additional smoothing steps as [53] recommends for ‘pollution’ of multigrid methods by reentrant corners.

Adaptive Coarsening. Another option is to determine detour-connected components of the support of basis functions. This could be achieved by assigning a ‘seed node’ to each DOF on the finest grid and computing geodesic distances from this seed node to neighboring DOF. During coarsening, coarse grid parent nodes could first inherit the seed of one of their descendants and geodesic distances (bounded by a detour parameter depending on the grid spacing of the current grid) could be computed for a larger neighborhood, forming the first detour-connected component of the support. If not all descendants are captured in this neighborhood, further

components of the support could be introduced until all descendants are processed. For each component, a separate instance of the coarse grid node could be introduced, resulting in a ‘cloning’ of DOF. In further coarsening steps, this might result in further cloning, but also in ‘recombination’ if basis functions are found to have detour-connected support on an even coarser level. Figure 8.2 shows an example of this cloning and recombination. This approach would require bookkeeping of the different instances for the restriction and prolongation operators, either by storing additional instances separately or by using multiple copies of the grid.

Computational Complexity. Distance information can be computed using a sweeping method [326, 188], see also [80, 261, 390]. These methods usually finish within a small constant number of iterations (even though this need not be true in the worst case) with $O(n^3)$ algorithmic and memory cost if the neighborhood for which distances are computed is of size n^3 where n of course depends on the detour parameter ζ . On the finest grid, the number of nodes is $O(N^3)$ and we need one neighborhood for each node. Neighborhood and distance information is always computed on the finest grid because we need to consider the full topology information about the domain. In each coarsening step the number of grid nodes decreases roughly by a factor of 2^3 , so only $1/8$ of the neighborhoods (on the finest grid) need to be considered further. Their size, however, is increased by a factor 2^3 . Multiple DOF for the same grid node result in multiple neighborhoods with different distance information. In the—unrealistic—worst case of 15-fold cloning, the memory requirement increases by a constant factor in each of the $O(\log N)$ coarsening steps. In total, the constants are relatively large and an implementation of this approach has not proven to be efficient.

Further Ideas. Besides this geometrically (that is, sample-specific) adapted coarsening, it may also be worth investigating the possibilities and performance of an algebraically adapted coarsening (which, most likely, depends on both specimen and

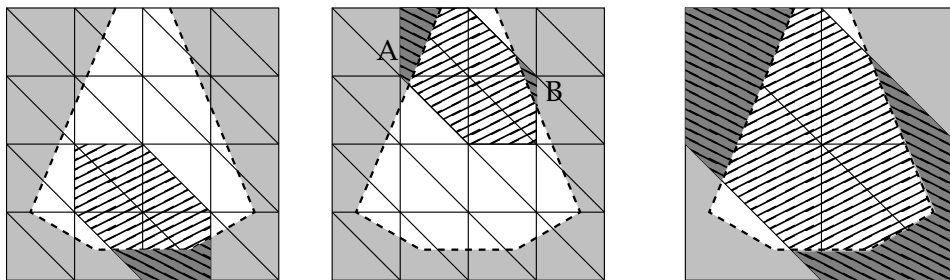


Figure 8.2. For the same example geometry as in Figure 5.4, the *left* basis function has connected support. The support of the *middle* basis function consists of two detour-disconnected components A and B, we could thus use two instances of the corresponding node. On the next coarsest level on the *right*, the two instances could be recombined because, for small nonzero detour parameter ζ , the basis function then has detour-connected support.

boundary conditions in a simulation). It may be possible (and possibly beneficial) to combine automatic coarsening methods known from algebraic multigrid solvers with the geometric information (regular structure in \mathcal{G}^\boxtimes , knowledge about interface) available. Another option could be the adaption of pseudo- L^2 -projection [97] originally developed for non-nested meshes. In the terminology of [74], these could be considered (light) ‘gray box’ methods. If Dirichlet nodes are not visible as DOF to an algebraic coarsening procedure, these will simply be ignored and need not be treated separately.

8.3 Ideas for a Discontinuous Coefficients Coarsening Procedure

Defining a multigrid coarsening strategy for CFE for discontinuous coefficients is a difficult task that remains an open problem. A very first idea for a coarsening scheme is to simply use standard neighborhoods with standard coarsening weights 0, 1/2, and 1. In any space dimension, this clearly introduces artificial kinks in the coarsened basis functions across faces of the fine grid not present on the coarse grid.

A Geometric Coarsening Scheme in 1D. A geometrically intuitive idea for a more refined coarsening scheme can be built on the approach that coarsened basis functions should not have ‘artificial’ kinks on edges of the coarse grid (because a basis function constructed immediately on the coarse grid, provided that the geometry is resolved there, cannot have those kinks). This method was not found to be an effective solver strategy and its presentation is included here only for the sake of completeness.

This geometric idea can be turned in a ‘slope balancing’ condition from which we can determine more appropriate coarsening weights. Suppose we construct a basis function ψ_c^{CFE} on the coarse grid with the edge $[c_{\text{init}}, c_{\text{term}}] \subset \text{supp } \psi_c^{\text{CFE}}$ (note that this does not imply $c \in [c_{\text{init}}, c_{\text{term}}]$ in 2D, cf. Figure 8.4, or in 3D). Then ψ_c^{CFE} has a kink on $[c_{\text{init}}, c_{\text{term}}]$ if and only if the interface intersects the edge, and the kink occurs at the

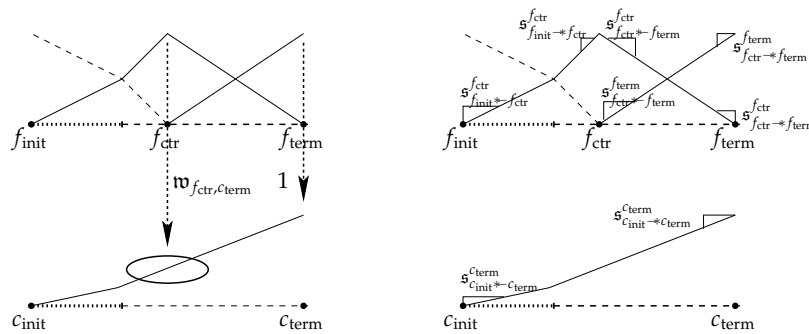


Figure 8.3. *Left:* Coarsening weights w can be chosen such that the coarsened basis function does not have artificial kinks at positions where a coarse basis function would not have a kink. *Right:* For this purpose, slopes s of the basis functions involved locally need to be balanced, resulting in new relevant slopes for the next coarsening step.

corresponding virtual node. In particular, there is no kink at the intermediate node $\frac{1}{2}(c_{\text{init}} + c_{\text{term}})$ which is only present on the fine grid. A coarsened basis function should also satisfy this property. Obviously, having a kink means that one-sided and other-sided slopes differ, so avoiding additional artificial kinks can be viewed as balancing two one-sided slopes, see Figure 8.3.

Extension to 2D and 3D. For extending this coarsening scheme to more than one space dimension, first all relevant edges of the fine grid for a coarse grid node have to be identified. Note that those edges need not be incident to the coarse grid node, due to the slightly extended supports of CFE basis functions for discontinuous coefficients, also other nearby edges may play a role here. Moreover, along one such relevant edge, more than the two fine grid basis functions of the incident nodes contribute to the coarsened basis function and hence need to be considered for the slope balancing, see Figure 8.4. In total, a not necessarily symmetric local system of equations needs to be solved for the slope balancing.

The relevant slope information needs to be computed once on the finest grid, any coarsening step $l + 1$ to level l then involves

1. computing coarsening weights $w_{f,c}$ based on slopes on fine grid
2. coarsening data about neighbors and relevant edges and thus determine neighborhoods $S(n)^l$ for the next coarsening step
3. computing (relevant) coarsened slopes from fine slopes and coarsening weights

Notice that in absence of kinks, this slope balancing simplifies to standard coarsening. Thus the slope information only needs to be stored explicitly for basis functions affected by the interface.

Drawbacks of This Coarsening Scheme. This construction is only based on properties of the basis functions themselves. In contrast, the construction of CFE basis functions on the finest grid is based on their interpolation capabilities. This approach hence neither depends on whether we are dealing with a scalar or a vector-valued

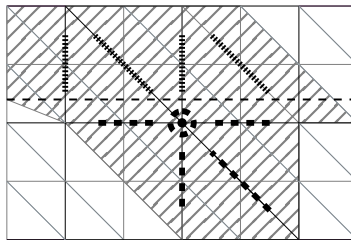


Figure 8.4. Coarsening for CFE for discontinuous coefficients requires to consider neighborhoods S which are larger than those for standard affine FE, resulting in larger supports for coarsened basis functions. Edges highlighted by dotted lines contribute with standard coarsening weights, additional artificial kinks need to be avoided on those edges highlighted by the thick dashed lines. The thin dashed line indicates the interface.

problem, nor does it distinguish between the isotropic and anisotropic cases. It moreover turns out that this approach leads to a violation of the partition of unity condition for the coarsened basis functions, making necessary a relaxation of the slope balancing condition.

Let us furthermore point out that kinks are avoided only across edges of the coarse grid. The CFE basis functions on the fine grid have kinks across virtual edges on the fine grid, and those virtual edges do not appear on the coarse grid (even in case of planar interfaces), as illustrated in Figure 5.7. The coarsening process does not remove such kinks by averaging them to zero (at least not near the interface). Consequently, even for simple planar interfaces, the coarsened basis functions do not coincide with those we could obtain by construction directly on the coarse grid.

Numerical Results. A CFE multigrid solver using $V_2(3,3)$ cycles for scalar isotropic discontinuous coefficients has been implemented with adaption of the coarsening weights so that the coarsened basis functions form a partition of unity. Figure 8.5 shows the convergence performance of this method compared to an SSOR-preconditioned CG solver as one example of the solvers shown in Figure 7.9, and a multigrid method using standard coarsening for affine FE on \mathcal{G}^\boxtimes (which clearly is not a generally useful approach for discontinuous coefficients across general interfaces). Additionally, both multigrid methods cycles have also been applied as preconditioners.

We observe that the multigrid preconditioning is not effective and that performing the coarsening described above (not surprisingly) takes longer than standard coarsening. In the cases considered here, the multigrid method is effective and not significantly slower than standard multigrid, but still outperformed by the SSOR-preconditioned CG solver. Depending on geometry and (scalar) kink ratio we also encountered cases where the multigrid solver diverged.

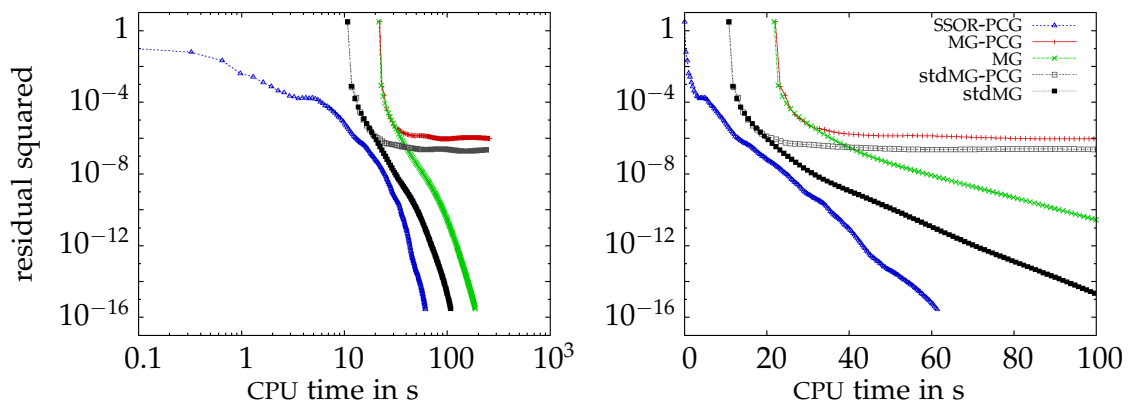


Figure 8.5. The plots compare the solver convergence of multigrid solvers and preconditioning using the coarsening scheme described here and standard affine FE coarsening, using a logarithmic and a linear time scale. The same bone interfaces as in Figure 7.9 were used, the scalar kink ratio was again $\kappa = 42$. An SSOR-preconditioned CG solver outperforms all multigrid-based solvers in this case.

Acknowledgments

First and foremost, I would like to thank my advisor Martin Rumpf for this challenging project and all the iterations in our discussions.

Thanks are also due to Deutsche Forschungsgemeinschaft for supporting me financially through project Ru567/8-2 ‘Multiscale Simulation and Validation of the Elastic Microstructures of Vertebral Bodies’, to Studienstiftung des Deutschen Volkes for their non-financial support and to the Hausdorff Center for Mathematics for computational resources.

I am moreover grateful to Hans-Joachim Wilke and Uwe Wolfram at the Institute of Orthopaedic Research and Biomechanics at University of Ulm for providing the μ CT datasets of the Aluminum foam and bone specimens (where thanks are also due to the anonymous donors). During many phone calls and meetings, Uwe explained a lot about biomechanics and what we actually simulated.

Furthermore I thank Stefan Sauter at University of Zurich for his advice on CFE and for our discussions about CFE multigrid solvers (even though the methods turned out not to be the ideal approach). Concerning the implementation, I thank Florian Liehr (formerly at University of Duisburg) for the implementation of the first generation of CFE code and Tobias Preusser at Fraunhofer MEVIS in Bremen for his part in implementing the second generation tpCFE.

Also, I would like to thank my colleagues at the Institute for Numerical Simulation at University of Bonn for the extremely nice and inspiring environment to work in, in particular and in alphabetical order Benedikt Wirth for answering many questions starting with ‘Benedict, you as an engineer ...’, Benjamin Berkels for various discussions, in particular visualization using VTK, and many pots of tea, Martin Lenz for his help with special C++ issues and his experience with homogenization, Martina Franken for her implementation of sweeping methods, Oliver Nemitz for listening to many ideas and pointing out mistakes, Orestis Vantzios for giving me an introduction to POV-Ray, and Stefan von Deylen for discussions and partial disagreement about various topics. In addition to them, Behrend Heeren, Benedict Geihe, Nadine Olischläger, Sascha Tölkes, and Simplicite Nemadjieu gave me countless suggestions for improvement after reading a first draft of this thesis. Our QuocMesh software library was also very helpful, despite my many complaints.

Without a good text editor, typesetting software and many other little tools, writing this thesis would have taken substantially more time. Many thanks to all those who contributed to the different open source software products. Thanks also to my fellow members of the CdE Dokuteam from whom I learnt a lot about typography.

Bibliography

- [1] *Encyclopædia Britannica Online*, 2010.
- [2] Sudarsan N. S. Achaya, *Multigrid conjugate gradient method*, Master's thesis, Friedrich-Alexander-Universität Erlangen, 2006.
- [3] Loyce Adams, *A multigrid algorithm for immersed interface problems*, Proceedings of the Seventh Copper Mountain Conference on Multigrid Methods, 1996, SEE N97-13750 01-64, pp. 1–14.
- [4] Loyce Adams and Zhilin Li, *The immersed interface/multigrid methods for interface problems*, SIAM Journal on Scientific Computing **24** (2002), no. 2, 463–479.
- [5] Mark Adams, Marian Brezina, Jonathan Hu, and Ray Tuminaro, *Parallel multigrid smoothing: Polynomial versus Gauss-Seidel*, Journal of Computational Physics **188** (2003), no. 2, 593–610.
- [6] Mark F. Adams, Harun H. Bayraktar, Tony M. Keaveny, and Panayiotis Papdopoulos, *Applications of algebraic multigrid to large-scale finite element analysis of whole bone micro-mechanics on the IBM SP*, Proceedings of the 2003 ACM/IEEE conference on Supercomputing, 2003, Conference on High Performance Networking and Computing, p. 26ff.
- [7] Robert A. Adams, *Sobolev spaces*, Pure and Applied Mathematics, vol. 65, Academic Press, 1975.
- [8] Jeroen Aerssens, Steven Boonen, Geert Lowet, and Jan Dequeker, *Interspecies differences in bone composition, density and quality: Potential implications for in vivo bone research*, Endocrinology **139** (1998), no. 2, 663–670.
- [9] Burak Aksoylu and Zuhail Yeter, *Robust multigrid preconditioners for cell-centered finite volume discretization of high-contrast diffusion equation*, Apr 2009, arXiv:0904.1885v1 [math.NA].
- [10] Grégoire Allaire, *Shape optimization by the homogenization method*, Applied Mathematical Sciences, vol. 146, Springer-Verlag, New York, 2002.
- [11] Pierre Alliez, David Cohen-Steiner, Mariette Yvinec, and Mathieu Desbrun, *Variational tetrahedral meshing*, ACM Transactions on Graphics **24** (2005), no. 3, 617–625.
- [12] Sergio F. Almonacid-Merino and J. Antonio Torres, *Mathematical models to evaluate temperature abuse effects during distribution of refrigerated solid foods*, Journal of Food Engineering **20** (1993), 223–245.
- [13] Todd Arbogast, *Numerical subgrid upscaling of two-phase flow in porous media*, 2000.
- [14] Todd Arbogast, *Numerical treatment of multiphase flows in porous media*, Lecture Notes in Physics, vol. 552, ch. Numerical Subgrid Upscaling of Two-Phase Flow in Porous Media, pp. 35–49, Springer, 2000.
- [15] Todd Arbogast, *Current trends in scientific computing*, Contemporary Mathematics, vol. 329, ch. An overview of subgrid upscaling for elliptic problems in mixed form, pp. 21–32, AMS, 2003.
- [16] Todd Arbogast, Susan Minkoff, and Phil Keenan, *An operator-based approach to upscaling the pressure equation*, Tech. Report 97-30, University of Texas at Austin, 1997.
- [17] Todd Arbogast, Susan E. Minkoff, and Philip T. Keenan, *Computational methods in contamination and remediation of water resources*, vol. 1, Computational Methods in Water Resources, no. XII, ch. An operator-based approach to upscaling the pressure equation, pp. 405–412, Computational Mechanics Publications, 1998.
- [18] C. G. Armstrong, D. J. Robinson, R. M. McKeag, T. S. Li, S. J. Bridgett, R. J. Donaghy, and C. A. McGleenan, *Medials for meshing and more*, Proceedings of the 4th International Meshing Roundtable, Sandia

- National Laboratories, October 1995, pp. 277–288.
- [19] G. P. Astrakhansev, *An iterative method of solving elliptic net problems*, USSR Computational Mathematics and Mathematical Physics **11** (1971), no. 2, 171–182, Translated by J. Berry.
- [20] G. P. Astrakhansev, *Method of fictitious domain for a second-order elliptic equation with natural boundary conditions*, USSR Computational Mathematics and Mathematical Physics **18** (1978), no. 1, 114–121, Translated by D. E. Brown.
- [21] P. Augat, H. Reeb, and L. E. Claes, *Prediction of fracture load at different skeletal sites by geometrical properties of the cortical shell*, Journal of Bone and Mineral Research **11** (1996), no. 9, 1356–1363.
- [22] Peter Augat, Thomas Link, Thomas F. Lang, John C. Lin, Sharmila Majumdar, and Harry K. Genant, *Anisotropy of the elastic modulus of trabecular bone specimens from different anatomical locations*, Medical Engineering & Physics **20** (1998), no. 2, 124–131.
- [23] Franz Aurenhammer, *Voronoi diagrams – a survey of a fundamental geometric data structure*, ACM Computing Surveys **23** (1991), no. 3, 345–405.
- [24] O. Axelsson, *A survey of preconditioned iterative methods for linear systems of algebraic equations*, BIT Numerical Mathematics **25** (1985), no. 1, 165–187.
- [25] Owe Axelsson, *Iterative solution methods*, Cambridge University Press, 1994.
- [26] A. O. Ayhan and H. F. Nied, *Stress intensity factors for three-dimensional surface cracks using enriched finite elements*, International Journal for Numerical Methods in Engineering **54** (2002), 899–921.
- [27] I. Babuška and J. M. Melenk, *The partition of unity method*, International Journal for Numerical Methods in Engineering **40** (1997), no. 4, 727–758.
- [28] Ivo Babuška, Uday Banerjee, and John E. Osborn, *Survey of meshless and generalized finite element methods: A unified approach*, Acta Numerica **12** (2003), 1–125.
- [29] Ivo Babuška, Uday Banerjee, and John E. Osborn, *Generalized finite element methods – main ideas, results and perspective*, International Journal of Computational Methods **1** (2004), no. 1, 67–103.
- [30] Timothy J. Baker, *Automatic mesh generation for complex three-dimensional regions using a constrained Delaunay triangulation*, Engineering with Computers **5** (1989), 161–175.
- [31] N. S. Bakhvalov, *On the convergence of a relaxation method with natural constraints on the elliptic operator*, USSR Computational Mathematics and Mathematical Physics **6** (1966), no. 5, 101–135, Translated by H. F. Cleaves.
- [32] Grey Ballard, James Demmel, Olga Holtz, and Oded Schwartz, *Communication-optimal parallel and sequential Cholesky decomposition*, February 2009, arXiv:0902.2537v1 [cs.NA].
- [33] Randolph E. Bank and Craig C. Douglas, *Sharp estimates for multigrid rates of convergence with general smoothing and acceleration*, SIAM Journal on Numerical Analysis **22** (1985), no. 4, 617–633.
- [34] Randolph E. Bank and Todd Dupont, *An optimal order process for solving finite element equations*, Mathematics of Computation **36** (1981), no. 153, 35–51.
- [35] Randolph E. Bank and R. Kent Smith, *The incomplete factorization multigraph algorithm*, SIAM Journal on Scientific Computing **20** (1999), no. 4, 1349–1364.
- [36] J. R. Barber, *Elasticity*, 2 ed., Kluwer, 2002.
- [37] Michael F. Barnsley, Robert L. Devaney, Benoît B. Mandelbrot, Heinz-Otto Peitgen, Dietmar Saupe, and Richard F. Voss, *The science of fractal images*, Springer-Verlag, New York, 1988, With contributions by Yuval Fisher and Michael McGuire.
- [38] John W. Barrett and Charles M. Elliott, *A finite-element method for solving elliptic equations with Neumann data on a curved boundary using unfitted meshes*, IMA Journal of Numerical Analysis **4** (1984), 309–325.
- [39] John W. Barrett and Charles M. Elliott, *Fitted and unfitted finite-element methods for elliptic equations with smooth interfaces*, IMA

- Journal of Numerical Analysis **7** (1987), 283–300.
- [40] John W. Barrett and Charles M. Elliott, *A practical finite element approximation of a semi-definite Neumann problem on a curved domain*, Numerische Mathematik **51** (1987), 23–36.
- [41] John W. Barrett and Charles M. Elliott, *Finite-element approximation of elliptic equations with a Neumann or Robin condition on a curved domain*, IMA Journal of Numerical Analysis **8** (1988), 321–342.
- [42] Harun H. Bayraktar, Atul Gupta, Ron Y. Kwon, and Tony M. Papadopoulos, Panayiotis and Keaveny, *The modified super-ellipsoid yield criterion for human trabecular bone*, Journal of Biomechanical Engineering **126** (2004), no. 6, 677–684.
- [43] R. Becker and R. Rannacher, *Weighted a posteriori error control in FE methods*, Tech. Report 96-1, Institut für Angewandte Mathematik, Universität Heidelberg, Jan. 1996.
- [44] T. Belytschko and T. Black, *Elastic crack growth in finite elements with minimal remeshing*, International Journal for Numerical Methods in Engineering **45** (1999), no. 5, 601–620.
- [45] T. Belytschko, Y. Krongauz, D. Organ, M. Fleming, and P. Krysl, *Meshless methods: An overview and recent developments*, Computer methods in applied mechanics and engineering **139** (1996), 3–47.
- [46] T. Belytschko, N. Moës, S. Usui, and C. Parimi, *Arbitrary discontinuities in finite elements*, International Journal for Numerical Methods in Engineering **50** (2001), no. 4, 993–1013.
- [47] Marshall Bern and David Eppstein, *Computing in Euclidian geometry*, Lecture Notes Series on Computing, vol. 1, ch. Mesh generation and optimal triangulation, pp. 23–90, World Scientific, Singapore, 1992.
- [48] Marshall Bern, David Eppstein, and John Gilbert, *Provably good mesh generation*, Proceedings of 31st Annual Symposium on Foundations of Computer Science, October 1990, pp. 231–241.
- [49] Marshall Bern and Paul Plassmann, *Mesh generation*, ch. 6, pp. 291–332, Elsevier Science, 1999.
- [50] R. P. Beyer and R. J. LeVeque, *Analysis of a one-dimensional model for the immersed boundary method*, SIAM Journal on Numerical Analysis **29** (1992), no. 2, 332–364.
- [51] Benjamin C. Bourne and Majorlein C. H. van der Meulen, *Finite element models predict cancellous apparent modulus when tissue modulus is scaled from specimen CT-attenuation*, Journal of Biomechanics **37** (2004), no. 5, 613–621.
- [52] Steven K. Boyd and Ralph Müller, *Smooth surface meshing for automated finite element model generation from 3D image data*, Journal of Biomechanics **39** (2006), no. 7, 1287–1295.
- [53] Dietrich Braess, *The convergence rate of a multigrid method with Gauss-Seidel relaxation for the Poisson equation*, Mathematics of Computation **42** (1984), no. 166, 505–519.
- [54] Dietrich Braess, *Towards algebraic multigrid for elliptic problems of second order*, Computing **55** (1995), 379–393.
- [55] Dietrich Braess, *Finite Elemente*, 2nd ed., Springer, 1997, Theorie, schnelle Löser und Anwendungen in der Elastizitätstheorie.
- [56] Helmut Brakhage, *Über die numerische Behandlung von Integralgleichungen nach der Quadraturformelmethode*, Numerische Mathematik **2** (1960), 183–196.
- [57] James H. Bramble, Joseph E. Pasciak, and Jinchao Xu, *Parallel multilevel preconditioners*, Mathematics of Computation **55** (1990), no. 191, 1–22.
- [58] James H. Bramble, Joseph E. Pasciak, and Jinchao Xu, *The analysis of multigrid algorithms with nonnested spaces or noninherited quadratic forms*, Mathematics of Computation **56** (1991), no. 56, 1–34.
- [59] Achi Brandt, *Multi-level adaptive solutions to boundary-value problems*, Mathematics of Computation **31** (1977), no. 138, 333–390.
- [60] Achi Brandt, *General highly accurate algebraic coarsening*, Electronic Transaction on Numerical Analysis **10** (2000), 1–20.

- [61] Achi Brandt and Dorit Ron, *Combinatorial optimization and vlsicad*, vol. 14, ch. Multigrid Solvers and Multilevel Optimization Strategies, pp. 1–69, Kluwer Academic Publishers, 2003.
- [62] Achi Brandt, *Methods of systematic upscaling*, Tech. Report MCS06-05, Weizmann Institute of Science, 2006.
- [63] M. Brezina, A. J. Cleary, R. D. Falgout, V. E. Henson, J. E. Jones, T. A. Manteuffel, S. F. McCormick, and J. W. Ruge, *Algebraic multigrid based on element interpolation (AMGe)*, *SIAM Journal on Scientific Computing* **22** (2000), no. 5, 1570–1592.
- [64] M. Brezina, R. Falgout, S. MacLachlan, T. Manteuffel, S. McCormick, and J. Ruge, *Adaptive smoothed aggregation (α SA)*, *SIAM Journal on Scientific Computing* **25** (2004), no. 6, 1896–1920.
- [65] M. Brezina, R. Falgout, S. MacLachlan, T. Manteuffel, S. McCormick, and J. Ruge, *Adaptive algebraic multigrid*, *SIAM Journal on Scientific Computing* **27** (2006), no. 4, 1261–1286.
- [66] A. Buades, B. Coll, and J. M. Morel, *A review of image denoising algorithms, with a new one*, *Multiscale Modeling and Simulation* **4** (2005), no. 2, 490–530.
- [67] Martin L. Buist and Andrew J. Pullan, *The effect of torso impedance on epicardial and body surface potentials: A modeling study*, *IEEE Transactions on Biomedical Engineering* **50** (2003), no. 7, 816–824.
- [68] Donna Calhoun, *A Cartesian grid method for solving the two-dimensional streamfunction-vorticity equations in irregular regions*, *Journal of Computational Physics* **176** (2002), 231–275.
- [69] Donna Calhoun and Randall J. LeVeque, *A Cartesian grid finite-volume method for the advection-diffusion equation in irregular geometries*, *Journal of Computational Physics* **157** (2000), 143–180.
- [70] Carsten Carstensen, *A posteriori error estimate for the mixed Finite Element method*, *Mathematics of Computation* **66** (1997), no. 218, 465–476.
- [71] Antonio Cazzani and Marco Rovati, *Extrema of Young’s modulus for cubic and transversely isotropic solids*, *International Journal of Solids and Structures* **40** (2003), 1713–1744.
- [72] Tony F. Chan and Barry F. Smith, *Domain decomposition and multigrid algorithms for elliptic problems on unstructured meshes*, *Electronic Transactions on Numerical Analysis* **2** (1994), 171–182.
- [73] Tony F. Chan and Luminita A. Vese, *Active contours without edges*, *IEEE Transactions on Image Processing* **10** (2001), no. 2, 266–277.
- [74] Tony F. Chan and W. L. Wan, *Robust multigrid methods for nonsmooth coefficient elliptic linear systems*, *Journal of Computational and Applied Mathematics* **123** (2000), 323–352.
- [75] C. S. Chang, *Measuring density and porosity of grain kernels using a gas pycnometer*, *Cereal Chemistry* **65** (1988), no. 1, 13–15.
- [76] M. C. Chang, C. L. Liu, and T. H. Chen, *Polymethylmethacrylate augmentation of pedicle screw for osteoporotic spinal surgery: a novel technique*, *Spine* **33** (2008), no. 10, E317–E324.
- [77] Siu-Wing Cheng, Tamal K. Dey, Herbert Edelsbrunner, Michael A. Facello, and Shang-Hua Teng, *Sliver exudation*, *Journal of the ACM* **47** (2000), no. 5, 883–904.
- [78] Yan Chevalier, Dieter Pahr, Helga Allmer, Mathieu Charlebois, and Philippe Zysset, *Validation of a voxel-based FE method for prediction of the uniaxial apparent modulus of human trabecular bone using macroscopic mechanical tests and nanoindentation*, *Journal of Biomechanics* **40** (2007), 3333–3340.
- [79] John H. Chi and Ziya L. Gokaslan, *Vertebroplasty and kyphoplasty for spinal metastases*, *Current Opinion in Supportive and Palliative Care* **2** (2008), no. 1, 9–13.
- [80] Chia Hsun Chiang, Po Jui Chiang, Jerry Chien-Chih Fei, and Jin Sin Liu, *A comparative study of implementing fast marching method and A* search for mobile robot path planning in grid environment: Effect of map resolution*, *Proceedings of the IEEE Workshop on Advanced Robotics and its Social Impacts*, 2007.

- [81] N. Chiba, I. Nishigaki, Y. Yamashita, C. Takizawa, and K. Fujishiro, *An automatic hexahedral mesh generation system based on the shape-recognition and boundary-fit methods*, Proceedings of 5th International Meshing Roundtable, Sandia National Laboratories, 1996, pp. 281–290.
- [82] E. Chow, A. Cleary, and R. Falgout, *Design of the hypre preconditioner library*, SIAM Conference on Object Oriented Methods for Interoperable Scientific and Engineering Computing, 1998.
- [83] Philippe G. Ciarlet, *Mathematical elasticity, volume I: Three-dimensional elasticity*, Studies in Mathematics and its Applications, vol. 20, Elsevier, 1988.
- [84] Andrew J. Cleary, Robert D. Falgout, Van Emden Henson, Jim E. Jones, Thomas A. Manteuffel, Stephen F. McCormick, Gerald N. Miranda, and John W. Ruge, *Robustness and scalability of algebraic multigrid*, SIAM Journal on Scientific Computing **21** (2000), no. 5, 1886–1908.
- [85] Ronald Cools, *An encyclopaedia of cubature formulas*, Journal of Complexity **19** (2003), 445–453.
- [86] Ronald Cools and Philip Rabinowitz, *Monomial cubature rules since “Stroud”: a compilation*, Journal of Computational and Applied Mathematics **48** (1993), no. 3, 309–326.
- [87] A. M. Cormack, *Representation of a function by its line integrals, with some radiological applications*, Journal of Applied Physics **34** (1963), no. 9, 2722–2727.
- [88] A. M. Cormack, *Representation of a function by its line integrals, with some radiological applications II*, Journal of Applied Physics **35** (1963), no. 10, 2908–2913.
- [89] Luis M. Cruz-Orive, Lars M. Karlsson, Søren E. Larsen, and Felix Wainschtein, *Characterizing anisotropy: A new concept*, Micron and Microscopia Acta **23** (1992), no. 1/2, 75–76.
- [90] Christophe Daux, Nicolas Moës, John Dolbow, Natarjan Sukumar, and Ted Belytschko, *Arbitrary branched and intersecting cracks with the extended finite element method*, International Journal for Numerical Methods in Engineering **48** (2000), 1741–1760.
- [91] P. M. de Zeeuw, *Matrix-dependent prolongations and restrictions in a black-box multigrid solver*, Journal of Computational and Applied Mathematics **33** (1990), 1–27.
- [92] Christian Decolon, *Analysis of composite structures*, Taylor & Francis, 2000.
- [93] Joel E. Dendy Jr., *Black box multigrid*, Journal of Computational Physics **48** (1982), 366–386.
- [94] Peter Deuffhard, Martin Weiser, and Martin Seebaß, *A new nonlinear elliptic multilevel FEM applied to regional hyperthermia*, Computing and Visualization in Science **3** (2000), no. 3, 115–120.
- [95] I. Diamant, R. Shahar, and A. Gefen, *How to select the elastic modulus for cancellous bone in patient-specific continuum models of the spine*, Medical and Biological Engineering and Computing **43** (2005), 465–472.
- [96] I. Diamant, R. Shahar, Y. Masharawi, and A. Gefen, *A method for patient-specific evaluation of vertebral cancellous bone strength: in-vitro validation*, Clinical Biomechanics **22** (2007), no. 3, 282–291.
- [97] Thomas Dickopf and Rolf Krause, *A pseudo- L^2 -projection for multilevel methods based on non-nested meshes*, INS Preprint 0908, Institut für Numerische Simulation, Universität Bonn, August 2009.
- [98] Ming Ding, Michel Dalstra, Carl C. Danielsen, Jesper Kabel, Ivan Hvid, and Frank Linde, *Age variations in the properties of human tibial trabecular bone*, Journal of Bone and Joint Surgery **79-B** (1997), 995–1002.
- [99] John Dolbow, *An extended finite element method with discontinuous enrichment for applied mechanics*, Dissertation, Northwestern University, 1999.
- [100] Qiang Du and Desheng Wang, *Tetrahedral mesh generation and optimization based on centroidal Voronoi tessellations*, International Journal for Numerical Methods in Engineering **56** (2003), no. 9, 1355–1373.

Bibliography

- [101] C. A. Duarte, I. Babuška, and J. T. Oden, *Generalized finite element methods for three-dimensional structural mechanics problems*, *Computers & Structures* **77** (2000), no. 2, 215–232.
- [102] C. A. Duarte, O. N. Hamzeh, T. J. Liszka, and W. W. Tworzydło, *A generalized finite element method for the simulation of three-dimensional dynamic crack propagation*, *Computer methods in applied mechanics and engineering* **190** (2001), no. 15–17, 2227–2262.
- [103] C. A. Duarte, D.-J. Kim, and D. M. Quaresima, *Arbitrarily smooth generalized finite element approximations*, *Computer methods in applied mechanics and engineering* **196** (2006), no. 1–3, 33–56.
- [104] C. Armando Duarte, *A review of some meshless methods to solve partial differential equations*, TICAM Report 95-06, Texas Institute for Computational and Applied Mathematics, University of Texas at Austin, U.S.A., 1995.
- [105] C. Armando Duarte and J. T. Oden, *hp clouds—a meshless method to solve boundary-value problems*, TICAM Report 95-05, Texas Institute for Computational and Applied Mathematics, University of Texas at Austin, 1995.
- [106] C. Armando Duarte and J. Tinsley Oden, *An h-p adaptive method using clouds*, *Computer methods in applied mechanics and engineering* **139** (1996), no. 1–4, 237–262.
- [107] C. Armando Duarte and J. Tinsley Oden, *h-p clouds—an h-p meshless method*, *Numerical Methods for Partial Differential Equations* **12** (1996), no. 6, 673–705.
- [108] Carlos Armando Duarte, *The hp cloud method*, Phd dissertation, University of Texas at Austin, December 1996.
- [109] Iain S. Duff and Gérard A. Meurant, *The effect of ordering on preconditioning conjugate gradients*, *BIT Numerical Mathematics* **29** (1989), no. 4, 635–657.
- [110] A. Düster, J. Parvizián, Z. Yang, and E. Bank, *The finite cell method for three-dimensional problems of solid mechanics*, *Computer methods in applied mechanics and engineering* **197** (2008), no. 45–48, 3768–3782.
- [111] A. R. East and N. J. Smale, *Combining a hybrid genetic algorithm and a heat transfer model to optimise an insulated box for use in the transport of perishables*, *Vaccine* **26** (2008), no. 10, 1322–1334.
- [112] E. N. Ebbesen, J. S. Thomsen, H. Beck-Nielsen, H. Nepper-Rasmussen, and L. Mosekilde, *Lumbar vertebral body compressive strength evaluated by dual-energy X-ray absorptiometry, quantitative computed tomography, and ashing*, *Bone* **25** (1999), no. 6, 713–724.
- [113] Kenneth Eriksson, Don Estep, Peter Hansbo, and Claes Johnson, *Introduction to adaptive methods for differential equations*, *Acta Numerica* (1995), 105–158.
- [114] R. D. Falgout, *An introduction to algebraic multigrid*, Tech. Report UCRL-JRNL-220851, Lawrence Livermore National Laboratory, 2006.
- [115] Robert D. Falgout, Jim E. Jones, and Ulrike Meier Yang, *The design and implementation of hypre, a library of parallel high performance preconditioners*, *Lecture Notes in Computational Science and Engineering* **51** (2004), 1–29.
- [116] Robert D. Falgout, Jim E. Jones, and Ulrike Meier Yang, *Conceptual interfaces in hypre*, *Future Generation Computer Systems* **22** (2006), no. 1–2, 239–251.
- [117] Robert D. Falgout and Ulrike Meier Yang, *Computational science – ICCS 2002*, *Lecture Notes in Computer Science*, vol. 2330, ch. hypre: A Library of High Performance Preconditioners, pp. 632–641, Springer, 2002, Proceedings of the International Conference on Computational Science, Part III.
- [118] Kenneth G. Faulkner, Christopher E. Cann, and Bruce H. Hasegawa, *Effect of bone distribution on vertebral strength: Assessment with patient-specific nonlinear Finite Element analysis*, *Radiology* **179** (1991), 669–674.
- [119] R. P. Fedorenko, *A relaxation method for solving elliptic difference equations*, USSR

- Computational Mathematics and Mathematical Physics **1** (1962), no. 4, 1092–1096, Translated by D. E. Brown.
- [120] D. Feuchter, I. Heppner, S. A. Sauter, and G. Wittum, *Bridging the gap between geometric and algebraic multi-grid methods*, Computing and Visualization in Science **6** (2003), no. 1, 1–16.
- [121] Aaron G. Filler, *The history, development and impact of computed imaging in neurological diagnosis and neurosurgery: CT, MRI, and DTI*, Nature Precedings, July 2009.
- [122] R. A. Finkel and J. L. Bentley, *Quad trees. A data structure for retrieval on composite keys*, Acta Informatica **4** (1974), 1–9.
- [123] J. Fish and V. Belsky, *Generalized aggregation multigrid solver*, International Journal for Numerical Methods in Engineering **40** (1997), no. 23, 4341–4361.
- [124] European Foundation for Osteoporosis and National Osteoporosis Foundation of the U.S.A., *Consensus development statement – who are candidates for prevention and treatment for osteoporosis?*, Osteoporosis International **7** (1997), 1–6.
- [125] P. Fransen, *Increasing pedicle screw anchoring in the osteoporotic spine by cement injection through the implant. Technical note and report of three cases*, Journal of Neurosurgery: Spine **7** (2007), no. 3, 366–369.
- [126] N. Frauböse and S. A. Sauter, *Composite finite elements and multi-grid part I: Convergence theory in 1-d*, Proceedings of the 17th GAMM-Seminar Leipzig (Leipzig, Germany), Max-Planck-Institute for Mathematics in the Sciences, 2001, pp. 69–86.
- [127] Thomas-Peter Fries and Hermann-Georg Matthies, *Classification and overview of meshfree methods*, Informatikbericht 2003-3, Institute of Scientific Computing, Technical University Braunschweig, 2004, (revised version).
- [128] Andrea Fuhlrott, *Implementierung der X-FEM in SLang und Verifizierung der Anwendbarkeit für Rissberechnungen*, Diplom thesis, Bauhaus-Universität Weimar, Institut für Strukturmechanik, Fakultät Bauingenieurwesen, 2004.
- [129] T. Gao, W. H. Zhang, J. H. Zhu, Y. J. Xu, and D. H. Bassir, *Topology optimization of heat conduction problem involving design-dependent heat load effect*, Finite Elements in Analysis and Design **44** (2008), no. 14, 805–813.
- [130] Michael J. Gardner, Demetris Demetrakopoulos, Michael K. Shindle, Matthew H. Griffith, and Joseph M. Lane, *Osteoporosis and skeletal fractures*, HSS Journal **2** (2006), no. 1, 62–69.
- [131] H. K. Genant, M. D. Guglielmi, and M. Jergas (eds.), *Bone densitometry and osteoporosis*, Springer-Verlag, 1998.
- [132] T. Gerstner, M. Rumpf, and U. Weikard, *Error indicators for multilevel visualization and computing on nested grids*, Computers & Graphics **24** (2000), no. 3, 363–373.
- [133] L. J. Gibson, *The mechanical behaviour of cancellous bone*, Journal of Biomechanics **18** (1985), no. 5, 317–328.
- [134] Lorna J. Gibson, *Biomechanics of cellular solids*, Journal of Biomechanics **38** (2005), no. 3, 377–399.
- [135] R. Glowinski and Yu. Kuznetsov, *Distributed Lagrange multipliers based on fictitious domain method for second order elliptic problems*, Computer Methods in Applied Mechanics and Engineering **196** (2007), no. 8, 1498–1506.
- [136] Vijay K. Goel and John D. Clausen, *Prediction of load sharing among spinal components of a C5-C6 motion segment using the finite element approach*, Spine **23** (1998), no. 6, 684–691.
- [137] N. A. Golias and T. D. Tsiboukis, *An approach to refining three-dimensional tetrahedral meshes based on Delaunay transformations*, International Journal for Numerical Methods in Engineering **37** (1994), no. 5, 793–812.
- [138] M.J. Gómez-Benito, J.M. García-Aznar, and M. Doblaré, *Finite element prediction of proximal femoral fracture patterns under different loads*, Journal of Biomechanical Engineering **127** (2005), no. 1, 9–14.
- [139] Dan Gordon and Rachel Gordon, *Geometric scaling: A simple and effective preconditioner*

Bibliography

- for linear systems with discontinuous coefficients, May 2009, arXiv:0812.2769v2 [cs.MS].
- [140] T. Grauschopf, M. Griebel, and H. Regler, *Additive multilevel preconditioners based on bilinear interpolation, matrix-dependent geometric coarsening and algebraic multigrid coarsening for second-order elliptic PDEs*, *Applied Numerical Mathematics* **23** (1997), no. 1, 63–95.
- [141] M. Griebel, D. Oeltz, and M. A. Schweitzer, *An algebraic multigrid method for linear elasticity*, Tech. Report 13, Rheinische Friedrich-Wilhelms Universität Bonn, SFB 611, Mai 2002.
- [142] Michael Griebel, Bram Metsch, Daniel Oeltz, and Marc Alexander Schweitzer, *Coarse grid classification: A parallel coarsening scheme for algebraic multigrid methods*, *Numerical Linear Algebra with Applications* **13** (2006), no. 2-3, 193–214.
- [143] Michael Griebel, Bram Metsch, and Marc Alexander Schweitzer, *Coarse grid classification - Part II: Automatic coarse grid agglomeration for parallel AMG*, SFB Preprint 271, SFB 611, Universität Bonn, 2006.
- [144] Y. Guéguen, M. Le Ravalec, and L. Ricard, *Upscaling: Effective medium theory, numerical methods and the fractal dream*, *Pure and Applied Geophysics* **163** (2006), 1175–1192.
- [145] Ramesh M. Gulrajani, *The forward problem of electrocardiography: From heart models to body surface potentials*, Proceedings of the 19th Annual International Conference of the IEEE Engineering in Medicine and Biology Society, 1997.
- [146] Ramesh M. Gulrajani, *The forward and inverse problems of electrocardiography*, *IEEE Engineering in Medicine and Biology* **17** (1998), no. 5, 84–101.
- [147] X. E. Guo and C. H. Kim, *Mechanical consequences of trabecular bone loss and its treatment: A three-dimensional model simulation*, *Bone* **30** (2002), no. 2, 404–411.
- [148] Yong Guo, Michael Oritz, Ted Belytschko, and Eduardo A. Repetto, *Triangular composite finite elements*, *International Journal for Numerical Methods in Engineering* **47** (2000), no. 1-3, 287–316.
- [149] W. Hackbusch and S. Sauter, *A new finite element approach for problems containing small geometric details*, *Archivum Mathematicum* **34** (1998), 105–117, Equadiff 9 issue.
- [150] W. Hackbusch and S. A. Sauter, *Composite finite elements for problems containing small geometric details. Part II: Implementation and numerical results*, *Computing and Visualization in Science* **1** (1997), no. 1, 15–25.
- [151] W. Hackbusch and S. A. Sauter, *Composite finite elements for problems with complicated boundary. Part III: Essential boundary conditions*, Tech. report, Universität Kiel, 1997.
- [152] W. Hackbusch and S. A. Sauter, *Composite finite elements for the approximation of PDEs on domains with complicated micro-structures*, *Numerische Mathematik* **75** (1997), no. 4, 447–472.
- [153] Wolfgang Hackbusch, *Multi-grid methods and applications*, Springer Series in Computational Mathematics, vol. 4, Springer, 1985.
- [154] Wolfgang Hackbusch, *Iterative solution of large sparse systems of equations*, *Applied Mathematical Sciences*, vol. 95, Springer, 1994.
- [155] Martin Hanke-Bourgeois, *Grundlagen der Numerischen Mathematik und des Wissenschaftlichen Rechnens*, Teubner, 2002.
- [156] Anita Hansbo and Peter Hansbo, *An unfitted finite element method, based on Nitsche's method, for elliptic interface problems*, *Computer methods in applied mechanics and engineering* **191** (2002), 5537–5552.
- [157] Anita Hansbo and Peter Hansbo, *A finite element method for the simulation of strong and weak discontinuities in solid mechanics*, *Computer methods in applied mechanics and engineering* **193** (2004), no. 33-35, 3523–3540.
- [158] Peter Hansbo, *Beyond the elements of finite elements: General principles for solid and fluid mechanics applications*, Lecture Notes, Chalmers University of Technology, Sweden, 2006.

- [159] T. P. Harrigan and R. W. Mann, *Characterization of microstructural anisotropy in orthotropic materials using a second rank tensor*, *Journal of Materials Science* **19** (1984), no. 3, 761–767.
- [160] Timothy P. Harrigan, Murali Jasty, Robert W. Mann, and William H. Harris, *Limitations of the continuum assumption in cancellous bone*, *Journal of Biomechanics* **21** (1988), no. 4, 269–275.
- [161] Q.-C. He and A. Curnier, *A more fundamental approach to damaged elastic stress-strain relations*, *International Journal for Solids and Structures* **32** (1995), no. 10, 1433–1457.
- [162] C.-J. Heine, *Finite element methods on unfitted meshes*, Preprint 09, Fakultät für Mathematik und Physik, Albert-Ludwigs-Universität Freiburg, 2008.
- [163] Van Emden Henson and Ulrike Meier Yang, *BoomerAMG: a parallel algebraic multigrid solver and preconditioner*, *Applied Numerical Mathematics* **41** (2002), no. 1, 155–177.
- [164] Magnus R. Hestenes and Eduard Stiefel, *Methods of conjugate gradients for solving linear systems*, *Journal of Research of the National Bureau of Standards* **49** (1952), no. 6, 409–436.
- [165] Tor Hildebrand, Andres Laib, Ralph Müller, Jan Dequeker, and Peter Rügsegger, *Direct three-dimensional morphometric analysis of human cancellous bone: Microstructural data from spine, femur, iliac crest, and calcaneus*, *Journal of Bone and Mineral Research* **14** (1999), no. 7, 1167–1174.
- [166] T. Hildebrandt and P. Rügsegger, *A new method for the model-independent assessment of thickness in three-dimensional images*, *Journal of Microscopy* **185** (1997), no. 1, 67–75.
- [167] Klaus Höllig, Christian Apprich, and Anja Streit, *Introduction to the Web-method and its applications*, *Advances in Computational Mathematics* **23** (2005), no. 1-2, 215–237.
- [168] Klaus Höllig and Ulrich Reif, *Nonuniform web-splines*, *Computer Aided Geometric Design* **20** (2003), no. 5, 277–294.
- [169] Klaus Höllig, Ulrich Reif, and Joachim Wipper, *Weighted extended B-spline approximation of Dirichlet problems*, *SIAM Journal on Numerical Analysis* **39** (2001), no. 2, 442–462.
- [170] Klaus Höllig, Ulrich Reif, and Joachim Wipper, *Multigrid methods with web-splines*, *Numerische Mathematik* **91** (2002), 237–255.
- [171] S. J. Hollister, J. M. Brennan, and N. Kikuchi, *A homogenization sampling procedure for calculating trabecular bone effective stiffness and tissue level stresses*, *Journal of Biomechanics* **27** (1994), no. 4, 433–444.
- [172] S. J. Hollister, D. P. Fyhrie, K. J. Jepsen, and S. A. Goldstein, *Application of homogenization theory to the study of trabecular bone mechanics*, *Journal of Biomechanics* **24** (1991), no. 9, 825–839.
- [173] S. J. Hollister and N. Kikuchi, *A comparison of homogenization and standard mechanics analyses for periodic porous composites*, *Computational Mechanics* **10** (1992), no. 2, 73–95.
- [174] S. J. Hollister and N. Kikuchi, *Homogenization theory and digital imaging: A basis for studying the mechanics and design principles of bone tissue*, *Biotechnology and Bioengineering* **43** (1994), 586–596.
- [175] Jasper Homminga, Harrie Weinans, Wolfgang Gowin, Dieter Felsenberg, and Rik Huiskes, *Osteoporosis changes the amount of vertebral trabecular bone at risk of fracture but not the vertebral load distribution*, *Spine* **26** (2001), no. 14, 1555–1560.
- [176] Godfrey N. Hounsfield, *A method of and apparatus for examination of a body by radiation such as X-ray or gamma radiation*, *British Patent Number 1283915*, 1972.
- [177] R. Huang, N. Sukumar, and J.-H. Prévost, *Modeling quasi-static crack growth with the extended finite element method. Part II: Numerical applications*, *International Journal of Solids and Structures* **40** (2003), no. 26, 7539–7552.
- [178] C. Huet, *Application of variational concepts to size effects in elastic heterogeneous bodies*, *Journal of the Mechanics and Physics of Solids* **38** (1990), no. 6, 813–841.

- [179] Morton A. Hyman, *Non-iterative numerical solution of boundary value problems*, Applied Scientific Research, Section B **2** (1952), 325–351.
- [180] C. G. J. Jacobi, *Über eine neue Auflösungsart der bei der Methode der kleinsten Quadrate vorkommenden linearen Gleichungen*, Astronomische Nachrichten **22** (1844), no. 528, 469–478.
- [181] Milan Jirásek and Ted Belytschko, *Computational resolution of strong discontinuities*, Proceedings of the Fifth World Congress on Computational Mechanics (Vienna, Austria) (H. A. Mang, F. G. Ramerstorfer, and J. Eberhardsteiner, eds.), July 2002.
- [182] Christopher R. Johnson, Robert S. MacLeod, and Philip R. Ershler, *A computer model for the study of electrical current flow in the human thorax*, Computers in Biology and Medicine **22** (1992), no. 5, 305–323.
- [183] I. T. Jolliffe, *Principal component analysis*, 2nd ed., Springer Series in Statistics, Springer, 2002.
- [184] Jim E. Jones and Stephen F. McCormick, *Parallel numerical algorithms*, ICASELaRC Interdisciplinary Series in Science and Engineering, ch. Parallel Multigrid Methods, Kluwer, 1997.
- [185] Jesper Kabel, Bert van Rietbergen, Michel Dalstra, Anders Odgaard, and Rik Huiskes, *The role of an effective isotropic tissue modulus in the elastic properties of cancellous bone*, Journal of Biomechanics **32** (1999), 673–680.
- [186] Deborah M. Kado, Warren S. Browner, Lisa Palermo, Michael C. Nevitt, Harry K. Genant, and Steven R. Cummings, *Vertebral fractures and mortality in older women*, Archives of Internal Medicine **159** (1999), no. 11, 1215–1220.
- [187] J. A. Kanis and O. Johnell, *Requirements for DXA for the management of osteoporosis in Europe*, Osteoporosis International **16** (2005), 229–238.
- [188] Chiu-Yen Kao, Stanley Osher, and Yen-Hsi Tsai, *Fast sweeping methods for static Hamilton-Jacobi equations*, SIAM Journal on Numerical Analysis **42** (2005), no. 6, 2612–2632.
- [189] M. Karlsson, C. Obrant, and P. O. Josefsson, *Rockwood and Green's fractures in adults*, ch. Fractures of Osteoporotic Bone, pp. 613–642, Lippincott Williams & Wilkins, 2005.
- [190] Tony M. Keaveny, Elise F. Morgan, Glen L. Niebur, and Oscar C. Yeh, *Biomechanics of trabecular bone*, Annual Review of Biomedical Engineering **3** (2001), 307–333.
- [191] R. A. Ketcham and T. M. Ryan, *Quantification and visualization of anisotropy in trabecular bone*, Journal of Microscopy **213** (2004), no. 2, 158–171.
- [192] Annette Kettler, Hans-Joachim Wilke, Rupert Dietl, Matthias Krammer, Christiano Lumenta, and Lutz Claes, *Stabilizing effect of posterior lumbar interbody fusion cages before and after cyclic loading*, Neurosurgical Focus **92** (2000), no. 1, 87–92.
- [193] Joyce H. Keyak, Stephen A. Rossi, Kimberly Jones, and Harry B. Skinner, *Prediction of femoral fracture load using automated finite element modeling*, Journal of Biomechanics **31** (1998), no. 2, 125–133.
- [194] Wisama Khalil and Etienne Dombre, *Modeling, identification & control of robots*, Taylor & Francis, 2003.
- [195] Ferdinand Kickingger, *Automatic mesh generation for 3D objects*, Tech. Report 96-1, Institut für Mathematik, Johannes-Kepler-Universität Linz, 1996.
- [196] S. Knapek, *Matrix-dependent multigrid-homogenization for diffusion problems*, SIAM Journal on Scientific Computing **20** (1999), no. 2, 515–533.
- [197] David L. Kopperdahl, Elise F. Morgan, and Tony M. Keaveny, *Quantitative computed tomography estimates of the mechanical properties of human vertebral trabecular bone*, Journal of Orthopaedic Research **20** (2002), no. 4, 801–805.
- [198] V. Kosmopoulos and T. S. Keller, *Damage-based finite-element vertebroplasty simulations*, European Spine Journal **13** (2004), no. 7, 617–625.
- [199] Piotr Kowalczyk, *Elastic properties of cancellous bone derived from finite element models of parameterized microstructure cells*,

- Journal of Biomechanics **36** (2003), no. 7, 961–972.
- [200] Tim Kröger, Inga Altrogge, Tobias Preusser, Philippe L. Pereira, Diethard Schmidt, Andreas Weihusen, and Heinz-Otto Peitgen, *Numerical simulation of radio frequency ablation with state dependent material parameters in three space dimensions*, Medical Image Computing and Computer-Assisted Intervention – MICCAI 2006 (R. Larsen, M. Nielsen, and J. Sporing, eds.), Lecture Notes in Computer Science, vol. 4191, Springer, 2006, pp. 380–388.
- [201] A. J. Ladd, J. H. Kinney, D. L. Haupt, and S. A. Goldstein, *Finite-element modeling of trabecular bone: comparison with mechanical testing and determination of tissue modulus*, Journal of Orthopaedic Research **16** (1998), no. 5, 622–628.
- [202] Anthony J. C. Ladd and John H. Kinney, *Numerical errors and uncertainties in finite-element modeling of trabecular bone*, Journal of Biomechanics **31** (1998), no. 10, 941–945.
- [203] Roderic Lakes, *Foam structures with a negative Poisson's ratio*, Science **235** (1987), 1038–1040.
- [204] P. C. Lauterbur, *Image formation by induced local interactions: Examples of employing nuclear magnetic resonance*, Nature **242** (1973), 190–191.
- [205] Randall J. LeVeque and Zhi Lin Li, *The immersed interface method for elliptic equations with discontinuous coefficients and singular sources*, SIAM Journal on Numerical Analysis **31** (1994), no. 4, 1019–1044.
- [206] E. Michael Lewiecki, *Vertebroplasty and kyphoplasty update*, Current Osteoporosis Reports **6** (2008), no. 3, 114–119.
- [207] Shaofan Li and Wing Kam Liu, *Meshfree and particle methods and their application*, Applied Mechanics Reviews **55** (2002), no. 1, 1–34.
- [208] Z. Li, T. Lin, Y. Lin, and R. C. Rogers, *An immersed finite element space and its approximation capability*, Numerical Methods for Partial Differential Equations **20** (2004), no. 3, 338–367.
- [209] Zhilin Li, *The immersed interface method - a numerical approach for partial differential equations with interfaces*, Dissertation, University of Washington, Seattle, WA, U.S.A., 1994.
- [210] Zhilin Li, *A note on immersed interface method for three-dimensional elliptic equations*, Computers and Mathematics with Applications **31** (1996), no. 3, 9–17.
- [211] Zhilin Li, *A fast iterative algorithm for elliptic interface problems*, SIAM Journal on Numerical Analysis **35** (1998), no. 1, 230–254.
- [212] Zhilin Li, *The immersed interface method using a finite element formulation*, Applied Numerical Mathematics **27** (1998), no. 3, 253–267.
- [213] Zhilin Li, *An overview of the immersed interface method and its applications*, Taiwanese Journal of Mathematics **7** (2003), no. 1, 1–49.
- [214] Zhilin Li, Tao Lin, and Xiaohui Wu, *New Cartesian grid methods for interface problems using the finite element formulation*, Numerische Mathematik **1996** (2003), no. 1, 61–98.
- [215] Michael A. K. Liebschner, William S. Rosenberg, and Tony M. Keaveny, *Effects of bone cement volume and distribution on vertebral stiffness after vertebroplasty*, Spine **26** (2001), no. 14, 1547–1554.
- [216] Florian Liehr, *Ein effizienter Löser für elastische Mikrostrukturen*, Diploma thesis, University Duisburg, 2004.
- [217] Florian Liehr, Tobias Preusser, Martin Rumpf, Stefan Sauter, and Lars Ole Schwen, *Composite finite elements for 3D image based computing*, Computing and Visualization in Science **12** (2009), no. 4, 171–188.
- [218] Thomas M. Link, Sharmila Majumdar, John C. Lin, Peter Augat, Robert G. Gould, David Newitt, Xiaolong Ouyang, Thomas F. Lang, Ashwini Matur, and Harry K. Genant, *Assessment of trabecular structure using high resolution CT images and texture analysis*, Journal of Computer Assisted Tomography **22** (1998), no. 1, 15–24.

Bibliography

- [219] Thomas M. Link, Sharmila Majumdar, John C. Lin, David Newitt, Peter Augat, Xiaolong Ouyang, Ashwini Mathur, and Harry K. Genant, *A comparative study of trabecular bone properties in the spine and femur using high resolution MRI and CT*, *Journal of Bone and Mineral Research* **13** (1998), no. 1, 122–132.
- [220] William E. Lorensen and Havey E. Cline, *Marching cubes: A high resolution 3D surface construction algorithm*, *ACM SIGGRAPH Computer Graphics* **21** (1987), no. 4, 163–169.
- [221] A. I. Lurie, *Theory of elasticity*, *Foundations of Engineering Mechanics*, Springer, 2005.
- [222] J. N. Lyness and Ronald Cools, *A survey of numerical cubature over triangles*, *Proceedings of Symposia in Applied Mathematics* **48**, 1994.
- [223] Scott P. MacLachlan and J. David Moulton, *Multilevel upscaling through variational coarsening*, *Water Resources Research* **42** (2006), W02418.
- [224] Robert S. MacLeod and Dana H. Brooks, *Recent progress in inverse problems in electrocardiology*, *IEEE Engineering in Medicine and Biology* **17** (1998), no. 1, 73–83.
- [225] A. Magid, S. R. Rotman, and A. M. Weiss, *Comment on “picture thresholding using an iterative selection method”*, *IEEE Transactions on Systems, Man and Cybernetics* **20** (1990), no. 5, 1238–1239.
- [226] Jean-François Maitre and François Musy, *Multigrid methods: Convergence theory in a variational framework*, *SIAM Journal on Numerical Analysis* **21** (1984), no. 4, 657–671.
- [227] S. Majumdar, M. Kothari, P. Augat, D. C. Newitt, T. M. Link, J. C. Lin, T. Lang, Y. Lu, and H. K. Genant, *High resolution magnetic resonance imaging: Three-dimensional trabecular bone architecture and biomechanical properties*, *Bone* **22** (1998), no. 5, 445–454.
- [228] Sharlima Majumdar, Jon Lin, Thomas Link, Jacob Millard, Peter Augat, Xiaolong Ouyang, David Newitt, Robert Gould, Manish Kothari, and Harry Genant, *Fractal analysis of radiographs: assessment of trabecular bone structure and prediction of elastic modulus and strength*, *Medical Physics* **26** (1999), no. 7, 1330–1340.
- [229] J. Mandel, M. Brezina, and P. Vaněk, *Energy optimization of algebraic multigrid bases*, *Computing* **62** (1999), no. 3, 205–228.
- [230] Michèle Marcotte, Ali R. Taherian, and Yousef Karimi, *Thermophysical properties of processed meat and poultry products*, *Journal of Food Engineering* **88** (2008), no. 3, 315–322.
- [231] R. Marcus and S. Majumdar, *Osteoporosis*, ch. The nature of osteoporosis, pp. 3–17, Academic Press, 2001.
- [232] Robert Marcus, *The nature of osteoporosis*, *Journal of Clinical Endocrinology and Metabolism* **81** (1996), no. 1, 1–5.
- [233] Ana-Maria Matache and Christoph Schwab, *Multiscale and multiresolution methods*, *Lecture Notes in Computational Science and Engineering*, vol. 20, ch. Generalized FEM for Homogenization Problems, pp. 197–237, Springer, Berlin, 2002.
- [234] Ana-Maria Matache and Christoph Schwab, *Two-scale FEM for homogenization problems*, *Mathematical Modelling and Numerical Analysis* **36** (2002), no. 4, 537–572.
- [235] Makoto Matsumoto and Takuji Nishimura, *Mersenne twister: A 623-dimensionally equidistributed uniform pseudo-random number generator*, *ACM Transactions on Modeling and Computer Simulation* **8** (1998), no. 1, 3–30.
- [236] Sergey V. Matveyev, *Approximation of isosurface in the marching cube: Ambiguity problem*, *IEEE Conference on Visualization*, 1994, pp. 288–292.
- [237] Dimitri J. Mavriplis, *Multigrid strategies for viscous flow solvers on anisotropic unstructured meshes*, *ICASE Report 98-6*, Nasa Langley Research Center, 1998, NASA/CR-1998-206910.
- [238] D. A. McCubbrey, D. D. Cody, E. L. Peterson, J. L. Kuhn, M. J. Flynn, and S. A. Goldstein, *Static and fatigue failure properties of thoracic and lumbar vertebral bodies and their relation to regional density*, *Journal of Biomechanics* **28** (1995), no. 8, 891–899.

- [239] James McNames, *An effective color scale for simultaneous color and gray-scale publications*, IEEE Signal Processing Magazine **23** (2006), no. 1, 82–87.
- [240] Jens Markus Melenk, *On generalized finite element methods*, Dissertation, University of Maryland, 1995.
- [241] Jens Markus Melenk and Ivo Babuška, *The partition of unity finite element method*, Research Report 96-01, Seminar für angewandte Mathematik, Eidgenössische Technische Hochschule Zürich, January 1996.
- [242] L. J. Melton III, M. Thamer, N. F. Ray, J. K. Chan, C. H. Chesnut III, T. A. Einhorn, C. C. Johnston, L. G. Raisz, S. L. Silverman, and E. S. Siris, *Fractures attributable to osteoporosis: report from the national osteoporosis foundation*, Journal of Bone Mineral Research **12** (1997), 16–23.
- [243] Anthony L. Mescher, *Junqueira's basic histology: Text and atlas*, 12th ed., McGraw-Hill, 2009.
- [244] Gary L. Miller, Dafna Talmor, and Shang-Hua Teng, *Optimal coarsening of unstructured meshes*, Journal of Algorithms **31** (1999), 29–65.
- [245] Gary L. Miller, Dafna Talmor, Shang-Hua Teng, and Noel Walkington, *A Delaunay based numerical method for three dimensions: generation, formulation, and partition*, Proceedings of the twenty-seventh annual ACM symposium on Theory of computing, Annual ACM Symposium on Theory of Computing, 1995, pp. 683–692.
- [246] Gary L. Miller, Dafna Talmor, Shang-Hua Teng, and Noel Walkington, *On the radius-edge condition in the control volume method*, SIAM Journal on Numerical Analysis **36** (1999), no. 6, 1690–1708.
- [247] Nicolas Moës, John Dolbow, and Ted Belytschko, *A finite element method for crack growth without remeshing*, International Journal for Numerical Methods in Engineering **46** (1999), 131–150.
- [248] H. M. Möller, *Kubaturformeln mit minimaler Knotenzahl*, Numerische Mathematik **25** (1976), 185–200.
- [249] Elise F. Morgan and Tony M. Keaveny, *Dependence of yield strain of human trabecular bone on anatomic site*, Journal of Biomechanics **34** (2001), 569–577.
- [250] Elsie F. Morgan, Oscar C. Yeh, and Tony M. Keaveny, *Damage in trabecular bone at small strains*, European Journal of Morphology **42** (2005), no. 1/2, 13–21.
- [251] J. D. Moulton, S. Knapek, and J. E. Dendy, *Multilevel upscaling in heterogeneous porous media*, CNLS research highlight, Los Alamos National Laboratories, January 1999.
- [252] J. David Moulton, Joel E. Dendy Jr., and James M. Hyman, *The black box multigrid numerical homogenization algorithm*, Journal of Computational Physics **142** (1998), no. 1, 80–108, Article No. CP985911.
- [253] Ralph Müller, Tor Hildebrand, and Peter Rügsegger, *Non-invasive bone biopsy: a new method to analyse and display the three-dimensional structure of trabecular bone*, Physics in Medicine and Biology **39** (1994), no. 1, 145–164.
- [254] David Mumford and Jayant Shah, *Optimal approximation by piecewise smooth functions and associated variational problems*, Communications on Pure and Applied Mathematics **42** (1989), no. 5, 577–685.
- [255] Elizabeth R. Myers and Sara E. Wilson, *Biomechanics of osteoporosis and vertebral fracture*, Spine **22** (1997), no. 24S, 25S–31S.
- [256] O. Nemitz, M. Rumpf, T. Tasdizen, and R. Whitaker, *Anisotropic curvature motion for structure enhancing smoothing of 3D MR angiography data*, Journal of Mathematical Imaging and Vision **27** (2007), no. 3, 217–229.
- [257] D. C. Newitt, S. Majumdar, B. van Rietbergen, G. von Ingersleben, S. T. Harris, H. K. Genant, C. Chesnut, P. Garnero, and B. MacDonald, *In vivo assessment of architecture and micro-finite element analysis derived indices of mechanical properties of trabecular bone in the radius*, Osteoporosis International **13** (2002), no. 1, 6–17.
- [258] R. A. Nicolaides, *On some theoretical and practical aspects of multigrid methods*, Mathematics of Computation **33** (1979), no. 147, 933–952.

- [259] Glen L. Niebur, Michael J. Feldstein, Jonathan C. Yuen, Tony J. Chen, and Tony M. Keaveny, *High-resolution finite element models with tissue strength asymmetry accurately predict failure of trabecular bone*, *Journal of Biomechanics* **33** (2000), 1575–1583.
- [260] Gregory M. Nielson and Bernd Hamann, *The asymptotic decider: Resolving the ambiguity in marching cubes*, *IEEE Conference on Visualization*, 1991, pp. 83–91.
- [261] Ola Nilsson and Andreas Söderström, *Euclidian distance transform algorithms: A comparative study*, Tech. Report 2, Linköping University, 2007.
- [262] J. J. O'Connor and E. F. Robertson, *MacTutor History of Mathematics*, 1997–2008, <http://www-history.mcs.st-andrews.ac.uk>.
- [263] J. T. Oden, C. A. M. Duarte, and O. C. Zienkiewicz, *A new cloud-based hp finite element method*, *Computer methods in mechanics and engineering* **153** (1998), 117–126.
- [264] Tinsley J. Oden, *Historical comments on finite elements*, *Proceedings of the ACM conference on History of scientific and numeric computation*, 1987, pp. 125–130.
- [265] Anders Odgaard, Jesper Kabel, Bert van Rietbergen, Michel Dalstra, and Rik Huiskes, *Fabric and elastic principal directions of cancellous bone are closely related*, *Journal of Biomechanics* **30** (1997), no. 5, 487–495.
- [266] Stanley Osher and James A. Sethian, *Fronts propagating with curvature dependent speed: Algorithms based on Hamilton–Jacobi formulations*, *Journal of Computational Physics* **79** (1988), no. 1, 12–49.
- [267] Martin Ostoja-Starzewski, *Material spatial randomness: From statistical to representative volume element*, *Probabilistic Engineering Mechanics* **21** (2006), 112–132.
- [268] Xiaolong Ouyang, Sharmila Majumdar, Thomas M. Link, Ying Lu, Peter Augat, John Lin, David Newitt, and Harry K. Genant, *Morphometric texture analysis of spinal trabecular bone structure assessed using orthogonal radiographic projections*, *Medical Physics* **25** (1998), no. 10, 2037–2045.
- [269] Dieter H. Pahr and Philippe K. Zysset, *Influence of boundary conditions on computed apparent elastic properties of cancellous bone*, *Biomechanics and Modeling in Mechanobiology* **7** (2007), no. 6, 463–476.
- [270] Nikhil R. Pal and Sankar K. Pal, *A review on image segmentation techniques*, *Pattern Recognition* **26** (1993), no. 9, 1277–1294.
- [271] Jamshid Parvizian, Alexander Düster, and Ernst Rank, *Finite cell method*, *Computational Mechanics* **41** (2007), no. 1, 121–133.
- [272] T. Pätz, T. Kröger, and T. Preusser, *Simulation of radiofrequency ablation including water evaporation*, *Proceedings of the World Congress on Medical Physics and Biomedical Engineering*, 2009.
- [273] Torben Pätz, *Composite FE für ein Mehrphasen-Modell zur Simulation von Radio-Frequenz-Ablation*, Diplom thesis, Universität Bremen, November 2008.
- [274] A. Pegoretti, L. Fambri, G. Zappini, and M. Bianchetti, *Finite element analysis of a glass fibre reinforced composite endodontic post*, *Biomaterials* **23** (2002), no. 13, 2667–2682.
- [275] Pietro Perona and Jitendra Malik, *Scale-space and edge detection using anisotropic diffusion*, *IEEE Transactions on Pattern Analysis and Machine Intelligence* **12** (1990), no. 7, 629–639.
- [276] Dzung L. Pham, Chenyang Xu, and Jerry L. Prince, *Current methods in image segmentation*, *Annual Reviews of Biomedical Engineering* **2** (2000), 315–337.
- [277] Anne Polikeit, Stephen J. Ferguson, Lutz P. Nolte, and Tracy E. Orr, *Factors influencing stresses in the lumbar spine after the insertion of intervertebral cages: finite element analysis*, *European Spine Journal* **12** (2003), 413–420.
- [278] Anne Polikeit, Stephen J. Ferguson, Lutz P. Nolte, and Tracy E. Orr, *The importance of the endplate for interbody cages in the lumbar spine*, *European Spine Journal* **12** (2003), 556–561.

- [279] Anne Polikeit, Lutz P. Nolte, and Stephen J. Ferguson, *Simulated influence of osteoporosis and disc degeneration on the load transfer in a lumbar functional spine unit*, *Journal of Biomechanics* **37** (2004), no. 7, 1061–1069.
- [280] T. Preußner and M. Rumpf, *An adaptive finite element method for large scale image processing*, *Journal of Visual Communication and Image Representation* **11** (2000), no. 2, 183–195.
- [281] Tobias Preusser, Martin Rumpf, Stefan Sauter, and Lars Ole Schwen, *3D composite finite elements for elliptic boundary value problems with discontinuous coefficients*, (2011), accepted at *SIAM Journal on Scientific Computing*.
- [282] Tobias Preusser, Martin Rumpf, and Lars Ole Schwen, *Finite element simulation of bone microstructures*, *Proceedings of the 14th Workshop on the Finite Element Method in Biomedical Engineering, Biomechanics and Related Fields*, University of Ulm, July 2007, pp. 52–66.
- [283] M. A. Price, C. G. Armstrong, and M. A. Sabin, *Hexahedral mesh generation by medial surface subdivision: Part I. solids with convex edges*, *International Journal for Numerical Methods in Engineering* **38** (1995), no. 19, 3335–3359.
- [284] J. W. Pugh, R. M. Rose, and E. L. Radin, *A structural model for the mechanical behavior of trabecular bone*, *Journal of Biomechanics* **6** (1973), no. 6, 657–670.
- [285] Alfio Quarteroni, Riccardo Sacco, and Fausto Saleri, *Numerical mathematics*, *Texts in Applied Mathematics*, vol. 37, Springer-Verlag, New York, 2000.
- [286] Isabelle Ramière, Philippe Angot, and Michel Belliard, *A fictitious domain approach with spread interface for elliptic problems with general boundary conditions*, *Computer Methods in Applied Mechanics and Engineering* **196** (2007), 766–781.
- [287] A. Randell, P. N. Sambrook, T. V. Nguyen, H. Lapsley, G. Jones, P. J. Kelly, and J. A. Eisman, *Direct clinical and welfare costs of osteoporotic fractures in elderly men and women*, *Osteoporosis International* **5** (1995), no. 6, 427–432.
- [288] M. Rech, S. Sauter, and A. Smolianski, *Two-scale composite finite element method of the Dirichlet problem on complicated domains*, *Tech. Report 17-2003*, Universität Zürich, 2003.
- [289] M. Rech, S. Sauter, and A. Smolianski, *Two-scale composite finite element method for Dirichlet problems on complicated domains*, *Numerische Mathematik* **102** (2006), 681–708.
- [290] Markus Rech, *Composite finite elements: An adaptive two-scale approach to the non-conforming approximation of Dirichlet problems on complicated domains*, *Dissertation*, Universität Zürich, 2006.
- [291] Jae-Young Rho, Ting Y. Tsui, and George M. Pharr, *Elastic properties of human cortical and trabecular lamellar bone measured by nanoindentation*, *Biomaterials* **18** (1997), no. 20, 1325–1330.
- [292] M. Richter, H.-J. Wilke, P. Kluger, L. Claes, and W. Puhl, *Biomechanical evaluation of a newly developed monocortical expansion screw for use in anterior internal fixation of the cervical spine: In vitro comparison with two established internal fixation systems*, *Spine* **24** (1999), no. 3, 207–212.
- [293] T. W. Ridler and S. Calvard, *Picture thresholding using an iterative selection method*, *IEEE Transactions on Systems, Man, and Cybernetics* **SMC-8** (1978), no. 8, 630–632.
- [294] Bernice E. Rogowitz and Lloyd A. Treinish, *Why should engineers and scientists be worried about color?*, *IBM Research Report*.
- [295] Annette Rudolf, *Simulation von Wärmeübergängen in der Distribution und Lagerung von kühlpflichtigen Lebensmitteln zur Optimierung stufenübergreifender QM- und Kühlkettenmanagementsysteme*, *Diplom thesis*, University of Bonn, December 2009.
- [296] Martin Rumpf, Lars Ole Schwen, Hans-Joachim Wilke, and Uwe Wolfram, *Numerical homogenization of trabecular bone specimens using composite finite elements*, *1st Conference on Multiphysics Simulation – Advanced Methods for Industrial Engineering*, Fraunhofer, 2010.

Bibliography

- [297] Vita Rutka, *Immersed interface methods for elliptic boundary value problems*, Dissertation, Technische Universität Kaiserslautern, 2005, D 386.
- [298] Vita Rutka and Andreas Wiegmann, *Explicit jump immersed interface method for virtual material design of the effective elastic moduli of composite materials*, Numerical Algorithms **43** (2006), no. 4, 309–330.
- [299] Vita Rutka, Andreas Wiegmann, and Heiko Andrä, *EJIM for calculation of effective elastic moduli in 3d linear elasticity*, Tech. Report 93, Fraunhofer ITWM, Kaiserslautern, Germany, 2006.
- [300] Hanan Samet, *The quadtree and related hierarchical data structures*, ACM Computing Surveys **16** (1984), no. 2, 187–260.
- [301] V. K. Saul'ev, *A method for automating the solution of boundary value problems on high-speed computers*, Doklady Mathematics **3** (1963), 763–766, original version: Doklady Adakemii Nauk SSSR **144** (1962), pp. 497–500.
- [302] V. K. Saul'ev, *On solution of some boundary value problems on high performance computers by fictitious domain method*, Siberian Mathematical Journal **4** (1963), 912–925.
- [303] S. Sauter, *Composite finite elements and multigrid*, Tech. report, Institut für Mathematik, 2002, Lecture Notes for the Zürich Summer School 2002.
- [304] S. A. Sauter and R. Warnke, *Composite finite elements for elliptic boundary value problems with discontinuous coefficients*, Computing **77** (2006), no. 1, 29–55.
- [305] Steve Schaffer, *A semicoarsening multigrid method for elliptic partial differential equations with highly discontinuous and anisotropic coefficients*, SIAM Journal on Scientific Computing **20** (1998), no. 1, 228–242.
- [306] Arne Schneck, *Konvergenz von Rekonstruktionsalgorithmen in der 2D-Tomographie: Der volldiskrete Fall*, Diplom thesis, Universität Karlsruhe, May 2006.
- [307] Will Schroeder, Ken Martin, and Bill Lorensen, *The visualization toolkit*, 4 ed., Kitware, 2006.
- [308] Michael Schünke, Erik Schulte, Udo Schumacher, Markus Voll, and Karl Wesker, *Allgemeine Anatomie und Bewegungssystem*, Thieme, Stuttgart/New York, 2005.
- [309] Lars Ole Schwen, *Numerical simulation of transport and diffusion in drainage media*, Diplom thesis, University of Duisburg-Essen, 2005.
- [310] Lars Ole Schwen, Tobias Preusser, and Martin Rumpf, *Composite finite elements for 3D elasticity with discontinuous coefficients*, Proceedings of the 16th Workshop on the Finite Element Method in Biomedical Engineering, Biomechanics and Related Fields, University of Ulm, 2009, accepted.
- [311] Lars Ole Schwen, Uwe Wolfram, Hans-Joachim Wilke, and Martin Rumpf, *Determining effective elasticity parameters of microstructured materials*, Proceedings of the 15th Workshop on the Finite Element Method in Biomedical Engineering, Biomechanics and Related Fields, University of Ulm, July 2008, pp. 41–62.
- [312] L. Ridgway Scott and Shangyou Zhang, *Higher-dimensional nonnested multigrid methods*, Mathematics of Computation **58** (1992), no. 198, 457–466.
- [313] J. A. Sethian and A. Wiegmann, *Structural boundary design via level set and immersed interface methods*, Journal of Computational Physics **163** (2000), no. 2, 489–528.
- [314] A. Vahid Shahidi and P. Savard, *Forward problem of electrocardiography: construction of human torso models and felt calculation using finite element method*, Medical and Biological Engineering and Computing **32** (1994), S25–S33.
- [315] John W. Sheldon, *On the numerical solution of elliptic difference equations*, Mathematical Tables and Other Aids to Computation **9** (1955), no. 51, 101–112.
- [316] Jonathan Richard Shewchuk, *Tetrahedral mesh generation by Delaunay refinement*, Proceedings of the fourteenth annual symposium on Computational geometry (Minneapolis, Minnesota, U.S.A.), 1998, pp. 86–95.
- [317] Jonathan Richard Shewchuk, *Lecture notes on Delaunay mesh generation*, 1999.

- [318] Jonathan Richard Shewchuk, *What is a good linear element? Interpolation, conditioning, and quality measures*, Proceedings of the 11th International Meshing Roundtable, Sandia National Laboratories, September 2002, pp. 115–126.
- [319] Kenji Shimada, Atsushi Yamada, and Takayuki Itoh, *Anisotropic triangular meshing of parametric surfaces via close packing of ellipsoidal bubbles*, Proceedings of the 6th International Meshing Roundtable, Sandia National Laboratories, October 1997, pp. 375–390.
- [320] G. H. Shortley and R. Weller, *The numerical solution of Laplace's equation*, Journal of Applied Physics **9** (1938), 334–344.
- [321] M. J. Silva and L. J. Gibson, *Modeling the mechanical behavior of vertebral trabecular bone: Effects of age-related changes in microstructure*, Bone **21** (1997), no. 2, 191–199.
- [322] Matthew J. Silva, Tony M. Keaveny, and Wilson C. Hayes, *Load sharing between the shell and centrum in the lumbar vertebral body*, Spine **22** (1997), no. 2, 140–150.
- [323] Th. H. Smit, E. Schneider, and A. Odgaard, *Star length distribution: a volume-based concept for the characterization of structural anisotropy*, Journal of Microscopy **191** (1998), no. 3, 249–257.
- [324] Nadin Stahn, *Composite finite elements and multigrid*, Dissertation, Universität Zürich, 2006.
- [325] F. L. Stazi, E. Budyn, J. Chessa, and T. Belytschko, *An extended finite element method with higher-order elements for curved cracks*, Computational Mechanics **31** (2003), no. 1-2, 38–48.
- [326] Christina Stöcker, Simon Vey, and Axel Voigt, *AMDiS – adaptive multidimensional simulations: Composite finite elements and signed distance functions*, WSEAS Transactions on Circuits and Systems **4** (2005), no. 3, 111–116.
- [327] M. Stolarska, D. L. Chopp, N. Moës, and T. Belytschko, *Modelling crack growth by level sets in the extended finite element method*, International Journal for Numerical Methods in Engineering **51** (2001), no. 8, 943–960.
- [328] T. Strouboulis, I. Babuška, and K. Copps, *The design and analysis of the Generalized Finite Element Method*, Computer Methods in Applied Mechanics and Engineering **181** (2000), no. 1-3, 43–69.
- [329] T. Strouboulis, K. Copps, and I. Babuška, *The generalized finite element method*, Computer Methods in Applied Mechanics and Engineering **190** (2001), no. 32-33, 4081–4193.
- [330] Klaus Stüben, *A review of algebraic multigrid*, Journal of Computational and Applied Mathematics **128** (2001), no. 1-2, 281–309.
- [331] N. Sukumar and J.-H. Prévost, *Modeling quasi-static crack growth with the extended finite element method. Part I: Computer implementation*, International Journal of Solids and Structures **40** (2003), no. 26, 7513–7537.
- [332] S. Tamari, *Optimum design of the constant-volume gas pycnometer for determining the volume of solid particles*, Measurement Science and Technology **15** (2004), 549–558.
- [333] Luc Tartar, *Optimal shape design*, Lecture Notes in Mathematics, vol. 1740, ch. An Introduction to the Homogenization Method in Optimal Design, pp. 47–156, Springer, 2001.
- [334] Shang-Hua Teng and Chi Wai Wong, *Unstructured mesh generation: Theory, practice and applications*, International Journal of Computational Geometry and Applications **10** (2000), no. 3, 227–266.
- [335] Vidar Thomée, *Galerkin finite element methods for parabolic problems*, 2nd ed., Springer Series in Computational Mathematics, vol. 25, Springer, Berlin, 2006.
- [336] P. Thoutireddy, J. F. Molinari, E. A. Repetto, and M. Ortiz, *Tetrahedral composite finite elements*, International Journal for Numerical Methods in Engineering **53** (2002), no. 6, 1337–1351.
- [337] P. J. Thurner, P. Wyss, R. Voide, M. Stauber, M. Stampanoni, U. Sennhauser, and R. Müller, *Time-lapsed investigation of*

- three-dimensional failure and damage accumulation in trabecular bone using synchrotron light*, *Bone* **39** (2006), 289–299.
- [338] G. M. Treece, R. W. Prager, and A. H. Gee, *Regularised marching tetrahedra: improved iso-surface extraction*, *Computers and Graphics* **23** (1999), no. 4, 583–598.
- [339] H. J. Trussell, *Comments on “picture thresholding using an iterative selection method”*, *IEEE Transactions on Systems, Man, and Cybernetics SMC-9* (1979), no. 5, 311.
- [340] Kerem Ün, Grant Bevill, and Tony M. Keaveny, *The effects of side-artifacts on the elastic modulus of trabecular bone*, *Journal of Biomechanics* **39** (2006), 1955–1963.
- [341] J. C. van der Linden, J. Homminga, J. A. N. Verhaar, and H. Weinans, *Mechanical consequences of bone loss in cancellous bone*, *Journal of Bone and Mineral Research* **16** (2001), no. 3, 457–465.
- [342] B. van Rietbergen, R. Huiskes, F. Eckstein, and P. Rügsegger, *Trabecular bone tissue strains in the healthy and osteoporotic human femur*, *Journal of Bone and Mineral Research* **18** (2003), no. 10, 1781–1788.
- [343] B. van Rietbergen, R. Müller, D. Ulrich, P. Rügsegger, and R. Huiskes, *Tissue stresses and strain in trabeculae of canine proximal femur can be quantified from computer reconstructions*, *Journal of Biomechanics* **32** (1999), 165–173.
- [344] B. van Rietbergen, A. Odgaard, J. Kabel, and R. Huiskes, *Direct mechanics assessment of elastic symmetries and properties of trabecular bone architecture*, *Journal of Biomechanics* **29** (1996), no. 12, 1653–1657, Technical Note.
- [345] B. van Rietbergen, H. Weinans, R. Huiskes, and A. Odgaard, *A new method to determine trabecular bone elastic properties and loading using micromechanical finite-element models*, *Journal of Biomechanics* **28** (1995), no. 1, 69–81.
- [346] B. van Rietbergen, H. Weinans, R. Huiskes, and B. J. W. Pollman, *Computational strategies for iterative solutions of large FEM applications employing voxel data*, *International Journal for Numerical Methods in Engineering* **39** (1996), 2473–2767.
- [347] Evan VanderZee, Anil N. Hirani, Damrong Guoy, and Edgar A. Ramos, *Well-centered triangulation*, *SIAM Journal on Scientific Computing* **31** (2010), no. 6, 4497–4523.
- [348] Petr Vaněk, Marian Brezina, and Jan Mandel, *Convergence of algebraic multigrid based on smoothed aggregation*, UCD CCM Report 126, University of Colorado at Denver, February 1998, updated April 1998.
- [349] Petr Vaněk and Jitka Kříšková, *Two-level method on unstructured meshes with convergence rate independent of the coarse-space size*, Tech. Report 33, University of Colorado at Denver, 1995.
- [350] Petr Vaněk, Jan Mandel, and Marian Brezina, *Algebraic multigrid on unstructured meshes*, UCD CCM Report 034, University of Colorado at Denver, 1994.
- [351] Petr Vaněk, Jan Mandel, and Marian Brezina, *Algebraic multigrid by smoothed aggregation for second and fourth order elliptic problems*, UCD CCM Report 036, University of Colorado at Denver, 1995.
- [352] Tetyana Vdovina, Susan E. Minkoff, and Oksana Korostyshevskaya, *Operator upscaling for the acoustic wave equation*, *Multiscale Modeling and Simulation* **4** (2005), no. 4, 1305–1338.
- [353] Pieter Verboven, D. Flick, B. M. Nicolai, and G. Alvarez, *Modelling transport phenomena in refrigerated food bulks, packages and stacks: basics and advances*, *International Journal of Refrigeration* **29** (2006), no. 6, 985–997.
- [354] Lara M. Vigneron, Jaques G. Verly, and Simon K. Warfield, *Medical simulation*, Lecture Notes in Computer Science, vol. 3078, ch. On Extended Finite Element Method (XFEM) for Modelling of Organ Deformations Associated with Surgical Cuts, pp. 134–143, Springer, Berlin/Heidelberg, 2004, International Symposium ISMS 2004.
- [355] Katharina Vogt, *Temperature as influence factor on the quality of meat during process and distribution*, December 2008, Term Essay, University of Bonn.

- [356] W. Voigt, *Ueber die Beziehung zwischen den beiden Elasticitätsconstanten isotroper Körper*, *Annalen der Physik* **274** (1889), no. 12, 573–587.
- [357] Richard von Mises, *Mechanik der Körper im plastisch-deformablen Zustand*, *Nachrichten von der Gesellschaft der Wissenschaften zu Göttingen, Mathematisch-Physikalische Klasse* **4** (1913), 582–592.
- [358] Liming M. Voo, Srirangam Kumaresan, Narayan Yoganandan, Frank A. Pintar, and Joseph F. Cusik, *Finite element analysis of cervical facetectomy*, *Spine* **22** (1997), no. 9, 964–969.
- [359] N. J. Wachter, G. D. Krischak, M. Mentzel, M. R. Sarkar, T. Ebinger, L. Kinzl, L. Claes, and P. Augat, *Correlation of bone mineral density with strength and microstructural parameters of cortical bone in vitro*, *Bone* **31** (2002), no. 1, 90–95.
- [360] John T. Wallis, *Methods towards better multigrid solver convergence*, 2008, arXiv:0805.3041v1 [math.NA].
- [361] Wing Lok Wan, *Scalable and multilevel iterative methods*, Dissertation, University of California, Los Angeles, 1998.
- [362] Wing Lok Wan, *Interface preserving coarsening multigrid for elliptic problems with highly discontinuous coefficients*, *Numerical Linear Algebra with Applications* **7** (2000), no. 7-8, 727–742.
- [363] Lijun Wang and Da-Wen Sun, *Recent developments in numerical modelling of heating and cooling processes in the food industry—a review*, *Trends in Food and Science Technology* **14** (2003), no. 10, 408–423.
- [364] Rainer Warnke, *Schnelle Löser für elliptische Randwertprobleme mit springenden Koeffizienten*, Dissertation, Universität Zürich, 2003.
- [365] Cari M. Whyne, Serena S. Hu, Stephen Klisch, and Jeffrey C. Lotz, *Effect of the pedicle and posterior arch on vertebral body strength predictions in Finite Element modeling*, *Spine* **23** (1998), no. 8, 899–907.
- [366] Andreas Wiegmann, *The explicit jump immersed interface method and interface problems for differential equations*, Dissertation, University of Washington, Seattle, U.S.A., 1998.
- [367] Andreas Wiegmann, *The explicit jump immersed interface method and integral formulas*, Tech. Report 43566, LBNL, June 1999.
- [368] Andreas Wiegmann and Kenneth P. Bube, *The immersed interface method for nonlinear differential equations with discontinuous coefficients and singular sources*, *SIAM Journal on Numerical Analysis* **35** (1998), no. 1, 177–200.
- [369] Andreas Wiegmann and Kenneth P. Bube, *The explicit-jump immersed interface method: Finite difference methods for PDEs with piecewise smooth solutions*, *SIAM Journal on Numerical Analysis* **37** (2000), no. 3, 827–862.
- [370] H.-J. Wilke, A. Kettler, and L. Claes, *Primary stabilizing effect of interbody fusion devices for the cervical spine: an in vitro comparison between three different cage types and bone cement*, *European Spine Journal* **9** (2000), no. 5, 410–416.
- [371] H.-J. Wilke, S. T. Krischak, K. H. Wenger, and L. E. Claes, *Load-displacement properties of the thoracolumbar calf spine: Experimental results and comparison to known human data*, *European Spine Journal* **6** (1997), no. 2, 129–137.
- [372] H.-J. Wilke, A. Rohlmann, S. Neller, M. Schultheiß, G. Bergmann, F. Graichen, and L. Claes, *It is possible to simulate physiologic loading conditions by applying pure moments?*, *Spine* **26** (2001), no. 6, 636–642.
- [373] Hans-Joachim Wilke, Annette Kettler, and Lutz Claes, *Are sheep spines a valid biomechanical model for human spines?*, *Spine* **22** (1997), no. 20, 2365–2374.
- [374] Hans-Joachim Wilke, Annette Kettler, Karl Howard Wenger, and Lutz Eberhard Claes, *Anatomy of the sheep spine and its comparison to the human spine*, *The Anatomical Record* **247** (1997), 542–555.
- [375] J. Willix, S. J. Lovatt, and N. D. Amos, *Additional thermal conductivity values of*

- foods measured by a guarded hot plate, *Journal of Food Engineering* **37** (1998), no. 2, 159–174.
- [376] S. Winter, S. Ströhla, and G. Kuhn, *Elastisch-plastisches Verhalten von Verbunden mit zellularem Kern*, 14. Symposium Verbundwerkstoffe und Werkstoffverbunde, Universität Wien, 2003, pp. 587–592.
- [377] Adam Wittek, Ron Kikinis, Simon K. Warfield, and Karol Miller, *Brain shift computation using a fully nonlinear biomechanical model*, *Medical Image Computing and Computer-Assisted Intervention – MICCAI 2005* (J. Duncan and G. Gerig, eds.), vol. 3750, 2005, pp. 583–590.
- [378] Julius Wolff, *Ueber die innere Architektur der Knochen und ihre Bedeutung für die Frage vom Knochenwachsthum*, *Virchows Archiv* **50** (1870), no. 3, 389–450.
- [379] Uwe Wolfram, Lars Ole Schwen, Ulrich Simon, Martin Rumpf, and Hans-Joachim Wilke, *Statistical osteoporosis models using composite finite elements: A parameter study*, *Journal of Biomechanics* **42** (2009), no. 13, 2205–2209.
- [380] Uwe Wolfram, Hans-Joachim Wilke, and Philippe K. Zysset, *Rehydration of vertebral trabecular bone: Influences on its anisotropy, its stiffness and the indentation work with a view to age, gender and vertebral level*, *Bone* **46** (2010), 348–354.
- [381] Uwe Wolfram, Hans-Joachim Wilke, and Philippe K. Zysset, *Transverse isotropic elastic properties of vertebral trabecular bone matrix measured using microindentation under dry conditions (effects of age, gender and vertebral level)*, *Journal of Mechanics in Medicine and Biology* **10** (2010), no. 1, 139–150.
- [382] Dae Gon Woo, Ye-Yeon Won, Han Sung Kim, and Dohyung Lim, *A biomechanical study of osteoporotic vertebral trabecular bone: The use of micro-CT and high-resolution finite element analysis*, *Journal of Mechanical Science and Technology* **21** (2007), 593–601.
- [383] Jinchao Xu, *Theory of multilevel methods*, PhD dissertation, Cornell University, May 1989.
- [384] Jinchao Xu, *Iterative methods by space decomposition and subspace correction*, *SIAM Review* **34** (1992), no. 4, 581–613.
- [385] O. C. Yeh and T. M. Keaveny, *Biomechanical effects of interspecimen variations in trabecular architecture: A three-dimensional finite element study*, *Bone* **25** (1999), no. 2, 223–228.
- [386] N. Yoganandan, S. Kumaresan, L. Voo, and F. A. Pintar, *Finite Element applications in human cervical spine modeling*, *Spine* **21** (1996), no. 15, 1824–1834.
- [387] David Young, *Iterative methods for solving partial differential equations of elliptic type*, *Transactions of the American Mathematical Society* **76** (1954), no. 1, 92–111.
- [388] H. Yserentant, *Old and new convergence proofs for multigrid methods*, *Acta Numerica* (1993), 285–326.
- [389] Jun Zhang, *Acceleration of five-point red-black Gauss-Seidel in multigrid for Poisson equation*, *Applied Mathematics and Computation* **80** (1996), no. 1, 73–93.
- [390] Hongkai Zhao, *A fast sweeping method for Eikonal equations*, *Mathematics of Computation* **74** (2005), no. 250, 603–627.
- [391] Wang Zhe, Meng Hui, Ge Manling, and Guyoa Dong, *A simulation of the abnormal EEG morphology by the 3-D finite element method*, *Proceedings of the 2005 IEEE Engineering in Medicine and Biology 27th Annual Conference (Shanghai, China), September 2005*, pp. 3620–3623.
- [392] P. K. Zysset, R. W. Goulet, and S. J. Hollister, *A global relationship between trabecular bone morphology and homogenized elastic properties*, *Journal of Biomedical Engineering* **120** (1999), 640–646.
- [393] P. K. Zysset, M. S. Ominsky, and A. A. Goldstein, *A novel 3D microstructural model for trabecular bone: I. The relationship between fabric and elasticity*, *Computer Methods in Biomechanics and Biomedical Engineering* **1** (1998), no. 4, 321–331.

Index

- active counterpart DOF, 76
- active counterpart node, 76
- adaptive methods, 5
- adjacent simplices, 34
- algebraic multigrid, 10
- AMG, 10
- aspect ratio, 31
- auxetic, 16

- block mass matrix, 60

- Cartesian grid, 5
- CFE basis functions
 - for complicated domains, 36
 - for discontinuous coefficients
 - scalar case, 42
 - vector-valued case, 47
- characteristic function, 36
- coarsening weights, 92
- composition weights, 34
- compression, 18
- computed tomography, 8
- conservation of energy, 20
- constrained nodes, 34
- constraining nodes, 34
 - geometrically, 34
 - patch, 34
- coupling condition, 20
- CT, 8

- deformation, 14
- Delaunay triangulation, 4
- denoising, 8
- density, 13
- detour-connected, 149
- Dewar flask, 123
- diameter-to-length ratio, 131

- Dirichlet boundary condition, 56
- displacement, 14
- DOF, 7

- Einstein summation convention, 20
- elastic energy, 15
- elasticity matrix, 60
- elasticity tensor, 14
- equilibrium of force, 23
- Euclidian gradient, 20
- Euler timestepping, implicit, 59
- even nodes, 90
- extended finite element method, 6

- fictitious domain method, 6
- Frobenius norm, vii
- fundamental cell, 11, 64

- Galerkin coarsening, 91
- generalized finite element method, 6
- geometric multigrid, 10
- GFEM, 6
- grid depth, 90

- heat flux, 13, 20
- helium micropycnometry, 148
- homogenization, 10
- hp clouds, 6
- HSV color map, 85, 109

- immersed interface method, 5
- implicit Euler timestepping, 59
- inactive node, 76
- interface, 28

- jump, 19

- kink ratio, 21

- Kronecker symbol, 17
- Lamé-Navier parameters, 16
- level set function, 28
- local auxiliary (sub-)mesh, 30
- magnetic resonance imaging, 8
- mass matrix, 58
- medical imaging, 3
- Mersenne twister, 131
- meshfree methods, 5
- meshing, 4
- meshless methods, 5
- MRI, 8
- Neumann boundary condition, 56
- orthotropic material, 17
- osteoporosis, 2
- partition of unity method, 6
- patch, 34
- periodic collapse, 77
- periodic domain for computation, 64
- periodic domain for evaluation, 64
- periodic extension, 77
- periodic restriction, 77
- pitch angle, 83
- PMMA, 3
- Poisson's ratio, 16
- polymethylmethacrylate, 3
- prototype functions, 21, 22, 24
- PUM, 6
- purely virtual nodes, 30
- reference configuration, 14
- regular cubic grid, 28
- regular nodes, 28, 30
- regular tetrahedral mesh, 28
- removal percentage, 131
- residual, 87
- rigid body motions, 18
- roll angle, 83
- segmentation, 8, 148
- shearing, 18
- signature, 29
- Sobolev space, 14
- specific heat capacity, 13
- stiffness matrix, 58
- strain tensor, 14
- stress, 14
- summation convention, 20
- Taylor approximation, 21
- Tb.Sp, 143
- thermal conductivity, 13
- thermal diffusivity, 13
- thresholding, 148
- trabecular separation, 143
- unfitted mesh, 6
- unreliability measure, 103
- upsampling, 10
- validation, 148
- vertebral fractures, 3
- vertebroplasty, 3
- virtual basis, 34
- virtual mesh, 30
- Voigt's notation, 15
- von Mises stress, 17
- Voronoi diagram, 4
- V cycles, 87
- WEB splines, 6
- weighted extended B-splines, 6
- W cycles, 87
- XFEM, 6
- yaw angle, 83
- Young's modulus, 16